Chamber and field studies on NO_3 reactivity and the detection of alkyl nitrates during the NO_3-induced oxidation of isoprene and terpenes

Dissertation

zur Erlangung des Grades

„Doktor der Naturwissenschaften"

im Promotionsfach Chemie

am Fachbereich Chemie, Pharmazie, Geographie und Geowissenschaften

der Johannes Gutenberg-Universität

in Mainz

Patrick Dewald

geboren in Gelsenkirchen

Mainz, 2022

D77
1. Berichterstatter:
2. Berichterstatter:
Tag der mündlichen Prüfung: 18.05.2022

“The greatest challenge to any thinker is stating the problem in a way that will allow a solution.”

(Bertrand Russell)

Contents

Abstract **1**

Zusammenfasung **4**

1 Outline of the thesis **5**

2 Introduction **7**

2.1 Tropospheric chemistry of reactive nitrogen species 8

2.2 Detection of atmospheric trace gases by CRDS 18

3 Overview of Results **23**

4 Evolution of NO_3 reactivity during the oxidation of isoprene **27**

5 Detection of isoprene-derived organic nitrates via TD-CRDS **45**

6 Measurements of NO_3 reactivity on the Kleiner Feldberg **65**

7 NO_3 reactivity inside a laboratory **101**

7.1 Introduction 101

7.2 Experimental 102

7.3 Results and Discussion 107

7.4 Summary and conclusions 111

8 Conclusions and outlook **113**

References **115**

Appendices **131**

A Supplement of Chapter 4 **132**

B Supplement of Chapter 5 **156**

C Supplement of Chapter 6 **170**

D Supplement to Chapter 7 **187**

Abstract

The reaction between the nitrate radical (NO_3) and volatile organic compounds (VOCs) can lead to alkyl nitrates (ANs). Some alkyl nitrates tend to deposit on particles to form secondary organic aerosols (SOA). The formation of SOA via the NO_3-initiated oxidation of VOCs with high AN yields such as isoprene or monoterpenes like limonene thus forms an important, irreversible NO_x loss path from the gas-phase and can be of great importance for air quality. This work focusses on direct measurements of VOC-induced NO_3 reactivity (k^{NO_3}) and ANs by cavity ring-down spectroscopy (CRDS) in field, chamber and indoor measurements:
Two chamber studies deal with the NO_3 + isoprene system: The first comprises 22 experiments at the large environmental SAPHIR chamber of the research centre in Jülich (FZJ) in scope of the NO3ISOP campaign and investigates the role of NO_3 during the primary and secondary oxidation of isoprene. Intercomparison of NO_3 reactivities derived from VOC measurements ($\Sigma k_i[VOC]_i$), box-model and nonstationary-state calculations (using NO_3, NO_2, N_2O_5 and O_3 mixing ratios) verified that the NO_3 reactivity measurements were accurate and allowed estimation of the rate constant for the reaction between NO_3 and isoprene-derived peroxy radicals (RO_2). The second was performed with another Teflon chamber (SCHARK) and focused on the quantification of isoprene-derived ANs (ISOP-NITs) with means of thermal-dissociation CRDS. Detailed experiments revealed that sampling ISOP-NITs through heated quartz glass inlets in the presence of O_3 yields to broad thermal dissociation profiles (isotherms) of ISOP-NITs overlapping with that of peroxy nitrates (PNs). A way to circumvent the interference of ISOP-NITs in the detection of PNs is deployment of a Teflon inlet.
Measurements of k^{NO_3} were also performed in a field campaign (TO2021) on the summit of the Kleiner Feldberg (KF, 825 m above sea level). k^{NO_3} was mainly determined by monoterpenes and in good agreement with $\Sigma k_i[VOC]_i$. k^{NO_3} contributed with ca. 16% to the overall NO_3 daytime loss and 50-60 % to the nighttime loss, which is caused by soil emissions of NO. Steady-state calculations allowed assessment of NO_3 mixing ratios and intercomparison with NO_3 measurements during previous campaigns on the KF.
Furthermore, NO_3 reactivity and mixing ratios of NO_2, O_3, NO_3 as well as N_2O_5 were measured for four days inside a laboratory. In the absence of NO, several pptv of N_2O_5 were detected, which was in good agreement with N_2O_5 mixing ratios derived from steady-state calculations. The indoor mixing ratios of NO_3 and N_2O_5 did not follow the typical diel cycle since photolysis is inefficient inside. Unidentified VOCs formed a relevant NO_3 sink.

Zusammenfassung

Die Reaktion zwischen dem Nitrat-Radikal (NO_3) und flüchtigen organischen Verbindungen (VOCs) führt unter anderem zur Bildung von Alkylnitraten (ANs). Manche Alklnitrate deponieren dabei auf Partikel und bilden so sekundäre organische Aerosole (SOA). Diese Entstehung von SOA aus der NO_3-initiierten Oxidation von VOCs mit hohen Ausbeuten an ANs, wie zum Beispiel im Falle von Isopren oder Monoterpenen wie Limonen, stellt einen wichtigen, irreversiblen Verlustprozess von NO_x in der Gas-Phase dar und kann somit von großer Bedeutung für die Luftqualität sein. Diese Arbeit fokussiert sich daher auf die direkte Messung von VOC-induzierter NO_3-Reaktivität (k^{NO_3}) und von ANs mittels Cavity-Ring-Down-Spektroskopie (CRDS) im Rahmen von Kammer-, Feld- und Indoor-Messungen.

Zwei Kammer-Studien beschäftigen sich mit dem NO_3-Isopren-System: Die erste Studie umfasst 22 Experimente, die an der großen Atmosphären-Simulationskammer (SAPHIR) am Forschungszentrum Jülich (FZJ) im Rahmen der NO3ISOP-Kampagne durchgeführt wurden, und untersucht die Rolle von NO_3 während der primären und sekundären Oxidation von Isopren. Der Vergleich zwischen k^{NO_3}, NO_3-Reaktivitäten aus VOC-Messungen ($\Sigma k_i[VOC]_i$), Modell-Simulationen und *nonstationary-state*-Rechnungen basierend auf Ratengleichungen (sowie Messungen von NO_3-, NO_2-, N_2O_5- und O_3-Konzentrationen) zeigt nicht nur, dass die direkten Messungen von k^{NO_3} akkurat sind, sondern ermöglicht auch die Bestimmung der Ratenkonstante für die Reaktion zwischen NO_3 und aus Isoprenoxidation stammender organischer Peroxy-Radikale (RO_2). Die zweite Kammer-Studie wurde mit einer anderen Teflon-Simulationskammer (SCHARK) durchgeführt und fokussiert sich auf die Quantifizierung von aus Isoprenoxidation stammenden organischen Nitraten (ISOP-NITs) mittels CRDS nach dessen thermischer Dissoziation zu NO_2. Eingehende Experimente zeigen, dass das Leiten von ISOP-NIT durch geheizte Quarzglas-Einlässe in der Anwesenheit von O_3 während der Probennahme zu einer Verbreiterung der thermischen Dissoziations-Profile (Isotherme) von ISOP-NITs führt, sodass diese mit der von Peroxy-Nitraten (PNs) überlappen. Einen Weg diese Problematik der Interferenz von ISOP-NITs in der Detektion von PNs zu umgehen bildet der Einsatz eines Teflon-Einlasses.

Direkte Messungen von k^{NO_3} wurden außerdem im Rahmen einer Feld-Kampagne (TO2021) auf der Spitze des Kleinen Feldbergs (KF, 825 m über dem Meeresspiegel) durchgeführt. k^{NO_3} wurde hauptsächlich von Monoterpenen bestimmt und ist in guter Übereinstimmung mit $\Sigma k_i[VOC]_i$. VOC-induzierte k^{NO_3} trägt mit ca. 16% am NO_3-Gesamtverlust bei Tag und mit nur 50-60% bei Nacht bei, wobei letzteres durch NO-Emissionen aus Böden verursacht wird. *Steady-state*-Rechnungen ermöglichen sowohl den Zugang zu NO_3-Konzentrationen für TO2021 sowie den Vergleich mit NO_3-Messungen während vergangener Kampagnen auf dem KF.

Desweiteren wurden k^{NO_3} und NO_2-, O_3-, NO_3- sowie N_2O_5-Konzentrationen über vier Tage in der Luft im Labor gemessen. In der Abwesenheit von NO, wurden einige pptv N_2O_5 detek-

tiert, was in guter Übereinstimmung mit den aus *steady-state*-Rechnungen ermittelten Werten ist. Die NO_3- und N_2O_5-Konzentrationen folgen nicht dem typischen Aussenluft-Tagesgang, da Photolyse von NO_3 in Innenräumen vernachlässigbar ist. Nicht identifizierte VOCs stellen selbst in Innenräumen einen signifikanten Verlustkanal für NO_3 dar.

CHAPTER 1

Objectives and outline of the thesis

The main objective of this thesis is to gain a deeper insight into the fate of the nitrate radical (NO_3) and its role during the oxidation of volatile organic compounds (VOCs) in the atmosphere. All studies presented in this work deal with the reaction between NO_3 + VOCs and the products formed:

$$NO_3 + VOC \rightarrow \text{products (e.g. alkyl nitrates)}$$

In the following chapter the atmospheric relevance of this reaction is outlined. In order to achieve the objective accurate quantification of NO_3 reactivity and alkyl nitrate mixing ratios is necessary which was accomplished with instruments relying on the technique of cavity ring-down spectroscopy (CRDS). This is why Chapter 2 introduces the reader not only to the chemistry of nitrogen oxides and the role of NO_3 in the troposphere, but also to the basic principle of the CRDS technique.
The third chapter presents a summary of the results of chamber, field and indoor measurements investigating NO_3 + VOC (e.g. isoprene, monoterpenes) reactions. Parts of the results have already been or are about to be published in peer-reviewed journals and each study is presented separately in Chapters 4-7:

- The first study in Chapter 4 deals with the evolution of the NO_3 reactivity during a chamber intensive of the NO_3 + isoprene system (NO3ISOP campaign) exploring different atmospherically relevant regimes. The analysis presented in this work aims to answer the question to which extent the NO_3 radical further contributes to secondary oxidation after the NO_3-initiated primary oxidation of isoprene. The results of this study have already been published:
  Dewald, P., Liebmann, J. M., Friedrich, N., Shenolikar, J., Schuladen, J., Rohrer, F., Reimer, D., Tillmann, R., Novelli, A., Cho, C., Xu, K., Holzinger, R., Bernard, F., Zhou, L.,

Mellouki, W., Brown, S. S., Fuchs, H., Lelieveld, J., and Crowley, J. N.: Evolution of NO_3 reactivity during the oxidation of isoprene, *Atmos. Chem. Phys.*, 20, 10 459–10 475, DOI: 10.5194/acp-20-10459-2020, **2020**.

- The second study in Chapter 5 also investigates the NO_3 + isoprene system in a simulation chamber, but the focus is on the detection of its main reaction products, i.e. alkyl nitrates (Wennberg et al., 2018), with means of thermal-dissociation CRDS. The results have also already been published and draw attention to possible problems and drawbacks that may occur during the quantification of isoprene-derived organic nitrates via their thermal dissociation:
  Dewald, P., Dörich, R., Schuladen, J., Lelieveld, J., and Crowley, J. N.: Impact of ozone and inlet design on the quantification of isoprene-derived organic nitrates by thermal dissociation cavity ring-down spectroscopy (TD-CRDS), *Atmos. Meas. Tech.*, 14, 5501–5519, DOI: 10.5194/amt-14-5501-2021, **2021**.

- In addition to the laboratory studies, the NO_3 reactivity setup was deployed during a field campaign (TO2021) on a semi-rural mountain site (Kleiner Feldberg), which is impacted by both biogenic and anthropogenic emissions. A quantitative analysis of the competing NO_3 loss processes (including reactions with monoterpenes and isoprene) in order to estimate the daytime and nighttime fate of the NO_3 radical is presented in a manuscript that has been submitted recently:
  Dewald, P., Nussbaumer, C.M., Schuladen, J., Ringsdorf, A., Edtbauer, A., Fischer, H., Williams, J., Lelieveld, J., and Crowley, J. N.: Fate of the nitrate radical at the summit of a semi-rural mountain site in Germany assessed with direct reactivity measurements, *Atmos. Chem. Phys. Discuss.*, 1–35, DOI: 10.5194/acp-2022-163, **2022**.

- Given the sparse availability of direct measurements of NO_3 mixing ratios (Nøjgaard, 2010; Arata et al., 2018) and the lack of NO_3 reactivity measurements in indoor environments, both quantities were measured in a four-day period inside a laboratory of the Max-Planck-Institute for Chemistry in the city of Mainz. This pilot study was performed with the intention of gaining insight into whether NO_3 chemistry may be of importance in indoor environments or not.

A summary of the conclusions and an outlook drawn from the above-mentioned studies are given in Chapter 8.

CHAPTER 2

Introduction

Both anthropogenic and biogenic emissions of reactive trace gases strongly affect chemical processes in the atmosphere and have a significant impact on climate and air quality (Crutzen and Lelieveld, 2001; Lelieveld et al., 2008; Pozzer et al., 2012). Especially with the beginning of the Industrial Revolution, processes like global warming as a consequence of increasing emissions of greenhouse gases like carbon dioxide (CO_2) (IPCC, 2014) or stratospheric ozone (O_3) depletion induced by emission of chlorofluorocarbons until the 1990s (Molina and Rowland, 1974; Crutzen, 1974; Solomon et al., 1986) emphasise the intensifying impact of anthropogenic emissions on our ecosystem - a circumstance that Nobel laureate Paul Crutzen accounted for by naming the epoch starting with the Industrial Revolution as "Anthropocene" (Crutzen and Stoermer, 2000). The most recent assessment report of the Intergovernmental Panel on Climate Change (IPCC) clearly attributed the accumulation of climate extremes (e.g. heatwaves, tropical cyclones) over the last years to human-induced processes. Moreover, the global surface temperature will increase by 1.5 - 2 °C, if greenhouse gas emissions are not rigorously decreased (IPCC, 2021).

Beside the impact on climate, chemistry that is initiated in the troposphere additionally impacts air quality: Pollution of the air e.g. with simple nitrogen oxides (NO_x = NO + NO_2) and volatile organic compounds (VOCs) of biogenic or anthropogenic origin enhances under certain conditions the formation of surface O_3 and, especially in urban environments, may lead to photochemical smog, which has negative effects on human health (Haagen-Smit, 1952; Chameides et al., 1988; Kampa and Castanas, 2008). Regular exposure to polluted ambient air increases the risk of suffering from cardiovascular diseases and reduces the life expectancy (Lelieveld et al., 2015, 2020).

Hence, a deep understanding of atmospheric chemistry and its underlying mechanisms is crucial for assessing the role of tropospheric oxidation processes on air composition. Due to the

harmful nature of O_3 and nitrogen oxides in particular, the regulation of NO_x emissions was included in various climate protection programmes (BMU, 2016; MTES, 2019). The chemical mechanisms taking place in a mixture of VOCs and NO_x are complex and can, depending on detailed conditions, result in efficient production of tropospheric ozone, which is toxic and acts as greenhouse gas in the upper troposphere (Crutzen and Lelieveld, 2001; Duncan et al., 2010; Pusede et al., 2015). For that reason, gaining insight into VOC oxidation processes as well as identifying significant sinks of NO_x in the troposphere are of great interest. The most important oxidizing agents of VOCs in the troposphere are O_3, hydroxyl radicals (OH) and nitrate radicals (NO_3) (Finlayson-Pitts and Pitts, 2000). Latter originate from oxidation of NO_x by O_3 and accounts for formation of alkyl nitrates ($RONO_2$, ANs) predominantly at nighttime (Wayne et al., 1991; Ng et al., 2017). Such organic nitrates may deposit on particulate matter to form secondary organic aerosols (SOA) and thus support irreversible NO_x removal from the gas phase (Fry et al., 2011; Ng et al., 2017; Fry et al., 2018; Mutzel et al., 2021) - an effect that can become competitive with removal by direct formation of nitric acid (HNO_3) via the reaction between NO_2 and OH (Romer Present et al., 2020). The non-methane VOC with the largest emission into the atmosphere is isoprene, which is why its degradation is of high relevance (Guenther et al., 2012). The oxidation of isoprene (and terpenes) by the nitrate radical was identified to be an efficient NO_x loss path, especially at night-time (Geyer and Platt, 2002; Fry et al., 2011; Foulds et al., 2021). This process can consequently have an important impact on the fate of NO_x, which is the main motivation for this work on NO_3 + VOC systems. An introduction into the tropospheric NO_x chemistry and its role in the oxidation of VOCs is given in the following sections of this chapter.

2.1 Chemistry of nitrogen oxides and other reactive nitrogen species in the troposphere

The atmosphere is formally divided into different layers. The measurements in this work deal with processes that take place within the first 13-17 km, the troposphere. Molecular nitrogen (N_2) and oxygen (O_2) with mixing ratios of 78 % and 21 % (values of dry air, Jacob (1999)) are the most abundant species in air. Water vapour (H_2O) concentrations vary within the lower percent range (Finlayson-Pitts and Pitts, 2000). Although air mainly consists of N_2 and O_2, their importance on tropospheric chemistry is low (Crutzen and Lelieveld, 2001). Trace gases, which owing to their high reactivity are only present in air with steady-state concentrations in the parts per billion by volume (ppbv) to parts per trillion by volume (pptv) range or even lower can have a strong impact on climate as already thoroughly discussed for the OH radical (Monks, 2005; Lelieveld et al., 2016). The same applies to NO_x, which may be oxidised to further nitrogen species once released into the atmosphere (to initiate e.g. the reaction of interest presented in Chapter 1). Mixing ratios of NO_x vary from the lower pptv range in

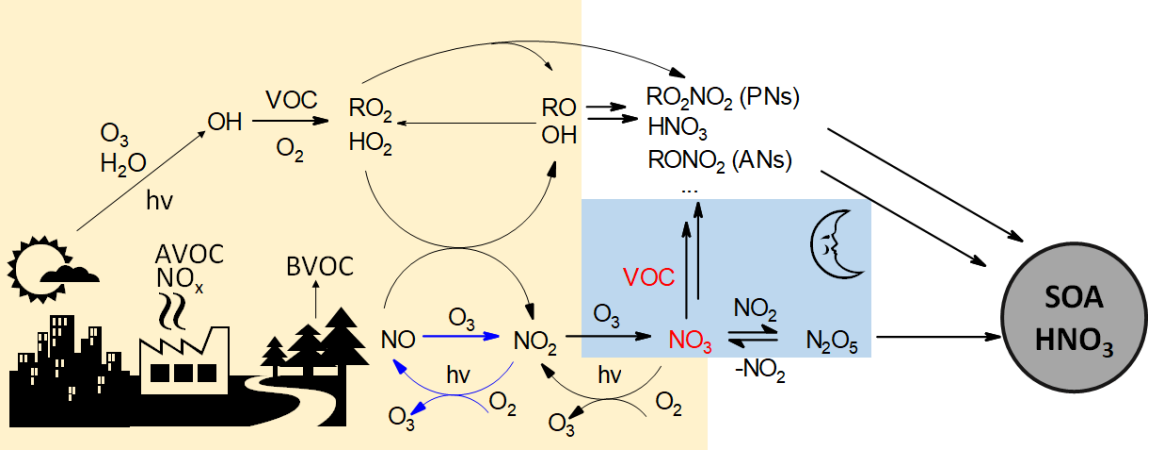

Figure 2.1: *Overview of atmospheric daytime and nighttime chemistry in relation to the photo-stationary NO_x cycle (blue). Processes impacting the NO_x cycle predominantly during daytime (e.g. the RO_x cycle) are within the yellow box, processes mostly relevant at nighttime are marked by the blue box. This work will focus on the oxidation of VOCs by NO_3 (red). Note that primary products of NO_3-initiated VOC oxidation are RO_2 as well (see Fig. 2.2) and that e.g. ozonolysis of VOCs may contribute to formation of RO_2, HO_2 and OH during both day- and nighttime. Scheme inspired and partially adapted from Monks (2005), Phillips et al. (2016) and Liu et al. (2022).*

remote areas (Stroud et al., 2002; Biswas et al., 2021), but increase to the ppbv range in urban areas (Wagner et al., 2012).

As already outlined in Chapter 1, this work focusses on the chemistry of the nitrate radical. Since NO_x is necessary to initiate this chemistry, this chapter introduces the reader to NO_x chemistry and that of other reactive nitrogen species formed. The role of reactive nitrogen species in relation to other important oxidants like OH or O_3 and their context in tropospheric oxidation chemistry has already been reviewed (Finlayson-Pitts and Pitts, 2000; Brown and Stutz, 2012) and thus only a brief overview of the key reactions is given here. Starting with NO_x and its fate during daytime, the atmospheric fate of the nitrate radical, dinitrogen pentoxide (N_2O_5) and the oxidation products of VOCs are considered. An overview of the most relevant reactions of nitrogen species in relation to other oxidation processes in the troposphere is depicted in Fig. 2.1 and these reactions are discussed in particular on the following pages.

2.1.1 NO_x and the Leighton relationship

The major sources of nitrogen oxides are of anthropogenic origin, e.g. from fuel combustion processes or human-initiated biomass burning (Jacob, 1999; IPCC, 2014) typically emitted as NO. The formation of NO occurs at high temperatures via thermal decomposition of molecular oxygen to O atoms (R1) in the ground state ($O(^3P)$, O onwards) and subsequent reaction with

molecular nitrogen (R2 and R3) according to the *Zel'dovich mechanism* (Zel'dovich, 1946).

$$O_2 + M \xrightarrow{\Delta} O + O + M \tag{R1}$$

$$O + N_2 \rightarrow NO + N \tag{R2}$$

$$N + O_2 \rightarrow NO + O \tag{R3}$$

Alternatively, an example for biogenic sources of NO_x are soils that emit nitric oxide arising from e.g. microbial activity (Pilegaard, 2013).
In the presence of O_3, NO is then oxidised to NO_2 (R4). During the daytime, NO_2 is photolysed to NO and O atoms (R5), which reform O_3 in the termolecular reaction with molecular oxygen (R6).

$$NO + O_3 \rightarrow NO_2 + O_2 \tag{R4}$$

$$NO_2 + h\nu \rightarrow NO + O \tag{R5}$$

$$O_2 + O + M \rightarrow O_3 + M \tag{R6}$$

As indicated in blue in Fig. 2.1 that gives a schematic representation of tropospheric NO_x chemistry, reactions R4 to R6 form a closed cycle in photo-stationary state as long as no other processes converting NO to NO_2 are involved (Leighton, 1961) - a cycle that is often referred to as the *Leighton relationship* (Wayne et al., 1991; Finlayson-Pitts and Pitts, 2000).

2.1.2 Impact of NO_x on daytime oxidation chemistry

This NO_x cycle can be influenced by other oxidation processes and in turn has a significant impact on surface ozone concentrations (Crutzen, 1979). In the troposphere, the photo-stationary state is affected by the presence of peroxy radicals (RO_2 and HO_2, yellow area in Fig. 2.1) originating e.g. from the oxidation of VOCs. During the daytime, the most reactive and relevant oxidizing agent for many VOCs is the OH radical (Larsen et al., 2001; Gligorovski et al., 2015; Wennberg et al., 2018). It is mainly generated from the photolysis ($\lambda \leq 420$ nm) of ozone leading to excited $O(^1D)$ atoms (R7). A small fraction of $O(^1D)$ reacts with water to form OH (R8), while the majority undergoes collisional relaxation to the ground state (R9) (Lelieveld et al., 2016). Note that quenching is not a net loss process since O_3 is then reformed via (R6) under atmospheric conditions.

$$O_3 + h\nu \rightarrow O(^1D) + O_2 \tag{R7}$$

$$O(^1D) + H_2O \rightarrow 2OH \tag{R8}$$

$$O(^1D) + M \rightarrow O + M \tag{R9}$$

In polluted environments, photolysis of nitrous oxide (HONO) or hydrogen peroxide (H_2O_2) can represent an additional OH source (Finlayson-Pitts and Pitts, 2000). Moreover, ozonolysis of isoprene or other alkenes yields OH radicals through the diel cycle at nighttime (Monks, 2005; Wennberg et al., 2018).
The OH radical itself can also remove NO_x from the Leighton cycle via its reaction with NO_2 to form HNO_3 (R10), which is highly soluble in water, readily undergoes heterogeneous reactions and can deposit on particles (R11) (Finlayson-Pitts and Pitts, 2000).

$$OH + NO_2 + M \rightarrow HNO_3 + M \tag{R10}$$

$$HNO_3 + surface \rightarrow products \tag{R11}$$

In addition, the OH radical may have an indirect impact on the Leighton relationship by reacting with VOCs, e.g. via H-abstraction as in case of methane (CH_4) (Crutzen and Lelieveld, 2001; Monks, 2005): Due to high abundance of O_2, the fate of the resulting alkyl radical is the formation of RO_2, which can convert NO to NO_2 and thus influence the photo-stationary state. Together with the photolysis of NO_2, this reaction sequence leads to the formation of ozone and the net reaction reveals that NO_2 can catalyse the production of O_3 within this oxidation process (sequence R12). A similar reaction sequence involving HO_2 (alternatively originating from photolysis of aldehydes or the OH-initiated oxidation of some VOCs) occurs during the OH-initiated oxidation of CO (sequence R13). In this sequence, HO_2 is converted to OH in the presence of NO yielding to NO_2 again catalysing O_3 formation.

$$\begin{gathered} RH + OH \rightarrow R + H_2O \\ R + O_2 + M \rightarrow RO_2 + M \\ RO_2 + NO \rightarrow RO + NO_2 \\ NO_2 + h\nu \rightarrow NO + O(^3P) \\ O(^3P) + O_2 + M \rightarrow O_3 + M \end{gathered}$$

$$net: RH + OH + 2O_2 \rightarrow RO + O_3 + H_2O \tag{R12}$$

$$OH + O_2 + CO \rightarrow CO_2 + HO_2$$
$$HO_2 + NO \rightarrow NO_2 + OH$$
$$NO_2 + h\nu \rightarrow NO + O(^3P)$$
$$O(^3P) + O_2 + M \rightarrow O_3 + M$$

$$net: CO + 2O_2 \rightarrow CO_2 + O_3 \tag{R13}$$

Note that in both sequences, the outcome of the net reaction depends on the detailed air composition such as the VOC to NO_x ratio (Crutzen and Lelieveld, 2001; Duncan et al., 2010; Pusede et al., 2015): In case of low NO_x concentrations, HO_2 in sequence R13 may alternatively react with O_3 (and thus remove it instead of catalysing its production) or other HO_2. Similarily, in sequence R12, RO_2 radicals may react with HO_2 or RO_2 or even undergo unimolecular reactions in a low-NO_x environment. The daytime (but also nighttime) oxidation of (non-methane) VOCs includes a huge variety of closed-shell products including e.g. formaldehyde, glyoxal, methacrolein or (in the presence of NO_x) organic nitrates. As organic nitrates may lead to NO_x removal (Fisher et al., 2016) from the gas-phase, this product class is described in more detail at this point.

Organic nitrates

Organic nitrates are generally divided into the two classes of alkyl nitrates ($RONO_2$, ANs) and peroxy nitrates (RO_2NO_2, PNs) and can serve as NO_x reservoirs or sinks (Horowitz et al., 2007). Peroxy nitrates can be subdivided into non-acyl ($ROONO_2$) and acyl ($RC(O)O_2NO_2$) peroxy nitrates. Non-acyl peroxy nitrates formed via R14 are not stable at ambient temperatures (thermal lifetime τ < 1 s at 298 K), which is why they are not important in the lower troposphere, while acyl peroxy nitrates are longer-lived (e.g. $\tau_{PAN} \sim 2440$ s at 298 K) (Kirchner et al., 1999) and are the only PNs considered in this work. Acyl-PNs are formed from the reaction between acyl peroxy radicals and NO_2 (R15).

$$RO_2 + NO_2 + M \rightarrow ROONO_2 + M \tag{R14}$$
$$RC(O)O_2 + NO_2 + M \rightarrow RC(O)O_2NO_2 + M \tag{R15}$$

Acyl peroxy radicals are primarily produced during daytime from OH-initiated VOC oxidation processes and the photolysis of aldehydes or ketones (Finlayson-Pitts and Pitts, 2000). The most prominent representative is peroxyacetyl nitrate (PAN, R = CH_3), which globally is formed mainly from acetaldehyde and methyl vinyl ketone (MVK) (Fischer et al., 2014). From

the oxidation of methacrolein ($CH_3C(CH_2)CHO$), one of many products from the daytime oxidation of isoprene (mostly biogenic), peroxymethacryloyl nitrate (MPAN, R = CH_2CCH_3) is formed (Wennberg et al., 2018). On the other hand, propionyl peroxy nitrate (PPN, R = CH_3CH_2) comes from the oxidation of propanal, which is mostly of anthropogenic origin (LaFranchi et al., 2009). Analysing the species contributing to PNs can thus help to identify whether an air mass is of biogenic or anthropogenic origin (Shepson et al., 1992).
Alkyl nitrates are thermally stable (thermal τ in the order of several days) (Morin and Bedjanian, 2017). During the daytime, ANs originate from the termolecular reaction between RO_2 and NO (R16). A huge fraction of RO_2 is alternatively consumed by the bimolecular reaction with NO (R17) to form alkoxy radicals (RO) (Atkinson and Arey, 2003). Alkoxy radicals can undergo bimolecular (or other) reactions to form further products (R18) (Orlando et al., 2003).

$$RO_2 + NO + M \rightarrow RONO_2 + M \quad \text{(R16)}$$

$$RO_2 + NO \rightarrow RO + NO_2 \quad \text{(R17)}$$

$$RO + \text{ e.g. } O_2 \rightarrow products \quad \text{(R18)}$$

Some low-volatility alkyl nitrates are of special interest as they are able to deposit on particles to form secondary organic aerosols (SOA, R19) (Zare et al., 2018; Romer Present et al., 2020).

$$RONO_2 + surface \rightarrow products \text{ (e.g. } HNO_3) \quad \text{(R19)}$$

2.1.3 Impact of NO_x on nighttime chemistry

At night-time, additional processes as marked by the blue box in Fig. 2.1 gain in importance. NO_2 (which is not photolyzed in the dark) can be further oxidized to the nitrate radical NO_3 (R20). Since NO_3 is not only photolabile (mainly R21) but also highly reactive to NO (R22), it has a short atmospheric lifetime (in the order of seconds) and is thus usually less relevant at the daytime (Wayne et al., 1991). Note that both reactions lead to reformation of NO_2.

$$NO_2 + O_3 \rightarrow NO_3 + O_2 \quad \text{(R20)}$$

$$NO_3 + h\nu \rightarrow NO_2 + O \quad \text{(R21)}$$

$$NO_3 + NO \rightarrow 2NO_2 \quad \text{(R22)}$$

However, owing to the lack of sunlight and (typically) also of NO, the nitrate radical becomes an important oxidizing agent of VOCs at nighttime (Atkinson and Arey, 2003; Brown et al., 2009; Ng et al., 2017; Liebmann et al., 2018; Wennberg et al., 2018). The NO_3 radical is in a thermal (highly temperature-dependent) equilibrium with NO_2 and N_2O_5 (R23). The latter is dominant at lower temperatures and can, in competition to the direct heterogeneous NO_3 sink, deposit on particles, serving as an indirect NO_3 loss path (R24) (Wayne et al., 1991). In

addition, the NO_3 radical is highly reactive to VOCs that include double-bonds, e.g. isoprene or monoterpenes like limonene or α-pinene (Ng et al., 2017; Wennberg et al., 2018).

$$NO_2 + NO_3 \rightleftharpoons N_2O_5 \tag{R23}$$

$$N_2O_5 \text{ or } NO_3 + surface \rightarrow products \text{ (e.g. } HNO_3) \tag{R24}$$

$$NO_3 + VOC \rightarrow products \text{ (e.g. organic nitrates)} \tag{R25}$$

The initial addition of NO_3 in the presence of O_2 leads to nitrated RO_2 radicals that, after further unimolecular or bimolecular reactions (e.g. with HO_2, RO_2, NO_3), form closed-shell products including organic nitrates (R25). This is the reaction of interest in this work since this path may yield to irreversible removal of NO_x from the gas-phase via R19 and thus has an impact on air quality (Fisher et al., 2016; Zare et al., 2018; Romer Present et al., 2020; Foulds et al., 2021). Despite its photolability and high reactivity to NO, NO_3-initiated VOC oxidation can become a significant source of ANs even during the daytime as shown by direct NO_3 reactivity measurements (Liebmann et al., 2018, 2019). Recent model calculations confirmed that daytime NO_3 accounts for up to 21% of organo-nitrates formed during summer months (Foulds et al., 2021).

The NO_3 + isoprene system

Isoprene is the non-methane VOC that is emitted with the largest rate during the day and usually of biogenic origin (Guenther et al., 2012). Nevertheless, various field studies showed that isoprene can still be abundant in the early evening (Stroud et al., 2002; Brown et al., 2009) so that its nighttime oxidation is also important with OH, NO_3 and O_3 being its most important oxidizing agents (Wennberg et al., 2018).
The NO_3-initiated oxidation of isoprene is thus of great atmospheric relevance (Hamilton et al., 2021). A simplified scheme of the first reaction steps in the NO_3 + isoprene system is shown in Fig. 2.2: The nitrate radical readily adds to double bonds - the isoprene molecule consequently features two possible reaction sites, but NO_3 predominantly attacks C1 (89 %) with almost equal addition of O_2 at the δ- or β-position under atmospheric conditions (Jenkin et al., 2015; Wennberg et al., 2018). Further oxidation of the nitrated RO_2 radicals via RO_2 self-reactions or by reaction with NO (at daytime), NO_3 or HO_2 yields to unsaturated, multifunctional nitrates or to nitrated alkoxy radicals (Finlayson-Pitts and Pitts, 2000; IUPAC, 2022). In contrast to isoprene-derived RO_2 radicals from the OH-initiated path, unimolecular decomposition routes become negligible under atmospheric conditions (Vereecken et al., 2021). Nitrated, isoprene-derived RO may decompose to closed-shell products via reaction with O_2 leading to e.g. carbonyl nitrates (under HO_2 formation) or, depending on the isomer, release NO_2 (Skov et al., 1992; Kwan et al., 2012). Recent experimental and theoretical studies reveal that isoprene-derived alkoxy radicals may both losing nitrate functionality by elimination of NO_2 or form

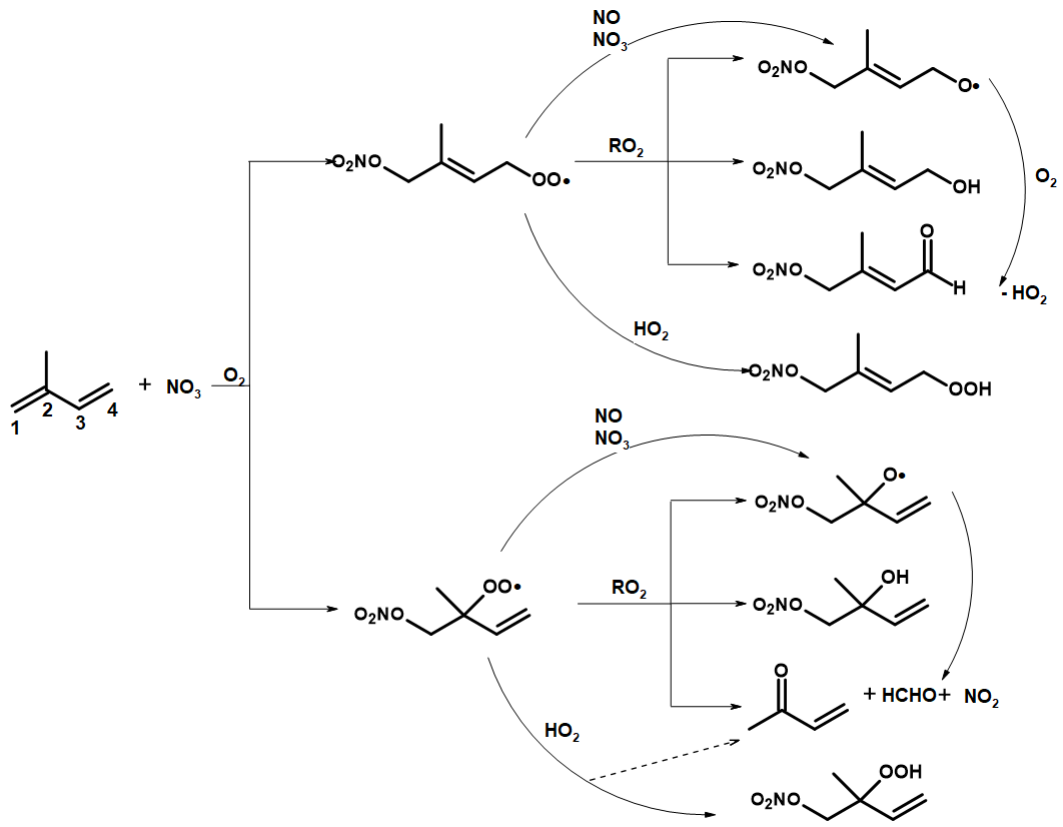

Figure 2.2: *NO_3-initiated oxidation of isoprene in the atmosphere and the resulting first-generation products (mostly organic nitrates), adapted from IUPAC (2022). Note that products from C4 addition and isomers of δ- or β-RO_2 radicals are omitted.*

epoxides (Vereecken et al., 2021). In any case, the product distribution and the overall organic nitrate yield will strongly depend on the fate, i.e. dominating reaction path, of the RO_2 radicals formed (Kwan et al., 2012; Schwantes et al., 2015). In addition, especially if conditions are not carefully chosen in chamber studies, isoprene-derived nitrates can be further oxidized e.g. by ozone leading to other nitrates (e.g propanone nitrate) but also lead to NO_2 elimination leading to formation of e.g. methyl glyoxal (Nguyen et al., 2016). This not only reduces the observed alkyl nitrate yields, but also expands the potential variety of products being detected within this process. The alkyl nitrate yields reported for this system are high with measurements between 60 and 100% (IUPAC, 2022). Note that most of the organic nitrates from this reaction not only contain a double-bond but also are multifunctional (Wu et al., 2020). This renders the oxidation mechanism complex and to subject of current research (as e.g. in Chapter 4). The multifunctionality of isoprene-derived nitrates may also be the main reason for problems that occur during the detection of the latter via their thermal decomposition to NO_2, which is detailed in Chapter 5.

2.1.4 Assessment of NO_3 lifetimes

As outlined in the previous section, knowledge of NO_3 lifetimes towards VOCs in competition with other NO_3 loss processes is crucial to understand the atmospheric fate of NO_x in some environments. Prior to the development of an instrument being able to directly measure NO_3 reactivity (named k^{NO_3} throughout this thesis) (Liebmann et al., 2017), NO_3 loss rates (L_{NO_3}) were deduced from NO_3, NO_2 and O_3 mixing ratios applying a *stationary ("steady")-state* approximation (Heintz et al., 1996; Geyer and Platt, 2002; Brown et al., 2003, 2007b; Crowley et al., 2011; Sobanski et al., 2016b): In this calculation one assumes that the summed loss rate L_{NO_3} is in balance with the production rate P_{NO_3} so that the time rate of change in the NO_3 concentration is zero:

$$\frac{d[NO_3]}{dt} = P_{NO_3} - L_{NO_3}[NO_3] \approx 0 \tag{2.1}$$

The oxidation of NO_2 by O_3 via R20 serves as the only significant NO_3 source in the atmosphere (Wayne et al., 1991) so that the production rate is linked to the abundance of NO_2 and O_3:

$$P_{NO_3} = k_{20}[O_3][NO_2] \tag{2.2}$$

Using Eq. 2.1 and Eq. 2.2 leads to NO_3 loss rates L_{NO_3} being the inverse of the NO_3 lifetime τ_{NO_3}:

$$L_{NO_3} = \frac{k_{20}[O_3][NO_2]}{[NO_3]} = \frac{1}{\tau_{NO_3}} \tag{2.3}$$

Note that L_{NO_3} derived from Eq. 2.3 includes every process resulting in NO_3 loss, i.e. both indirect losses via heterogeneous uptake of N_2O_5 (R24) and direct NO_3 uptake on particles as well as homogeneous losses. This expression is only valid, if steady-state is achieved. Model calculations imply that this is usually the case, when NO_3 lifetimes are sufficiently short and if the thermal equilibrium between NO_2, NO_3 and N_2O_5 is not perturbed by sudden changes in NO_2 (Brown et al., 2003). If direct measurements of both NO_3 and N_2O_5 are available, one can extend the numerator by the derivatives of NO_3 and N_2O_5 with time as in Eq. 2.4:

$$L_{NO_3,nss} = \frac{k_{22}[O_3][NO_2] - \frac{d[NO_3]}{dt} - \frac{d[N_2O_5]}{dt}}{[NO_3]} = \frac{1}{\tau_{NO_3,nss}} \tag{2.4}$$

This equation as presented in McLaren et al. (2010) is still valid if steady-state is not achieved, equilibrium with N_2O_5 is still required though.
If no NO_3 measurements are available, the NO_3 reactivity (or lifetime) can be used to calculate NO_3 mixing ratios, if all loss processes are known (Liebmann et al., 2018): The contribution of VOCs (R25) in this work is accessible by direct measurements of k^{NO_3} but can alternatively be deduced from the sum of the product between the concentration of each VOC ($[VOC]_i$) and the corresponding rate coefficient k_i for its reaction with NO_3. This necessitates however that measurements of all VOCs being reactive to NO_3 are available. Analogously the impact of reaction with NO (R22) can be added. During the daytime, photolysis frequencies (J_{NO_3}) have to be taken into account as well. The impact of heterogeneous uptake of N_2O_5 (R24) can be added if the heterogeneous loss frequency ($f_{het,indir}$) and the equilibrium constant for R23 (K_{23}) are known. Direct heterogeneous uptake of NO_3 can be added directly with the corresponding loss frequency ($f_{het,dir}$). Summing up all contributions leads to the following expression for L_{NO_3}:

$$L_{NO_3} = \Sigma k_i[VOC]_i + k_{22}[NO] + J_{NO_3} + K_{23}[NO_2]f_{het,indir} + f_{het,dir} \tag{2.5}$$

Another way to deduce NO_3 reactivities that is shown in this work in Chapter 4, is with the help of box model simulations using a chemical degradation scheme. But this method also relies on observations and necessitates a deep knowledge of all oxidation processes affecting NO_3.

2.1.5 Meteorological impact on NO_3 lifetimes

Beside all the purely chemical aspects described above, boundary-layer chemistry can be highly impacted by meteorological effects: One aspect, which can be observed with changing

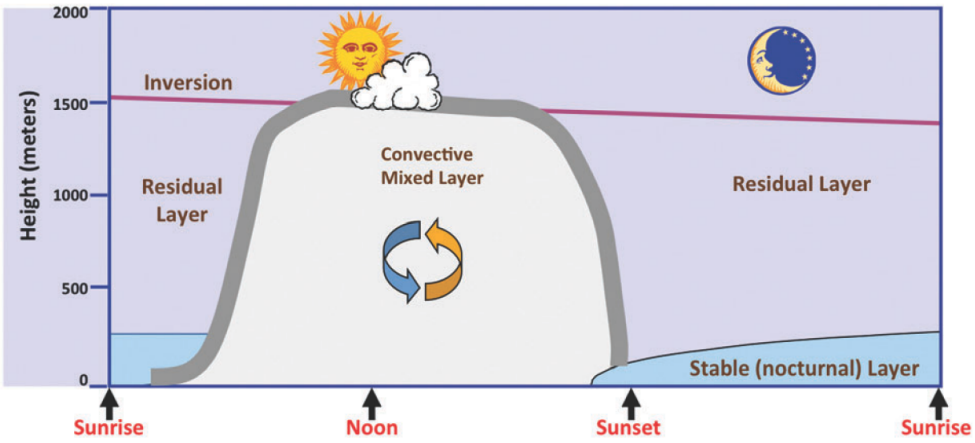

Figure 2.3: *Temporal evolution of the atmospheric boundary layer: During the daytime, convective mixing results in a vertically mixed layer. At night, a statically stable nocturnal boundary layer (NBL) with reduced vertical mixing forms. Above the top of the NBL a residual layer that is mostly decoupled from ground emissions builds up. This illustration is taken from Brown and Stutz (2012).*

height and stability of the nocturnal boundary layer (NBL), are characteristic vertical profiles of nighttime NO_3 mixing ratios and NO_3 reactivity (Brown et al., 2007a; Sobanski et al., 2016b). In contrast to the free atmosphere, the boundary layer is highly influenced by emissions and heat fluxes undergoing a diel cycle as depicted in Fig 2.3: At daytime, the air is well mixed due to convective forces. During the nighttime on the other hand, especially during fair weather, the ground temperature can be lower than that of the surrounding air. As a consequence, a statically stable layer, in which vertical mixing is strongly reduced, forms (Stull, 1988, 2017) and trace gases that are emitted near the ground are not necessarily homogeneously mixed within the NBL. If this is fulfilled for trace gases like NO or alkenes that are the main atmospheric reactants for NO_3 (Ng et al., 2017), this effect results in increasing NO_3 lifetimes and concentrations (or decreasing NO_3 reactivities) with increasing height as observed in measurements and model calculations of vertical profiles (Stutz et al., 2004; Geyer and Stutz, 2004; Brown et al., 2007a).

2.2 Detection of atmospheric trace gases with means of cavity ring-down spectroscopy

As mentioned at the beginning of this chapter, the results and conclusions of this work are based on chamber and field measurements made with two custom-built cavity ring-down spectrometers. Consequently, the basic principle of this measurement technique is outlined in this section. For more detailed insights into CRDS please refer to the thorough reviews e.g. by Berden et al. (2000) or Brown (2003). Generally, there are different kinds of CRDS techniques, but this section focusses on cavity ring-down spectroscopy with modulated light sources as applied for both instruments in this work. A typical setup of such a cavity ring-down spec-

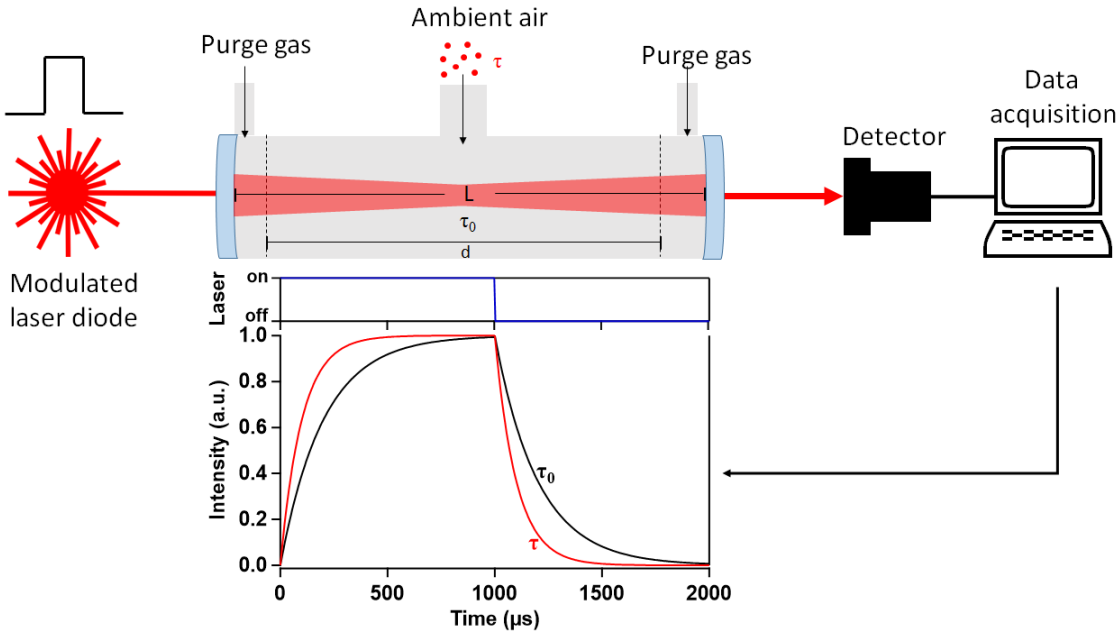

Figure 2.4: *Scheme of an exemplary cavity ring-down spectrometer and the resulting signal using a modulated light source, adapted from Brown (2003).*

trometer is depicted in Fig. 2.4. CRDS is based on conventional absorption spectroscopy considering the attenuation of the intensity of light proceeding through an absorbing medium. A relation between this change of the intensity and the concentration of the absorbing species is described by the LAMBERT-BEER law. However, the species of interest (e.g. NO_2, NO_3) are usually only abundant in very small concentrations (i.e. in the order of pptv to ppbv) in the atmosphere. As a consequence, their absorption would only lead to a very small attenuation compared to the background intensity of the light source, which is why modifications of the conventional absorption spectroscopy setup are necessary in order to increase the sensitivity sufficiently. A way to achieve this is to introduce both a modulation of the light source and to increase the optical path length by forcing multiple passes through the absorbing medium with highly reflective mirrors. As indicated in Fig. 2.4, the core of each CRDS setup is the cavity consisting of two high-reflectivity mirrors (reflectivity R $\sim$ 0.99998). Emission of a modulated laser diode with a wavelength matching with an absorption band of the analyte is coupled into the cavity. A detector, in this case a photomultiplier, monitors the intensity of the light exiting the cavity. Light that entered the cavity during the *on*-phase of the laser is reflected several times between the two mirrors resulting in an effective optical path length of typically several tens of kilometres. During the *off*-phase, a small fraction of light (the mirrors have a transmission of 20 ppm) is coupled out of the cavity during each passage resulting in a mono-exponential decay ("ring-down") of the light intensity. With the help of electronic components these decay constants (ring-down times) are extracted. If no species that absorbs or scatters at the wavelength of the light source is inside the cavity, the ring-down (or decay) time is τ_0 and only determined by the characteristics of the cavity (mostly the performance of the mirrors

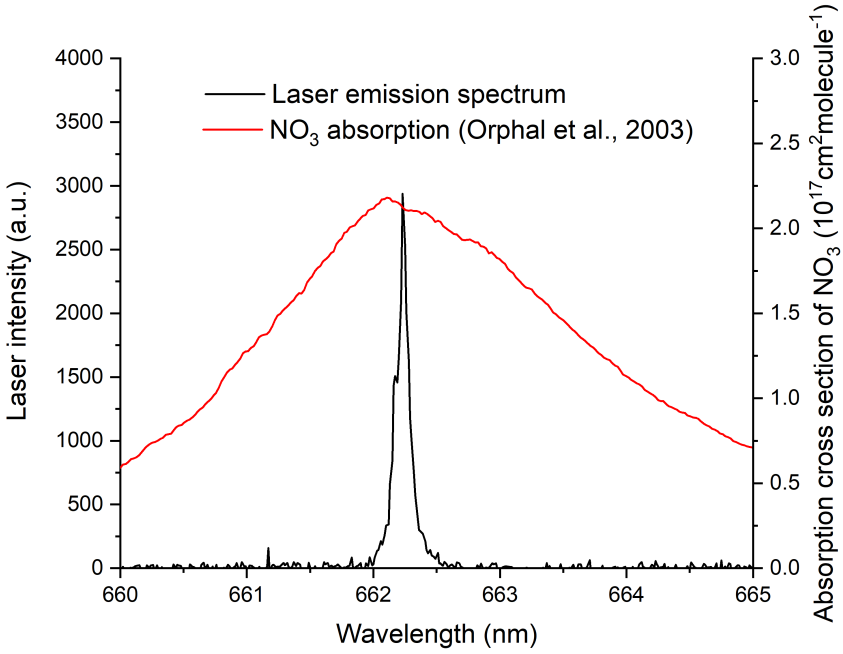

Figure 2.5: *Absorption cross section of the nitrate radical (Orphal et al., 2003) and emission spectrum of the laser diode used in the NO_3 reactivity setup in the range between 660-665 nm.*

and Rayleigh scattering) itself. As soon as a species that absorbs at the wavelength of the light source is present in the cavity, the ring-down time is shortened to τ. The extent of the change between τ_0 and τ, forming the basis of this technique, is determined by the concentration of the analyte $[X]$ and thus allows estimation of the latter using Eq 2.6.

$$[X] = \frac{L}{d} \cdot \frac{1}{\sigma c} \cdot (\frac{1}{\tau} - \frac{1}{\tau_0}) \tag{2.6}$$

Beside the ring-down times τ_0 and τ as well as the speed of light c, the effective cross-section σ, which is derived from the overlap between the absorption band of the analyte and the normalised emission spectrum of the light source, is needed. Furthermore, to avoid contamination of the mirror surface (which would drastically reduce τ) the mirrors are typically purged with synthetic air. This reduces the mechanical distance L to an effective (optical) distance d.
An example of the of the spectral overlap between the NO_3 absorption spectrum (Orphal et al., 2003) with a typical emission of the red laser diode implemented in the NO_3 reactivity setup is shown in Fig. 2.5. The effective cross-section can be derived from the convolution of the reference absorption spectrum and the normalised laser emission spectrum. Note that the presence of an additional species absorbing at the same wavelength (e.g. H_2O) would cause an additional reduction of the ring-down time and thus bias the measurement. In case of NO_3, τ_0 is estimated on a regular basis by titration with NO which allows selective elimination of NO_3 while other species (e.g. H_2O) are unaffected. Some species like N_2O_5 or alkyl nitrates can be

detected indirectly via their thermal dissociation (TD-CRDS) to NO_3 (R26) or NO_2 (R27) prior to entering the cavity as described for example in Sobanski et al. (2016a).

$$N_2O_5 + \Delta \rightarrow NO_3 + NO_2 \quad \text{(R26)}$$

$$RONO_2 + \Delta \rightarrow NO_2 + RO \quad \text{(R27)}$$

CHAPTER 3

Overview of Results

I. The NO_3 + isoprene system

As already pointed out in the introductory chapters, the fate of the NO_3 radical in atmospherically relevant systems, especially the reaction between NO_3 and isoprene, forms focus of the analysis presented in this work. Chamber studies provide well-defined conditions and thus give, in contrast to the complexity of ambient air, a great opportunity to evaluate the impact of particular reaction paths in more detail. The first two publications thus deal with chamber studies of the NO_3 + isoprene system:

a) The role of NO_3 in primary and secondary oxidation

In Chapter 4, I investigate the evolution of the NO_3 reactivity in scope of a series of experiments in a large environmental outdoor chamber in Jülich (NO3ISOP campaign). Isoprene is of high atmospheric relevance (Guenther et al., 2012) and NO_3 becomes its major oxidant at nighttime (Wennberg et al., 2018) leading to formation of alkyl nitrates in high yields (IUPAC, 2022). The involvement of NO_3 in secondary oxidation of initially formed radicals or closed-shell products has not been directly measured so far. I compared my direct NO_3 reactivity measurements with expected reactivities from VOC measurements ($\Sigma k_i[VOC]_i$, mostly isoprene only), non-stationary-state reactivities (as in Eq. 2.4) using NO_3, NO_2 and O_3 measurements according to McLaren et al. (2010) as well as to model calculations using the Master Chemical Mechanism (MCM v3.3.1) (Jenkin et al., 2015). The intercomparisons revealed that closed-shell products do not contribute to the isoprene-induced NO_3 reactivity significantly and that a rate coefficient of 4.6 x 10^{-12} $cm^3 molecule^{-1} s^{-1}$ for the reaction of NO_3 with isoprene-derived RO_2 radicals is necessary in order to bring modelled and non-stationary state reactivities into agreement. This value is twice the value used in MCM, which is based on the one measured for

the reaction between NO_3 and ethyl peroxy radicals (Jenkin et al., 2015; IUPAC, 2022). Consequently, this study contributes to reassess the atmospheric isoprene oxidation mechanism (Vereecken et al., 2021). This result is also in accordance with an analysis presented in Hjorth et al. (1990) who indirectly estimated a rate coefficient of 5 x 10^{-12} $cm^3 molecule^{-1} s^{-1}$ for an alkene-derived RO_2 radical ($(CH_3)_2C(ONO_2)C(CH_3)_2O_2$) more similar to isoprene-derived RO_2.

b) Detection of isoprene-derived organic nitrates

In Chapter 5 on the other hand, I highlight challenges encountered when products, i.e. organic nitrates, from the NO_3 + isoprene system are quantified with the TD-CRDS setup described in Sobanski et al. (2016a). To date, mostly unsaturated compounds such as isopropyl nitrate and peroxy acetyl nitrate (PAN) have been used as reference compounds to characterize setups used to detect alkyl and peroxy nitrates based on their thermal dissociation (Day et al., 2002; Di Carlo et al., 2013; Wild et al., 2014; Thieser et al., 2016; Sobanski et al., 2016a; Keehan et al., 2020). I used a Teflon chamber (SCHARK) situated in a laboratory of the Max Planck Institute for Chemistry (MPIC) to generate isoprene-derived organic nitrates that in contrast to such reference compounds are, as already shown in Fig. 2.2, mostly multifunctional and unsaturated (Wennberg et al., 2018; Wu et al., 2020). This study reveals that the separate detection of isoprene-derived peroxy and alkyl nitrates by their thermal dissociation can be biased by ozone-assisted, heterogeneous reactions of the multifunctional organic nitrates on the surface of heated quartz glass inlets. This behaviour is not observed for saturated reference compounds and this study underlines the importance of characterizing instruments with molecules that are actually abundant in the atmosphere under conditions as close as possible to those found in outdoor environments. In addition, I present a way to effectively circumvent this problem by deploying a thermal dissociation inlet made of PFA instead of quartz glass for the detection of PNs.

II. Field measurements of NO_3 reactivity

In Chapter 6, I analyze field measurements of NO_3 reactivity at the summit of the Kleiner Feldberg mountain. I compared NO_3 reactivities to reactivities expected from measurements of VOCs, NO and actinic fluxes (as in Eq. 2.5). As already observed during the NO3ISOP campaign in Jülich, the measured NO_3 reactivities were in excellent agreement to those calculated from VOC concentrations and the corresponding rate coefficient for the reaction with NO_3 ($\Sigma k_i[VOC]_i$). The analysis reveals that NO_3 was mainly consumed by monoterpenes (84%) predominantly emitted by e.g. coniferous trees (Hakola et al., 2003, 2012) and that isoprene (7%) was of minor importance. At daytime, reactions with VOCs contributed with ca. 16% to the overall NO_3 and thus is competitive to the OH-initiated path of alkyl nitrate formation. This is in agreement with NO_3 reactivity measurements in a boreal forest and on top of the Hohenpeissenberg mountain, where VOC-induced daytime NO_3 reactivity contributed

with ca. 20 % to the overall NO_3 loss (Liebmann et al., 2018, 2019). During the nighttime, reaction with NO (R22) became competitive with VOC oxidation (R25) as an NO_3 loss path. Stationary-state calculations (as in Eq. 2.3) allowed me the conversion of overall NO_3 loss rates (as in Eq. 2.5) and NO_3 production rates to NO_3 mixing ratios. Intercomparison with direct NO_3 measurements during previous campaigns between 2008 and 2015 on the Kleiner Feldberg showed that during TO2021, NO_3 loss rates were higher, while NO_3 production rates (P_{NO_3}) were comparably low.

III. Indoor measurements of NO_3 reactivity

Measurements of NO_3, NO_2, O_3, N_2O_5 mixing ratios and NO_3 reactivity were carried out inside a laboratory of the MPIC situated in the city of Mainz for four days over weekend in order to check the relevance of NO_3 radicals in indoor chemistry. In Chapter 7, I show that this measurement gives comprehensive information on the fate of NO_3 as I measured both NO_3 reactivity and ambient NO_3 (and N_2O_5) mixing ratios simultaneously as already carried out during the NO3ISOP campaign. In contrast to TO2021, every NO_3 loss path including heterogeneous reactions are included in the measurement and the overall loss rate (from Eq. 2.3.) so that I was able to check for consistency with the sum of particular loss rates (as in Eq. 2.5). The NO_3 reactivities often exceeded the upper detection limit of 1.7 s^{-1} when several tens of ppbv of NO were present in the laboratory. This is accompanied by both NO_2 production and O_3 depletion, so that P_{NO_3} drastically decreased. Under these conditions neither N_2O_5 nor NO_3 was detected. During VOC-dominated periods, when P_{NO_3} and NO_3 reactivities were mostly between 0.1 and 0.4 s^{-1} (thus much higher than during TO2021), several pptv of N_2O_5 but still no NO_3 was observed. Steady-state mixing ratios of N_2O_5 were in excellent agreement with the measurement, but at the same time up to 2 pptv NO_3 were expected. Filter losses form the most likely explanation for the lack of NO_3 according to the measurements. The abundance of N_2O_5 was decoupled from the day-night-transitions, due to low photolysis rates of NO_3 in the laboratory even at daytime. These results are consistent with the observations reported in the only available literature about indoor NO_3 measurements (Arata et al., 2018; Nøjgaard, 2010) in which detectable amounts of NO_3 in indoor environments were only observed when NO was quantitatively depleted by artificial addition of O_3. With this pilot study, I emphasize that NO_3 may be a relevant indoor oxidant in ventilated buildings.

Author contribution

I performed the measurements of NO_3 reactivity and NO_2 mixing ratios during the NO3ISOP and TO2021 campaign as well as all measurements in the laboratory except for the CIMS measurement of PAN and CRDS measurements of NO_x. I did all the presented analysis and wrote the manuscripts. I drew the above-mentioned conclusions and put them into context of the cited literature.

CHAPTER 4

Evolution of NO_3 reactivity during the oxidation of isoprene

The results of the study in this chapter have already been published in the peer-reviewed journal *Atmospheric Chemistry and Physics*. The publication is thus reproduced on the subsequent pages and deals with the following:
The underlying chemistry during the oxidation of isoprene by NO_3 under typically atmospheric conditions was investigated with the SAPHIR environmental chamber of the research centre in Jülich (*Forschungszentrum Jülich, FZJ*) in scope of the NO3ISOP campaign in a series of 22 experiments in which NO_2 (5-30 ppbv) and O_3 (50-100 ppbv) forming NO_3 via R20 were mixed with isoprene (3-22 ppbv) under dry and humid conditions. I compared directly measured NO_3 reactivities with reactivities derived from (1) VOC measurements, (2) nonstationary-state calculations and (3) model calculations based on the Master Chemical Mechanism (MCM). These comparisons suggested that NO_3 does not contribute the secondary oxidation of closed-shell products and that the rate coefficient for the reaction between isoprene-derived peroxy radicals (RO_2) and NO_3 is higher than expected by the MCM.

Author contribution
I performed direct measurements of NO_3 reactivity as well as of NO_2, analyzed the presented data sets, did the model calculations, wrote the manuscript and, with the help of , revised it. All named co-authors provided auxiliary data and commented on the manuscript. Please refer to the section "Author contribution" in the publication itself for detailed information.

Atmos. Chem. Phys., 20, 10459–10475, 2020
https://doi.org/10.5194/acp-20-10459-2020

Atmospheric Chemistry and Physics
Open Access
EGU

Evolution of NO_3 reactivity during the oxidation of isoprene

Patrick Dewald[1], Jonathan M. Liebmann[1], Nils Friedrich[1], Justin Shenolikar[1], Jan Schuladen[1], Franz Rohrer[2], David Reimer[2], Ralf Tillmann[2], Anna Novelli[2], Changmin Cho[2], Kangming Xu[3], Rupert Holzinger[3], François Bernard[4,a], Li Zhou[4], Wahid Mellouki[4], Steven S. Brown[5,6], Hendrik Fuchs[2], Jos Lelieveld[1], and John N. Crowley[1]

[1]Atmospheric Chemistry Department, Max-Planck-Institut für Chemie, 55128 Mainz, Germany
[2]Institute of Energy and Climate Research, IEK-8: Troposphere, Forschungszentrum Jülich GmbH, 52428 Jülich, Germany
[3]Institute for Marine and Atmospheric Research, IMAU, Utrecht University, Utrecht, the Netherlands
[4]Institut de Combustion, Aérothermique, Réactivité et Environnement (ICARE), CNRS (UPR 3021)/OSUC, 1C Avenue de la Recherche Scientifique, 45071 Orléans CEDEX 2, France
[5]NOAA Chemical Sciences Laboratory, 325 Broadway, Boulder, CO 80305, USA
[6]Department of Chemistry, University of Colorado Boulder, Boulder, CO 80209, USA
[a]now at: Laboratoire de Physique et Chimie de l'Environnement et de l'Espace (LPC2E), Centre National de la Recherche Scientifique (CNRS), Université d'Orléans, Observatoire des Sciences de l'Univers en région Centre – Val de Loire (OSUC), Orléans, France

Correspondence: John N. Crowley (john.crowley@mpic.de)

Received: 16 April 2020 – Discussion started: 11 May 2020
Revised: 7 July 2020 – Accepted: 31 July 2020 – Published: 8 September 2020

Abstract. In a series of experiments in an atmospheric simulation chamber (SAPHIR,[1] Forschungszentrum Jülich, Germany), NO_3 reactivity (k^{NO_3}) resulting from the reaction of NO_3 with isoprene and stable trace gases formed as products was measured directly using a flow tube reactor coupled to a cavity ring-down spectrometer (FT-CRDS). The experiments were carried out in both dry and humid air with variation of the initial mixing ratios of ozone (50–100 ppbv), isoprene (3–22 ppbv) and NO_2 (5–30 ppbv). k^{NO_3} was in excellent agreement with values calculated from the isoprene mixing ratio and the rate coefficient for the reaction of NO_3 with isoprene. This result serves to confirm that the FT-CRDS returns accurate values of k^{NO_3} even at elevated NO_2 concentrations and to show that reactions of NO_3 with stable reaction products like non-radical organic nitrates do not contribute significantly to NO_3 reactivity during the oxidation of isoprene. A comparison of k^{NO_3} with NO_3 reactivities calculated from NO_3 mixing ratios and NO_3 production rates suggests that organic peroxy radicals and HO_2 account for $\sim 50\,\%$ of NO_3 losses. This contradicts predictions based on numerical simulations using the Master Chemical Mechanism (MCM version 3.3.1) unless the rate coefficient for reaction between NO_3 and isoprene-derived RO_2 is roughly doubled to $\sim 5 \times 10^{-12}$ cm^3 molecule^{-1} s^{-1}.

[1]Simulation of Atmospheric PHotochemistry In a large Reaction

1 Introduction

The atmospheric oxidation of volatile organic compounds (VOCs) of both biogenic and anthropogenic origin has a great impact on tropospheric chemistry and global climate (Lelieveld et al., 2008). Isoprene is one of the major organic (non-methane) compounds that is released in the environment by vegetation and contributes $\sim 50\,\%$ to the overall emission of VOCs into the atmosphere (Guenther et al., 2012). The most important initiators of oxidation for biogenic VOCs in the atmosphere are hydroxyl radicals (OH), ozone (O_3) and nitrate radicals (NO_3) (Geyer et al., 2001; Atkinson and Arey, 2003; Lelieveld et al., 2016; Wennberg et al., 2018). Our focus in this study is on NO_3, which is formed via the sequential oxidation of NO by ozone (Reactions R1 and R2). During the daytime, NO_3 mixing ratios are very low, owing to its efficient reaction with NO (Reaction R6) and its rapid photolysis (Reactions R7 and R8). Generally, NO_3 is present in mixing ratios greater than a few

parts per trillion by volume (pptv) only at night-time, when it can become the major oxidizing agent for VOCs including isoprene (Reaction R5). In forested regions, reactions with biogenic trace gases, however, can contribute significantly to the daytime reactivity of NO_3 (Liebmann et al., 2018a, b).

Moreover, NO_2, NO_3 and N_2O_5 exist in thermal equilibrium (Reactions R3 and R4) so that the heterogeneous loss of N_2O_5 (and NO_3) at surfaces (Reactions R9 and R10) impacts on the lifetime of NO_3 in the atmosphere (Martinez et al., 2000; Brown et al., 2003, 2006, 2009b; Crowley et al., 2010).

$$NO + O_3 \rightarrow NO_2 + O_2 \quad \text{(R1)}$$
$$NO_2 + O_3 \rightarrow NO_3 + O_2 \quad \text{(R2)}$$
$$NO_2 + NO_3 + M \rightarrow N_2O_5 + M \quad \text{(R3)}$$
$$N_2O_5 + M \rightarrow NO_2 + NO_3 + M \quad \text{(R4)}$$
$$NO_3 + \text{isoprene} \rightarrow \text{products (e.g. } RONO_2, RO_2) \quad \text{(R5)}$$
$$NO_3 + NO \rightarrow 2NO_2 \quad \text{(R6)}$$
$$NO_3 + h\nu \rightarrow NO + O_2 \quad \text{(R7)}$$
$$NO_3 + h\nu \rightarrow NO_2 + O \quad \text{(R8)}$$
$$N_2O_5 + \text{surface} \rightarrow \text{products (e.g. } HNO_3) \quad \text{(R9)}$$
$$NO_3 + \text{surface} \rightarrow \text{products (e.g. particle nitrate)} \quad \text{(R10)}$$
$$RONO_2 + \text{surface} \rightarrow \text{products (e.g. } HNO_3) \quad \text{(R11)}$$

Although isoprene is mainly emitted by vegetation at daytime (Sharkey and Yeh, 2001; Guenther et al., 2012), during which its main sink reaction is with the OH radical (Paulot et al., 2012), it accumulates in the nocturnal boundary layer (Warneke et al., 2004; Brown et al., 2009a) where reactions of NO_3 and O_3 determine its lifetime (Wayne et al., 1991; Brown and Stutz, 2012; Wennberg et al., 2018). The rate constant (at 298 K) for the reaction between isoprene and NO_3 is 6.5×10^{-13} cm^3 molecule^{-1} s^{-1}, which is several orders of magnitude larger than for the reaction with O_3 (1.28×10^{-17} cm^3 molecule^{-1} s^{-1}) (Atkinson et al., 2006; IUPAC, 2020) and thus compensating for the difference in mixing ratios of NO_3 (typically 1–100 pptv) and O_3 (typically 20–80 ppbv) (Edwards et al., 2017). NO_3 is often the most important nocturnal oxidant of biogenic VOCs (Mogensen et al., 2015), especially in remote, forested environments where it reacts almost exclusively with biogenic isoprene and terpenes (Ng et al., 2017; Liebmann et al., 2018a, b). The reaction between isoprene and NO_3 leads initially to the formation of nitro isoprene peroxy radicals (NISOPOO, e.g. $O_2NOCH_2C(CH_3)$=$CHCH_2OO$) that can either react with NO_3, forming mostly a nitro isoprene aldehyde (NC4CHO, e.g. $O_2NOCH_2C(CH_3)$=CHCHO) and methyl vinyl ketone (MVK) or react further with other organic peroxy (RO_2), or hydroperoxy (HO_2) radicals, forming nitrated carbonyls, peroxides and alcohols (Schwantes et al., 2015).

The organic nitrates formed ($RONO_2$) can deposit on particles (Reaction R11); therefore, the NO_3 + isoprene system contributes to the formation of secondary organic aerosol (SOA) (Rollins et al., 2009; Fry et al., 2018). Together with heterogeneous uptake of N_2O_5 or NO_3 on particle surfaces (Reactions R9 and R10), the build-up of SOA from isoprene oxidation products forms a significant pathway for removal of reactive nitrogen species (NO_x) from the gas phase; a detailed understanding of the reaction between isoprene and NO_3 is therefore crucial for assessing its impact on SOA formation and NO_x lifetimes.

In this study, the NO_3-induced oxidation of isoprene was examined in an environmental chamber equipped with a large suite of instruments, including a cavity ring-down spectrometer coupled to a flow tube reactor (FT-CRDS) for direct NO_3 reactivity measurement (Liebmann et al., 2017). The NO_3 lifetime in steady state (the inverse of its overall reactivity) has often been derived from NO_3 mixing ratios and production rates, with the latter depending on the mixing ratios of NO_2 and O_3 (Heintz et al., 1996; Geyer and Platt, 2002; Brown et al., 2004; Sobanski et al., 2016b). The steady-state approach works only if NO_3 is present at sufficiently high mixing ratios to be measured (generally not the case during daytime), breaks down to a varying extent if a steady state is not achieved (Brown et al., 2003; Sobanski et al., 2016b), and may be influenced by heterogeneous losses of NO_3 or N_2O_5 (Crowley et al., 2011; Phillips et al., 2016), which are difficult to constrain. Comparing the steady-state calculations with the FT-CRDS approach (which derives the NO_3 reactivity attributable exclusively to VOCs) can provide insight into the main contributions to NO_3 reactivity and its evolution as the reaction progresses. In the following, we present the results of direct NO_3 reactivity measurements in the SAPHIR (Simulation of Atmospheric PHotochemistry In a large Reaction) environmental chamber under controlled conditions and explore the contributions of isoprene, peroxy radicals and stable oxidation products to NO_3 reactivity over a period of several hours as the chemical system resulting from NO_3-induced oxidation of isoprene evolves.

2 Measurement and instrumentation

An intensive study of the NO_3 + isoprene system (NO3ISOP campaign) took place at the SAPHIR chamber of the Forschungszentrum Jülich over a 3-week period in August 2018. The aim of NO3ISOP was to improve our understanding of product formation in the reaction between NO_3 and isoprene as well as its impact on the formation of SOA. Depending on the conditions (high or low HO_2/RO_2, temperature, humidity, and daytime or night-time), a large variety of oxidation products, formed via different reaction paths, exist (Wennberg et al., 2018). During NO3ISOP, the impact of varying experimental conditions on the formation of gas-phase products as well as secondary organic aerosol formation and composition was explored within 22 different experiments (see Table 1). Typical conditions were close to those found in the atmosphere with 5 ppbv of NO_2, 50–100 ppbv of

O_3 and 3 ppbv of isoprene, or (when high product formation rates were required) NO_2 was raised to 25 ppbv and isoprene to 10 ppbv. The high O_3 mixing ratios in the chamber ensured that NO was not detectable (< 10 pptv) in the darkened chamber.

The first 11 experiments of NO3ISOP were dedicated to gas-phase chemistry; in the second part seed aerosol ($(NH_4)_2SO_4$) was added and the focus shifted to aerosol measurements. Due to a contamination event in the chamber, the experiment from the 7 August is not considered for further analysis. The SAPHIR chamber and the measurements and instruments that are relevant for the present analysis are described briefly below.

2.1 The SAPHIR chamber

The atmospheric simulation chamber SAPHIR has been described in detail on various occasions (Rohrer et al., 2005; Bossmeyer et al., 2006; Fuchs et al., 2010), and we present only a brief description of some important features here: the outdoor chamber consists of two layers of FEP (fluorinated ethylene propylene) foil defining a cylindrical shape with a volume of 270 m^3 and a surface area of 320 m^2. The chamber is operated at ambient temperature and its pressure is ~ 30 Pa above ambient level. A shutter system in the roof enables the chamber to be completely darkened or illuminated with natural sunlight. Two fans result in rapid (2 min) mixing of the gases in the chamber, which was flushed with synthetic air (obtained from mixing high-purity nitrogen and oxygen) at a rate of 250 $m^3\,h^{-1}$ for several hours between each experiment. Leakages and air consumption by instruments leads to a dilution rate of typically $1.4 \times 10^{-5}\,s^{-1}$. Coupling to a separate plant chamber enabled the introduction of plant emissions into the main chamber (Hohaus et al., 2016).

2.2 NO_3 reactivity measurements: FT-CRDS

The FT-CRDS instrument for directly measuring NO_3 reactivity (k^{NO_3}) has been described in detail (Liebmann et al., 2017) and only a brief summary is given here. NO_3 radicals are generated by sequential oxidation of NO with O_3 (Reactions R1 and R2) in a darkened, thermostated glass reactor at a pressure of 1.3 bar. The reactor surfaces are coated with Teflon (DuPont, FEPD 121) to reduce the loss of NO_3 and N_2O_5 at the surface during the ~ 5 min residence time. The gas mixture exiting the reactor (400 sccm) is heated to 140 °C before being mixed with either zero air or ambient air (at room temperature) and enters the FEP-coated flow tube where further NO_3 production (Reaction R2), equilibrium reaction with N_2O_5 (Reactions R3 and R4), and NO_3 loss via reactions with VOCs/NO (Reactions R5/R6) or with the reactor wall (Reaction R10) take place. NO_3 surviving the flow reactor after a residence time of 10.5 s is quantified by CRDS at a wavelength of 662 nm. The NO_3 reactivity is calculated from relative change in NO_3 concentration when mixed with zero air or ambient air. In order to remove a potential bias by ambient NO_3/N_2O_5, sampled air is passed through an uncoated 2 L glass flask (~ 60 s residence time) heated to 45 °C to favour N_2O_5 decomposition before reaching the flow tube. Ambient NO_3 (or other radicals, e.g. RO_2) is lost by its reaction with the glass walls. In addition to the reaction of interest (Reaction R5), Reactions (R2) to (R4) and (R10) affect the measured NO_3 concentration so that corrections via numerical simulation of this set of reactions are necessary to extract k^{NO_3} from the measured change in NO_3 concentration, necessitating accurate measurement of O_3, NO and especially NO_2 mixing ratios. For this reason, the experimental setup was equipped with a second cavity for the measurement of NO_2 at 405 nm as described recently (Liebmann et al., 2018b). In its current state the instrument's detection limit is $\sim 0.005\,s^{-1}$. By diluting highly reactive ambient air with synthetic air, ambient reactivities up to $45\,s^{-1}$ can be measured. The overall uncertainty in k^{NO_3} results from instability of the NO_3 source and the CRDS detection of NO_3 and NO_2 as well as uncertainty introduced by the numerical simulations. Under laboratory conditions, measurement errors result in an uncertainty of 16 %. The uncertainty associated with the numerical simulation was estimated by Liebmann et al. (2017), who used evaluated rate coefficients and associated uncertainties (IUPAC), to show that the uncertainty in k^{NO_3} is highly dependent on the ratio between the NO_2 mixing ratio and the measured reactivity. If a reactivity of $0.046\,s^{-1}$ (e.g. from 3 ppbv of isoprene) is measured at 5 ppbv of NO_2 (typical for this campaign), the correction derived from the simulation would contribute an uncertainty of 32 % to the resulting overall uncertainty of 36 %. For an experiment with 25 ppbv of NO_2 and 10 ppbv of isoprene, large uncertainties (> 100 %) are associated with the correction procedure as the NO_3 loss caused by reaction with NO_2 exceeds VOC-induced losses. Later we show that data obtained even under unfavourable conditions (high NO_2 mixing ratios) are in accord with isoprene measurements, which suggests that the recommended uncertainties in rate coefficients for Reactions (R3) and (R4) are overly conservative.

The sampled air was typically mixed with ~ 50 pptv of NO_3 radicals, and the reaction between NO_3 and RO_2 radicals generated in the flow tube (Reaction R5) represents a potential bias to the measurement of k^{NO_3}. In a typical experiment (e.g. 3 ppbv of isoprene), the reactivity of NO_3 towards isoprene is $0.046\,s^{-1}$. A simple calculation shows that a total of 20 pptv of RO_2 radicals has been formed after 10.5 s reaction between NO_3 and isoprene in the flow tube. Assuming a rate coefficient of $\sim 5 \times 10^{-12}\,cm^3\,molecule^{-1}\,s^{-1}$ for reaction between NO_3 and RO_2, we calculate a 5 % contribution of RO_2 radicals to NO_3 loss. In reality, this value represents a very conservative upper limit as RO_2 is present at lower concentrations throughout most of the flow tube, and its concentration will be significantly reduced by losses to the reactor wall and self-reaction. In our further analysis we therefore do not consider this reaction.

Table 1. Experimental conditions in the SAPHIR chamber during the NO3ISOP campaign.

Date	T (°C)	H_2O (%)	D/N	O_3 (ppbv)	NO_2 (ppbv)	Isoprene (ppbv)	Seed aerosol	Notes
31 July	25–35	0	N	90–120	1–5	0	–	
1 August	22–31	0	N	85–115	2–5	1.2	–	
2 August	23–38	0	N	85–120	2–5	2.5	–	
3 August	30–42	1.3–2.7	D → N	45–100	1–5	2.5	–	
6 August	20–44	1.4	N → D	40–110	1–6	3.2	–	
7 August	20–41	0.45–0.6	N	45–60	3–4.5	2.3	–	contamination
8 August	22–28	0	N	75–115	13–30	8	–	
9 August	20–27	0	N	65–115	6–2.5	3	–	CO and propene
10 August	17–28	0	N	40–65	3–5.5	1.8	–	
12 August	14–36	0	N → D	70–115	4–12	3	–	CO
13 August	28–24	0	N	75–110	12–23	6	–	
14 August	18–24	0	N	70–110	13–22	13	$(NH_4)_2SO_4$	reduced fan operation
15 August	20–28	1.3–2	N	80–115	8–21	9	$(NH_4)_2SO_4$	
16 August	20–28	1.6	N → D	80–115	2–5	3	$(NH_4)_2SO_4$	
17 August	18–26	1.2–1.7	N → D	0–400	0–17	0	–	isobutyl nitrate, calibration
18 August	14–31	1.3–1.4	N → D	80–110	2–5	3.5	$(NH_4)_2SO_4$	β-caryophyllene
19 August	16–31	0.07	N	0–110	0–20	3	$(NH_4)_2SO_4$	MVK, N_2O_5 as NO_2 source
20 August	20–26	1.2–19	N	85–130	3–5	6	$(NH_4)_2SO_4$	β-caryophyllene
21 August	20–30	1.5–1.9	N	55–130	2–5	4.5	$(NH_4)_2SO_4$	CO and propene
22 August	18–33	1.3–17	N	75–110	2.5–8.5	5	$(NH_4)_2SO_4$	plant emissions
23 August	18–31	1.5–2.2	N	45–100	3.5–5	4	$(NH_4)_2SO_4$	
24 August	17–23	1–1.6	N	85–110	2.3–5.5	22	NH_4HSO_4	β-caryophyllene

D/N denotes if the experiment was conducted with the chamber roof opened (D: daytime) or closed (N: night-time) and in which order a transition was done. Only maximum values of measured isoprene are listed.

2.3 VOC measurements: PTR-ToF-MS

During the NO3ISOP campaign, isoprene and other VOCs were measured by two different PTR-ToF-MS (proton transfer reaction time-of-flight mass spectrometer) instruments. The PTR-TOF1000 (IONICON Analytic GmbH) has a mass resolution $> 1500\,m/\Delta m$ and a limit of detection of < 10 ppt for a 1 min integration time. The instrumental background was determined every hour by pulling the sample air through a heated tube (350 °C) filled with a Pt catalyst for 10 min. Data processing was done using PTRwid (Holzinger, 2015), and the quantification and calibration was done once per day, following the procedure as described recently (Holzinger et al., 2019).

The Vocus PTR (Tofwerk AG and Aerodyne Research Inc.) features a newly designed focusing ion–molecule reactor, resulting in a resolving power of $12\,000\,m/\Delta m$ (Krechmer et al., 2018). Calibration was performed on an hourly basis for 5 min. The isoprene measurements of the two instruments agreed mostly within the uncertainties (14 %). An exemplary comparison between the two instruments of an isoprene measurement can be found in the Supplement (Fig. S1). For the evaluation of the experiment on the 2 August, only data from the PTR-TOF1000 were available. For all the other experiments of the campaign, isoprene and monoterpene mixing ratios were taken from the Vocus PTR, owing to its higher resolution and data coverage.

2.4 NO_3, N_2O_5, NO_2, NO, and O_3 measurements

The NO_3/N_2O_5 mixing ratios used for analysis are from a harmonized data set including the measurements from two CRDS instruments. Data availability, quality and consistency with the expected $NO_3/N_2O_5/NO_2$ equilibrium ratios were criteria for selecting which data set to use for each experiment. Both instruments measure NO_3 (and N_2O_5 after its thermal decomposition to NO_3 in a heated channel) using cavity ring-down spectroscopy at a wavelength of ~ 662 nm. The 5-channel device operated by the Max Planck Institute (MPI) additionally measured NO_2 and has been described recently in detail (Sobanski et al., 2016a). Its NO_3 channel has a limit of detection (LOD) of 1.5 pptv (total uncertainty of 25 %); the N_2O_5 channel has a LOD of 3.5 pptv (total uncertainty of 28 % for mixing ratios between 50 and 500 pptv). Air was subsampled from a bypass flow drawing ~ 40 SLPM through a 4 m length of 0.5 in. (inner diameter, i.d.) PFA (perfluoroalkoxy alkane) tubing from the chamber. Variation of the bypass flow rate was used to assess losses of NO_3 (< 10 %) in transport to the instrument, for which correction was applied. Air entering the instrument was passed through a Teflon membrane filter (Pall Corp., 47 mm, 0.2 µm pore), which was changed every 60 min. Corrections for loss

of NO_3 and N_2O_5 on the filter and inlet lines were carried out as described previously (Sobanski et al., 2016a).

The second CRDS was built by the NOAA Chemical Sciences Laboratory (Dubé et al., 2006; Fuchs et al., 2008, 2012; Wagner et al., 2011; Dorn et al., 2013) and operated by the Institut de Combustion, Aérothermique, Réactivité et Environnement (ICARE). During the NO3ISOP campaign, the NOAA-CRDS was positioned beneath the chamber, and air was sampled through an individual port in the floor. The sampling flow rate was 5.5–7 L min^{-1} through a Teflon FEP line (i.d. 1.5 mm, total length about 0.9 m) extending by about 50 cm (i.d. 4 mm) with 25 cm (i.d. 4 mm) in the chamber. A Teflon filter (25 µm thickness, 47 mm diameter, 1–2 µm pore size) was placed downstream of the inlet to remove aerosol particles and changed automatically at an interval of 1.5–2 h, depending on the conditions of the experiments, such as the amount of aerosol in the chamber. The instrument was operated with a noise equivalent 1σ detection limit of 0.25 and 0.9 pptv in 1 s for the NO_3 and N_2O_5 channels, respectively. The total uncertainties (1σ) of the NOAA-CRDS instrument were 25 % (NO_3) and −8 %/+11 % (N_2O_5).

NO_2 mixing ratios were taken from a harmonized data set combining the measurements of the 5-channel CRDS with that of the NO_3 reactivity setup as well as the NO_x measurement of a thermal dissociation CRDS setup (Thieser et al., 2016). The NO_x measurement could be considered a NO_2 measurement since during dark periods of the experiments NO would have been present at extremely low levels. The total uncertainty associated with the NO_2 mixing ratios is 9 %.

NO was measured with a LOD of 4 pptv via chemiluminescence (CL; Ridley et al., 1992) detection (ECO Physics, model TR780), and ozone was quantified with a LOD of 1 ppbv by ultraviolet absorption spectroscopy at 254 nm (Ansyco, ozone analyser 41M). Both instruments operate with an accuracy (1σ) of 5 %.

2.5 Box model

The results of the chamber experiments were analysed using a box model based on the oxidation of isoprene by NO_3, OH and O_3 as incorporated in the Master Chemical Mechanism (MCM), version 3.3.1 (Saunders et al., 2003; Jenkin et al., 2015). In this work, the analysis focusses on the fate of the NO_3 radical, so the oxidation of some minor products was omitted in order to reduce computation time. Moreover, the most recently recommended rate coefficient (IUPAC, 2020) for the reaction between NO_3 and isoprene ($k_5 = 2.95 \times 10^{-12} \exp(-450/T)$ cm^3 $molecule^{-1}$ s^{-1}) was used instead of the value found in the MCM v3.3.1, which is 6.8 % higher. Chamber-specific parameters such as temperature and pressure as well as the time of injection and amount of trace gases added (usually O_3, NO_2 and isoprene) were the only constraints to the model. The chamber dilution flow was implemented as first-order loss rates for all trace gases and wall loss rates for NO_3 or N_2O_5 were introduced (see Sect. 3.2). The numerical simulations were performed with FACSIMILE/CHEKMAT (release H010, date 28 April 1987, version 1) at 1 min time resolution (Curtis and Sweetenham, 1987). The chemical scheme used is listed in the Supplement (Table S1).

3 Results and discussion

An overview of the experimental conditions (e.g. isoprene, NO_3, NO_2 and O_3 mixing ratios) on each day of the campaign is given in Fig. 1. The temperature in the chamber was typically between 20 and 30 °C but increased up to 40 °C when the chamber was opened to sunlight. The relative humidity was close to 0 % during most of the experiments before 14 August. After this date, the experiments focussed on secondary organic aerosol formation and humidified air was used.

We divide the experiments into two broad categories according to the initial conditions: type 1 experiments were undertaken with NO_3 production from 5 ppbv of NO_2 and 100 ppbv of O_3. The addition of isoprene with mixing ratios of ∼ 3 ppbv resulted in NO_3 reactivities of around 0.05 s^{-1} at the time of injection. The NO_3 and N_2O_5 mixing ratios were typically of the order of several tens of parts per trillion by volume (pptv) in the presence of isoprene under dry conditions. During humid experiments (with seed aerosol), NO_3 mixing ratios were mostly below the LOD in the presence of isoprene, owing to increased uptake of NO_3/N_2O_5 on particles. An exceptionally large isoprene injection (∼ 20 ppbv) resulted in the maximum NO_3 reactivity of 0.4 s^{-1} on the 24 August. In type 2 experiments, higher NO_3 production rates were achieved by using 25 ppbv of NO_2 and 100 ppbv of O_3. In these experiments, with the goal of generating high concentrations of organic oxidation products, isoprene mixing ratios of 10 ppbv resulted in reactivities of ∼ 0.2 s^{-1} at the time of isoprene injection. Owing to high NO_3 production rates, several hundred parts per trillion of NO_3 and a few parts per billion of N_2O_5 were present in the chamber.

Figure 1 shows that once isoprene has been fully removed at the end of each experiment, the NO_3 reactivity tends towards its LOD of 0.005 s^{-1}, indicating that the evolution of the NO_3 reactivity is closely linked to the changing isoprene mixing ratio.

3.1 Comparison of k^{NO_3} with calculated reactivity based on measurements of VOCs

The VOC contribution to the NO_3 reactivity is the summed first-order loss rate coefficient attributed to all non-radical VOCs present in the chamber that can be transported to the FT-CRDS according to Eq. (1):

$$k^{NO_3} = \sum k_i [\mathrm{VOC}]_i, \quad (1)$$

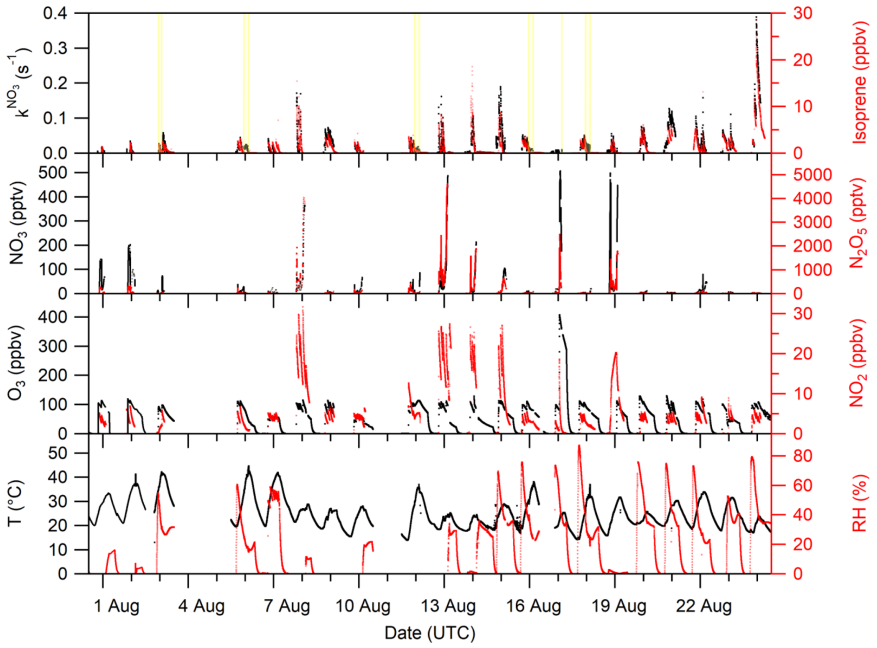

Figure 1. Overview of the temperature (T); relative humidity (RH); VOC-induced NO_3 reactivity (k^{NO_3}); and the O_3, NO_2, NO_3, N_2O_5, and isoprene mixing ratios during the NO3ISOP campaign. The yellow shaded area in the upper panel represent phases of the experiment when the chamber roof was opened. The ticks mark 12:00 UTC of the corresponding day.

where k_i is the rate coefficient (cm^3 molecule^{-1} s^{-1}) for the reaction between a VOC of concentration $[VOC]_i$ and NO_3.

Reliable values of k^{NO_3} and VOC data are available from the 2 August onwards (see Table 1 for experimental conditions) and were used to compare FT-CRDS measurements of k^{NO_3} with $\Sigma k_i[VOC]_i$. For most of the experiments, isoprene was the only VOC initially present in the chamber, and at the beginning of the experiments k^{NO_3} should be given by k_5[isoprene], with the latter measured by the PTR-MS instruments (see above). On the 9 and 21 August, both isoprene and propene (100 ppbv) were injected into the chamber; the summed NO_3 reactivity from these trace gases was then k_5[isoprene] $+ k_{propene}$[propene], with $k_{propene} = 9.5 \times 10^{-15}$ cm^3 molecule^{-1} s^{-1} at 298 K (IUPAC, 2020). As no propene data were available, the propene mixing ratios were assessed with the model (see above) based on injected amounts as well as subsequent loss by oxidation chemistry (mainly ozonolysis) and dilution. On the 22 August, coupling to a plant emission chamber permitted the introduction of monoterpenes and isoprene into the main chamber so that the NO_3 reactivity was k_5[isoprene] $+$ $k_{monoterpenes}$[monoterpenes]. The uncertainty in $\Sigma k_i[VOC]_i$ was propagated from the standard deviation of the isoprene and monoterpene mixing ratios and from the uncertainties of 41 % in k_5, 58 % in $k_{propene}$ (IUPAC, 2020) and 47 % in $k_{monoterpenes}$ (average uncertainty of three dominant terpenes; see below).

Figure 2a depicts an exemplary time series of k^{NO_3} and $\Sigma k_i[VOC]_i$ between the 9 and 13 August. The measured k^{NO_3} and values of $\Sigma k_i[VOC]_i$ calculated from measured isoprene (and modelled propene in the case of the 9 August) are, within experimental uncertainty, equivalent, indicating that the NO_3 reactivity can be attributed entirely to its reaction with isoprene (and other reactive trace gases like propene) injected into the chamber.

The correlation between k^{NO_3} and $\Sigma k_i[VOC]_i$ for the entire campaign data set is illustrated in Fig. 2b. Type 2 experiments (high NO_2 mixing ratios) were included despite the unfavourable conditions for measurement of k^{NO_3}, which result in large correction factors via numerical simulation (see above). The data points obtained on the 14 August display large variability, which is likely to have been caused by non-operation of the fans leading to poor mixing in the chamber. An unweighted linear regression of the whole data set yields a slope of 0.962 ± 0.003, indicating excellent agreement between the directly measured NO_3 and those calculated from Eq. (1). The intercept of (0.0023 ± 0.0004) s^{-1} is below the LOD of the reactivity measurement. A correlation coefficient of 0.95 underlines the linearity of the whole data set despite increased scatter caused by the unfavourable conditions during type 2 experiments. Note that data from the 7 August (chamber contamination) were not used. On the 15 and 21 August, additional flushing of the chamber with synthetic air (150–300 m^3) and humidification shortly before the actual beginning of the experiment resulted in a constant back-

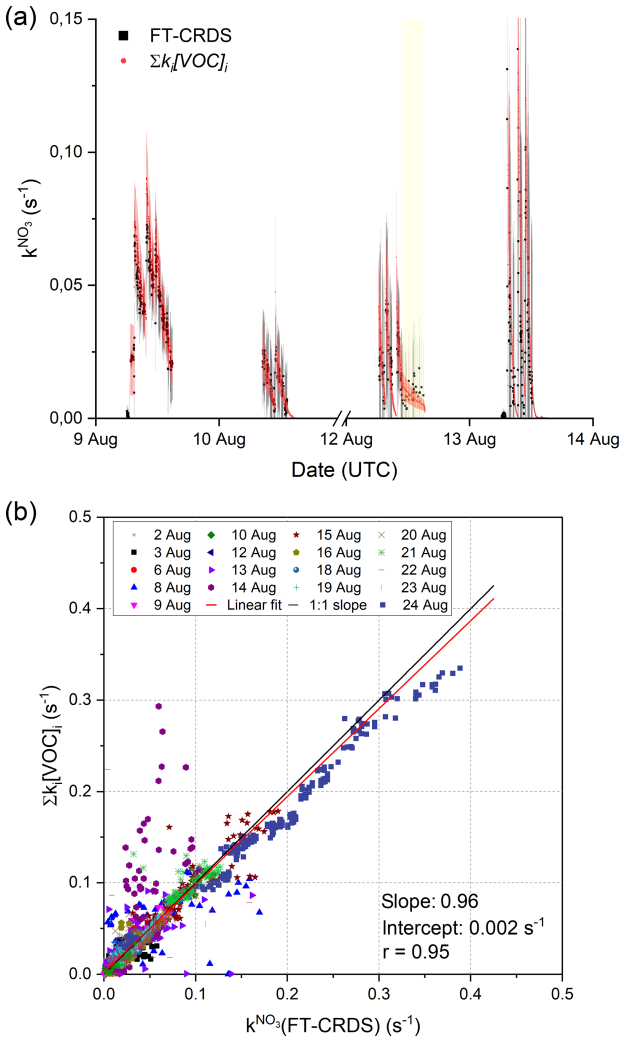

Figure 2. **(a)** 4 d time series of k^{NO_3} and $\Sigma k_i[\mathrm{VOC}]_i$. The total uncertainty in k^{NO_3} was calculated as described by Liebmann et al. (2017) and is indicated by the grey shaded area. The red shaded area shows the associated uncertainty of the calculated reactivities and are derived from error propagation using the standard deviation of the isoprene mixing ratios and an uncertainty of 41 % for the rate coefficient for reaction between NO_3 and isoprene (IUPAC, 2020). The ticks mark 00:00 UTC of the corresponding date, and yellow shaded areas represent periods in which the chamber roof was opened. **(b)** Correlation between $\Sigma k_i[\mathrm{VOC}]_i$ and k^{NO_3} measurements. The red line represents a least-squares linear fit to the entire data set, while the black line illustrates an ideal slope of 1 : 1.

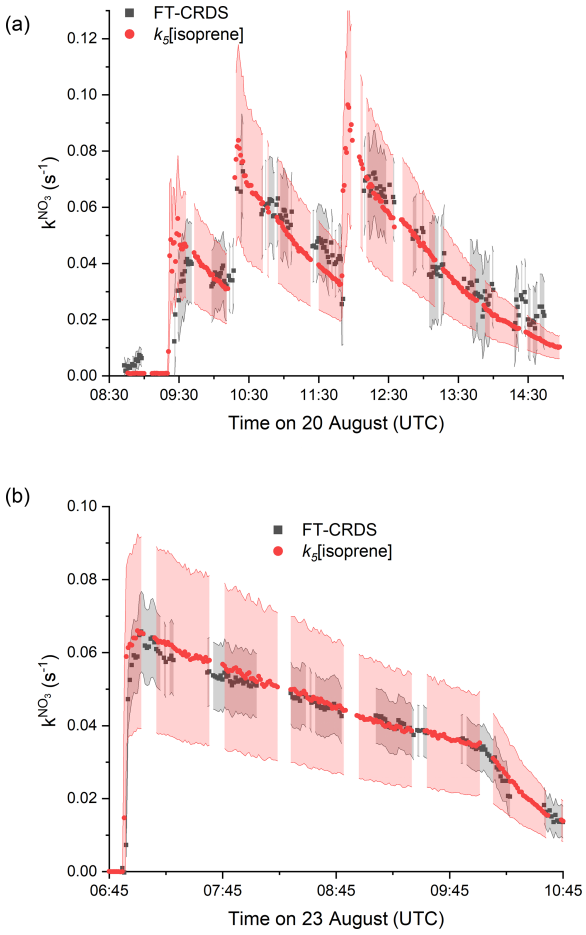

Figure 3. Measured reactivity (k^{NO_3}, black data points) and reactivity calculated from Eq. (1) (red data points), which is equivalent to k_5[isoprene]. The grey shaded area represents the total uncertainty in k^{NO_3}; the red shaded areas represent the total uncertainty in k_5[isoprene] and were estimated as explained in Fig. 2. **(a)** 20 August: type 1 experiment with initial mixing ratios of $NO_2 = 4.6$ ppbv and $O_3 = 120$ ppbv. **(b)** 23 August: only O_3 (100 ppbv) and isoprene (4 ppbv) were initially present.

ground reactivity in k^{NO_3} of 0.04 s^{-1} on the 15 August and 0.012 s^{-1} on the 21 August. High background reactivity was not observed during other humid experiments if the chamber was flushed extensively with synthetic air ($\sim 2000\ m^3$) during the night between experiments and if the additional flushing was omitted. The trace gas(es) causing this background reactivity could not be identified with the available measurements, but they are probably released from the chamber walls during flushing and humidification. In order to make a detailed comparison with the VOC data, the background reactivity, which was fairly constant, was simply added.

A more detailed examination of k^{NO_3} data from two type 1 experiments (low NO_2) is given in Fig. 3. The grey shaded areas indicate the total uncertainty associated with the FT-CRDS measurement of k^{NO_3} (Liebmann et al., 2017); the scatter in the data stems mostly from the correction procedure via numerical simulation.

On the 20 August (Fig. 3a), in addition to NO_2 and O_3, $(NH_4)_2SO_4$ seed aerosol ($\sim 50\ \mu g\ cm^{-3}$) and β-caryophyllene (~ 2 ppbv) were injected at 08:40 UTC in order to favour formation of secondary organic aerosol. The

instrument was zeroing until shortly after the injection of this terpene. As the lifetime of β-caryophyllene is extremely short in the chamber under the given conditions (~ 150 s), only the small fraction of unreacted β-caryophyllene contributes to the k^{NO_3} signal observed after 08:40 UTC. At 09:20, 10:13 and 11:50 UTC isoprene was injected into the chamber, resulting in step-like increases in the measured NO_3 reactivity. Each increase in reactivity and the ensuing evolution over time match well with the calculated values of k_5[isoprene] (red data points). The red shaded area indicates the overall uncertainty in the latter. Clearly, within experimental uncertainty, the NO_3 reactivity is driven almost entirely by reaction with isoprene, with negligible contribution from stable, secondary products.

During the experiment of the 23 August (Fig. 3b), only isoprene and ozone were present in the chamber for the first 4 h. Isoprene depletion is dominated by ozonolysis at this phase, whereas the sudden drop in k^{NO_3} is caused by an increased dilution flow during humidification of the chamber around 10:00 UTC. The absence of NO_2 results in a more accurate, less scattered measurement of k^{NO_3} and underscores the reliability of the measurement under favourable conditions. All of the observed reactivity can be assigned to isoprene that was injected at 06:52 UTC. This implies that stable secondary oxidation of products from isoprene ozonolysis (such as formaldehyde, MACR (methacrolein), MVK) are insignificant for k^{NO_3}, which is consistent with the low rate coefficients (e.g. $k_{MACR+NO_3} = 3.4 \times 10^{-15}$ cm^3 molecule^{-1} s^{-1} as highest of the three; IUPAC, 2020).

The results of a type 2 experiment with NO_2 mixing ratios of ~ 20 ppbv as well as higher isoprene mixing ratios (injections of ~ 8 and ~ 3 ppbv under dry conditions) are depicted in Fig. 4a. Despite the requirement of large correction factors to k^{NO_3} owing to the high NO_2 to isoprene ratios, fair agreement between measured k^{NO_3} and the expected reactivity is observed for each of the isoprene injections at 07:30, 09:20 and 10:50 UTC. The agreement may indicate that the uncertainty in k^{NO_3} (grey shaded area), which is based on uncertainty in, for example, the rate coefficient for reaction between NO_3 and NO_2 (Liebmann et al., 2017), is overestimated.

In Fig. 4b we display the results of an experiment on 12 August, in which the initially darkened chamber (first ~ 4 h) was opened to sunlight (final 4 h). NO_2 mixing ratios varied between 12 and 4 ppbv and isoprene was injected (~ 3 ppbv) three times at 05:55, 07:40 and 09:45 UTC. During the dark phase, measured k^{NO_3} follows k_5[isoprene]. At 11:00 UTC the chamber was opened to sunlight, during which approximately 5 ppbv of NO_2, 200–150 pptv of NO and < 1 ppbv of isoprene were present in the chamber. In this phase, the loss of NO_3 was dominated by its photolysis and reaction with NO. Within experimental uncertainty, the measured daytime k^{NO_3} after correction for both NO_2 and NO (correction factors between 0.05 and 0.02) during the sunlit period was still close to k_5[isoprene].

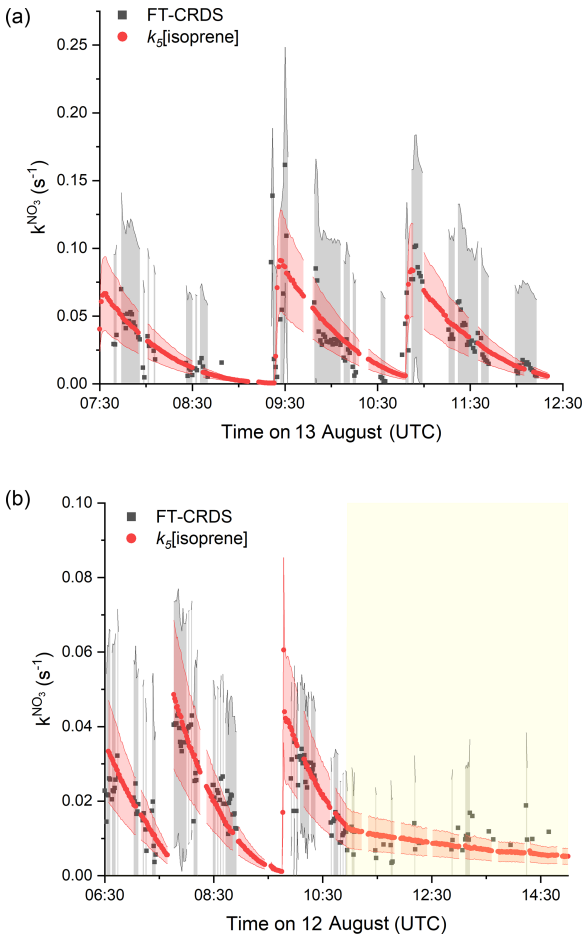

Figure 4. Measured (black) and expected (red) NO_3 reactivity using Eq. (1). The corresponding uncertainties were estimated as described in Fig. 2 and are indicated as shaded areas. **(a)** Type 2 experiment is from the 13 August under dry conditions with initial mixing ratios of $NO_2 = 25$ ppbv and $O_3 = 104$ ppbv. **(b)** Experiment from the 12 August is with NO_2 mixing ratios between 7 and 12 ppbv and initial mixing ratio of $O_3 = 79$ ppbv. The yellow shaded area denotes the period with the chamber roof opened after 11:00 UTC.

On the 22 August, the SAPHIR chamber was filled with air from a plant chamber (SAPHIR-PLUS) containing six European oaks (*Quercus robur*) which emit predominantly isoprene but also monoterpenes, mainly limonene, 3-carene and α-pinene (van Meeningen et al., 2016).

The time series of measured NO_3 reactivity (k^{NO_3}, black data points) after coupling to the plant chamber at 08:00 UTC is shown in Fig. 5. Data after 11:40 UTC are not considered, because the chamber lost its pressure after several recoupling attempts to the plant chamber. Also plotted (red data points) is the NO_3 reactivity calculated from $\Sigma k_i[\mathrm{VOC}]_i$, whereby both isoprene and the total terpene mixing ratio (up to 500 pptv) were measured by the Vocus PTR-MS. As only the mixing ratio of the sum of the monoterpenes

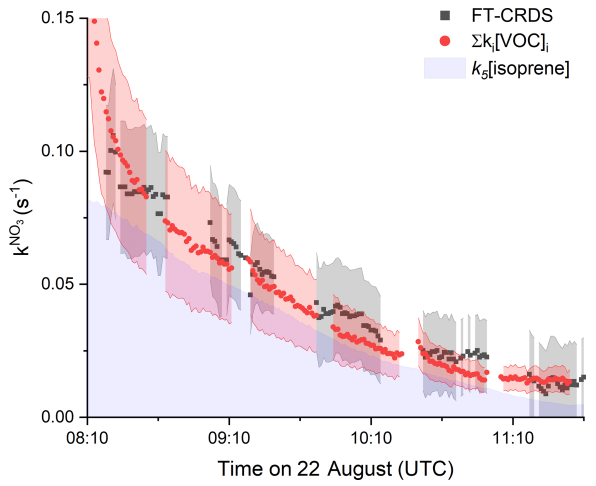

Figure 5. Results from 22 August between 08:00 and 11:40 UTC. Comparison between k^{NO_3} (black data points, uncertainty as grey shaded area) and NO_3 reactivity calculated from $\Sigma k_i[\mathrm{VOC}]_i$ (red data points) using the measured isoprene and Σmonoterpenes mixing ratios. The associated uncertainty (red area) was derived by error propagation by considering the standard deviations of the VOC mixing ratios as well as the uncertainties of the rate coefficients (41 % for k_5 and 47 % for $k_{\mathrm{monoterpenes}}$). The uncertainty of k^{NO_3} was estimated as explained in Fig. 2. The contribution of isoprene to the observed reactivity is indicated by the area in purple.

was known, an average value of the very similar NO_3 rate coefficients (IUPAC, 2020) for limonene, 3-carene and α-pinene was used for the calculation of $\Sigma k_i[\mathrm{VOC}]_i$ with $k_{\mathrm{monoterpenes}} = 9.1 \times 10^{-12}$ cm^3 molecule^{-1} s^{-1} (analogously averaged uncertainty of 47 %). Figure 5 indicates very good agreement between measured and calculated NO_3 reactivity, with ∼ 70 % of the overall reactivity caused by isoprene, which is indicated by the purple shaded area. Despite being present at much lower mixing ratios that isoprene, the terpenes contribute ∼ 30 % to the overall NO_3 reactivity, which reflects the large rate constants for reaction of NO_3 with terpenes.

The experiments described above indicate that, for a chemical system initially containing only isoprene as the reactive organic trace gas, the measured values of k^{NO_3} can be fully assigned to the isoprene present in the chamber over the course of its degradation. During the NO3ISOP campaign, not only NO_3 reactivity but also OH reactivity (k^{OH}) was measured; the experimental technique is described briefly in the Supplement. A detailed analysis of the OH reactivity data set will be subject of a further publication, and in Fig. S1 we only compare values of k^{NO_3} and k^{OH} obtained directly after isoprene injections, where k^{OH} should not be significantly influenced by the reaction of OH with secondary products. As shown in Fig. S2, isoprene concentrations derived from both k^{NO_3} and k^{OH} are generally in good agreement when [isoprene] < 5 ppbv.

The oxidation of isoprene by NO_3 in air results in the formation of stable (non-radical) products as well as organic peroxy radicals (RO_2) that can also react with NO_3. As radicals (e.g. NO_3, RO_2 and HO_2) are not sampled by the FT-CRDS, the equivalence of k^{NO_3} and k_5[isoprene] indicates that non-radical, secondary oxidation products do not contribute significantly to the NO_3 reactivity.

3.2 Steady-state and model calculations: role of RO_2 and chamber walls

The contribution of RO_2, HO_2 and stable products to NO_3 reactivity was examined using a box model based on the chemical mechanistic oxidation processes of isoprene by NO_3, OH and O_3 as incorporated in the Master Chemical Mechanism, version 3.3.1 (Saunders et al., 2003; Jenkin et al., 2015; Khan et al., 2015). A numerical simulation (Fig. 6) of the evolution of NO_3 reactivity was initialized using the experimental conditions of the first isoprene injection on 10 August (5.5 ppbv NO_2, 60 ppbv O_3 and 2 ppbv isoprene, dry air), including chamber-specific parameters such as temperature, the NO_3 and N_2O_5 wall loss rates (quantified in detail below), and the dilution rate. In the model, NO_3 reacts with both stable products and peroxy radicals. One of several major stable oxidation products according to MCM is an organic nitrate with aldehyde functionality ($O_2NOC_4H_6CHO$, NC4CHO). As the corresponding rate coefficient for the reaction of this molecule with NO_3 is not known, MCM uses a generic rate coefficient based on the IUPAC-recommended temperature-dependent expression for acetaldehyde + NO_3 scaled with a factor of 4.25 to take differences in molecular structure into account. The maximum modelled mixing ratio of NC4CHO was ∼ 5 ppbv in type 2 experiments, which would result in a NO_3 reactivity of 0.001 s^{-1}. This value is below the instrument's LOD and would only become observable at extremely low isoprene concentrations. As apparent in Fig. 6, the contribution of stable oxidation products (blue) to the NO_3 reactivity is insignificant compared to the primary oxidation of isoprene (red).

Since the rate coefficients for reaction of isoprene-derived peroxy radicals and NO_3 are (unlike NO_3+HO_2) poorly constrained by experimental data, the MCM uses a generic value of 2.3×10^{-12} cm^3 molecule^{-1} s^{-1}, which is based on the rate coefficient for the reaction between NO_3 and $C_2H_5O_2$. The modelled overall NO_3 reactivity when reactions with RO_2 and HO_2 are included (black line) is on average 22 % higher than the reactivity associated only with isoprene, with the major contributors to the additional NO_3 reactivity being nitrooxy isopropyl peroxy radicals ($O_2NOC_5H_8O_2$, NISOPOO) formed in the primary oxidation step. As neither RO_2 nor HO_2 radicals will survive the inlet tubing (and heated glass flask) between the SAPHIR chamber and the FT-CRDS instrument, our measurement of k^{NO_3} does not include their contribution. The measured values of k^{NO_3} (black data points) scatter around the isoprene-induced reactivity

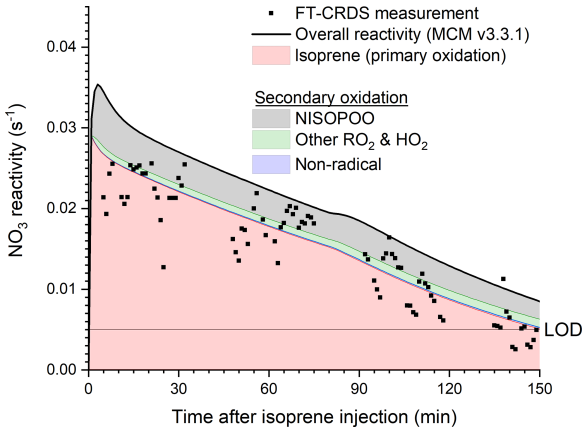

Figure 6. Experimental results for k^{NO_3} and numerical simulation (MCM v3.3.1) of the NO_3 reactivity following the first isoprene injection of the experiment on the 10 August. The simulation was run with 1 min resolution; initial conditions were 60 ppbv of O_3, 5.5 ppbv of NO_2 and 2 ppbv of isoprene and used actual chamber temperatures, which increased from 293 to 301 K during the course of the experiment. Wall losses of NO_3 and N_2O_5 were parameterized as described in the text. Individual contributions to the NO_3 reactivity of isoprene, peroxy radicals and secondary oxidation products are highlighted.

(red), which is understood to result from the minor role of stable (non-radical) oxidation products (blue) in removing NO_3 and the exclusion of peroxy radicals in the measurement.

Another method of deriving NO_3 reactivity is to calculate it from NO_3 (and/or N_2O_5) mixing ratios and production rates under the assumption of steady state as has been carried out on several occasions for the analysis of ambient NO_3 measurements (Heintz et al., 1996; Geyer and Platt, 2002; Brown et al., 2004; Sobanski et al., 2016b). In contrast to our direct measurement of k^{NO_3}, all loss processes (including reaction of NO_3 with RO_2 and HO_2 and uptake of NO_3 and N_2O_5 to surfaces) are assessed using the steady-state calculations. A comparison between k^{NO_3} and NO_3 reactivity based on a steady-state analysis should enable us to extract the contribution of peroxy radicals and wall losses of NO_3 in the SAPHIR chamber. In steady state, the NO_3 reactivity ($k_{ss}^{NO_3}$) is derived from the ratio between the NO_3 production rate via Reaction (R2) with rate coefficient k_2 and the mixing ratios of O_3, NO_2 and NO_3 (Eq. 2).

$$k_{ss}^{NO_3} = \frac{k_2\,[O_3]\,[NO_2]}{[NO_3]} \tag{2}$$

Acquiring steady state can take several hours if the NO_3 lifetime is long, temperatures are low or NO_2 mixing ratios are high (Brown et al., 2003). In the NO3ISOP experiments, the NO_3 reactivities were generally high, and steady state is achieved within a few minutes of isoprene being injected into the chamber. However, NO_2 reinjections in the chamber during periods of low reactivity at the end of an experiment when isoprene was already depleted can lead to a temporary breakdown of the steady-state assumption. In order to circumvent this potential source of error, the non-steady-state reactivities ($k_{nss}^{NO_3}$) based on NO_3 and N_2O_5 measurements (McLaren et al., 2010) were calculated using Eq. (3).

$$k_{nss}^{NO_3} = \frac{k_2\,[O_3]\,[NO_2] - \frac{d[NO_3]}{dt} - \frac{d[N_2O_5]}{dt}}{[NO_3]} \tag{3}$$

This expression is similar to Eq. (2) except for the subtraction of the derivatives $d[NO_3]/dt$ and $d[N_2O_5]/dt$ from the production term. A comparison of $k_{ss}^{NO_3}$ and $k_{nss}^{NO_3}$ is given in the Supplement and verifies the assumptions above: as soon as isoprene is injected into the system, $k_{ss}^{NO_3}$ and $k_{nss}^{NO_3}$ are equivalent (see Fig. S3a), but $k_{ss}^{NO_3}$ shows short-term deviations at NO_2 reinjections (see Fig. S3b). As the non-steady-state reactivities are less affected by such events, the latter were used for the comparison with the measured NO_3 reactivities. The steady-state and the non-steady-state calculations are only valid if equilibrium between NO_3 and N_2O_5 is established. Moreover, the N_2O_5 measurements are usually less sensitive to instrument-specific losses under dry conditions. For this reason, measured NO_3 mixing ratios were checked for consistency with the equilibrium to N_2O_5 using the equilibrium constant K_{eq} for Reactions (R3)/(R4) as well as the measured N_2O_5 and NO_2 mixing ratios as denoted in Eq. (4) for this analysis. In the case when a significant deviation was observed, NO_3 mixing ratios from $[NO_2]$, $[N_2O_5]$ and K_{eq} were used.

$$[NO_3]_{eq} = \frac{[N_2O_5]}{K_{eq}[NO_2]} \tag{4}$$

A time series of measured k^{NO_3} and calculated $k_{nss}^{NO_3}$ is depicted in Fig. 7a, which shows the results from experiments in the absence of aerosol only. It is evident that $k_{nss}^{NO_3}$ is much higher than k^{NO_3}. In Fig. 7b we plot k^{NO_3} versus $k_{nss}^{NO_3}$: an unweighted, orthogonal, linear fit has a slope of 0.54 ± 0.01 and indicates that the measured values of k^{NO_3} are almost a factor of 2 lower than $k_{nss}^{NO_3}$. Propagation of the uncertainties in k_2 (15 %; IUPAC, 2020) and the NO_3, NO_2 and O_3 mixing ratios (25 %, 9 % and 5 %, respectively) results in an overall uncertainty of 31 % for $k_{nss}^{NO_3}$, which cannot account for its deviation to k^{NO_3}.

The fact that $k_{nss}^{NO_3}$ is significantly larger than k^{NO_3} indicates that NO_3 can be lost by reactions other than those with reactive, stable VOCs that can be sampled by the FT-CRDS instrument. As discussed above, RO_2 represents the most likely candidate to account for some additional loss of NO_3; the numerical simulations (MCM v3.3.1) predict an additional reactivity of the order of ~ 22 % based on a generic value for $k_{NO_3+RO_2}$. However, in order to bring k^{NO_3} and $k_{nss}^{NO_3}$ into agreement, either the RO_2 level or the rate coefficient for reaction between NO_3 and RO_2 (especially

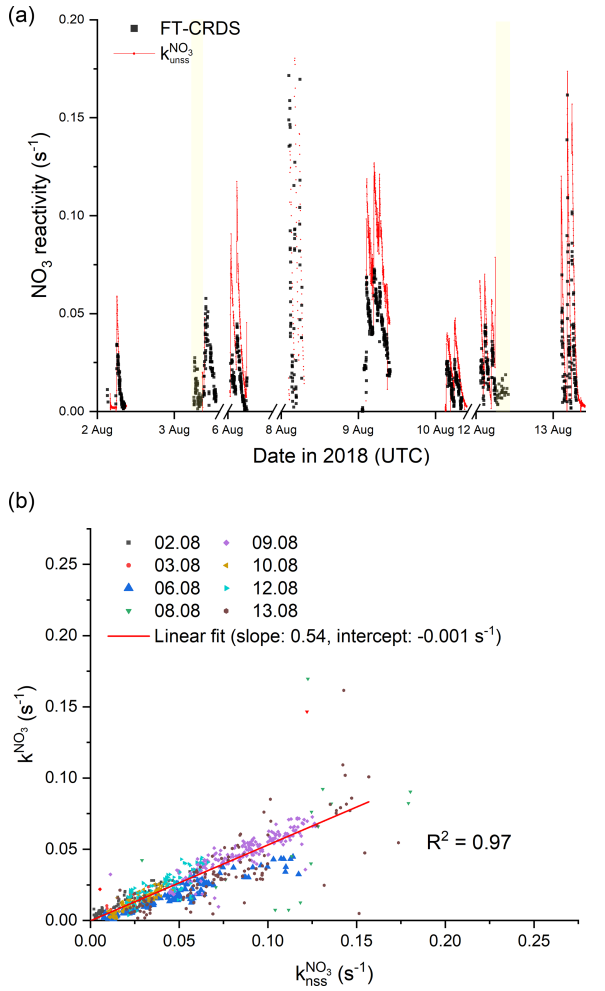

Figure 7. (a) Overview of measured (black) and calculated NO_3 reactivity with Eq. (3) (red). The ticks mark 00:00 UTC of the corresponding day. The yellow areas denote periods with an opened chamber roof. For the sake of clarity, the uncertainties are not included. **(b)** Correlation plot between k^{NO_3} and $k^{NO_3}_{nss}$. The red line represents an unweighted, orthogonal linear regression ($R^2 = 0.97$) of the complete data set.

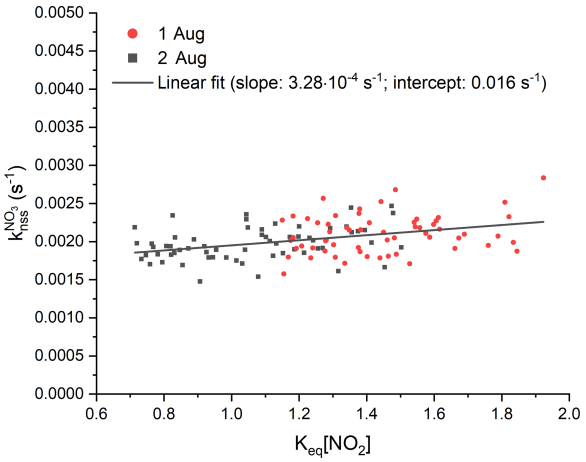

Figure 8. Analysis of the contribution of wall losses of NO_3 and N_2O_5 to NO_3 reactivity, $k^{NO_3}_{nss}$, are using experimental data during isoprene-free periods on the 1 August (red) and 2 August (black). Least-squares linear fit of the data is shown with a black line and yielded to an intercept $k^{NO_3}_{wall}$ of 0.016 s^{-1} and to a slope $k^{N_2O_5}_{wall}$ of 3.28×10^{-4} s^{-1}. For the sake of better clarity, error bars are not included.

NISOPOO) would have to be a factor of 2 larger than incorporated into the model (see below). Alternatively, losses of NO_3 (and N_2O_5) to surfaces enhance $k^{NO_3}_{nss}$ but not k^{NO_3}. As no aerosol was present in the experiments analysed above, the only surface available is provided by the chamber walls.

In order to quantify the contribution of NO_3 and N_2O_5 wall losses to $k^{NO_3}_{nss}$, we analysed the experiments from the 1 and 2 August during isoprene-free periods, i.e. when no RO_2 radicals are present and (in the absence of photolysis and NO) uptake of NO_3 (or N_2O_5) to the chamber walls represents the only significant sink. Consequently, plotting $k^{NO_3}_{nss}$ from this period against $K_{eq}[NO_2]$ enables separation of direct NO_3 losses (Reaction R10) from indirect losses via N_2O_5 uptake (Reaction R9) and to derive first-order loss rates ($k^{wall}_{NO_3}$ and $k^{wall}_{N_2O_5}$) of NO_3 and N_2O_5 according to Eq. (5) (Allan et al., 2000; Brown et al., 2009b; Crowley et al., 2010; McLaren et al., 2010).

$$k^{NO_3}_{nss} = k^{NO_3}_{wall} + k^{N_2O_5}_{wall} K_{eq}[NO_2] \quad (5)$$

The results from the isoprene-free periods of experiments on the 1 and 2 August are shown in Fig. 8. A linear regression of the data yields a slope ($k^{N_2O_5}_{wall}$) of $(3.28 \pm 1.15) \times 10^{-4}$ s^{-1} and an intercept ($k^{NO_3}_{wall}$) of (0.0016 ± 0.0001) s^{-1}, indicating that NO_3 losses dominate and that heterogeneous removal of N_2O_5 does not contribute significantly to the overall loss rate constant of ~ 0.002 s^{-1}. The data reproducibility from one experiment to the next indicates that the NO_3/N_2O_5 wall loss rates are unchanged if the experimental conditions, i.e. dry air and no aerosols, are comparable. Humidification of the air, on the other hand, may facilitate heterogeneous reactions of NO_3 or N_2O_5 with the chamber walls and increase corresponding loss rates. This might be an explanation for observation of a larger difference between k^{NO_3} and $k^{NO_3}_{nss}$ during an experiment under humid conditions on the 6 August (Fig. 7b, blue triangles). Lack of extensive isoprene-free periods on this day impede the extraction of wall loss rates with this approach: even after subtraction of k^{NO_3} from $k^{NO_3}_{nss}$, Eq. (5) is not applicable in experiments once isoprene is present (and becomes the dominant sink of NO_3) as reactions of RO_2 indirectly co-determine the NO_2 mixing ratios.

For further analysis, the wall loss rate constants of NO_3 and N_2O_5 were fixed as long as there was neither humidity nor particles in the chamber, and they are considered in-

variant with time after isoprene injections. This implicitly assumes that low-volatility oxidation products that deposit on chamber walls do not enhance the reactivity of the walls to NO_3. As these products have less double bonds than isoprene and react only very slowly with NO_3, this assumption would appear reasonable.

We examined the effect of introducing the NO_3 and N_2O_5 wall loss rate constants calculated as described above into the chemical scheme used in the box model (MCM v3.3.1). The results from three different model outputs for the experiment on the 2 August are summarized in Fig. 9, which compares simulated and measured mixing ratios of NO_3, N_2O_5, NO_2, O_3 and isoprene (following its addition at 11:00 UTC) as well as the measured and non-steady-state NO_3 reactivities k^{NO_3} and $k_{nss}^{NO_3}$. The omission of NO_3/N_2O_5 wall losses (model 1) results in simulated NO_3 and N_2O_5 mixing ratios up to 1400 and 1600 pptv, respectively, during the isoprene-free period, which exceed measurements by factors of 4–8. This is because the only loss process for these species in this phase is the dilution rate that is 2 orders of magnitude lower than the estimated wall loss rates. Such high amounts of NO_3/N_2O_5 in the parts per billion range result in rapid depletion of nearly half of the total injected isoprene within the first minute, which is why model 1 cannot describe the measurements either before or after the injection. Model 2 (red lines) includes the estimated wall loss rates and reproduces the measurements more accurately: the NO_2 and O_3 mixing ratios are accurately simulated. Furthermore, NO_3 and N_2O_5 mixing ratios that are only 10 % to 30 % higher than those measured and therefore NO_3 reactivities lower than $k_{nss}^{NO_3}$ (orange circles) are predicted.

The evolution of the isoprene mixing ratio is reproduced by the model, which is why k^{NO_3} (mostly determined by k_5[isoprene], purple area) is only slightly lower than the simulated overall reactivity by model 2. After quantification of NO_3/N_2O_5 wall losses, NO_3+RO_2 reactions remain the only source of additional NO_3 reactivity to explain the difference between k^{NO_3} and $k_{nss}^{NO_3}$. As already mentioned above, the model may underestimate the effect of RO_2-induced losses of NO_3 either because the RO_2 mixing ratios are underestimated or because the rate coefficient $k_{RO_2+NO_3}$ is larger than assumed.

The result of a simulation (model 3) with $k_{RO_2+NO_3}$ set to 4.6×10^{-12} cm^3 molecule^{-1} s^{-1} (twice the generic value in MCM v3.3.1) is displayed as the blue lines in Fig. 9. The O_3, NO_2, N_2O_5 and isoprene mixing ratios are only slightly affected by this change in the reaction constant, whereas its impact on the NO_3 mixing ratios as well as on the reactivity is very significant. The higher rate coefficient for reaction of NO_3 with RO_2 would be sufficient for the observed discrepancy between the overall reactivity $k_{nss}^{NO_3}$ and k^{NO_3} within the uncertainties associated with the analysis. Optimum agreement irrespective of uncertainties would be achieved with a value of 9.2×10^{-12} cm^3 molecule^{-1} s^{-1} for $k_{RO_2+NO_3}$ (i.e. a factor of 4 higher than in MCM), which is demonstrated in a comparable experiment under dry conditions on the 10 August (see Fig. S4 in the Supplement).

There are only few experimental studies on reactions of NO_3 with RO_2, and the rate coefficient for reaction of NO_3 with isoprene-derived RO_2 has never been measured. For the reaction between NO_3 and the methyl peroxy radical (CH_3O_2), values between 1.0×10^{-12} and 2.3×10^{-12} cm^3 molecule^{-1} s^{-1} have been reported (Crowley et al., 1990; Biggs et al., 1994; Daele et al., 1995; Helleis et al., 1996; Vaughan et al., 2006), with a preferred value of 1.2×10^{-12} cm^3 molecule^{-1} s^{-1} (Atkinson et al., 2006). Increasing the length of the C−C backbone in the peroxy radical appears to increase the rate coefficient, with values of 2.3×10^{-12} cm^3 molecule^{-1} s^{-1} preferred for reaction of NO_3 with $C_2H_5O_2$ (Atkinson et al., 2006), whereas the presence of electron-withdrawing groups attached to the peroxy carbon atom reduces the rate coefficient (Vaughan et al., 2006). A single study of the reaction between NO_3 and an acylperoxy radical indicates that the rate coefficient (4.0×10^{-12} cm^3 molecule^{-1} s^{-1}) may be larger than the MCM adopted value of 2.3×10^{-12} cm^3 molecule^{-1} s^{-1} (Canosa-Mas et al., 1996). Similarly, an indirect study (Hjorth et al., 1990) of the rate coefficient for the reaction between NO_3 and a nitro-substituted C_6 peroxy radical ($(CH_3)_2C(ONO_2)C(CH_3)_2O_2$) reports a value of 5×10^{-12} cm^3 molecule^{-1} s^{-1}, which may be appropriate for longer-chain peroxy radicals derived from biogenic trace gases. In light of the large uncertainty associated with the kinetics of $RO_2 + NO_3$ reactions, a rate coefficient of 4.6×10^{-12} cm^3 molecule^{-1} s^{-1} for reaction between NISOPOO and NO_3 is certainly plausible.

We note, however, that use of a faster rate coefficient for the reaction between RO_2 and NISOPOO, RO_2 isomerization processes and differentiation between the fates of the main NISOPOO isomers as proposed by Schwantes et al. (2015) would result in lower RO_2 mixing ratios. If $k_{NISOPOO+RO_2}$ in MCM v3.3.1 is set to a value of 5×10^{-12} cm^3 molecule^{-1} s^{-1} (average over all isomers, Schwantes et al., 2015), a slightly higher value of 5.2×10^{-12} cm^3 molecule^{-1} s^{-1} for $k_{RO_2+NO_3}$ would be necessary to bring modelled and measured NO_3 reactivity into agreement within associated uncertainties. Conversely, increasing RO_2 concentrations by the required factor of 2 would necessitate a significant reduction in the model rate coefficients for $RO_2 + RO_2$ or $RO_2 + HO_2$ reactions, which contradicts experimental results (Boyd et al., 2003; Schwantes et al., 2015) and is considered unlikely.

Differences in measurement of $k_{nss}^{NO_3}$ and modelled NO_3 reactivity could also result from incorrectly modelled product yields, owing to the simplified mechanism used, which, for example, does not consider in detail the formation of methyl vinyl ketone (MVK) via β-NISOPOO isomers or the reaction between NO_3 and other main products like hydroxy isopropyl nitrates (e.g. $O_2NOCH_2C(CH_3)CHCH_2OH$, ISOPCNO3) and nitrooxy

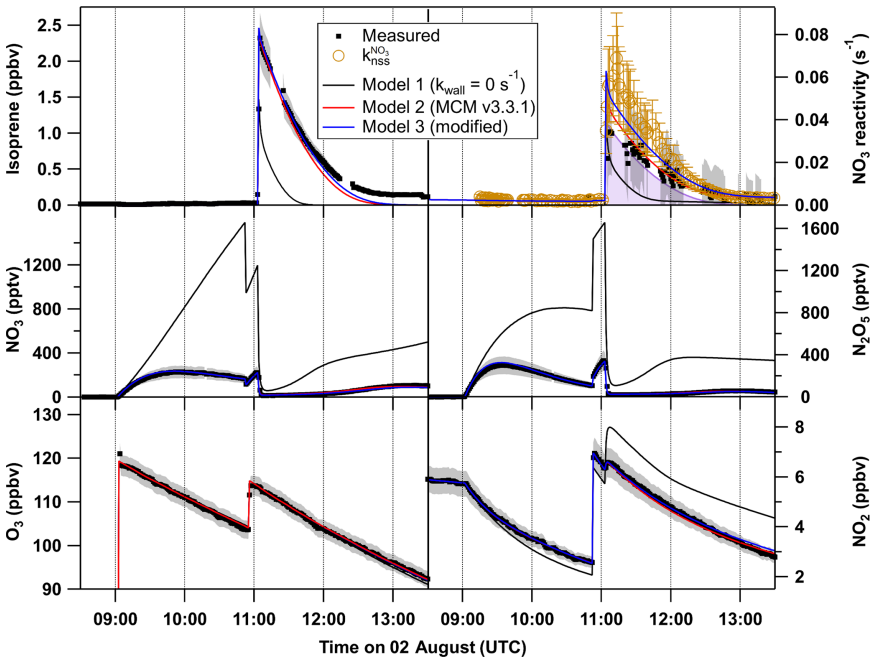

Figure 9. O_3, NO_2, NO_3, N_2O_5 and isoprene mixing ratios and NO_3 reactivity on 2 August (black). The grey shaded area symbolizes the overall uncertainty associated with each measurement. Orange circles denote the reactivity obtained using Eq. (3). The results of the numerical simulation using MCM v.3.3.1 with NO_3 and N_2O_5 wall loss rates set to $0\,s^{-1}$ (model 1) are shown by black lines. The model output with introduction of NO_3 and N_2O_5 wall loss rates of $0.016\,s^{-1}$ and $3.3 \times 10^{-4}\,s^{-1}$, respectively, for each of the reactants is shown by a red line (model 2), whereas the blue line (model 3) shows the result of model 2 with the rate coefficient for reaction between NO_3 and RO_2 set to $4.6 \times 10^{-12}\,cm^3\,molecule^{-1}\,s^{-1}$, which is twice the value estimated by the MCM.

isopropyl hydroperoxide ($O_2NOCH_2C(CH_3)CHCH_2OOH$, NISOPOOH). However, none of these products is expected to react sufficiently rapidly with NO_3 to make a difference: the rate coefficient for reaction of NO_3 with MVK is $< 6 \times 10^{-16}\,cm^3\,molecule^{-1}\,s^{-1}$ and that for 2-methyl-3-butene-2-ol (a comparable molecule to ISOPCNO3) is $1.2 \times 10^{-14}\,cm^3\,molecule^{-1}\,s^{-1}$ at 298 K (IUPAC, 2020). Even parts per billion amounts of these products would not cause significant additional NO_3 reactivity.

On the other hand, the FT-CRDS will underestimate the reactivity of NO_3 if products that are formed do not make it to the inlet (i.e. traces gases with high affinity for surfaces). One potential candidate for this category is NISOPOOH, formed in the reaction between NISOPOO and HO_2. There are no kinetic data on the reaction of NO_3 with NISOPOOH, though given the lack of reactivity of NO_3 towards organic peroxides it is very unlikely that the rate coefficient would be larger than for $NO_3 + O_2NOCH_2C(CH_3)$=CHCHO. Analysis of one experiment (9 August, Fig. 7b), in which HO_2 production (and thus the yield of NISOPOOH) was enhanced by the addition of propene and CO, shows that the difference between k^{NO_3} and $k_{nss}^{NO_3}$ on that day is comparable to those of the other experiments. This would also indicate that the influence of the potential non-detection of the hydroperoxide on the analysis should be low.

All in all, the results of the analysis above strongly suggest that the difference between directly measured and non-steady-state reactivity $k_{nss}^{NO_3}$ is caused by reactions of NO_3 with RO_2 with the results best explained when a rate coefficient of $\sim 5 \times 10^{-12}\,cm^3\,molecule^{-1}\,s^{-1}$ is used. Quantifying the impact of peroxy radicals on the fate of NO_3, however, is challenging. The rate coefficients for $RO_2 + NO_3$ are scarce and uncertain and the rate constants for self-reaction of RO_2 derived from NO_3 + isoprene have not been determined in direct kinetic measurement but via analyses of non-radical product yields.

4 Summary and conclusion

Direct measurements of NO_3 reactivity (k^{NO_3}) in chamber experiments exploring the NO_3-induced oxidation of isoprene showed excellent agreement with NO_3 loss rate constants calculated from isoprene mixing ratios, thus underlining the reliability of the reactivity measurements even under unfavourable conditions with as much as 25 ppbv of NO_2 in the chamber. The main contributor to the overall uncertainty in k^{NO_3} is the correction (via numerical simulation) for the reaction of NO_3 with NO_2 and the thermal decomposition of the N_2O_5 product. The results of the NO3ISOP campaign

indicate that previously derived overall uncertainties (Liebmann et al., 2017) that considered an uncertainty of 10 % in the rate coefficients of both reactions (Burkholder et al., 2015) and an 8 % uncertainty for the NO_2 mixing ratios are too large.

The measured reactivity, k^{NO_3}, could be completely assigned to the reaction between NO_3 and isoprene, indicating that contributions from reactions of non-radical oxidation products are minor, which is consistent with predictions of the current version of the Master Chemical Mechanism.

Values of NO_3 reactivity as calculated from NO_3 and N_2O_5 mixing ratios and the NO_3 production term were found to be a factor of ~ 1.85 higher than the directly measured NO_3 reactivities (k^{NO_3}). A box model analysis indicates that the most likely explanation is a larger fractional loss of NO_3 via reactions with organic peroxy radicals (RO_2) formed during the oxidation of isoprene. A rate coefficient ($k_{RO_2+NO_3} = \sim 5 \times 10^{-12}\,cm^3\,molecule^{-1}\,s^{-1}$) is necessary to align model predictions (MCM v.3.3.1) and observations within associated uncertainties.

Data availability. The data from the experiments in the SAPHIR chamber used in this work are available on the EUROCHAMP data home page (https://data.eurochamp.org/data-access/chamber-experiments/, EUROCHAMP, 2020).

Supplement. The supplement related to this article is available online at: https://doi.org/10.5194/acp-20-10459-2020-supplement.

Author contributions. HF, AN and SSB designed and conducted the chamber experiments. PD, JML and JaS were responsible for the NO_3 reactivity measurements. CC and AN were responsible for the OH reactivity measurements. JuS, JNC, FB, LZ, SSB and WM were responsible for the NO_3 and N_2O_5 measurements and its evaluation. KX, RH, RT and DR were responsible for the PTR-MS measurements of VOCs. PD, NF, JML and JuS took and evaluated NO_2 and NO_x data. FR was responsible for O_3 and NO measurements. PD did the analysis and, with the help of JNC, wrote the paper. JL, HF, SSB, AN, CC, JML, FB, RH, KX and RT contributed to the article.

Competing interests. The authors declare that they have no conflict of interest.

Special issue statement. This article is part of the special issue "Simulation chambers as tools in atmospheric research (AMT/ACP/GMD inter-journal SI)". It is not associated with a conference.

Acknowledgements. We thank Chemours for provision of the FEP sample used to coat the cavities and flow tube reactor of the NO_3 reactivity setup.

Financial support. This research has been supported by Horizon 2020 (EUROCHAMP-2020 (grant no. 730997) and SARLEP (grant no. 681529)) and French National Research Agency/Labex VOLTAIRE (grant no. ANR-10-LABX-100-01).

The article processing charges for this open-access publication were covered by the Max Planck Society.

Review statement. This paper was edited by Thomas Karl and reviewed by two anonymous referees.

References

Allan, B. J., McFiggans, G., Plane, J. M. C., Coe, H., and McFadyen, G. G.: The nitrate radical in the remote marine boundary layer, J. Geophys. Res.-Atmos., 105, 24191–24204, 2000.

Atkinson, R. and Arey, J.: Gas-phase tropospheric chemistry of biogenic volatile organic compounds: a review, Atmos. Environ., 37, S197–S219, 2003.

Atkinson, R., Baulch, D. L., Cox, R. A., Crowley, J. N., Hampson, R. F., Hynes, R. G., Jenkin, M. E., Rossi, M. J., Troe, J., and IUPAC Subcommittee: Evaluated kinetic and photochemical data for atmospheric chemistry: Volume II – gas phase reactions of organic species, Atmos. Chem. Phys., 6, 3625–4055, https://doi.org/10.5194/acp-6-3625-2006, 2006.

Biggs, P., Canosa-Mas, C. E., Fracheboud, J.-M., Shallcross, D. E., and Wayne, R. P.: Investigation into the kinetics and mechanism of the reaction of NO_3 with CH_3O_2 at 298 K and 2.5 Torr: a potential source of OH in the night-time troposphere?, J. Chem. Soc., Faraday Trans., F90, 1205–1210, https://doi.org/10.1039/FT9949001205, 1994.

Bossmeyer, J., Brauers, T., Richter, C., Rohrer, F., Wegener, R., and Wahner, A.: Simulation chamber studies on the NO_3 chemistry of atmospheric aldehydes, Geophys. Res. Lett., 33, L18810, https://doi.org/10.1029/2006GL026778, 2006.

Boyd, A. A., Flaud, P. M., Daugey, N., and Lesclaux, R.: Rate constants for $RO_2 + HO_2$ reactions measured under a large excess of HO_2, J. Phys. Chem. A, 107, 818–821, 2003.

Brown, S. S. and Stutz, J.: Nighttime radical observations and chemistry, Chem. Soc. Rev., 41, 6405–6447, 2012.

Brown, S. S., Stark, H., and Ravishankara, A. R.: Applicability of the steady state approximation to the interpretation of atmospheric observations of NO_3 and N_2O_5, J. Geophys. Res.-Atmos., 108, 4539, https://doi.org/10.1029/2003JD003407, 2003.

Brown, S. S., Dibb, J. E., Stark, H., Aldener, M., Vozella, M., Whitlow, S., Williams, E. J., Lerner, B. M., Jakoubek, R., Middlebrook, A. M., DeGouw, J. A., Warneke, C., Goldan, P. D., Kuster, W. C., Angevine, W. M., Sueper, D. T., Quinn, P. K., Bates, T. S., Meagher, J. F., Fehsenfeld, F. C., and Ravishankara, A. R.: Nighttime removal of NO_x in the sum-

mer marine boundary layer, Geophys. Res. Lett., 31, L07108, https://doi.org/10.1029/2004GL019412, 2004.

Brown, S. S., Ryerson, T. B., Wollny, A. G., Brock, C. A., Peltier, R., Sullivan, A. P., Weber, R. J., Dube, W. P., Trainer, M., Meagher, J. F., Fehsenfeld, F. C., and Ravishankara, A. R.: Variability in nocturnal nitrogen oxide processing and its role in regional air quality, Science, 311, 67–70, 2006.

Brown, S. S., deGouw, J. A., Warneke, C., Ryerson, T. B., Dubé, W. P., Atlas, E., Weber, R. J., Peltier, R. E., Neuman, J. A., Roberts, J. M., Swanson, A., Flocke, F., McKeen, S. A., Brioude, J., Sommariva, R., Trainer, M., Fehsenfeld, F. C., and Ravishankara, A. R.: Nocturnal isoprene oxidation over the Northeast United States in summer and its impact on reactive nitrogen partitioning and secondary organic aerosol, Atmos. Chem. Phys., 9, 3027–3042, https://doi.org/10.5194/acp-9-3027-2009, 2009a.

Brown, S. S., Dube, W. P., Fuchs, H., Ryerson, T. B., Wollny, A. G., Brock, C. A., Bahreini, R., Middlebrook, A. M., Neuman, J. A., Atlas, E., Roberts, J. M., Osthoff, H. D., Trainer, M., Fehsenfeld, F. C., and Ravishankara, A. R.: Reactive uptake coefficients for N_2O_5 determined from aircraft measurements during the Second Texas Air Quality Study: Comparison to current model parameterizations, J. Geophys. Res.-Atmos., 114, D00F10, https://doi.org/10.1029/2008JD011679, 2009b.

Burkholder, J. B., Sander, S. P., Abbatt, J., Barker, J. R., Huie, R. E., Kolb, C. E., Kurylo, M. J., Orkin, V. L., Wilmouth, D. M., and Wine, P. H.: Chemical Kinetics and Photochemical Data for Use in Atmospheric Studies, Evaluation No. 18, JPL Publication 15-10, Jet Propulsion Laboratory, Pasadena, available at: http://jpldataeval.jpl.nasa.gov (last access: 7 September 2020), 2015.

Canosa-Mas, C. E., King, M. D., Lopez, R., Percival, C. J., Wayne, R. P., Shallcross, D. E., Pyle, J. A., and Daele, V.: Is the reaction between $CH_3C(O)O_2$ and NO_3 important in the night-time troposphere?, J. Chem. Soc., Faraday Trans., 92, 2211–2222, 1996.

Crowley, J. N., Burrows, J. P., Moortgat, G. K., Poulet, G., and LeBras, G.: Room temperature rate coefficient for the reaction between CH_3O_2 and NO_3, Int. J. Chem. Kinet., 22, 673–681, 1990.

Crowley, J. N., Schuster, G., Pouvesle, N., Parchatka, U., Fischer, H., Bonn, B., Bingemer, H., and Lelieveld, J.: Nocturnal nitrogen oxides at a rural mountain-site in south-western Germany, Atmos. Chem. Phys., 10, 2795–2812, https://doi.org/10.5194/acp-10-2795-2010, 2010.

Crowley, J. N., Thieser, J., Tang, M. J., Schuster, G., Bozem, H., Beygi, Z. H., Fischer, H., Diesch, J.-M., Drewnick, F., Borrmann, S., Song, W., Yassaa, N., Williams, J., Pöhler, D., Platt, U., and Lelieveld, J.: Variable lifetimes and loss mechanisms for NO_3 and N_2O_5 during the DOMINO campaign: contrasts between marine, urban and continental air, Atmos. Chem. Phys., 11, 10853–10870, https://doi.org/10.5194/acp-11-10853-2011, 2011.

Curtis, A. R. and Sweetenham, W. P.: Facsimile, Atomic Energy Research Establishment, Report R-12805, Harwell Laboratory, Oxfordshire, UK, 1987.

Daele, V., Laverdet, G., Lebras, G., and Poulet, G.: Kinetics of the reactions CH_3O+NO, CH_3O+NO_3, and $CH_3O_2+NO_3$, J. Phys. Chem., 99, 1470–1477, https://doi.org/10.1021/j100005a017, 1995.

Dorn, H.-P., Apodaca, R. L., Ball, S. M., Brauers, T., Brown, S. S., Crowley, J. N., Dubé, W. P., Fuchs, H., Häseler, R., Heitmann, U., Jones, R. L., Kiendler-Scharr, A., Labazan, I., Langridge, J. M., Meinen, J., Mentel, T. F., Platt, U., Pöhler, D., Rohrer, F., Ruth, A. A., Schlosser, E., Schuster, G., Shillings, A. J. L., Simpson, W. R., Thieser, J., Tillmann, R., Varma, R., Venables, D. S., and Wahner, A.: Intercomparison of NO_3 radical detection instruments in the atmosphere simulation chamber SAPHIR, Atmos. Meas. Tech., 6, 1111–1140, https://doi.org/10.5194/amt-6-1111-2013, 2013.

Dubé, W. P., Brown, S. S., Osthoff, H. D., Nunley, M. R., Ciciora, S. J., Paris, M. W., McLaughlin, R. J., and Ravishankara, A. R.: Aircraft instrument for simultaneous, in situ measurement of NO_3 and N_2O_5 via pulsed cavity ring-down spectroscopy, Rev. Sci. Instrum., 77, 034101, https://doi.org/10.1063/1.2176058, 2006.

Edwards, P. M., Aikin, K. C., Dube, W. P., Fry, J. L., Gilman, J. B., de Gouw, J. A., Graus, M. G., Hanisco, T. F., Holloway, J., Huber, G., Kaiser, J., Keutsch, F. N., Lerner, B. M., Neuman, J. A., Parrish, D. D., Peischl, J., Pollack, I. B., Ravishankara, A. R., Roberts, J. M., Ryerson, T. B., Trainer, M., Veres, P. R., Wolfe, G. M., Warneke, C., and Brown, S. S.: Transition from high- to low-NO_x control of night-time oxidation in the southeastern US, Nat. Geosci., 10, 490–495, https://doi.org/10.1038/Ngeo2976, 2017.

EUROCHAMP: Database of Atmospheric Simulation Chamber Studies, available at: https://data.eurochamp.org/data-access/chamber-experiments/, last accesss: 8 September 2020.

Fry, J. L., Brown, S. S., Middlebrook, A. M., Edwards, P. M., Campuzano-Jost, P., Day, D. A., Jimenez, J. L., Allen, H. M., Ryerson, T. B., Pollack, I., Graus, M., Warneke, C., de Gouw, J. A., Brock, C. A., Gilman, J., Lerner, B. M., Dubé, W. P., Liao, J., and Welti, A.: Secondary organic aerosol (SOA) yields from NO_3 radical + isoprene based on nighttime aircraft power plant plume transects, Atmos. Chem. Phys., 18, 11663–11682, https://doi.org/10.5194/acp-18-11663-2018, 2018.

Fuchs, H., Dube, W. P., Cicioira, S. J., and Brown, S. S.: Determination of inlet transmission and conversion efficiencies for in situ measurements of the nocturnal nitrogen oxides, NO_3, N_2O_5 and NO_2, via pulsed cavity ring-down spectroscopy, Anal. Chem., 80, 6010–6017, 2008.

Fuchs, H., Ball, S. M., Bohn, B., Brauers, T., Cohen, R. C., Dorn, H.-P., Dubé, W. P., Fry, J. L., Häseler, R., Heitmann, U., Jones, R. L., Kleffmann, J., Mentel, T. F., Müsgen, P., Rohrer, F., Rollins, A. W., Ruth, A. A., Kiendler-Scharr, A., Schlosser, E., Shillings, A. J. L., Tillmann, R., Varma, R. M., Venables, D. S., Villena Tapia, G., Wahner, A., Wegener, R., Wooldridge, P. J., and Brown, S. S.: Intercomparison of measurements of NO_2 concentrations in the atmosphere simulation chamber SAPHIR during the NO3Comp campaign, Atmos. Meas. Tech., 3, 21–37, https://doi.org/10.5194/amt-3-21-2010, 2010.

Fuchs, H., Simpson, W. R., Apodaca, R. L., Brauers, T., Cohen, R. C., Crowley, J. N., Dorn, H.-P., Dubé, W. P., Fry, J. L., Häseler, R., Kajii, Y., Kiendler-Scharr, A., Labazan, I., Matsumoto, J., Mentel, T. F., Nakashima, Y., Rohrer, F., Rollins, A. W., Schuster, G., Tillmann, R., Wahner, A., Wooldridge, P. J., and Brown, S. S.: Comparison of N_2O_5 mixing ratios during NO3Comp 2007 in SAPHIR, Atmos. Meas. Tech., 5, 2763–2777, https://doi.org/10.5194/amt-5-2763-2012, 2012.

Geyer, A. and Platt, U.: Temperature dependence of the NO_3 loss frequency: A new indicator for the contribution of NO_3 to the oxidation of monoterpenes and NO_x removal in the atmosphere, J. Geophys. Res.-Atmos., 107, 4431, https://doi.org/10.1029/2001JD001215, 2002.

Geyer, A., Alicke, B., Konrad, S., Schmitz, T., Stutz, J., and Platt, U.: Chemistry and oxidation capacity of the nitrate radical in the continental boundary layer near Berlin, J. Geophys. Res.-Atmos., 106, 8013–8025, 2001.

Guenther, A. B., Jiang, X., Heald, C. L., Sakulyanontvittaya, T., Duhl, T., Emmons, L. K., and Wang, X.: The Model of Emissions of Gases and Aerosols from Nature version 2.1 (MEGAN2.1): an extended and updated framework for modeling biogenic emissions, Geosci. Model Dev., 5, 1471–1492, https://doi.org/10.5194/gmd-5-1471-2012, 2012.

Heintz, F., Platt, U., Flentje, H., and Dubois, R.: Long-term observation of nitrate radicals at the tor station, Kap Arkona (Rugen), J. Geophys. Res.-Atmos., 101, 22891–22910, 1996.

Helleis, F., Moortgat, G. K., and Crowley, J. N.: Kinetic investigations of the reaction of CD_3O_2 with NO and NO_3 at 298 K, J. Phys. Chem., 100, 17846–17854, 1996.

Hjorth, J., Lohse, C., Nielsen, C. J., Skov, H., and Restelli, G.: Products and Mechanisms of the Gas-Phase Reactions between NO_3 and a Series of Alkenes, J. Phys. Chem., 94, 7494–7500, https://doi.org/10.1021/j100382a035, 1990.

Hohaus, T., Kuhn, U., Andres, S., Kaminski, M., Rohrer, F., Tillmann, R., Wahner, A., Wegener, R., Yu, Z., and Kiendler-Scharr, A.: A new plant chamber facility, PLUS, coupled to the atmosphere simulation chamber SAPHIR, Atmos. Meas. Tech., 9, 1247–1259, https://doi.org/10.5194/amt-9-1247-2016, 2016.

Holzinger, R.: PTRwid: A new widget tool for processing PTR-TOF-MS data, Atmos. Meas. Tech., 8, 3903–3922, https://doi.org/10.5194/amt-8-3903-2015, 2015.

Holzinger, R., Acton, W. J. F., Bloss, W. J., Breitenlechner, M., Crilley, L. R., Dusanter, S., Gonin, M., Gros, V., Keutsch, F. N., Kiendler-Scharr, A., Kramer, L. J., Krechmer, J. E., Languille, B., Locoge, N., Lopez-Hilfiker, F., Materić, D., Moreno, S., Nemitz, E., Quéléver, L. L. J., Sarda Esteve, R., Sauvage, S., Schallhart, S., Sommariva, R., Tillmann, R., Wedel, S., Worton, D. R., Xu, K., and Zaytsev, A.: Validity and limitations of simple reaction kinetics to calculate concentrations of organic compounds from ion counts in PTR-MS, Atmos. Meas. Tech., 12, 6193–6208, https://doi.org/10.5194/amt-12-6193-2019, 2019.

IUPAC: Task Group on Atmospheric Chemical Kinetic Data Evaluation, edited by: Ammann, M., Cox, R. A., Crowley, J. N., Herrmann, H., Jenkin, M. E., McNeill, V. F., Mellouki, A., Rossi, M. J., Troe, J., and Wallington, T. J., available at: http://iupac.pole-ether.fr/index.html, last access: 7 September 2020.

Jenkin, M. E., Young, J. C., and Rickard, A. R.: The MCM v3.3.1 degradation scheme for isoprene, Atmos. Chem. Phys., 15, 11433–11459, https://doi.org/10.5194/acp-15-11433-2015, 2015.

Khan, M. A. H., Cooke, M. C., Utembe, S. R., Archibald, A. T., Derwent, R. G., Xiao, P., Percival, C. J., Jenkin, M. E., Morris, W. C., and Shallcross, D. E.: Global modeling of the nitrate radical (NO_3) for present and pre-industrial scenarios, Atmos. Res., 164, 347–357, https://doi.org/10.1016/j.atmosres.2015.06.006, 2015.

Krechmer, J., Lopez-Hilfiker, F., Koss, A., Hutterli, M., Stoermer, C., Deming, B., Kimmel, J., Warneke, C., Holzinger, R., Jayne, J., Worsnop, D., Fuhrer, K., Gonin, M., and de Gouw, J.: Evaluation of a New Reagent-Ion Source and Focusing Ion-Molecule Reactor for Use in Proton-Transfer-Reaction Mass Spectrometry, Anal. Chem., 90, 12011–12018, https://doi.org/10.1021/acs.analchem.8b02641, 2018.

Lelieveld, J., Butler, T. M., Crowley, J. N., Dillon, T. J., Fischer, H., Ganzeveld, L., Harder, H., Lawrence, M. G., Martinez, M., Taraborrelli, D., and Williams, J.: Atmospheric oxidation capacity sustained by a tropical forest, Nature, 452, 737–740, 2008.

Lelieveld, J., Gromov, S., Pozzer, A., and Taraborrelli, D.: Global tropospheric hydroxyl distribution, budget and reactivity, Atmos. Chem. Phys., 16, 12477–12493, https://doi.org/10.5194/acp-16-12477-2016, 2016.

Liebmann, J. M., Schuster, G., Schuladen, J. B., Sobanski, N., Lelieveld, J., and Crowley, J. N.: Measurement of ambient NO3 reactivity: design, characterization and first deployment of a new instrument, Atmos. Meas. Tech., 10, 1241–1258, https://doi.org/10.5194/amt-10-1241-2017, 2017.

Liebmann, J., Karu, E., Sobanski, N., Schuladen, J., Ehn, M., Schallhart, S., Quéléver, L., Hellen, H., Hakola, H., Hoffmann, T., Williams, J., Fischer, H., Lelieveld, J., and Crowley, J. N.: Direct measurement of NO_3 radical reactivity in a boreal forest, Atmos. Chem. Phys., 18, 3799–3815, https://doi.org/10.5194/acp-18-3799-2018, 2018a.

Liebmann, J. M., Muller, J. B. A., Kubistin, D., Claude, A., Holla, R., Plass-Dülmer, C., Lelieveld, J., and Crowley, J. N.: Direct measurements of NO_3 reactivity in and above the boundary layer of a mountaintop site: identification of reactive trace gases and comparison with OH reactivity, Atmos. Chem. Phys., 18, 12045–12059, https://doi.org/10.5194/acp-18-12045-2018, 2018b.

Martinez, M., Perner, D., Hackenthal, E. M., Kulzer, S., and Schutz, L.: NO_3 at Helgoland during the NORDEX campaign in October 1996, J. Geophys. Res.-Atmos., 105, 22685–22695, 2000.

McLaren, R., Wojtal, P., Majonis, D., McCourt, J., Halla, J. D., and Brook, J.: NO_3 radical measurements in a polluted marine environment: links to ozone formation, Atmos. Chem. Phys., 10, 4187–4206, https://doi.org/10.5194/acp-10-4187-2010, 2010.

Mogensen, D., Gierens, R., Crowley, J. N., Keronen, P., Smolander, S., Sogachev, A., Nölscher, A. C., Zhou, L., Kulmala, M., Tang, M. J., Williams, J., and Boy, M.: Simulations of atmospheric OH, O_3 and NO_3 reactivities within and above the boreal forest, Atmos. Chem. Phys., 15, 3909–3932, https://doi.org/10.5194/acp-15-3909-2015, 2015.

Ng, N. L., Brown, S. S., Archibald, A. T., Atlas, E., Cohen, R. C., Crowley, J. N., Day, D. A., Donahue, N. M., Fry, J. L., Fuchs, H., Griffin, R. J., Guzman, M. I., Herrmann, H., Hodzic, A., Iinuma, Y., Jimenez, J. L., Kiendler-Scharr, A., Lee, B. H., Luecken, D. J., Mao, J., McLaren, R., Mutzel, A., Osthoff, H. D., Ouyang, B., Picquet-Varrault, B., Platt, U., Pye, H. O. T., Rudich, Y., Schwantes, R. H., Shiraiwa, M., Stutz, J., Thornton, J. A., Tilgner, A., Williams, B. J., and Zaveri, R. A.: Nitrate radicals and biogenic volatile organic compounds: oxidation, mechanisms, and organic aerosol, Atmos. Chem. Phys., 17, 2103–2162, https://doi.org/10.5194/acp-17-2103-2017, 2017.

Paulot, F., Henze, D. K., and Wennberg, P. O.: Impact of the isoprene photochemical cascade on tropical ozone, Atmos. Chem. Phys., 12, 1307–1325, https://doi.org/10.5194/acp-12-1307-2012, 2012.

Phillips, G. J., Thieser, J., Tang, M., Sobanski, N., Schuster, G., Fachinger, J., Drewnick, F., Borrmann, S., Bingemer, H., Lelieveld, J., and Crowley, J. N.: Estimating N_2O_5 uptake coefficients using ambient measurements of NO_3, N_2O_5, $ClNO_2$ and particle-phase nitrate, Atmos. Chem. Phys., 16, 13231–13249, https://doi.org/10.5194/acp-16-13231-2016, 2016.

Ridley, B. A., Grahek, F. E., and Walega, J. G.: A small, high-sensitivity, medium-response ozone detector suitable for measurements from light aircraft, J. Atmos. Ocean. Tech., 9, 142–148, 1992.

Rohrer, F., Bohn, B., Brauers, T., Brüning, D., Johnen, F.-J., Wahner, A., and Kleffmann, J.: Characterisation of the photolytic HONO-source in the atmosphere simulation chamber SAPHIR, Atmos. Chem. Phys., 5, 2189–2201, https://doi.org/10.5194/acp-5-2189-2005, 2005.

Rollins, A. W., Kiendler-Scharr, A., Fry, J. L., Brauers, T., Brown, S. S., Dorn, H.-P., Dubé, W. P., Fuchs, H., Mensah, A., Mentel, T. F., Rohrer, F., Tillmann, R., Wegener, R., Wooldridge, P. J., and Cohen, R. C.: Isoprene oxidation by nitrate radical: alkyl nitrate and secondary organic aerosol yields, Atmos. Chem. Phys., 9, 6685–6703, https://doi.org/10.5194/acp-9-6685-2009, 2009.

Saunders, S. M., Jenkin, M. E., Derwent, R. G., and Pilling, M. J.: Protocol for the development of the Master Chemical Mechanism, MCM v3 (Part A): tropospheric degradation of non-aromatic volatile organic compounds, Atmos. Chem. Phys., 3, 161–180, https://doi.org/10.5194/acp-3-161-2003, 2003.

Schwantes, R. H., Teng, A. P., Nguyen, T. B., Coggon, M. M., Crounse, J. D., St Clair, J. M., Zhang, X., Schilling, K. A., Seinfeld, J. H., and Wennberg, P. O.: Isoprene NO_3 Oxidation Products from the $RO_2 + HO_2$ Pathway, J. Phys. Chem. A, 119, 10158–10171, https://doi.org/10.1021/acs.jpca.5b06355, 2015.

Sharkey, T. D. and Yeh, S.: Isoprene emission from plants, Annu. Rev. Plant. Phys., 52, 407–436, https://doi.org/10.1146/annurev.arplant.52.1.407, 2001.

Sobanski, N., Schuladen, J., Schuster, G., Lelieveld, J., and Crowley, J. N.: A five-channel cavity ring-down spectrometer for the detection of NO_2, NO_3, N_2O_5, total peroxy nitrates and total alkyl nitrates, Atmos. Meas. Tech., 9, 5103–5118, https://doi.org/10.5194/amt-9-5103-2016, 2016a.

Sobanski, N., Tang, M. J., Thieser, J., Schuster, G., Pöhler, D., Fischer, H., Song, W., Sauvage, C., Williams, J., Fachinger, J., Berkes, F., Hoor, P., Platt, U., Lelieveld, J., and Crowley, J. N.: Chemical and meteorological influences on the lifetime of NO_3 at a semi-rural mountain site during PARADE, Atmos. Chem. Phys., 16, 4867–4883, https://doi.org/10.5194/acp-16-4867-2016, 2016b.

Thieser, J., Schuster, G., Schuladen, J., Phillips, G. J., Reiffs, A., Parchatka, U., Pöhler, D., Lelieveld, J., and Crowley, J. N.: A two-channel thermal dissociation cavity ring-down spectrometer for the detection of ambient NO_2, RO_2NO_2 and $RONO_2$, Atmos. Meas. Tech., 9, 553–576, https://doi.org/10.5194/amt-9-553-2016, 2016.

van Meeningen, Y., Schurgers, G., Rinnan, R., and Holst, T.: BVOC emissions from English oak (*Quercus robur*) and European beech (*Fagus sylvatica*) along a latitudinal gradient, Biogeosciences, 13, 6067–6080, https://doi.org/10.5194/bg-13-6067-2016, 2016.

Vaughan, S., Canosa-Mas, C. E., Pfrang, C., Shallcross, D. E., Watson, L., and Wayne, R. P.: Kinetic studies of reactions of the nitrate radical (NO_3) with peroxy radicals (RO_2): an indirect source of OH at night?, Phys. Chem. Chem. Phys., 8, 3749–3760, 2006.

Wagner, N. L., Dubé, W. P., Washenfelder, R. A., Young, C. J., Pollack, I. B., Ryerson, T. B., and Brown, S. S.: Diode laser-based cavity ring-down instrument for NO_3, N_2O_5, NO, NO_2 and O_3 from aircraft, Atmos. Meas. Tech., 4, 1227–1240, https://doi.org/10.5194/amt-4-1227-2011, 2011.

Warneke, C., de Gouw, J. A., Goldan, P. D., Kuster, W. C., Williams, E. J., Lerner, B. M., Jakoubek, R., Brown, S. S., Stark, H., Aldener, M., Ravishankara, A. R., Roberts, J. M., Marchewka, M., Bertman, S., Sueper, D. T., McKeen, S. A., Meagher, J. F., and Fehsenfeld, F. C.: Comparison of daytime and nighttime oxidation of biogenic and anthropogenic VOCs along the New England coast in summer during New England Air Quality Study 2002, J. Geophys. Res.-Atmos., 109, D10309, https://doi.org/10.1029/2003JD004424, 2004.

Wayne, R. P., Barnes, I., Biggs, P., Burrows, J. P., Canosamas, C. E., Hjorth, J., Lebras, G., Moortgat, G. K., Perner, D., Poulet, G., Restelli, G., and Sidebottom, H.: The Nitrate Radical – Physics, Chemistry, and the Atmosphere, Atmos. Environ., 25, 1–203, 1991.

Wennberg, P. O., Bates, K. H., Crounse, J. D., Dodson, L. G., McVay, R. C., Mertens, L. A., Nguyen, T. B., Praske, E., Schwantes, R. H., Smarte, M. D., St Clair, J. M., Teng, A. P., Zhang, X., and Seinfeld, J. H.: Gas-Phase Reactions of Isoprene and Its Major Oxidation Products, Chem. Rev., 118, 3337–3390, https://doi.org/10.1021/acs.chemrev.7b00439, 2018.

CHAPTER 5

Detection of isoprene-derived organic nitrates via TD-CRDS

The results of the study in this chapter have already been published in the peer-reviewed journal *Atmospheric Measurement Techniques*. The publication is thus reproduced on the subsequent pages and deals with the following:
Whilst the previous chapter focussed on the fate of the NO_3 radical itself, this chapter turns the attention to the organic nitrates that are formed in the NO_3 + isoprene system (see Fig. 2.2). I generated such isoprene-derived organic nitrates (ISOP-NITs) in another simulation chamber (SCHARK) and monitored the ISOP-NITs with a thermal-dissociation cavity ring-down spectrometer (TD-CRDS) as described in Sobanski et al. (2016a). However, the separate detection of peroxy nitrates and ISOP-NITs is impeded when a quartz glass thermal-dissociation inlet is used in the presence of O_3. In this study, I investigate potential interfering species and the role of surface-catalysed processes. Using a thermal-dissociation inlet made of PFA for the detection of peroxy nitrates forms a viable solution for this problem.

Author contribution
I performed all measurements except the CIMS measurement of PAN, did the analysis and model calculations, wrote the manuscript and, with the help of , revised it.
Please refer to the section "Author contribution" in the publication itself for detailed information.

Atmos. Meas. Tech., 14, 5501–5519, 2021
https://doi.org/10.5194/amt-14-5501-2021

Atmospheric Measurement Techniques
Open Access
EGU

Impact of ozone and inlet design on the quantification of isoprene-derived organic nitrates by thermal dissociation cavity ring-down spectroscopy (TD-CRDS)

Patrick Dewald, Raphael Dörich, Jan Schuladen, Jos Lelieveld, and John N. Crowley

Atmospheric Chemistry Department, Max-Planck-Institut für Chemie, 55128 Mainz, Germany

Correspondence: John N. Crowley (john.crowley@mpic.de)

Received: 4 May 2021 – Discussion started: 7 May 2021
Revised: 15 July 2021 – Accepted: 16 July 2021 – Published: 12 August 2021

Abstract. We present measurements of isoprene-derived organic nitrates (ISOP-NITs) generated in the reaction of isoprene with the nitrate radical (NO_3) in a 1 m^3 Teflon reaction chamber. Detection of ISOP-NITs is achieved via their thermal dissociation to nitrogen dioxide (NO_2), which is monitored by cavity ring-down spectroscopy (TD-CRDS). Using thermal dissociation inlets (TDIs) made of quartz, the temperature-dependent dissociation profiles (thermograms) of ISOP-NITs measured in the presence of ozone (O_3) are broad (350 to 700 K), which contrasts the narrower profiles previously observed for, for example, isopropyl nitrate (iPN) or peroxy acetyl nitrate (PAN) under the same conditions. The shape of the thermograms varied with the TDI's surface-to-volume ratio and with material of the inlet walls, providing clear evidence that ozone and quartz surfaces catalyse the dissociation of unsaturated organic nitrates leading to formation of NO_2 at temperatures well below 475 K, impeding the separate detection of alkyl nitrates (ANs) and peroxy nitrates (PNs). The use of a TDI consisting of a non-reactive material suppresses the conversion of isoprene-derived ANs at 473 K, thus allowing selective detection of PNs. The potential for interference by the thermolysis of nitric acid (HNO_3), nitrous acid (HONO) and O_3 is assessed.

1 Introduction

Understanding the atmospheric fate of nitrogen oxide (NO) and nitrogen dioxide (NO_2) is critical as both trace gases have a great impact on air quality and human health (Crutzen and Lelieveld, 2001; Lelieveld et al., 2015). Ambient measurements of trace gases that function as NO_x reservoirs or sinks (where $NO_x = NO + NO_2$) are thus needed to provide insight into NO_x removal and transport. Organic compounds with nitrate functionality can serve as NO_x reservoirs in the troposphere (Thornton et al., 2002; Horowitz et al., 2007) and are generally categorized as peroxy nitrates (PNs, RO_2NO_2, with peroxy acetyl nitric anhydride (PAN) being its most abundant representative in the troposphere) and alkyl (aliphatic) nitrates (ANs, $RONO_2$). PNs are formed via the reaction of organic peroxy radicals (RO_2) with NO_2 (Reaction R1); ANs are formed via the minor (termolecular) channel of the reaction of RO_2 with NO (Reaction R2a). The competitive bimolecular process leads to alkoxy radicals (RO, Reaction R2b). During the daytime, RO_2 is formed mainly by the oxidation of volatile organic compounds (VOCs) by hydroxyl radicals (OH) in air (Reaction R3), with ozonolysis important at night (Reaction R4):

$$RO_2 + NO_2 + M \rightarrow RO_2NO_2 + M \quad \text{(R1)}$$
$$RO_2 + NO + M \rightarrow RONO_2 + M \quad \text{(R2a)}$$
$$RO_2 + NO \rightarrow RO + NO_2 \quad \text{(R2b)}$$
$$VOC + OH(+O_2) \rightarrow RO_2 + \text{products} \quad \text{(R3)}$$
$$VOC + O_3(+O_2) \rightarrow RO_2 + \text{products}. \quad \text{(R4)}$$

At night-time, when OH radicals and NO are significantly less abundant, the NO_3 radical can initiate the oxidation of many VOCs that contain a double bond (Ng et al., 2017). NO_3, formed in the oxidation of NO_2 by O_3 (Reaction R5), is photolysed rapidly by sunlight (Reaction R6) and also reacts efficiently with NO (Reaction R7) so that it is generally of

Published by Copernicus Publications on behalf of the European Geosciences Union.

minor importance during the day (Wayne et al., 1991).

$$NO_2 + O_3 \rightarrow NO_3 + O_2 \quad \text{(R5)}$$
$$NO_3 + h\nu \rightarrow NO + O_2 \quad \text{(R6)}$$
$$NO_3 + NO \rightarrow 2NO_2 \quad \text{(R7)}$$

NO_3 readily undergoes reactions with many unsaturated organic trace gases of biogenic origin including isoprene, monoterpenes and sesquiterpenes to form organic nitrates in high yields (Ng et al., 2017; Wennberg et al., 2018; Mellouki et al., 2021). The focus of this work is the formation of organic nitrates in its reaction (in air) with the C_5-diene isoprene (ISOP, Reaction R8):

$$NO_3 + ISOP(+O_2) \rightarrow\rightarrow \text{ISOP-NIT}, \quad \text{(R8)}$$

where ISOP-NIT represents an isoprene-derived nitrate. Approximately $500\,Tg\,yr^{-1}$ of isoprene is released to the atmosphere (Guenther et al., 2012), and a large fraction of the organic nitrates formed at night-time is attributed to the reaction between NO_3 and isoprene (Reaction R8) (Carlton et al., 2009). The atmospheric oxidation of isoprene involving OH, O_3 and NO_3 as oxidizing agents is complex and leads to a huge variety of products (Ng et al., 2017; Wennberg et al., 2018) including multifunctional, unsaturated nitrates such as $O_2NOCH_2C(CH_3)$=CHCHO, $O_2NOCH_2C(CH_3)$=$CHCH_2OH$ or $O_2NOCH_2C(CH_3)$=$CHCH_2OOH$ among other secondary oxidation products like dinitrates or epoxides (Wu et al., 2021).

Studies of the NO_3-induced oxidation of isoprene in air report AN yields between 60 % and 100 % (Barnes et al., 1990; Berndt and Boge, 1997; Perring et al., 2009; Kwan et al., 2012; Schwantes et al., 2015; IUPAC, 2021; Wu et al., 2021; Brownwood et al., 2021), and the NO_3-induced oxidation of isoprene is responsible for a dominant fraction of organic nitrates observed in rural environments with strong biogenic emissions (Beaver et al., 2012). The major fate of isoprene-derived organic nitrates formed in the boundary layer is deposition onto particulate matter to form nitric acid (HNO_3) or secondary organic aerosols (SOAs) leading to largely irreversible removal of NO_x from the gas phase (Ng et al., 2008; Rollins et al., 2009; Fry et al., 2018; Hamilton et al., 2021).

Individual isoprene nitrates have been measured selectively in the atmosphere by mass-spectrometric methods (Wolfe et al., 2007; Wu et al., 2021). An alternative detection scheme, in which the sum of all atmospheric PNs (ΣPNs) and ANs (ΣANs) are separately measured, takes advantage of their different C–N bond energy by combining thermal dissociation to NO_2 (Reactions R9 and R10) with detection of the latter with means of laser-induced fluorescence (TD-LIF) or cavity ring-down spectroscopy (TD-CRDS).

$$RO_2NO_2 + M \rightarrow RO_2 + NO_2 + M \quad \text{(R9)}$$
$$RONO_2 + M \rightarrow RO + NO_2 + M \quad \text{(R10)}$$

Several instruments using thermal dissociation inlets consisting of fused silica (quartz) with residence times between tens to hundreds of milliseconds have been described in the literature (Day et al., 2002; Paul et al., 2009; Wild et al., 2014; Sobanski et al., 2016; Thieser et al., 2016; Keehan et al., 2020). In these instruments, quantitative conversion of PAN is reported for temperatures between 375 and 420 K. Generally, the temperature dependence of the instrument's response to ANs has been tested using mostly saturated organic nitrates such as isopropyl nitrate (iPN) and isobutyl nitrate, which are dissociated to NO_2 at temperatures between 500 and 675 K. The temperatures at which PNs and ANs are quantitatively converted to NO_2 thus differ by ~ 200 K and are largely independent of their organic backbone (Kirchner et al., 1999; Wild et al., 2014) allowing separate measurement of the sum of all alkyl nitrates (ΣANs) and of the sum of all peroxy nitrates (ΣPNs). These observations have provided the basis for analysis of field data in which an unknown mixture of PNs and ANs are present. We note, however, that most of the first-generation ANs formed in the NO_3 + isoprene system still contain a double bond (Barnes et al., 1990; Skov et al., 1992; Schwantes et al., 2015), which renders them more reactive towards oxidizing agents than, for example, iPN. A well-characterized thermogram for aliphatic nitrates derived from the oxidation of, for example, isoprene is thus a pre-requirement for extracting the mixing ratios of PNs and ANs from ambient measurements when using a TD inlet. To date, only one such thermogram has been presented (Brownwood et al., 2021) which appears to be the result of a single experiment (i.e. no variation of experimental conditions) using a sample that was not stable over time. The thermogram also features slopes before and after the AN transition temperature, which is consistent with the ideal behaviour of, for example, iPN.

In this study, we generated ISOP-NITs by reacting isoprene and NO_3 in a Teflon simulation chamber and used a custom-built, five-channel cavity ring-down spectrometer (CRDS) (Sobanski et al., 2016) to analyse the organic nitrates formed. In the presence of O_3 we find that ISOP-NIT does not behave like the saturated analogue iPN in our quartz TD inlet and we characterized the processes (both gas-phase and surface-catalysed processes) that lead to the observed behaviour. We also examined the potential role of surface-catalysed dissociation of HNO_3 and nitrous acid (HONO) to NO_2 as well as the effect of humidity as a potential bias to measurements of PNs and ANs.

2 Experiment

2.1 Simulation chamber

In order to analyse organic nitrates formed from the NO_3 + isoprene system under realistic operational conditions for the five-channel CRDS (e.g. normal sample flow

rates), we constructed a dynamic, flow-through simulation chamber "SCHARK" (Simulation CHamber for Atmospheric Reactions and Kinetics) of volume 1 m^3 (cubic, all sides $\sim$ 1 m long) made of PFA foil of 0.005 in. ($\sim$ 0.13 mm) thickness (Ingeniven). The chamber is operated at ambient pressure and temperature; a magnetically coupled, Teflon-coated propeller-type stirrer situated in the centre of the chamber floor ensures continuous mixing of the air. The trace-gas inlets and sampling ports were located at opposite corners of the cubic chamber to reduce the potential of sampling gas that had not yet mixed. The PFA foil is surrounded by a $120 \times 120 \times 120$ cm cube constructed of four Perspex and two steel walls; the interspace (0.7 m^3) is permanently flushed with 1 SLPM (L (STP) min^{-1}) of dry synthetic "zero air" in order to avoid contamination through permeation of trace gases present in the laboratory air. The Perspex walls serve as observation windows and were covered with light-tight material during the experiments described here.

Zero air was provided by passing pressurized air through a commercial air purifier (CAP 180, Fuhr GmbH). Humidification of the air was achieved with a permeation source (MH-110-24-F-4, Perma Pure LLC) filled with deionized water. Typical total flow rates of 15 or 23 SLPM zero air into the chamber result in exchange rates k_{exch} of 2.7 or $4.2 \times 10^{-4}\,s^{-1}$, i.e. lifetimes of gases in the chamber of $\sim$ 40–60 min. Note that in "flow-through" operation, the concentrations of trace gases in the chamber are controlled both by chemical processes and by the rate of flow into (and out of) the chamber so that "steady state" is achieved on the order of hours.

Ozone mixing ratios in SCHARK were measured by sampling 2 SLPM through a $\sim$ 3 m long section of 0.25 in. (outer diameter, OD) PFA tubing to a commercial ozone monitor (2B Technologies, model 205) with a detection limit of $\sim$ 1 part per billion by volume (ppbv) and 5 % uncertainty. O_3 measurements were also used to establish the time required (under standard flow conditions) to achieve complete mixing within the chamber ($<$ 1 min) and to derive the exchange rate by monitoring the exponential rise or decay of O_3 when its supply was switched on or off (Fig. S1 in the Supplement). O_3 (up to 600 ppbv) was generated by passing a fraction of the air flowing into the chamber through a UV-transparent cuvette ($\sim$ 70 cm^3) illuminated by a low-pressure Hg lamp (PenRay) that dissociated O_2 (to O atoms and thus O_3) at 185 nm.

A known flow of isoprene entered the chamber as a dilute sample from a 12 L stainless-steel storage canister (Landefeld GmbH) which was prepared manometrically from evaporation of pure isoprene (Acros Organics, 98 %) and mixed with helium (5.0, Westfalen). The isoprene concentration in the storage canister was quantified indirectly by measuring the NO_3 reactivity via flow-tube CRDS (Liebmann et al., 2017; Dewald et al., 2020) and was found to be 46.5 ppmv, in agreement (within 15 %) with the manometrically derived mixing ratio. A gas sample of isopropyl nitrate (Sigma Aldrich, 58 ppmv in N_2 5.0, Westfalen) was prepared in a similar fashion.

Two methods of in situ NO_3 generation were employed. In the first, NO_3 was produced in the chamber via the reaction of NO_2 with O_3 (Reaction R5), whereby O_3 was generated as described above and NO_2 was taken from a bottled sample (Air Liquide, 1 ppmv in N_2). Typical concentrations of NO_2 and O_3 were 6–10 and 100–160 ppbv, respectively. Alternatively, NO_3 was generated in the thermal decomposition of N_2O_5 (Reaction R11) which was eluted into the chamber by passing a regulated flow of N_2 over N_2O_5 crystals held at temperatures between -78 and -70 °C.

$$N_2O_5 + M \rightarrow NO_3 + NO_2 + M \quad \text{(R11)}$$

N_2O_5 was synthesized by the sequential, gas-phase oxidation of NO (5 % in N_2, Westfalen) in an excess of O_3 (Davidson et al., 1978) and trapped at -78 °C (acetone and dry ice). In this case, O_3 was obtained by electrical discharge through oxygen (5.0, Westfalen) using a commercial generator (Ozomat Com, Anseros). Note that the latter method enables us to generate NO_3 in the chamber in an O_3-free environment.

2.2 Detection of organic nitrates by cavity ring-down spectroscopy (CRDS)

Simultaneous measurements of the mixing ratios of NO_2, NO_3, N_2O_5, ΣANs and ΣPNs in the SCHARK chamber were made using a five-channel cavity ring-down spectrometer (CRDS) that has been described in detail (Sobanski et al., 2016), and only a brief summary of key features of the instrument is given here. Each of the five cavities consists of FEP-coated (FEPD 121, DuPont) stainless-steel tubes which are equipped with two high-reflectivity mirrors (see below) supported 90 cm apart (L). The volumes in front of the mirrors are purged with dry synthetic air, which results in a reduction of the effective optical path length from 90 to 62.1 cm (d). The standard expression Eq. (1) is used to derive in-cavity concentrations $[X]$ from the difference in ring-down constant in the absence (k_0) and presence (k) of an absorber X:

$$[X] = \frac{L}{d} \cdot \frac{1}{c\sigma_{\text{eff}}} \cdot (k - k_0)\,, \quad (1)$$

where c is the speed of light and σ_{eff} is the effective cross-section derived from the overlap of the laser emission and the NO_2 (Vandaele et al., 1998) or NO_3 absorption spectrum (Orphal et al., 2003).

Three of the cavities are operated at 409 nm for detection of NO_2, whereby 409 nm light is provided by a square-wave-modulated (2500 Hz) laser diode. The three 409 nm cavities, thermostated to 303 K and typically operated at a pressure of $\sim$ 733 hPa, sampled from SCHARK at a total flow rate of 6 SLPM, which initially passes through a 2.3 m long PFA inlet (1.5 m with OD 0.25 in. and 0.8 m with OD 0.125 in.) before being split into three equal flows. One flow is directed to

a cavity via an unheated, 60 cm long PFA tube (0.375 in. OD) to measure NO_2. The other two flows are directed through thermal dissociation inlets (TDIs) in which PNs and ANs are converted to NO_2. At the given conditions (i.e. flow rate, pressure, residence time in the heated section), keeping our TDI at temperatures close to 448 K results in quantitative conversion of PNs to NO_2 so that the cavity sampling via this inlet measures the sum of PNs + NO_2. Heating our second TDI to ≈ 650 K results in the complete conversion of ANs to NO_2 so that the sum of ANs + PNs + NO_2 can be measured as described in the literature cited in the introduction. The choice of material for these TD inlets has a profound influence on the results obtained, as described below.

The standard deviation (2σ) of consecutive baseline measurements defines the limits of detection (LODs), which are 38, 44 and 90 pptv for [NO_2], [ΣPNs] and [ΣANs] respectively under laboratory conditions. The total uncertainty for the NO_2 measurement is 9 %, which includes uncertainty in the (effective) NO_2 cross-sections. For the measurements of ANs and PNs the associated uncertainties are highly dependent on the concentrations of other trace gases and the corrective procedure accounting for radical recombination effects (Sobanski et al., 2016).

For simplicity, we refer to the three cavities as the "NO_2 cavity" (room-temperature inlet), the "PN cavity" (TD inlet at circa 473 K in which ΣPNs + NO_2 are measured) and the "AN cavity" (TD inlet at circa 673 K in which ΣANs + ΣPNs + NO_2 are measured).

The remaining two cavities of the CRDS were operated at 662 nm (laser modulation at 625 Hz) for detection of NO_3. While one cavity is thermostated to 303 K (and detects NO_3 only), the second one (as well as an FEP-coated glass reactor located upstream) is thermostated to 373 K so that N_2O_5 is stoichiometrically converted NO_3 and the summed mixing ratio of NO_3 and N_2O_5 is obtained. The two 662 nm cavities sampled air from SCHARK at a total flow rate of 15 SLPM through a ∼ 1.5 m 1/4 in. (OD) PFA tube. Corrections to the mixing ratios were made to account for loss of NO_3 and N_2O_5 during transport to and through the cavities. Using the method described in Sobanski et al. (2016), NO_3 transmission was found to be 89 % in both cavities. The NO_3 and N_2O_5 measurements are not central to this study but allowed the quantitative surveillance of NO_3 (and indirect N_2O_5) consumption by isoprene.

Figure 1 shows three types of thermal dissociation inlets (TDIs) used to convert organic nitrates to NO_2. In the original version of this instrument (Sobanski et al., 2016) the ΣPNs and ΣAN cavities sampled via 12 mm ID quartz TD inlets (TDI-1), with a length of 55 cm, the first ∼ 10 cm of which was wrapped with heating wire. In order to reduce bias caused, for example, by the reformation of the organic nitrate after its thermal dissociation, this section was filled with glass beads (Sigma-Aldrich G9268, ø ∼ 0.5 mm) to provide a surface for heterogeneous loss of radicals. The glass beads were supported on a 2 cm thick glass frit and reduce the

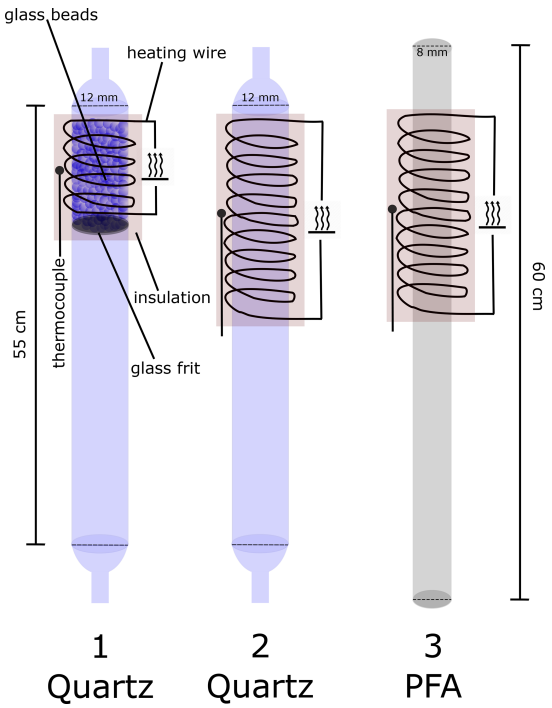

Figure 1. Schematic diagram of the thermal dissociation inlets TDI-1, TDI-2 and TDI-3.

pressure downstream by ≈ 28 hPa compared to TDI-1. Problems associated with temperature-dependent flow resistance through these small beads and the need for an extra filter (upstream) to prevent their transport into the inlet lines when flows were temporarily reversed (e.g. during instrument shutdown) led us to switch to larger beads (Merck, ø = 3 mm), and these were used throughout this study in TDI-1. TDI-2 is made of a quartz glass tube with the same dimensions as TDI-1 but features a longer heated section (20 cm) and is free of additional surfaces like glass beads or frits. TDI-2 is thus similar to many other thermal dissociation inlets described in the literature (see above). TDI-3 is constructed from a 55 cm long PFA tube (0.375 in. OD), where the first 20 cm is heated. The melting point of PFA is lower than the temperature required to thermally dissociate ANs, so TDI-3 could only be used for the measurement of PNs + NO_2. The temperature of the external wall of the TD inlets was measured with a K-type thermocouple situated at the centre of the heated section, which was insulated with mineral wool. At a flow rate of 2 SLPM and an operating pressure of 733 mbar, approximate residence times in the inlets without glass beads are 0.20 s (in TDI-2 at 650 K) and 0.13 s (TDI-3 at 450 K) when assuming a homogeneous temperature distribution equal to that measured on the outer wall of the tubing.

3 Results and discussion

Figure 2 shows the result of an experiment in which 150 sccm NO_2 (1 ppmv in air) was flowed into SCHARK along with isoprene (7 sccm of 46.5 ppmv in He) and 24 SLPM zero air of which 5 SLPM was passed over the low-pressure Hg-lamp zero air to generate O_3 ($\sim$ 96 ppbv). NO_2 was sampled (as usual) via the room-temperature PFA inlet, the ΣPNs (473 K) and ΣAN cavities (673 K) both sampled via TDI-1 (quartz tube with glass beads). O_3 was added at 09:30 and NO_2 at 10:00 (all times are local times, LT).

Just prior to the addition of isoprene at 12:00 LT, the system is close to steady state with $\sim$ 5 ppbv NO_2 and 92 ppbv O_3. After subtraction of the measured N_2O_5 mixing ratios, a residual signal of $\sim$ 100 pptv is detected in both the PN and AN channels, which may be caused, as discussed below, by interference of HNO_3 in the AN channel and a memory effect of the glass beads in the PN channel (Sect. 3.1 and 3.2). Note that after addition of isoprene, both NO_3 and N_2O_5 are reduced drastically ($NO_3 \sim 3$ pptv, $N_2O_5 \sim 5$ pptv) and the thermal dissociation of N_2O_5 no longer contributes to NO_2 signals in the PN and AN channels (Sobanski et al., 2016; Thieser et al., 2016).

At 14:00 LT, the cavity sampling from the 673 K TD inlet indicated $\sim$ 610 pptv for the summed mixing ratio of ΣANs + ΣPNs, whereas the cavity sampling from the 473 K TD inlet (ΣPNs) indicated $\sim$ 400 pptv. Since the signal in the ΣAN channel includes both the contribution of peroxy and alkyl nitrates, this implies that only 210 pptv (34 %) of the detected products can be attributed to alkyl nitrates, which is inconsistent with the high yields (60 %–100 %) of ANs that result from the reaction of NO_3 with isoprene (Barnes et al., 1990; Berndt and Boge, 1997; Perring et al., 2009; Rollins et al., 2009; Kwan et al., 2012; Schwantes et al., 2015; IUPAC, 2021; Brownwood et al., 2021). Compared to ANs, we expect the mixing ratios of, for example, PAN, $O_2NOCH_2C(CH_3)$=CHC(O)O_2NO_2 or methacryloyl peroxynitrate (MPAN) in this system to be negligible as their precursors such as $O_2NOCH_2C(CH_3)$=CHCHO (Jenkin et al., 2015) or methacrolein (Kwok et al., 1996; Berndt and Boge, 1997; Schwantes et al., 2015) are oxidized only inefficiently in the dark. The formation of PNs only takes place once isoprene has been depleted so that secondary oxidation of the above-mentioned aldehydes by OH or NO_3 leading to further acyl-peroxy radicals (which form PNs) become at least competitive to the primary oxidation of isoprene. This is however never the case in the present experiments as isoprene is continuously flowed into the chamber and remains according to model calculations (see below) at a level of $\approx$ 11.4 ppbv. Given the high abundance of O_3 and isoprene in this system, ozonolysis of the latter together with the associated formation and decomposition of Criegee intermediates to acetylperoxy radicals $CH_3C(O)O_2$ (Nguyen et al., 2016; Vansco et al., 2020) should make PAN the most important, potential contributor to a signal in the PN cavity. However, according to the branching ratios given in Nguyen et al. (2016), this reaction path is a minor one and $CH_3C(O)O_2$ (and thus PAN) should be formed in negligible amounts.

In order to identify the origin of the unexpectedly high ΣPN signal when NO_3 and isoprene are mixed in the dark, thermograms of the NO_3 + isoprene system were recorded in an experiment where $\sim$ 2.8 ppbv of isoprene-derived nitrates (as measured with TDI-2 at 625 K) was generated by flowing NO_2 (200 sccm of 1 ppmv) and isoprene (9.8 sccm of 46.5 ppmv) in 15 SLPM dry synthetic air (with 5 SLPM over the Hg lamp for generation of $\sim$ 150 ppbv O_3). Similar to the experiment in Fig. 2, N_2O_5 mixing ratios are expected to be suppressed to a few parts per trillion by volume under these conditions so that its thermal dissociation (to NO_2) did not contribute to the ΣPN and ΣAN signals. Using this chemical system, we simultaneously measured ISOP-NIT thermograms once steady state established using TDI-1 (quartz, glass beads, 10 cm heated section) and TDI-2 (quartz, no glass beads, 20 cm heated section) both initially held at 703 K. Subsequently, both TDIs were cooled to ambient temperature over a period of $\sim$ 1.75 h. The ΣAN signals from this experiment are plotted against the inlet temperature in Fig. 3a to generate the ISOP-NIT thermogram. This is displayed along with an isopropyl-nitrate thermogram (iPN, red data points) measured using the same inlets under the same flow conditions but using iPN diluted to 5.5 ppbv in dry synthetic air sampled directly through a PFA line (together with 1.5 ppbv NO_2 impurity) to the instrument.

For iPN, we observe a well-defined onset of thermal dissociation at $\sim$ 525 K with a plateau (maximum conversion) at $\sim$ 650 K as reported previously for this set-up (Sobanski et al., 2016). When measuring iPN, TDI-1 results in a slightly steeper thermogram than TDI-2 in the 575–650 K range, which may be related to changes in gas flow and heat transfer within the inlet caused by the glass beads. Neither TD-inlet type results in dissociation to NO_2 at temperatures $<$ 500 K. In contrast, the ISOP-NIT thermograms (normalized to the signal at the plateau at 625 K of TDI-2) indicate formation of NO_2 over a much broader range of temperatures (350–700 K).

The effect of humidifying the air was examined in an almost identical experiment conducted with NO_2 (150 sccm of 1 ppmv) and isoprene (7 sccm of 46.5 ppmv) in 15 SLPM synthetic air with relative humidity (in SCHARK) of 33.5 % at 22 °C. In this case, $\sim$ 2.3 ppbv ISOP-NIT was formed. The thermograms obtained with TDI-1 and TDI-2 under these conditions are depicted in Fig. 3b. The broad thermogram measured with TDI-1 is very similar to that obtained under dry conditions (Fig. 3a), although even at room temperature an additional NO_2 signal of 500 pptv is detected. Sampling via TDI-2 yields an ISOP-NIT thermogram that has similar features to that obtained under dry conditions, although the peak at $\sim$ 400 K has well-defined minima on both flanks and is shifted to higher temperatures. In separate experiments, humidified synthetic air (RH = 40 %, 23 °C) and

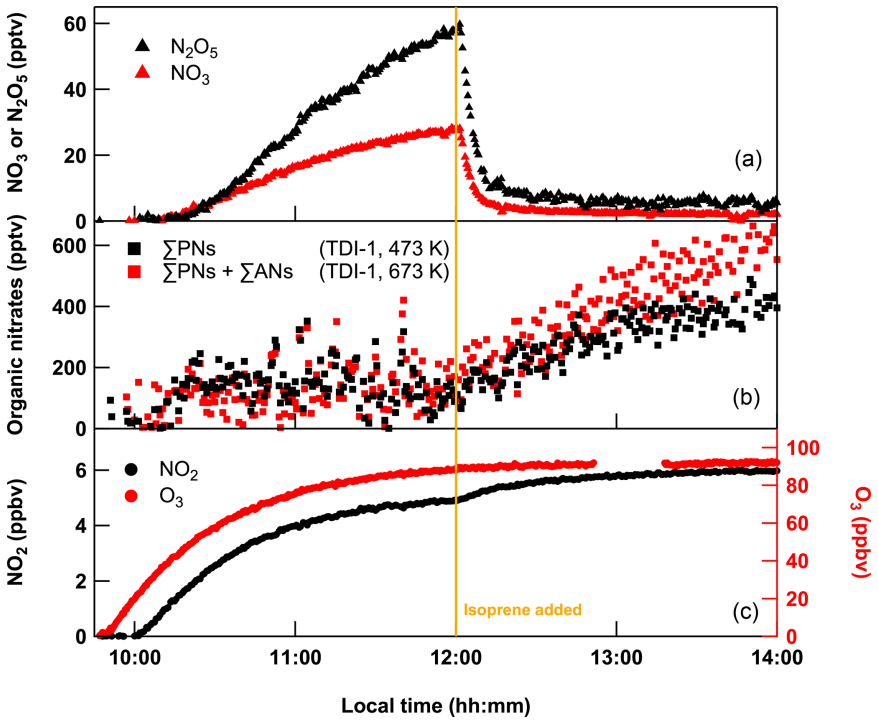

Figure 2. Evolution of the mixing ratios of NO_2, ΣPNs, ΣPNs + ΣANs, N_2O_5 and O_3 when flowing 150 sccm NO_2 (from 1 ppmv bottle), 7 sccm isoprene (from a 46.5 ppmv cylinder) and 24 SLPM of zero air (of which 5 SLPM was passed over a PenRay lamp) into SCHARK. Isoprene was added at 12:00 LT after the system was close to steady state. Note that the NO_2 and N_2O_5 mixing ratios were subtracted from the organic nitrate signals **(b)**.

NO_2 (10.8 ppbv) were sampled through a PFA line directly to the instrument. The thermogram (in the absence of isoprene or ISOP-NIT) using TDI-2 was recorded and can be found in the Supplement (Fig. S2) revealing that the presence of water and NO_2 in the inlet is sufficient to reproduce some features displayed in Fig. 3b with TDI-2. It is well known that H_2O and NO_2 can react on surfaces to form HONO and HNO_3 (Pitts et al., 1984; Finlayson-Pitts et al., 2003), and their formation in SCHARK was verified in Sect. 3.1. In the presence of H_2O, the efficiency of conversion of ISOP-NIT to NO_2 drops to about 5 % at ∼460 K. This is much less than under dry conditions whereby 20 % conversion of ISOP-NIT was observed between 375 and 475 K (Fig. 3a). Within a framework for surface-catalysed conversion of ISOP-NIT to NO_2 presented below, this observation can be interpreted as arising from the competitive adsorption to the surface of nitrated hydroperoxides and H_2O; i.e. H_2O (which is vastly more abundant) reduces the surface coverage of the organic nitrate at the surface.

The results in Figs. 2 and 3 show that separate detection of ANs and PNs based on their thermal dissociation can be problematic for the NO_3 + isoprene system. Identifying the cause of this and providing potential solutions to circumvent the problem is the aim of this work. To do this, we first focus on the "dry" experiment and highlight two regions of the thermograms in which large deviations from the expected behaviour are observed.

3.1 Thermograms of ISOP-NIT

3.1.1 Region I (T > 648 K)

Figure 3a indicates that, at temperatures above 648 K (shaded region I), the behaviour of the two TDIs diverges significantly: while use of TDI-1 (glass beads) results in an increase in NO_2 with increasing temperature, the use of TDI-2 leads to a decrease in the NO_2 signal in the same temperature range. The increase in NO_2 continues at temperatures above that required to convert ANs to NO_2, which implies the presence of a NO_2-containing trace gas where the NO_2 moiety is more strongly bound than in ANs.

In order to assess to which extent this behaviour is potentially caused by inorganic trace gases that are not directly related to isoprene oxidation, an experiment with only NO_2 (2.75 ppbv) and O_3 (146 ppbv) in 23 SLPM dry synthetic air was performed. The steady-state concentration of $N_2O_5 + NO_3$ was measured as 78 pptv. The resulting thermograms using TDI-1 and TDI-2 and after subtraction of the signal from the NO_2 cavity (i.e. unheated inlet) are depicted in Fig. 4. No significant additional signal is observed

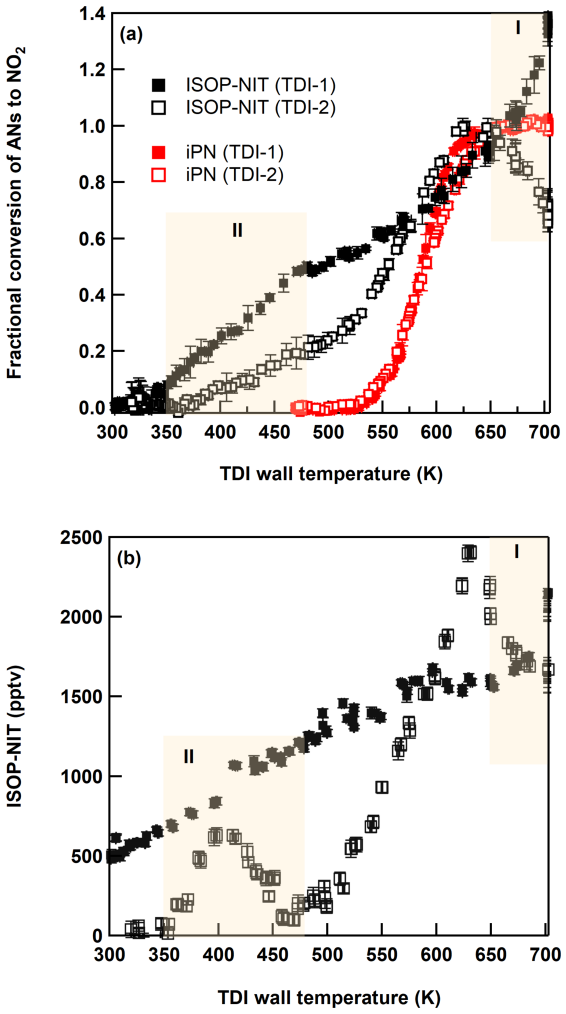

Figure 3. **(a)** Thermograms (relative to the signal at 650 K) of isoprene-derived organic nitrates (ISOP-NIT) and isopropyl nitrate (iPN) obtained with TDI-1 (solid symbols) and TDI-2 (open symbols) under dry conditions. **(b)** Absolute thermograms of ISOP-NIT obtained with TDI-1 (solid symbols) and TDI-2 (open symbols) under humid conditions (RH = 34 %, 22 °C). Regions (I and II) with unexpected detection of NO_2 are shaded yellow. Error bars denote standard deviation (1σ, 30 s) of the signal.

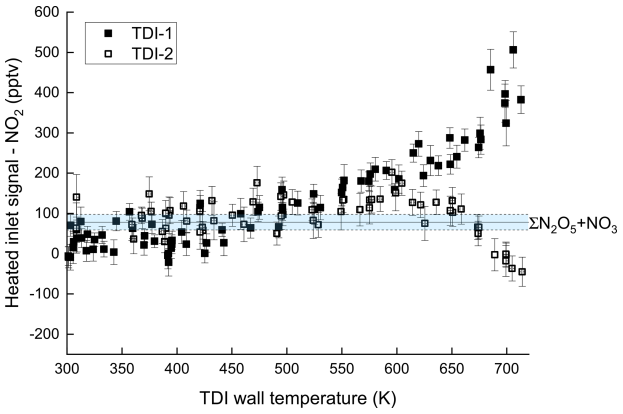

Figure 4. Temperature-dependent NO_2 detection when sampling 2.75 ppbv NO_2 and 146 ppbv O_3 in 23 SLPM dry synthetic air from SCHARK through TDI-1 and TDI-2. The signal from the NO_2 cavity (no TDI) has been subtracted from both datasets. The mixing ratios of $N_2O_5 + NO_3$ (with associated uncertainty) are indicated by the blue area.

below 475 K (region I) in either of the inlets. In region II ($T > 675$ K) on the other hand, we observed an increase (by ~ 500 pptv) in the signal at 703 K with TDI-1, whereas ~ 50 pptv is lost in TDI-2. In order to identify the trace gas(es) responsible for the signals observed in the system without isoprene, an iodide chemical ionization mass spectrometer (I-CIMS; Eger et al., 2019) described in the Supplement (Sect. S8) was coupled to the experiment. As shown in the Supplement (Fig. S3) both HNO_3 and nitrous acid (HONO) were observed as soon as O_3 and NO_2 were present in the chamber and their formation is enhanced in the presence of water vapour, which is a common phenomenon in Teflon chambers (Pitts et al., 1984). We also found that reversing the flows and sampling the air into the CIMS *after* passing through the TDI-1 or TDI-2 (at 475 K) resulted in removal of the HNO_3. Sampling through TDI-1 also led to loss of HONO.

Various TD-CRDS and TD-LIF instruments report the detection of HNO_3 as NO_2 following thermal dissociation at temperatures around 700 K (Day et al., 2002; Wild et al., 2014; Thieser et al., 2016). The sensitivity of the present set-up to HNO_3 was investigated by sampling nitric acid from a calibrated permeation source (Friedrich et al., 2020) via TDI-1 and TDI-2 simultaneously. In these experiments, 22 ppbv HNO_3 (with 780 pptv NO_2 impurity) in dry synthetic air was delivered to the TDIs along with 350 ppbv O_3. The HNO_3 mixing ratio was derived using a known permeation rate (Friedrich et al., 2020) and dilution factor. Figure 5 shows the temperature-dependent conversion efficiency of HNO_3 to NO_2 in the presence of ozone (squares) with TDI-1 (black solid symbols) and TDI-2 (open symbols). Conversion of HNO_3 to NO_2 starts at ~ 550 K and increases with rising temperature. At 680 K, the conversion efficiency is 23 % for TDI-1 and 8 % for TDI-2. No significant conversion of HNO_3 to NO_2 was observed when ozone was absent (blue data points) and was drastically reduced when the synthetic air was humidified to RH = 55 % at room temperature (red data points). The effect of water vapour is consistent with previous observations on the effect of humidity (Sobanski et al., 2016; Thieser et al., 2016; Friedrich et al., 2020).

The decomposition of HNO_3 to NO_2 thus only occurs in the presence of ozone under dry conditions, and its rate increases greatly at $T > 650$ K. This is consistent with the observations in Fig. 3b for TDI-1 and represents a likely

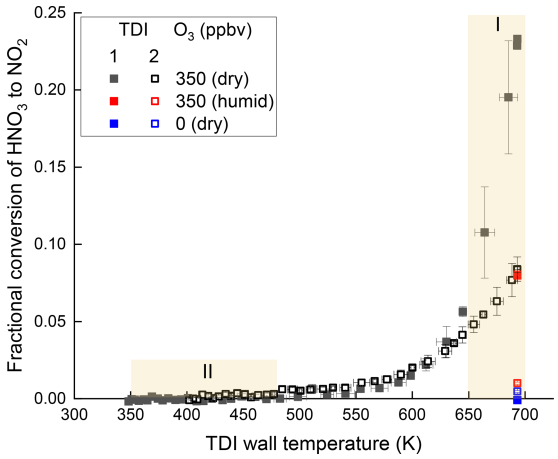

Figure 5. Thermograms of nitric acid (22 ppbv) in either dry (black) or humidified air (RH = 55 % at 23 °C, red) obtained with TDI-1 (closed squares) and TDI-2 (open squares). The O_3 mixing ratio was either zero or 350 ppbv in the non-humidified experiment and 350 ppbv in the humidified experiment. The error bars denote standard deviation (1σ, 1 min) of the signal.

explanation for the increase in signal when sampling from SCHARK to investigate the NO_3 + isoprene system. The apparently more efficient (∼ factor three) conversion of HNO_3 to NO_2 in TDI-1 than in TDI-2 is explained by the loss of NO_2 at high temperatures in TDI-2 through the reaction with O atoms (see Sect. 3.2). In TDI-1 this is prevented by the removal of O atoms by the glass beads (e.g. via scavenging or surface-catalysed recombination to O_2).

The ozone-assisted conversion of HNO_3 to NO_2 cannot be explained by known gas-phase processes as the reaction between HNO_3 and $O(^3P)$ (Reaction R12) has a low rate coefficient ($k_{13} < 3 \times 10^{-17}$ cm^3 molecule^{-1}s^{-1} at 298 K; Burkholder et al., 2016) and results mainly in the formation of OH and NO_3 (Reaction R12). The more efficient conversion of HNO_3 to NO_2 in TDI-1 (with glass beads) compared to TDI-2 indicates that a surface-catalysed process involving either ozone or $O(^3P)$ is involved (Reaction R13).

$$HNO_3 + O(^3P) \rightarrow NO_3 + OH \quad \text{(R12)}$$

$$HNO_3 + O_3 \text{ or } O(^3P) + \text{surface} \rightarrow NO_2 + \text{products} \quad \text{(R13)}$$

Assuming that, in a Langmuir–Hinshelwood type process, the first step in the surface-catalysed reaction is physical adsorption of HNO_3 to the surface, the strong reduction in conversion of HNO_3 to NO_2 under humid conditions is explained by the competitive adsorption of HNO_3 and H_2O, the latter favoured by its much larger concentrations. That is, H_2O drives HNO_3 from the surface and thus protects it from surface reactions.

3.1.2 Region II (T = 350–475 K)

In region II (350–475 K, shaded area in Fig. 3), instead of the near-zero signal expected in the absence of significant amounts of PNs or N_2O_5, we observe a monotonic increase in NO_2 with the temperature which is a factor of ∼ 2 steeper in TDI-1 than in TDI-2. The signal in TDI-1 at 475 K, where only PNs are expected to dissociate, is ∼ 50 % of the maximum signal at 650 K. There are several potential explanations for this behaviour, which include the following: (1) the formation and detection of thermally less stable ANs (e.g. including dinitrates), which dissociate at lower temperatures than, for example, iPN; (2) the formation of non-acyl, isoprene-derived peroxy nitrates (RO_2NO_2) that are sufficiently long-lived to build up to appreciable concentrations in SCHARK; and (3) chemical processes taking place in the TD inlets that convert ISOP-NIT to NO_2. Scenario (1) appears unlikely as several studies have shown that the O–N bond strength in various alkyl nitrates is very similar (Hao et al., 1994; Wild et al., 2014). We also note that the formation of dinitrates (in the absence of NO) only takes place when isoprene levels are very low and the first-generation nitrates formed in the NO_3 + isoprene reaction can react with a further NO_3. This can be ruled out for the present experiments in which the isoprene mixing ratio is always much larger than that of the first-generation nitrates formed, which in any case react much more slowly with NO_3 than does isoprene. The second explanation requires that RO_2 formed in the initial reaction between NO_3 and isoprene react with NO_2 to form RO_2NO_2. Given our experimental conditions, we would indeed expect that the main fate of any RO_2 formed in the reaction between NO_3 and isoprene is reaction with NO_2, which will dominate over self-reaction or reaction with NO_3, other RO_2 or HO_2. Non-acyl RO_2NO_2 are however generally highly thermally unstable, with lifetimes (at room temperature) of seconds or minutes, with respect to re-dissociation to $RO_2 + NO_2$.

For isoprene-derived RO_2NO_2 to contribute to the signal observed in region II would require that the RO_2–NO_2 bond strength be comparable to those of acyl nitrates such as PAN. The dominant 1,4-peroxy radical formed when NO_3 reacts with isoprene has a nitrate group separated by two carbon atoms from the peroxy carbon. It seems unlikely that this could have a stabilizing effect on the O–N bond in RO_2NO_2 in the same way that an α-carbonyl group does. Indeed, chamber experiments investigating the products of the NO_3 + isoprene reaction in detail (Barnes et al., 1990; Wu et al., 2021) have identified neither acyl- nor non-acyl-RO_2NO_2 as stable or semi-stable products formed from primary oxidation.

In support of scenario 3, Sect. 3.2 to 3.3 describe the evidence for chemical reactions leading to NO_2 formation that bypass the thermodynamic barrier for direct NO_2 formation but are surface-catalysed and require the presence of O_3 in either SCHARK or in the inlet. These processes are peculiar

to alkyl nitrates with a C=C double bond and thus have not been observed in TD inlets tested only with saturated alkyl nitrates such as the frequently used isopropyl nitrate.

3.2 The role of O_3

To further investigate the conversion of ISOP-NITs to NO_2 at low temperatures in the TD inlets, we generated NO_3 via the room-temperature thermal decomposition of N_2O_5, thus ruling out chemical processes that were initiated or catalysed by O_3.

In these experiments, N_2O_5 was transported into SCHARK by passing a flow of 0.1 SLPM dry synthetic air over a crystalline N_2O_5 sample cooled to −78 °C with further dilution in a 15 SLPM flow of zero air. The combined concentration of $N_2O_5 + NO_3$ that remains after the reaction with ∼ 22 ppbv isoprene (7 sccm of 46.5 ppmv) was measured as 40.5 pptv. The use of high isoprene concentrations guarantees that the thermal decomposition of N_2O_5 does not contribute significantly to the thermograms. Under these conditions several parts per billion by volume of ISOP-NIT were formed. A constant flow (2 SLPM) of zero air was passed over a low-pressure Hg lamp and added between the sampling port of SCHARK and the inlets and TD inlets of the NO_2, PN and AN cavities. This way the O_3 mixing ratio in the TD inlets could be varied without affecting the chemistry in the chamber.

Figure 6 presents the results of one such experiment in which ISOP-NIT was sampled from SCHARK using TDI-1 and TDI-2, both initially held at 703 K with thermograms obtained by decreasing the temperature of both inlets in 25 K steps. At each temperature step (periods of 20 min), after recording the signal under O_3-free conditions (black squares), a low (40–54 ppbv, green triangles), medium (97–111 ppbv, blue triangles) and high (185–219 ppbv, orange circles) mixing ratio of O_3 was added in front of the TD inlets. Before cooling to the next temperature, the signal without O_3 was measured again and agreed within 30–150 pptv to the value at the beginning of the corresponding period. To enable comparison with "ideal" behaviour, the thermogram of isopropyl nitrate (iPN, red circles) recorded from an experiment while flowing 162 ppbv O_3 (and 3 ppbv NO_2 impurity) through SCHARK is also plotted.

Figure 6a displays a thermogram obtained when sampling ISOP-NITs from SCHARK via TDI-1 (glass beads). In the presence of O_3, the thermograms are very broad with substantial NO_2 formation between 350 and 475 K (shaded region II) and in this sense are comparable to those displayed in Fig. 3, where NO_3 was obtained from the reaction of NO_2 with O_3. In region I, the effect of going from ∼ 50 to ∼ 200 ppb of ozone is to increase the NO_2 generated drastically. This is the opposite of that observed when sampling via TDI-2 and thus in agreement with the results of the experiment depicted in Fig. 3, where the increase in signal was assigned to detection of HNO_3. For the experiments in which

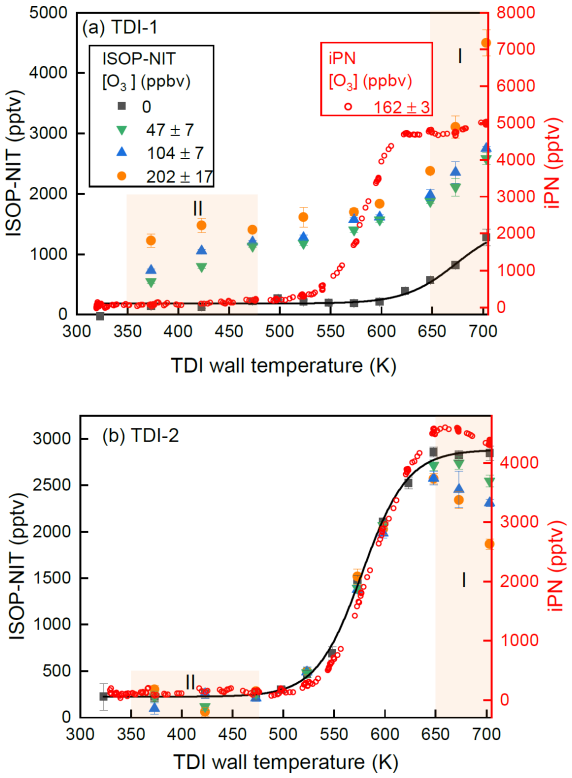

Figure 6. (a) Thermograms of isoprene-derived nitrates generated by mixing N_2O_5 (as NO_3 source) and ∼ 20 ppbv isoprene in SCHARK under dry conditions and sampling via TDI-1. The mixing ratio of O_3 (added only to the inlets) was varied from 0 to 202 ppbv. A thermogram of isopropyl nitrate (iPN) in the presence of 162 ppbv O_3 (and 3 ppbv NO_2 impurity) sampled through the same TDI is shown for comparison. The black solid line is a Boltzmann sigmoidal fit of the ozone-free experiment. The error bars show the standard deviation of the signal (1σ). **(b)** Same as **(a)** but using TDI-2.

NO_3 was generated in the room-temperature thermal dissociation of N_2O_5, HNO_3 can arise from reactions of N_2O_5 with moisture on the walls and is present as impurity in the N_2O_5 sample. As described above, the presence of glass beads has two effects which operate in the same direction in this temperature regime: the conversion of HNO_3 to NO_2 is catalysed by the surface provided by the glass beads, and at the same time the loss of NO_2 (via reaction with $O(^3P)$) is reduced as $O(^3P)$ is scavenged by the glass surface.

For TDI-1, the thermograms obtained without ozone (black squares) differ greatly to those in which ozone was present. Without ozone, NO_2 is not generated at temperatures lower than 550 K but its concentration increases rapidly at temperatures above ∼ 600 K with no indication of a plateau being reached. The thermograms obtained in this NO_3–isoprene system using TDI-1 in the absence of ozone bear little resemblance to that of iPN. Furthermore, during pe-

riods without ozone or heat in TDI-1, compounds of lower volatility like ISOP-NITs or HNO_3 appear to deposit on the glass beads and frit. This would form an explanation for a "memory effect" observed for TDI-1, whereby after exposure to HNO_3 or organic nitrates during unheated periods, an increase in the NO_2 signal followed by a slow decrease taking several hours is observed as soon as pure synthetic air and ozone were added to the flow through the heated inlet. An example of this phenomenon is shown in Fig. S4 in which (at peak signal) 60 ppbv of NO_2 was detected just by heating TDI-1 to 703 K in the presence of O_3 in synthetic air. In order to avoid bias in results caused by this effect, a cleaning procedure was adopted prior to all experiments whereby the inlet was heated to 703 K and exposed to ozone in synthetic air until a constant, low residual signal, usually between 20 and 200 pptv, was established. This memory effect seen for TDI-1 is also observed when a thermogram of ISOP-NIT (generated in a system similar to the experiment in Fig. 3) is measured by going from cold to hot temperatures (Fig. S5).

In Fig. 6b we present the results of the same experiment using TDI-2. The non-zero signal ($\sim$ 250 pptv) at temperatures between $\sim$ 320 and 450 K) results from instability in the baseline. In the absence of ozone, the organic nitrates generated in the NO_3-initiated oxidation of isoprene follow a well-defined thermogram (black squares and solid line) between 475 and 650 K, which is very similar to the thermogram measured for iPN (red circles). The addition of ozone does not result in the formation of NO_2 in region II but does induce NO_2 losses for temperatures above 650 K (region I). The fact that ISOP-NIT was not converted to NO_2 at temperatures < 475 K suggests that the observation of a large signal in Fig. 3a (region II, white squares) is linked to O_3-induced chemistry in SCHARK, which will be discussed in more detail in Sect. 3.3. The loss of NO_2 in region I increases with increasing amounts of O_3 with $\sim$ 35 % of the NO_2 formed at 625 K lost when O_3 was increased to $\sim$ 200 ppbv. The same behaviour is observed in the thermogram of iPN, which confirms that this process is independent of the nature of the nitrate but solely linked to thermal decomposition of O_3 and subsequent reactions of $O(^3P)$ with NO_2.

3.2.1 Thermal dissociation and gas-phase reactions of O_3 and $O(^3P)$

An important clue to the underlying chemical processes that lead to the conversion of ANs to NO_2 at temperatures lower than those required to break the O–N bond is the fact that the thermogram of iPN (measured with TDI-1) is not significantly affected by the presence of 163 ppbv O_3, whereas thermograms of ISOP-NIT, the vast majority of which are unsaturated, are greatly broadened when O_3 is present.

It is well known that $O(^3P)$ reacts rapidly (via electrophilic addition) to C=C double bonds (Leonori et al., 2015), and we thus assessed the potential impact of NO_2 formation via reactions of O_3 or $O(^3P)$ (formed in the thermal dissociation of O_3 in the TDIs) with ISOP-NIT.

The concentration of $O(^3P)$ in the TDIs depends on the concentration and rate of thermal decomposition of O_3 and thus on the gas temperature as well as its rate of recombination with O_2, reactions with O_3, NO_2, isoprene, isoprene nitrates and loss to the walls:

$$O_3 + M \rightarrow O(^3P) + O_2 + M \quad \text{(R14)}$$

$$O(^3P) + O_2 + M \rightarrow O_3 + M \quad \text{(R15)}$$

$$O(^3P) + O_3 \rightarrow 2O_2 \quad \text{(R16)}$$

$$O(^3P) + \text{surface} \rightarrow \text{products} \quad \text{(R17)}$$

$$NO_2 + O(^3P) \rightarrow NO + O_2 \quad \text{(R18)}$$

$$\text{ISOP-NIT} + O_3 \rightarrow \text{products} + NO_2 \quad \text{(R19)}$$

$$\text{ISOP-NIT} + O(^3P) \rightarrow \text{products} + NO_2 \quad \text{(R20)}$$

$$\text{ISOP} + O_3 \rightarrow \text{products} \quad \text{(R21)}$$

$$\text{ISOP} + O(^3P) \rightarrow \text{products}. \quad \text{(R22)}$$

The contribution (in addition to the thermal dissociation of ISOP-NIT) to NO_2 formation via Reactions (R19) and (R20) in TDI-2 was assessed via numerical simulation (FACSIMILE/CHEKMAT release H010; Curtis and Sweetenham, 1987). The rate coefficients for the most important reactions are listed in Table 1; the complete reaction scheme is listed in the Supplement (Sect. S9). Reaction times in heated and unheated section of TDI-2 were calculated from the temperature, internal diameter of the quartz tube and the flow rate. The rate coefficients for the gas-phase reactions of isoprene (IUPAC, 2021) and 2-methyl-2-butene (Herron and Huie, 1973) with $O(^3P)$ and O_3 were used as surrogates for the reactions of ISOP-NIT for which data are not available. The temperature-dependent dissociation rate coefficient of *n*-propyl nitrate was used to account for NO_2 from the thermal dissociation of isoprene-derived nitrates (Morin and Bedjanian, 2017). Wall loss of $O(^3P)$ in the instrument was estimated to be 90 s^{-1} using the method as described in Thieser et al. (2016) and implemented in the model run.

The initial conditions for the simulation were 1 ppbv ISOP-NIT, 10 ppbv isoprene and 5 ppbv NO_2 at a cavity pressure of 724 hPa and a temperature of 298 K. The results obtained are shown by black curves in Fig. 7. For temperatures up to 575 K the simulated thermograms with and without O_3 are almost identical, whereas at higher temperatures, the amount of NO_2 exiting the inlet decreases because of its reaction with $O(^3P)$ (Reaction R17), in broad agreement with the experiments carried out using TDI-2 as shown in Fig. 3b. The model simulations show (Fig. 7) that almost no $O(^3P)$ is formed by the thermal dissociation of O_3 at the lower temperatures of region II. Only at higher temperatures is a significant fraction of O_3 (27 % at 703 K) converted to $O(^3P)$ with the majority subsequently lost at the inlet walls. These calculations underline the observation that the low temperature

Table 1. Central reactions used for numerical simulation of the thermal dissociation of organic nitrates in TDI-2.

Reaction	Rate constant	Reference
ISOP-NIT + M → RO + NO_2 + M	$3.16 \times 10^{15} \exp(-19676/T)$ s^{-1}	Morin and Bedjanian (2017)
$O_3 \rightarrow O(^3P) + O_2$	Pressure dependent (see text)	Peukert et al. (2013)
$O(^3P) + O_2 + M \rightarrow O_3 + M$	$6.0 \times 10^{-34} (T/300)^{-2.6}$ [M] cm^3 $molecule^{-1}$ s^{-1}	IUPAC (2021)
$O(^3P) + O_3 \rightarrow 2O_2$	$8.0 \times 10^{-12} \exp(-2060/T)$ cm^3 $molecule^{-1}$ s^{-1}	IUPAC (2021)
$O(^3P)$ + ISOP-NIT → products + NO_2	$3.9 \times 10^{-12} \exp(680/T)$ cm^3 $molecule^{-1}$ s^{-1} [a]	Herron and Huie (1973)
$O(^3P)$ + ISOP → products	3.5×10^{-11} cm^3 $molecule^{-1}$ s^{-1} (298 K)	Paulson et al. (1995)
$O(^3P)$ + wall	$90\ s^{-1}$	See text
$O(^3P) + NO_2 \rightarrow NO + O_2$	$5.1 \times 10^{-12} \exp(198/T)$ cm^3 $molecule^{-1}$ s^{-1}	IUPAC (2021)
O_3 + ISOP → products	$1.05 \times 10^{-14} \exp(-2000/T)$ cm^3 $molecule^{-1}$ s^{-1}	IUPAC (2021)
O_3 + ISOP-NIT → products + NO_2	$1.05 \times 10^{-14} \exp(-2000/T)$ cm^3 $molecule^{-1}$ s^{-1} [b]	IUPAC (2021)

Notes: [a] value for 2-methyl-2-butene used. [b] Value for isoprene used.

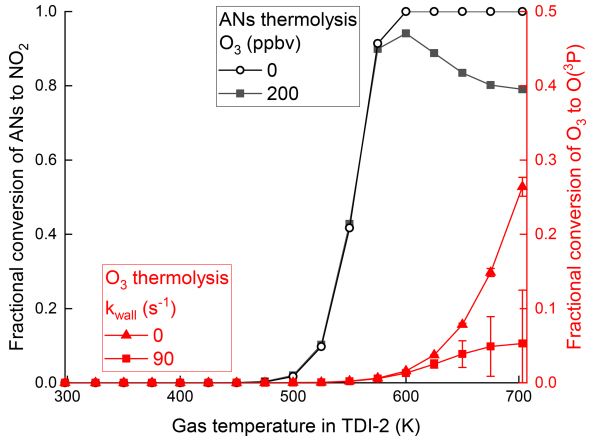

Figure 7. Black lines and data points denote simulated, fractional conversion of *n*-propyl nitrate to NO_2 for TDI-2 without and with O_3 (200 ppbv). Red lines and data points denote simulated fractional conversion of O_3 to $O(^3P)$ within the heated section of TDI-2 with and without wall loss of $O(^3P)$. Error bars denote the standard deviation (1σ) of the fractional conversion changing over time passed in the heated section.

formation of NO_2 from ISOP-NIT seen when using TDI-1 cannot be explained with known gas-phase chemistry.

In summary, the experimental observations and the numerical simulations indicate that the presence of O_3 is required in the inlet for TDI-1 and in the chamber for TDI-2 to generate NO_2 from isoprene-derived nitrates at temperatures less than 475 K. We have shown that the generation of NO_2 from alkyl nitrates at low temperatures using TDI-1 requires that the organic nitrate has a double bond and that, while gas-phase reactions of $O(^3P)$ are responsible for the loss of NO_2 at high temperatures, they are *not* responsible for the conversion of isoprene-derived nitrates at lower temperatures in either of the TD inlets. The presence of glass beads (large surface area) favours the formation of NO_2 from ISOP-NIT at low temperatures. Altogether, these observations indicate that a surface-catalysed reaction involving ozone is the process most likely to be responsible for the conversion of ISOP-NIT to NO_2 at temperatures below those required for the gas-phase thermolysis.

3.2.2 Surface-catalysed reactions with ozone

Quartz tubes contain impurities and surface defects that can provide reactive sites (RSs) at elevated temperatures, and the surface-catalysed chemistry of ozone on, for example, mineral silicates is well known (Bulanin et al., 1994; Hanisch and Crowley, 2003a, b; Usher et al., 2003). O_3 can be surface-catalytically converted to O_2 (Reaction R25) by the formation and loss of reactive, oxygenated surface sites (RSOs) via Reactions (R23) and (R24).

$$RS + O_3 \rightarrow RSO + O_2 \quad \text{(R23)}$$

$$RSO + O_3 \rightarrow RS + 2O_2 \quad \text{(R24)}$$

$$2O_3 \rightarrow 3O_2 \quad \text{(R25)}$$

In order to test for ozone loss in our set-up, O_3 in synthetic air was passed through the TDIs. The O_3 mixing ratio prior to entering the inlets was measured continuously using the ozone monitor (UV absorption). The ozone exiting the TD inlets was converted to NO_2 (by addition of 1 ppmv NO (Reaction R4) in a 1.5 m long PFA tubing with 0.5 in. OD and a residence time of 5.2 s) and then measured in the 409 nm cavities. Figure 8a shows the results of such an experiment for TDI-1. The concentration of ozone before entering the inlets was 20.5 ppbv (open dots), which was detected as 17.1 ppbv after passing through the inlet at 298 K (black squares, 11:15 to 11:55 LT). This represents a transition efficiency of 0.83, which matches that expected when considering the reaction time, NO concentration and the rate coefficient ($k_4 = 1.9 \times 10^{-14}$ cm^3 $molecule^{-1}$ s^{-1}, IUPAC, 2021).

At ≈ 12:00 LT, upon heating the inlet to 473 K the ozone exiting TDI-1 was depleted by up to 27 %, while heating to

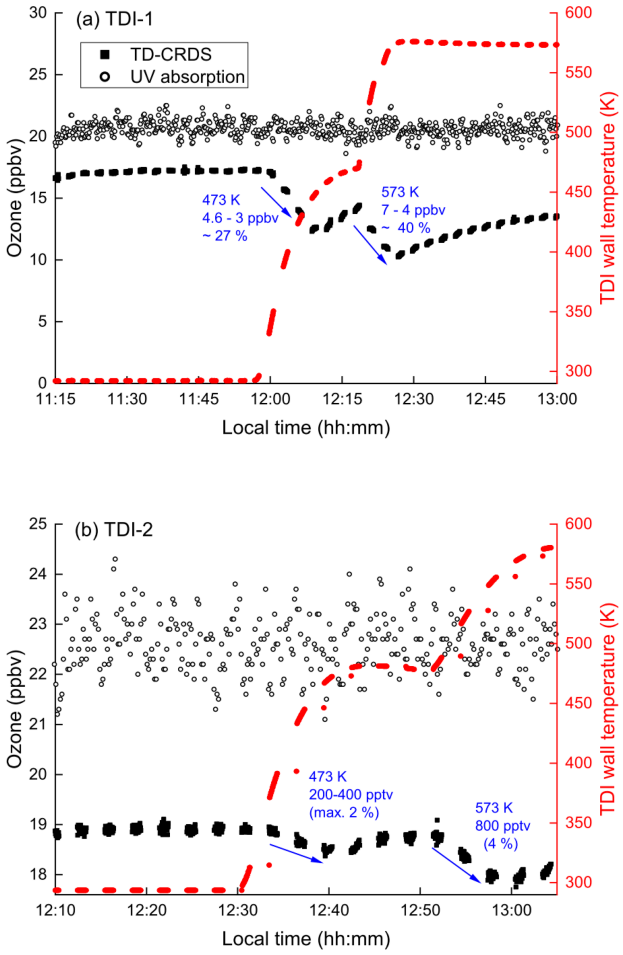

Figure 8. Time series of O_3 mixing ratios before and after passing though TDI-1 **(a)** or TDI-2 **(b)**.

573 K results in further loss (up to 40 %). An analogous experiment using TDI-2 (Fig. 8b) showed that while some O_3 was also lost (e.g. 4 % at 573 K), this was much less than in TDI-1. As the gas-phase thermal decomposition of O_3 is negligible under these conditions (0.6 % at 575 K, Fig. 7), the loss of O_3 when passing through the TD inlets indicates that surface-catalysed ozone decomposition takes place (Reactions R23 and R24), especially in TDI-1 where larger surface areas are available.

We now consider the possibility that the conversion of isoprene-derived nitrates to NO_2 can be catalysed by surfaces in the presence of O_3. We note that previous work has shown that the heterogeneous ozonolysis of alkenes on glass or other surfaces can be more efficient than its analogous, gas-phase process (Dubowski et al., 2004; Stokes et al., 2008; Ray et al., 2013) and now consider the possibility that RSO is the mediating reactive species in TDI-1 in our experiments.

$$\mathrm{RSO} + \mathrm{ISOP\text{-}NIT} \rightarrow \mathrm{NO_2} + \mathrm{products} \qquad \text{(R26)}$$

We first examine the possible contributors to ISOP-NIT formed in the reaction of NO_3 with isoprene, in which the dominant initial step (in air) is a sequential 1,4 addition of NO_3 and O_2 to form δ- and β-peroxy radicals, e.g. $O_2NOCH_2C(CH_3)=CHCH_2OO$ (Schwantes et al., 2015). In the presence of NO_3, RO_2 or HO_2, the peroxy radicals react further to form "first-generation" isoprene nitrates which contain carbonyl, hydroperoxidic and alcoholic groups such as $O_2NOCH_2C(CH_3)=CHCHO$, $O_2NOCH_2C(CH_3)=CHCH_2OOH$ and $O_2NOCH_2C(CH_3)=CHCH_2OH$, respectively. Note that most of the known, first-generation organic nitrates retain a C=C double bond.

A hypothetical ISOP-NIT degradation scheme involving the initial attachment of RS-O to the remaining double bond is given in Fig. 9. We consider only the fate of the most stable surface adducts, i.e. tertiary radical in case of δ-products and secondary radicals in case of β-products. Both radical adducts will react with O_2 to form organic peroxy radicals which may undergo H shifts (via five- or six-membered rings) resulting in formation of a radical with its unpaired electron in the direct vicinity of the nitrate functionality. Such unimolecular processes may become competitive to bimolecular reactions under atmospheric conditions (Møller et al., 2019). A possible fate of this radical is decomposition to form a carbonyl compound via NO_2 elimination (Hjorth et al., 1990; Berndt and Boge, 1995; Vereecken et al., 2021). For δ-products, the tertiary product may also eliminate NO_2 under the formation of an epoxide.

With TDI-2, the conversion of ISOP-NIT to NO_2 at low temperatures (region I) is only observed when O_3 is present in the chamber (Fig. 3a), but not when it is added only to the inlet (Fig. 6b) implying that the presence of O_3 as an oxidizing agent in SCHARK is the main difference between these two reaction systems. This suggests that the ozonolysis of isoprene may play an important role. As the reaction between isoprene and O_3 leads to the formation of OH and additional HO_2 (Zhang et al., 2002; Malkin et al., 2010; Cox et al., 2020), the fraction of RO_2 reacting with HO_2 in this system is enhanced when compared to the experiments in which NO_3 was generated from N_2O_5. The major product from the reaction between nitrated δ- and β-peroxy radicals with HO_2 is hydroperoxides, such as $O_2NOCH_2C(CH_3)=CHCH_2OOH$ (Schwantes et al., 2015). With the intention of assessing the effect of O_3 on hydroperoxide yields, further model calculations were performed using the Framework for 0-D Atmospheric Modelling (F0AM) (Wolfe et al., 2016). The NO_3 isoprene oxidation scheme is still the subject of current research and uncertain, which is why the Master Chemical Mechanism (MCM, version 3.3.1, http://mcm.leeds.ac.uk, last access: 7 August 2021) (Jenkin et al., 2015) and the Reduced Caltech Isoprene Mechanism Plus (RCIMP, version 5, https://data.caltech.edu/records/247, last access: 7 August 2021) (Wennberg et al., 2018; Bates and Jacob, 2019) were applied. Figure 10 shows the calculated fraction of hy-

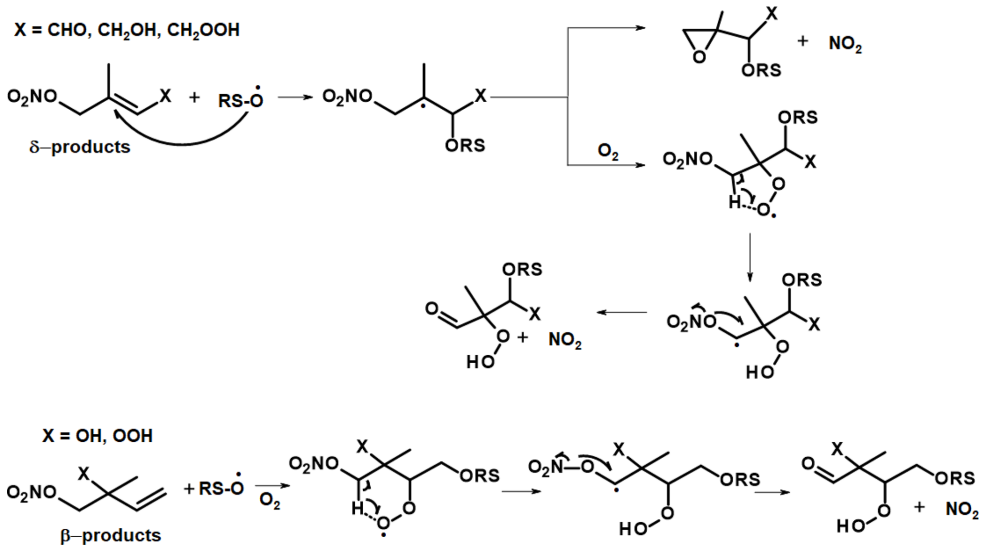

Figure 9. Possible mechanism for surface-catalysed conversion of first-generation ISOP-NIT in TDI-1. RS-O represents a reactive surface site.

droperoxides to ISOP-NIT using both models and mixing 22 ppbv isoprene with either 10.8 ppbv NO_2 and 150 ppbv O_3 (runs 1 and 3) or 3 ppbv N_2O_5 (runs 2 and 4) to achieve NO_3 in a flow-through chamber with an exchange rate of $2.73 \times 10^{-4}\,s^{-1}$. Generally, the MCM predicts higher hydroperoxide yields than RCIMP. A possible reason might be that MCM has higher rates of HO_2 reformation from reactions of isoprene-derived alkoxy radicals than RCIMP does. For that reason, MCM only predicts an increase in the hydroperoxide yield by a factor of 1.33 when the NO_3 source is changed from N_2O_5 to $NO_2 + O_3$ (model runs 1 and 2), whereas RCIMP predicts a factor of 2.56 (model runs 3 and 4). The calculations thus broadly support the hypothesis that unsaturated, nitrated hydroperoxides are involved in the low temperature (surface-catalysed) formation of NO_2 from ISOP-NIT. Indeed, hydroperoxides not only have high affinity for surfaces but also have a rather weak O–O bond with a dissociation energy of ≈ 45 kcal mol^{-1} (Bach and Schlegel, 2020), and several routes to surface-catalysed elimination of NO_2 appear feasible. Decomposition of isoprene-derived hydroperoxides within the sampling line has been observed for other instruments (Rivera-Rios et al., 2014). A possible degradation mechanism for an isoprene-derived hydroperoxide which is abundant from the NO_3 + isoprene system (Schwantes et al., 2015) is depicted in Fig. 11. In this case, $O_2NOCH_2C(CH_3)$=$CHCH_2OOH$ coordinates via hydrogen bonds to the SiO_2 surface prior to cleavage of the O–O bond to form OH and an alkoxy radical. The latter may dissociate via unimolecular reactions to form closed-shell products under elimination of NO_2 (Wennberg et al., 2018; Vereecken et al., 2021).

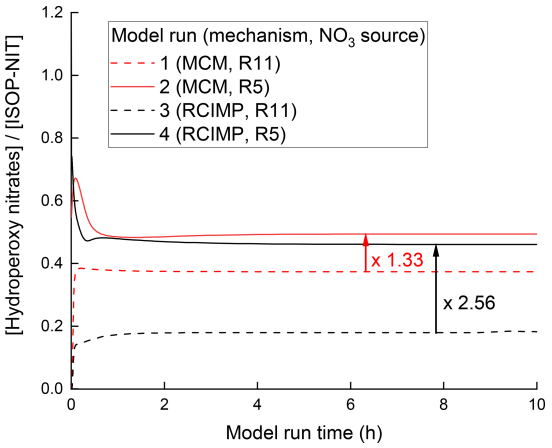

Figure 10. Simulated fractional contribution of hydroperoxy nitrates to ISOP-NIT using schemes taken from the MCM (red) and from RCIMP (black). The simulations reproduce the experimental conditions in Figs. 3 and 6, with 22 ppbv of isoprene together with either 3 ppbv N_2O_5 as NO_3 source (runs 1 and 3) or 10.8 ppbv $NO_2 + 150$ ppbv O_3 (runs 2 and 4).

3.3 Elimination of O_3 and surface-catalysed conversion of ANs at low temperatures

Our findings clearly show that the combination of heated quartz surfaces and ozone catalyse the decomposition of the unsaturated nitrates formed in the reaction between NO_3 and isoprene at temperatures below 473 K. While the exemplary, surface-catalysed processes depicted in Figs. 9 and 11 fulfil the requirement of conversion of ISOP-NIT to NO_2, we stress that these are purely hypothetical and we cannot state

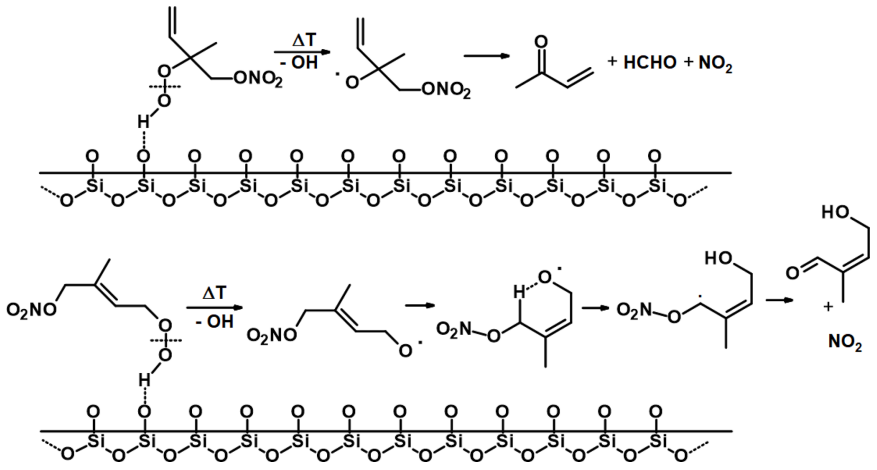

Figure 11. Potential degradation pathways of isoprene-derived hydroperoxides on a heated quartz surface.

with any certainty that they are the reactions responsible for our observations. While it would be highly interesting to investigate such processes using different (e.g. surface sensitive) techniques, this is clearly beyond the scope of this paper and of the experimental capabilities of this research project. Instead, we take the more pragmatic approach and indicate potential methods to eliminate such unwanted reactions when using TD inlets.

In principal, as the processes that convert ISOP-NIT to NO_2 are clearly surface-catalysed (involving formation of RSO), their impact can be reduced by using a surface that does not support formation of RSO. We therefore tested a third TD inlet (TDI-3), consisting of 55 cm PFA tubing (0.375 in. OD) with a 20 cm heated section. PFA tubing has been routinely used as TDI for measurement of, for example, PAN, as it is relatively unreactive to the peroxy radicals formed (Phillips et al., 2013). The C–F bond of PFA is very strong and nonpolar, which should reduce the formation of RSO as well as adsorption of ISOP-NIT to the surface. The performance of a TDI made of PFA (TDI-3) was examined by performing an experiment with SCHARK analogous to the one shown in Fig. 2. The resulting time series of NO_2, ΣPNs (using TDI-3 heated to 448 K) and ΣANs (using TDI-2 heated to 648 K) are depicted in Fig. 12. At first, O_3 (5 SLPM synthetic air passed over a Hg lamp) and NO_2 (200 sccm of 1 ppmv) in 25 SLPM dry synthetic air were constantly introduced into SCHARK. After detectable amounts of NO_3 and N_2O_5 had been formed, isoprene (9.8 sccm of 46.5 ppmv) was added leading (as expected) to almost quantitative depletion of NO_3 and N_2O_5.

During the following 3 h the signal in the ΣAN cavity (TDI-2) increased to ∼ 1.2 ppbv, while the signal in the ΣPN channel (∼ 40 pptv) was close to the detection limit. A CIMS measurement obtained during this experiment validates that PAN mixing ratios are lower than 50 pptv. This result already confirms that (1) the ANs derived from NO_3 + isoprene reaction are not detected at $T < 448$ K when PFA is used instead of quartz and (2) as expected, there is no significant generation of peroxy nitrates in these experiments which would be detectable with both ovens at $T = 448$ K (see Fig. S6 in the Supplement).

This result not only confirms that the previous detection of ISOP-NITs at low TD-inlet temperatures when using TDI-2 and especially TDI-1 was caused by heterogeneous reactions at the quartz surface, but also provides a solution to the problem of the separate measurement of ΣANs and ΣPNs using TD inlets.

We recall, however, that the reason for adding glass beads to the inlet was to suppress recombination reactions of NO_2 with peroxy radicals by providing a surface to scavenge the latter. The use of a PFA tube rather than quartz will certainly exacerbate this effect, as the rate of loss of RO_2 to PFA surfaces is expected to be lower than on quartz (Wooldridge et al., 2010). This implies that corrective procedures based on numerical simulation may be necessary in some environments as shown by Thieser et al. (2016), and this may limit the useful deployment of the method to regions where NO_x levels are sufficiently low that reaction of RO_2 with NO and NO_2 become insignificant. In addition, similar to the observations of Sobanski et al. (2016), $ClNO_2$ can interfere with the detection of ANs. The experiment shown in Fig. S7 reveals that $ClNO_2$ is detected with TDI-2 at 698 K, but not with TDI-3 at 448 K.

4 Summary, conclusions and implications for atmospheric measurements of ΣPNs and ΣANs

We have shown that the detection of isoprene-derived organic nitrates via its thermal dissociation in quartz/glass inlets can (in the presence of O_3) be accompanied by undesirable side reactions which broaden the thermograms and thus impede

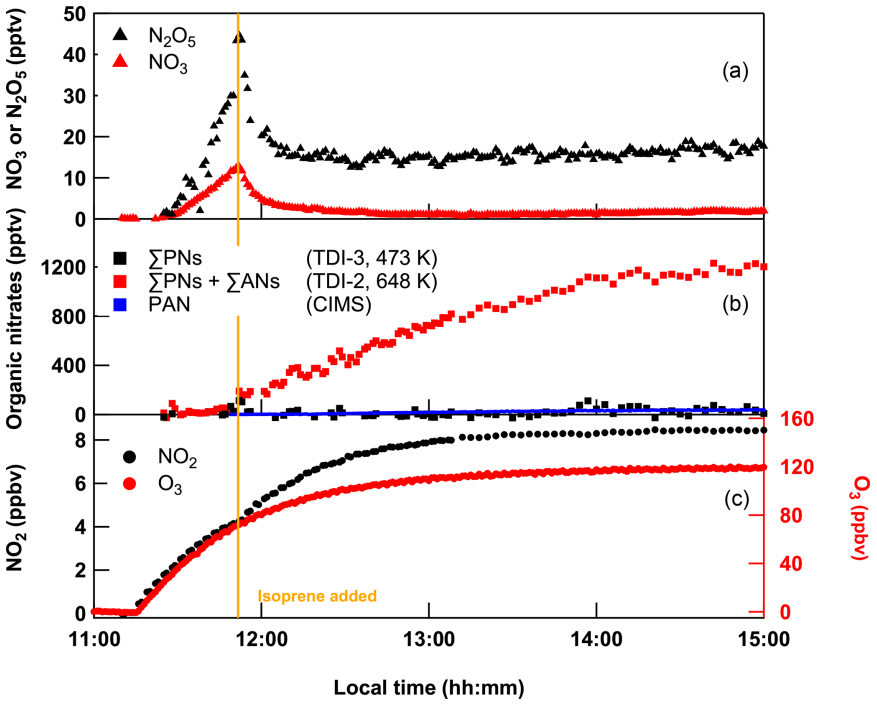

Figure 12. Mixing ratios of NO_2, ΣPNs with TDI-3 and ΣPNs + ΣANs with TDI-2 obtained from constant introduction of 200 sccm NO_2, and 9.8 sccm isoprene in 25 SLPM (of which 5 SLPM was passed over a PenRay lamp to generate O_3) dry synthetic air into SCHARK. A CIMS measurement of PAN is appended (blue squares).

the separation of PN and AN signals by sampling through TD inlets at different temperatures as is commonly practised. While our experiments deal with the nitrates formed in the NO_3-initiated oxidation of isoprene, it is very likely that similar broadening of thermograms would also occur with nitrates formed from the oxidation of other terpenoids, as some organic nitrates derived from night-time oxidation of, for example, limonene still contain a double bond (Fry et al., 2011) and/or contain hydroperoxy groups.

Specifically, we find that the presence of O_3 in either the quartz TD inlet or in a Teflon simulation chamber results in the generation of NO_2 from isoprene-derived nitrates in TD inlets made of quartz at temperatures less than 475 K and that this only occurs when the organic nitrate either has a double bond or a hydroperoxy group (or both). The formation of NO_2 from ISOP-NIT was accelerated in the presence of glass beads, which indicates that a surface-catalysed reaction involving ozone and reactive surface sites is the process most likely to be responsible both for the conversion of ISOP-NIT to NO_2 at low temperatures (375–475 K) and the conversion of HNO_3 to NO_2 at high temperatures (> 550 K). By avoiding the use of O_3 or using a non-quartz TD inlet, we were able to show that the ISOP-NIT thermogram is entirely consistent with those of saturated alkyl nitrates.

We show that surface-catalysed reactions on quartz TD inlets involving O_3 represent a potential source of bias in measurements of ΣANs and ΣPNs during field observations, especially when isoprene is abundant. For example, we previously reported results from two campaigns carried out using the TD-CRDS system described here on the same rural mountain site (Kleiner Feldberg) and season (but in different years). We found that the average, relative abundance of ΣPNs and ΣANs was quite different with ΣANs ≈ ΣPNs during the PARADE campaign in 2011 and ΣPNs > ΣANs during the NOTOMO campaign in 2015 (Sobanski et al., 2017). In 2011, the TD inlet was a quartz tube (i.e. similar to TDI-2) (Thieser et al., 2016), whereas in 2015 the inlet contained glass beads (i.e. similar to TDI-1) (Sobanski et al., 2016). With our present understanding of the role of surfaces and O_3 in TD inlets, we cannot rule out that the observations during 2015 were biased to lower values for ΣANs and higher values for ΣPNs, although, as discussed by Sobanski et al. (2017), there are other, meteorological factors which would have contributed.

For the detection of PNs we have shown that (at the lower temperature required to thermally dissociate PNs to NO_2) surface catalytic effects that convert ANs (or other species) to NO_2 can be completely avoided by using a TD inlet made of a non-reactive material like PFA (TDI-3). In this case, O_3 does not appear to have any impact.

When using a quartz TD inlet for conversion of ANs + PNs to NO_2 at higher temperatures, the surface re-

actions that shift thermograms to lower temperatures are of less significance as, in any case, the role of the TD inlet is to convert all ANs and all PNs to NO_2. However, in order to avoid detection of HNO_3 or HONO other materials may be more suitable than quartz. Sapphire, commonly used in microwave discharge generated plasmas owing to its high purity and non-reactive surface, may represent a useful alternative. Under humid conditions, some of the observed interferences become negligible: HNO_3 appears not to interfere with the AN measurement, and the interference of ANs to the PN measurement is reduced in TDI-2, but not in TDI-1.

This study emphasizes the importance of characterizing thermal dissociation inlets under conditions which are similar to those found in the atmosphere. We recognize that the impact of surface catalytic processes will vary from one inlet to the next (even if made from the same material), and all quartz TDIs will not necessarily exhibit the same degree of conversion of biogenic VOC-derived ANs at low temperature. For this reason, thermograms should be measured using trace gases that are abundant in the atmosphere and the effect of, for example, O_3 and water vapour should be thoroughly investigated.

Data availability. The data underlying the figures are available on request from the corresponding author.

Supplement. The supplement related to this article is available online at: https://doi.org/10.5194/amt-14-5501-2021-supplement.

Author contributions. PD conducted the experiments, analysed the data and wrote the manuscript. RD was responsible for the CIMS measurements. JS designed and built SCHARK. JNC designed the experiments and together with JL contributed to the manuscript.

Competing interests. The authors declare that they have no conflict of interest.

Disclaimer. Publisher's note: Copernicus Publications remains neutral with regard to jurisdictional claims in published maps and institutional affiliations.

Financial support. The article processing charges for this open-access publication were covered by the Max Planck Society.

Review statement. This paper was edited by Hendrik Fuchs and reviewed by two anonymous referees.

References

Bach, R. D. and Schlegel, H. B.: Bond Dissociation Energy of Peroxides Revisited, J. Phys. Chem. A, 124, 4742–4751, https://doi.org/10.1021/acs.jpca.0c02859, 2020.

Barnes, I., Bastian, V., Becker, K. H., and Tong, Z.: Kinetics and products of the reactions of NO_3 with monoalkenes, dialkenes, and monoterpenes, J. Phys. Chem., 94, 2413–2419, https://doi.org/10.1021/j100369a041, 1990.

Bates, K. H. and Jacob, D. J.: A new model mechanism for atmospheric oxidation of isoprene: global effects on oxidants, nitrogen oxides, organic products, and secondary organic aerosol, Atmos. Chem. Phys., 19, 9613–9640, https://doi.org/10.5194/acp-19-9613-2019, 2019.

Beaver, M. R., Clair, J. M. St., Paulot, F., Spencer, K. M., Crounse, J. D., LaFranchi, B. W., Min, K. E., Pusede, S. E., Wooldridge, P. J., Schade, G. W., Park, C., Cohen, R. C., and Wennberg, P. O.: Importance of biogenic precursors to the budget of organic nitrates: observations of multifunctional organic nitrates by CIMS and TD-LIF during BEARPEX 2009, Atmos. Chem. Phys., 12, 5773–5785, https://doi.org/10.5194/acp-12-5773-2012, 2012.

Berndt, T. and Boge, O.: Products and Mechanism of the Reaction of NO_3 with Selected Acyclic Monoalkenes, J. Atmos. Chem., 21, 275–291, https://doi.org/10.1007/Bf00696759, 1995.

Berndt, T. and Boge, O.: Gas-phase reaction of NO_3 radicals with isoprene: A kinetic and mechanistic study, Int. J. Chem. Kinet., 29, 755–765, https://doi.org/10.1002/(sici)1097-4601(1997)29:10<755::aid-kin4>3.0.co;2-l, 1997.

Brownwood, B., Turdziladze, A., Hohaus, T., Wu, R., Mentel, T. F., Carlsson, P. T. M., Tsiligiannis, E., Hallquist, M., Andres, S., Hantschke, L., Reimer, D., Rohrer, F., Tillmann, R., Winter, B., Liebmann, J., Brown, S. S., Kiendler-Scharr, A., Novelli, A., Fuchs, H., and Fry, J. L.: Gas-Particle Partitioning and SOA Yields of Organonitrate Products from NO_3-Initiated Oxidation of Isoprene under Varied Chemical Regimes, ACS Earth Space Chem., 5, 785–800, https://doi.org/10.1021/acsearthspacechem.0c00311, 2021.

Bulanin, K. M., Alexeev, A. V., Bystrov, D. S., Lavalley, J. C., and Tsyganenko, A. A.: IR Study of Ozone Adsorption on SiO_2, J. Phys. Chem., 98, 5100–5103, https://doi.org/10.1021/j100070a026, 1994.

Burkholder, J. B., Sander, S. P., Abbatt, J., Barker, J. R., Huie, R. E., Kolb, C. E., Kurylo, M. J., Orkin, V. L., Wilmouth, D. M., and Wine, P. H.: Chemical Kinetics and Photochemical Data for Use in Atmospheric Studies, Evaluation No. 18, JPL Publication 15-10, Jet Propulsion Laboratory, Pasadena, available at: http://jpldataeval.jpl.nasa.gov (last access: last access: 7 August 2021), 2016.

Carlton, A. G., Wiedinmyer, C., and Kroll, J. H.: A review of Secondary Organic Aerosol (SOA) formation from isoprene, Atmos. Chem. Phys., 9, 4987–5005, https://doi.org/10.5194/acp-9-4987-2009, 2009.

Cox, R. A., Ammann, M., Crowley, J. N., Herrmann, H., Jenkin, M. E., McNeill, V. F., Mellouki, A., Troe, J., and Wallington, T. J.: Evaluated kinetic and photochemical data for atmospheric chemistry: Volume VII – Criegee intermediates, Atmos. Chem. Phys., 20, 13497–13519, https://doi.org/10.5194/acp-20-13497-2020, 2020.

Crutzen, P. J. and Lelieveld, J.: Human impacts on atmospheric chemisty, Annu. Rev. Earth Planet. Sci., 29, 17–45, https://doi.org/10.1146/annurev.earth.29.1.17, 2001.

Curtis, A. R. and Sweetenham, W. P.: Facsimile, Atomic Energy Research Establishment, Report R-12805, Harwell Laboratory, Oxfordshire, UK, 1987.

Davidson, J. A., Viggiano, A. A., Howard, C. J., Dotan, I., Fehsenfeld, F. C., Albritton, D. L., and Ferguson, E. E.: Rate Constants for Reactions of O_2^+, NO_2^+, NO^+, H_3O^+, CO_3^-, NO_2^- and Halide Ions with N_2O_5 at 300 K, J. Chem. Phys., 68, 2085–2087, https://doi.org/10.1063/1.436032, 1978.

Day, D. A., Wooldridge, P. J., Dillon, M. B., Thornton, J. A., and Cohen, R. C.: A thermal dissociation laser-induced fluorescence instrument for in situ detection of NO_2, peroxy nitrates, alkyl nitrates, and HNO_3, J. Geophys. Res.-Atmos., 107, ACH 4-1–ACH 4-14, https://doi.org/10.1029/2001jd000779, 2002.

Dewald, P., Liebmann, J. M., Friedrich, N., Shenolikar, J., Schuladen, J., Rohrer, F., Reimer, D., Tillmann, R., Novelli, A., Cho, C., Xu, K., Holzinger, R., Bernard, F., Zhou, L., Mellouki, W., Brown, S. S., Fuchs, H., Lelieveld, J., and Crowley, J. N.: Evolution of NO_3 reactivity during the oxidation of isoprene, Atmos. Chem. Phys., 20, 10459–10475, https://doi.org/10.5194/acp-20-10459-2020, 2020.

Dubowski, Y., Vieceli, J., Tobias, D. J., Gomez, A., Lin, A., Nizkorodov, S. A., McIntire, T. M., and Finlayson-Pitts, B. J.: Interaction of gas-phase ozone at 296 K with unsaturated self-assembled monolayers: A new look at an old system, J. Phys. Chem. A, 108, 10473–10485, https://doi.org/10.1021/jp046604x, 2004.

Eger, P. G., Helleis, F., Schuster, G., Phillips, G. J., Lelieveld, J., and Crowley, J. N.: Chemical ionization quadrupole mass spectrometer with an electrical discharge ion source for atmospheric trace gas measurement, Atmos. Meas. Tech., 12, 1935–1954, https://doi.org/10.5194/amt-12-1935-2019, 2019.

Finlayson-Pitts, B. J., Wingen, L. M., Sumner, A. L., Syomin, D., and Ramazan, K. A.: The heterogeneous hydrolysis of NO_2 in laboratory systems and in outdoor and indoor atmospheres: An integrated mechanism, Phys. Chem. Chem. Phys., 5, 223–242, https://doi.org/10.1039/B208564J, 2003.

Friedrich, N., Tadic, I., Schuladen, J., Brooks, J., Darbyshire, E., Drewnick, F., Fischer, H., Lelieveld, J., and Crowley, J. N.: Measurement of NO_x and NO_y with a thermal dissociation cavity ring-down spectrometer (TD-CRDS): instrument characterisation and first deployment, Atmos. Meas. Tech., 13, 5739–5761, https://doi.org/10.5194/amt-13-5739-2020, 2020.

Fry, J. L., Kiendler-Scharr, A., Rollins, A. W., Brauers, T., Brown, S. S., Dorn, H.-P., Dubé, W. P., Fuchs, H., Mensah, A., Rohrer, F., Tillmann, R., Wahner, A., Wooldridge, P. J., and Cohen, R. C.: SOA from limonene: role of NO_3 in its generation and degradation, Atmos. Chem. Phys., 11, 3879–3894, https://doi.org/10.5194/acp-11-3879-2011, 2011.

Fry, J. L., Brown, S. S., Middlebrook, A. M., Edwards, P. M., Campuzano-Jost, P., Day, D. A., Jimenez, J. L., Allen, H. M., Ryerson, T. B., Pollack, I., Graus, M., Warneke, C., de Gouw, J. A., Brock, C. A., Gilman, J., Lerner, B. M., Dubé, W. P., Liao, J., and Welti, A.: Secondary organic aerosol (SOA) yields from NO_3 radical + isoprene based on nighttime aircraft power plant plume transects, Atmos. Chem. Phys., 18, 11663–11682, https://doi.org/10.5194/acp-18-11663-2018, 2018.

Guenther, A. B., Jiang, X., Heald, C. L., Sakulyanontvittaya, T., Duhl, T., Emmons, L. K., and Wang, X.: The Model of Emissions of Gases and Aerosols from Nature version 2.1 (MEGAN2.1): an extended and updated framework for modeling biogenic emissions, Geosci. Model Dev., 5, 1471–1492, https://doi.org/10.5194/gmd-5-1471-2012, 2012.

Hamilton, J. F., Bryant, D. J., Edwards, P. M., Ouyang, B., Bannan, T. J., Mehra, A., Mayhew, A. W., Hopkins, J. R., Dunmore, R. E., Squires, F. A., Lee, J. D., Newland, M. J., Worrall, S. D., Bacak, A., Coe, H., Percival, C., Whalley, L. K., Heard, D. E., Slater, E. J., Jones, R. L., Cui, T. Q., Surratt, J. D., Reeves, C. E., Mills, G. P., Grimmond, S., Sun, Y. L., Xu, W. Q., Shi, Z. B., and Rickard, A. R.: Key Role of NO_3 Radicals in the Production of Isoprene Nitrates and Nitrooxyorganosulfates in Beijing, Environ. Sci. Technol., 55, 842–853, https://doi.org/10.1021/acs.est.0c05689, 2021.

Hanisch, F. and Crowley, J. N.: Ozone decomposition on Saharan dust: an experimental investigation, Atmos. Chem. Phys., 3, 119–130, https://doi.org/10.5194/acp-3-119-2003, 2003a.

Hanisch, F. and Crowley, J. N.: Heterogeneous reactivity of NO and HNO_3 on mineral dust in the presence of ozone, Phys. Chem. Chem. Phys., 5, 883–887, https://doi.org/10.1039/B211503D, 2003b.

Hao, C. S., Shepson, P. B., Drummond, J. W., and Muthuramu, K.: Gas-chromatographic detector for selective and sensitive detection of atmospheric organic nitrates, Anal. Chem., 66, 3737–3743, https://doi.org/10.1021/ac00093a032, 1994.

Herron, J. T. and Huie, R. E.: Rate Constants for the Reactions of Atomic Oxygen (O^3P) with Organic Compounds in the Gas Phase, J. Phys. Chem. Ref. Data, 2, 467–518, https://doi.org/10.1063/1.3253125, 1973.

Hjorth, J., Lohse, C., Nielsen, C. J., Skov, H., and Restelli, G.: Products and Mechanisms of the Gas-Phase Reactions between NO_3 and a Series of Alkenes, J. Phys. Chem., 94, 7494–7500, https://doi.org/10.1021/j100382a035, 1990.

Horowitz, L. W., Fiore, A. M., Milly, G. P., Cohen, R. C., Perring, A., Wooldridge, P. J., Hess, P. G., Emmons, L. K., and Lamarque, J.-F.: Observational constraints on the chemistry of isoprene nitrates over the eastern United States, J. Geophys. Res., 112, D12S08, https://doi.org/10.1029/2006JD007747, 2007.

IUPAC: Task Group on Atmospheric Chemical Kinetic Data Evaluation, edited by: Ammann, M., Cox, R. A., Crowley, J. N., Herrmann, H., Jenkin, M. E., McNeill, V. F., Mellouki, A., Rossi, M. J., Troe, J., and Wallington, T. J., available at: http://iupac.pole-ether.fr/index.html, last access: 23 April 2021.

Jenkin, M. E., Young, J. C., and Rickard, A. R.: The MCM v3.3.1 degradation scheme for isoprene, Atmos. Chem. Phys., 15, 11433–11459, https://doi.org/10.5194/acp-15-11433-2015, 2015.

Keehan, N. I., Brownwood, B., Marsavin, A., Day, D. A., and Fry, J. L.: A thermal-dissociation–cavity ring-down spectrometer (TD-CRDS) for the detection of organic nitrates in gas and particle phases, Atmos. Meas. Tech., 13, 6255–6269, https://doi.org/10.5194/amt-13-6255-2020, 2020.

Kirchner, F., Mayer-Figge, A., Zabel, F., and Becker, K. H.: Thermal stability of peroxynitrates, Int. J. Chem. Kinet., 31, 127–144, https://doi.org/10.1002/(SICI)1097-4601(1999)31:2<127::AID-KIN6>3.0.CO;2-L, 1999.

Kwan, A. J., Chan, A. W. H., Ng, N. L., Kjaergaard, H. G., Seinfeld, J. H., and Wennberg, P. O.: Peroxy radical chemistry and OH radical production during the NO_3-initiated oxidation of isoprene, Atmos. Chem. Phys., 12, 7499–7515, https://doi.org/10.5194/acp-12-7499-2012, 2012.

Kwok, E. S. C., Aschmann, S. M., Arey, J., and Atkinson, R.: Product formation from the reaction of the NO_3 radical with isoprene and rate constants for the reactions of methacrolein and methyl vinyl ketone with the NO_3 radical, Int. J. Chem. Kinet., 28, 925–934, https://doi.org/10.1002/(SICI)1097-4601(1996)28:12<925::AID-KIN10>3.0.CO;2-B, 1996.

Lelieveld, J., Evans, J. S., Fnais, M., Giannadaki, D., and Pozzer, A.: The contribution of outdoor air pollution sources to premature mortality on a global scale, Nature, 525, 367–371, https://doi.org/10.1038/nature15371, 2015.

Leonori, F., Balucani, N., Nevrly, V., Bergeat, A., Falcinelli, S., Vanuzzo, G., Casavecchia, P., and Cavallotti, C.: Experimental and Theoretical Studies on the Dynamics of the $O(^3P)$ + Propene Reaction: Primary Products, Branching Ratios, and Role of Intersystem Crossing, J. Phys. Chem. C, 119, 14632–14652, https://doi.org/10.1021/jp512670y, 2015.

Liebmann, J. M., Schuster, G., Schuladen, J. B., Sobanski, N., Lelieveld, J., and Crowley, J. N.: Measurement of ambient NO_3 reactivity: design, characterization and first deployment of a new instrument, Atmos. Meas. Tech., 10, 1241–1258, https://doi.org/10.5194/amt-10-1241-2017, 2017.

Malkin, T. L., Goddard, A., Heard, D. E., and Seakins, P. W.: Measurements of OH and HO_2 yields from the gas phase ozonolysis of isoprene, Atmos. Chem. Phys., 10, 1441–1459, https://doi.org/10.5194/acp-10-1441-2010, 2010.

Mellouki, A., Ammann, M., Cox, R. A., Crowley, J. N., Herrmann, H., Jenkin, M. E., McNeill, V. F., Troe, J., and Wallington, T. J.: Evaluated kinetic and photochemical data for atmospheric chemistry: volume VIII – gas-phase reactions of organic species with four, or more, carbon atoms ($\geq C_4$), Atmos. Chem. Phys., 21, 4797–4808, https://doi.org/10.5194/acp-21-4797-2021, 2021.

Møller, K. H., Bates, K. H., and Kjaergaard, H. G.: The Importance of Peroxy Radical Hydrogen-Shift Reactions in Atmospheric Isoprene Oxidation, J. Phys. Chem. A, 123, 920–932, https://doi.org/10.1021/acs.jpca.8b10432, 2019.

Morin, J. and Bedjanian, Y.: Thermal decomposition of n-propyl and n-butyl nitrates: Kinetics and products, J. Anal. Appl. Pyrolysis, 124, 576–583, https://doi.org/10.1016/j.jaap.2017.01.014, 2017.

Ng, N. L., Kwan, A. J., Surratt, J. D., Chan, A. W. H., Chhabra, P. S., Sorooshian, A., Pye, H. O. T., Crounse, J. D., Wennberg, P. O., Flagan, R. C., and Seinfeld, J. H.: Secondary organic aerosol (SOA) formation from reaction of isoprene with nitrate radicals (NO_3), Atmos. Chem. Phys., 8, 4117–4140, https://doi.org/10.5194/acp-8-4117-2008, 2008.

Ng, N. L., Brown, S. S., Archibald, A. T., Atlas, E., Cohen, R. C., Crowley, J. N., Day, D. A., Donahue, N. M., Fry, J. L., Fuchs, H., Griffin, R. J., Guzman, M. I., Herrmann, H., Hodzic, A., Iinuma, Y., Jimenez, J. L., Kiendler-Scharr, A., Lee, B. H., Luecken, D. J., Mao, J., McLaren, R., Mutzel, A., Osthoff, H. D., Ouyang, B., Picquet-Varrault, B., Platt, U., Pye, H. O. T., Rudich, Y., Schwantes, R. H., Shiraiwa, M., Stutz, J., Thornton, J. A., Tilgner, A., Williams, B. J., and Zaveri, R. A.: Nitrate radicals and biogenic volatile organic compounds: oxidation, mechanisms, and organic aerosol, Atmos. Chem. Phys., 17, 2103–2162, https://doi.org/10.5194/acp-17-2103-2017, 2017.

Nguyen, T. B., Tyndall, G. S., Crounse, J. D., Teng, A. P., Bates, K. H., Schwantes, R. H., Coggon, M. M., Zhang, L., Feiner, P., Milller, D. O., Skog, K. M., Rivera-Rios, J. C., Dorris, M., Olson, K. F., Koss, A., Wild, R. J., Brown, S. S., Goldstein, A. H., de Gouw, J. A., Brune, W. H., Keutsch, F. N., Seinfeldcj, J. H., and Wennberg, P. O.: Atmospheric fates of Criegee intermediates in the ozonolysis of isoprene, Phys. Chem. Chem. Phys., 18, 10241–10254, https://doi.org/10.1039/c6cp00053c, 2016.

Orphal, J., Fellows, C. E., and Flaud, P. M.: The visible absorption spectrum of NO_3 measured by high-resolution Fourier transform spectroscopy, J. Geophys. Res.-Atmos., 108, 4077, https://doi.org/10.1029/2002JD002489, 2003.

Paul, D., Furgeson, A., and Osthoff, H. D.: Measurements of total peroxy and alkyl nitrate abundances in laboratory-generated gas samples by thermal dissociation cavity ring-down spectroscopy, Rev. Sci. Instrum., 80, 114101, https://doi.org/10.1063/1.3258204, 2009.

Paulson, S. E., Orlando, J. J., Tyndall, G. S., and Calvert, J. G.: Rate Coefficients for the Reactions of $O(^3P)$ with Selected Biogenic Hydrocarbons, Int. J. Chem. Kinet., 27, 997–1008, https://doi.org/10.1002/kin.550271005, 1995.

Perring, A. E., Wisthaler, A., Graus, M., Wooldridge, P. J., Lockwood, A. L., Mielke, L. H., Shepson, P. B., Hansel, A., and Cohen, R. C.: A product study of the isoprene + NO_3 reaction, Atmos. Chem. Phys., 9, 4945–4956, https://doi.org/10.5194/acp-9-4945-2009, 2009.

Peukert, S. L., Sivaramakrishnan, R., and Michael, J. V.: High temperature shock tube studies on the thermal decomposition of O_3 and the reaction of dimethyl carbonate with O-Atoms, J. Phys. Chem. A, 117, 3729–3738, https://doi.org/10.1021/jp400613p, 2013.

Phillips, G. J., Pouvesle, N., Thieser, J., Schuster, G., Axinte, R., Fischer, H., Williams, J., Lelieveld, J., and Crowley, J. N.: Peroxyacetyl nitrate (PAN) and peroxyacetic acid (PAA) measurements by iodide chemical ionisation mass spectrometry: first analysis of results in the boreal forest and implications for the measurement of PAN fluxes, Atmos. Chem. Phys., 13, 1129–1139, https://doi.org/10.5194/acp-13-1129-2013, 2013.

Pitts, J. N., Sanhueza, E., Atkinson, R., Carter, W. P. L., Winer, A. M., Harris, G. W., and Plum, C. N.: An investigation of the dark formation of nitrous acid in environmental chambers, Int. J. Chem. Kinet., 16, 919–939, https://doi.org/10.1002/kin.550160712, 1984.

Ray, D., Malongwe, J. K., and Klan, P.: Rate Acceleration of the Heterogeneous Reaction of Ozone with a Model Alkene at the Air-Ice Interface at Low Temperatures, Environ. Sci. Technol., 47, 6773–6780, https://doi.org/10.1021/es304812t, 2013.

Rivera-Rios, J. C., Nguyen, T. B., Crounse, J. D., Jud, W., St Clair, J. M., Mikoviny, T., Gilman, J. B., Lerner, B. M., Kaiser, J. B., de Gouw, J., Wisthaler, A., Hansel, A., Wennberg, P. O., Seinfeld, J. H., and Keutsch, F. N.: Conversion of hydroperoxides to carbonyls in field and laboratory instrumentation: Observational bias in diagnosing pristine versus anthropogenically controlled atmospheric chemistry, Geophys. Res. Lett., 41, 8645–8651, https://doi.org/10.1002/2014gl061919, 2014.

Rollins, A. W., Kiendler-Scharr, A., Fry, J. L., Brauers, T., Brown, S. S., Dorn, H.-P., Dubé, W. P., Fuchs, H., Mensah, A., Mentel, T.

F., Rohrer, F., Tillmann, R., Wegener, R., Wooldridge, P. J., and Cohen, R. C.: Isoprene oxidation by nitrate radical: alkyl nitrate and secondary organic aerosol yields, Atmos. Chem. Phys., 9, 6685–6703, https://doi.org/10.5194/acp-9-6685-2009, 2009.

Schwantes, R. H., Teng, A. P., Nguyen, T. B., Coggon, M. M., Crounse, J. D., St Clair, J. M., Zhang, X., Schilling, K. A., Seinfeld, J. H., and Wennberg, P. O.: Isoprene NO_3 Oxidation Products from the $RO_2 + HO_2$ Pathway, J. Phys. Chem. A, 119, 10158–10171, https://doi.org/10.1021/acs.jpca.5b06355, 2015.

Skov, H., Hjorth, J., Lohse, C., Jensen, N. R., and Restelli, G.: Products and mechanisms of the reactions of the nitrate (NO_3) with isoprene, 1,3-butadiene and 2,3-dimethyl-1,3-butadiene in air, Atmos. Environ. A, 26, 2771–2783, https://doi.org/10.1016/0960-1686(92)90015-d, 1992.

Sobanski, N., Schuladen, J., Schuster, G., Lelieveld, J., and Crowley, J. N.: A five-channel cavity ring-down spectrometer for the detection of NO_2, NO_3, N_2O_5, total peroxy nitrates and total alkyl nitrates, Atmos. Meas. Tech., 9, 5103–5118, https://doi.org/10.5194/amt-9-5103-2016, 2016.

Sobanski, N., Thieser, J., Schuladen, J., Sauvage, C., Song, W., Williams, J., Lelieveld, J., and Crowley, J. N.: Day and nighttime formation of organic nitrates at a forested mountain site in south-west Germany, Atmos. Chem. Phys., 17, 4115–4130, https://doi.org/10.5194/acp-17-4115-2017, 2017.

Stokes, G. Y., Buchbinder, A. M., Gibbs-Davis, J. M., Scheidt, K. A., and Geiger, F. M.: Heterogeneous Ozone Oxidation Reactions of 1-Pentene, Cyclopentene, Cyclohexene, and a Menthenol Derivative Studied by Sum Frequency Generation, J. Phys. Chem. A, 112, 11688–11698, https://doi.org/10.1021/jp803277s, 2008.

Thieser, J., Schuster, G., Schuladen, J., Phillips, G. J., Reiffs, A., Parchatka, U., Pöhler, D., Lelieveld, J., and Crowley, J. N.: A two-channel thermal dissociation cavity ring-down spectrometer for the detection of ambient NO_2, RO_2NO_2 and $RONO_2$, Atmos. Meas. Tech., 9, 553–576, https://doi.org/10.5194/amt-9-553-2016, 2016.

Thornton, J. A., Wooldridge, P. J., Cohen, R. C., Martinez, M., Harder, H., Brune, W. H., Williams, E. J., Roberts, J. M., Fehsenfeld, F. C., Hall, S. R., Shetter, R. E., Wert, B. P., and Fried, A.: Ozone production rates as a function of NO_x abundances and HO_x production rates in the Nashville urban plume, J. Geophys. Res.-Atmos., 107, ACH 7-1–ACH 7-17, https://doi.org/10.1029/2001JD000932, 2002.

Usher, C. R., Michel, A. E., and Grassian, V. H.: Reactions on Mineral Dust, Chem. Rev., 103, 4883–4940, https://doi.org/10.1021/cr020657y, 2003.

Vandaele, A. C., Hermans, C., Simon, P. C., Carleer, M., Colin, R., Fally, S., Merienne, M. F., Jenouvrier, A., and Coquart, B.: Measurements of the NO_2 absorption cross-section from $42\,000\,cm^{-1}$ to $10\,000\,cm^{-1}$ (238–1000 nm) at 220 K and 294 K, J. Quant. Spectrosc. Radiat. Transfer, 59, 171–184, https://doi.org/10.1016/S0022-4073(97)00168-4, 1998.

Vansco, M. F., Caravan, R. L., Zuraski, K., Winiberg, F. A. F., Au, K., Trongsiriwat, N., Walsh, P. J., Osborn, D. L., Percival, C. J., Khan, M. A. H., Shallcross, D. E., Taatjes, C. A., and Lester, M. I.: Experimental Evidence of Dioxole Unimolecular Decay Pathway for Isoprene-Derived Criegee Intermediates, J. Phys. Chem. A, 124, 3542–3554, https://doi.org/10.1021/acs.jpca.0c02138, 2020.

Vereecken, L., Carlsson, P. T. M., Novelli, A., Bernard, F., Brown, S. S., Cho, C., Crowley, J. N., Fuchs, H., Mellouki, W., Reimer, D., Shenolikar, J., Tillmann, R., Zhou, L., Kiendler-Scharr, A., and Wahner, A.: Theoretical and experimental study of peroxy and alkoxy radicals in the NO_3-initiated oxidation of isoprene, Phys. Chem. Chem. Phys., 23, 5496–5515, https://doi.org/10.1039/D0CP06267G, 2021.

Wayne, R. P., Barnes, I., Biggs, P., Burrows, J. P., Canosamas, C. E., Hjorth, J., Lebras, G., Moortgat, G. K., Perner, D., Poulet, G., Restelli, G., and Sidebottom, H.: The Nitrate Radical – Physics, Chemistry, and the Atmosphere, Atmos. Environ., 25, 1–203, https://doi.org/10.1016/0960-1686(91)90192-A, 1991.

Wennberg, P. O., Bates, K. H., Crounse, J. D., Dodson, L. G., McVay, R. C., Mertens, L. A., Nguyen, T. B., Praske, E., Schwantes, R. H., Smarte, M. D., St Clair, J. M., Teng, A. P., Zhang, X., and Seinfeld, J. H.: Gas-Phase Reactions of Isoprene and Its Major Oxidation Products, Chem. Rev., 118, 3337–3390, https://doi.org/10.1021/acs.chemrev.7b00439, 2018.

Wild, R. J., Edwards, P. M., Dube, W. P., Baumann, K., Edgerton, E. S., Quinn, P. K., Roberts, J. M., Rollins, A. W., Veres, P. R., Warneke, C., Williams, E. J., Yuan, B., and Brown, S. S.: A measurement of total reactive nitrogen, NOy, together with NO_2, NO, and O_3 via cavity ring-down spectroscopy, Environ. Sci. Technol., 48, 9609–9615, https://doi.org/10.1021/es501896w, 2014.

Wolfe, G. M., Thornton, J. A., McNeill, V. F., Jaffe, D. A., Reidmiller, D., Chand, D., Smith, J., Swartzendruber, P., Flocke, F., and Zheng, W.: Influence of trans-Pacific pollution transport on acyl peroxy nitrate abundances and speciation at Mount Bachelor Observatory during INTEX-B, Atmos. Chem. Phys., 7, 5309–5325, https://doi.org/10.5194/acp-7-5309-2007, 2007.

Wolfe, G. M., Marvin, M. R., Roberts, S. J., Travis, K. R., and Liao, J.: The Framework for 0-D Atmospheric Modeling (F0AM) v3.1, Geosci. Model Dev., 9, 3309–3319, https://doi.org/10.5194/gmd-9-3309-2016, 2016.

Wooldridge, P. J., Perring, A. E., Bertram, T. H., Flocke, F. M., Roberts, J. M., Singh, H. B., Huey, L. G., Thornton, J. A., Wolfe, G. M., Murphy, J. G., Fry, J. L., Rollins, A. W., LaFranchi, B. W., and Cohen, R. C.: Total Peroxy Nitrates (ΣPNs) in the atmosphere: the Thermal Dissociation-Laser Induced Fluorescence (TD-LIF) technique and comparisons to speciated PAN measurements, Atmos. Meas. Tech., 3, 593–607, https://doi.org/10.5194/amt-3-593-2010, 2010.

Wu, R., Vereecken, L., Tsiligiannis, E., Kang, S., Albrecht, S. R., Hantschke, L., Zhao, D., Novelli, A., Fuchs, H., Tillmann, R., Hohaus, T., Carlsson, P. T. M., Shenolikar, J., Bernard, F., Crowley, J. N., Fry, J. L., Brownwood, B., Thornton, J. A., Brown, S. S., Kiendler-Scharr, A., Wahner, A., Hallquist, M., and Mentel, T. F.: Molecular composition and volatility of multi-generation products formed from isoprene oxidation by nitrate radical, Atmos. Chem. Phys., 21, 10799–10824, https://doi.org/10.5194/acp-21-10799-2021, 2021.

Zhang, D., Lei, W. F., and Zhang, R. Y.: Mechanism of OH formation from ozonolysis of isoprene: kinetics and product yields, Chem. Phys. Lett., 358, 171–179, https://doi.org/10.1016/S0009-2614(02)00260-9, 2002.

CHAPTER 6

Measurements of NO_3 reactivity on the Kleiner Feldberg

The results presented in this study have been published as an open discussion in the peer-reviewed journal *Atmospheric Chemistry and Physics*. For that reason, the manuscript is reproduced on the subsequent pages and deals with the following:
The NO_3 reactivity setup was deployed during the TO2021 campaign which took place in July 2021 at the Taunus Observatory on top of the Kleiner Feldberg mountain (825 m above sea level). I compared the NO_3 reactivities to reactivities expected from actinic flux, VOC and NO measurements. Furthermore, I calculated fractional loss paths (reactions with VOCs, NO and photolysis) of NO_3 in the gas-phase in order to assess both dominant daytime and nighttime fate of the nitrate radical. With the help of drone-assisted measurements of vertical temperature profiles, I discuss the impact of boundary layer dynamics on NO_3 lifetimes. At nighttime, significant amounts of NO were present and plant physiological processes or microbial activity in soils are suspected to account for this. Calculations of steady-state NO_3 mixing ratios (as in Eq. 2.3), NO_3 production rates (as in Eq. 2.2) overall NO_3 loss rates enabled intercomparison of results from TO2021 with NO_3 measurements during previous campaigns on this site. During TO2021, NO_3 loss rates were higher, whereas NO_3 production rates were lower compared to the other campaigns between 2008 and 2015.

Author contribution
I performed measurements of NO_3 reactivity and of NO_2, did the presented analysis and model calculation, wrote the manuscript and, with the help of and others, revised it. Co-authors provided auxiliary measurements and commented on the manuscript. Please refer to the section "Author contribution" in the manuscript itself for details.

https://doi.org/10.5194/acp-2022-163
Preprint. Discussion started: 7 March 2022

Atmospheric Chemistry and Physics Discussions

Fate of the nitrate radical at the summit of a semi-rural mountain site in Germany assessed with direct reactivity measurements

Patrick Dewald, Clara M. Nussbaumer, Jan Schuladen, Akima Ringsdorf, Achim Edtbauer, Horst Fischer, Jonathan Williams, Jos Lelieveld and John N. Crowley

Atmospheric Chemistry Department, Max Planck Institut für Chemie, 55128 Mainz, Germany

Correspondence to: John N. Crowley (john.crowley@mpic.de)

Abstract. The reactivity of NO_3 plays an important role in modifying the fate of reactive nitrogen species at nighttime. High reactivity (e.g. towards unsaturated VOCs) can lead to formation of organic nitrates and secondary organic aerosol, whereas low reactivity opens the possibility of heterogeneous NO_X losses via formation and uptake of N_2O_5 to particles.

We present direct NO_3 reactivity measurements (k^{NO_3}) that quantify the VOC-induced losses of NO_3 during the TO2021 campaign at the summit of the Kleiner Feldberg mountain (825 m, Germany) in July 2021. k^{NO_3} was on average ~ 0.035 s^{-1} during the daytime, ~ 0.015 s^{-1} for almost half of the nights and below the detection limit of 0.006 s^{-1} for the other half, which may be linked to sampling from above the nocturnal surface layer. NO_3 reactivities derived from VOC measurements and the corresponding rate coefficient were in good agreement with k^{NO_3}, with monoterpenes representing 84 % of the total reactivity. The fractional contribution F of k^{NO_3} to the overall NO_3 loss rate (which includes additional reaction of NO_3 with NO and photolysis) were on average ~16 % during the daytime and ~50-60 % during the nighttime. The relatively low nighttime value of F is related to the presence of several tens of pptv of NO on several nights. NO_3 mixing ratios were not measured but steady-state calculations resulted in nighttime values between < 1 pptv and 12 pptv. A comparison of results from TO2021 with direct measurements of NO_3 during previous campaigns between 2008 and 2015 at this site revealed that NO_3 loss rates were remarkably high during TO2021, while NO_3 production rates were low.

We observed NO mixing ratios of up to 80 pptv at night which has implications for the cycling of reactive nitrogen at this site. With O_3 present at levels of mostly 25 to 60 ppbv, NO is oxidised to NO_2 on a time-scale of a few minutes. We find that to maintain NO mixing ratios of e.g. 40 pptv requires a ground-level NO emission rate of 0.33 pptv s^{-1} (into a shallow surface layer of 10 m depth). This in turn requires rapid deposition of NO_2 to the surface (vd_{NO2} ~ 0.15 cm s^{-1}) to reduce nocturnal NO_2 levels to match the observations.

1 Introduction

Nitric oxide (NO) and nitrogen dioxide (NO_2) are atmospheric pollutants, which exert a great impact on climate and air quality (Pozzer et al., 2012; Lelieveld et al., 2020). As NO_2 is the source of boundary layer ozone (O_3, which is phytotoxic and a cause

https://doi.org/10.5194/acp-2022-163
Preprint. Discussion started: 7 March 2022


Atmospheric Chemistry and Physics Discussions

of respiratory illness), understanding the processes that remove NO_x (= NO + NO_2) are of great importance (Crutzen and Lelieveld, 2001; Lelieveld et al., 2016; Edwards et al., 2017). The formation of long-lived or soluble organic nitrates during the oxidation of volatile organic compounds (VOCs) provides a mechanism to convert NO_X to NO_Z (where NO_z includes both organic and inorganic nitrates in the gas- and particle-phase), which may be transported away from the source region or removed via dry- or wet-deposition, respectively (Rollins et al., 2012; Present et al., 2020).

The major initiators of VOC oxidation are hydroxyl radicals (OH), ozone (O_3) and the nitrate radical (NO_3) (Ng et al., 2017; Wennberg et al., 2018) with OH reactions most important during the daytime (Lelieveld et al., 2008). The NO_3 radical is generally considered to be important only at nighttime (Brown and Stutz, 2012) although in some environments, it can also contribute substantially to the oxidation of unsaturated VOC during the day (Liebmann et al., 2018a; Liebmann et al., 2018b). NO_3 is formed almost exclusively in the sequential oxidation of NO by O_3 (R1 and R2). During daytime, NO_3 is lost via rapid photolysis (R5 and R6, with a lifetime of seconds) and an efficient reaction with NO (k_7 = 2.6 x 10^{-11} cm^3 $molecule^{-1}$ s^{-1} at 298 K) (IUPAC, 2022), which result in low mixing ratios (Wayne et al., 1991). NO_3 also reacts with NO_2 to form dinitrogen pentoxide (N_2O_5), which is in thermal equilibrium with NO_3 and NO_2 (R3, R4).

$NO + O_3 \rightarrow NO_2 + O_2$ (R1)

$NO_2 + O_3 \rightarrow NO_3 + O_2$ (R2)

$NO_3 + NO_2 + M \rightarrow N_2O_5 + M$ (R3)

$N_2O_5 + M \rightarrow NO_3 + NO_2 + M$ (R4)

$NO_3 + hv \rightarrow NO + O_2$ (R5)

$NO_3 + hv \rightarrow NO_2 + O$ (R6)

$NO_3 + NO \rightarrow 2NO_2$ (R7)

Reactions R1 - R4 can result in permanent loss of NO_x from the gas phase through deposition or uptake to particles of e.g. NO_3 or N_2O_5 (R8, R9) (Crowley et al., 2011; Phillips et al., 2016).

$N_2O_5 \rightarrow$ particle (or deposition) (R8)

$NO_3 \rightarrow$ particle (or deposition) (R9)

In forested regions during the night, NO_3 reacts predominantly with unsaturated volatile organic compounds (VOC) often of biogenic origin such as isoprene or monoterpenes, which results in the formation of alkyl nitrates ($RONO_2$) (R10) (Hallquist et al., 1999; Fry et al., 2014; Wu et al., 2021). Depending on the biogenic VOC involved, the $RONO_2$ formed may have low volatility and may deposit to surfaces or transfer to the particle phase to form secondary organic aerosols (SOA) (R11) (Place et al., 2022). The reaction between NO_3 and BVOC consequently represents a loss of NO_X from the gas-phase and thus has an impact on air quality via suppression of ozone formation and increases in SOA levels (Fry et al., 2011; Romer Present et al., 2020).

$NO_3 + VOC (+ O_2) \rightarrow\rightarrow RONO2$ (R10)

$RONO_2 \rightarrow$ deposition/SOA (R11)

https://doi.org/10.5194/acp-2022-163
Preprint. Discussion started: 7 March 2022


Atmospheric Chemistry and Physics Discussions

The nocturnal NO_3 lifetime close to the surface is generally short (typically in the range of minutes) owing to the build-up in concentration of reactive gases emitted from the biosphere into a shallow nocturnal boundary layer (Liebmann et al., 2018a; Liebmann et al., 2018b). Longer NO_3 lifetimes (sometimes exceeding 1 hour) have been derived from NO_3 measurements in very clean regions (Allan et al., 2000; Martinez et al., 2000), from measurements in the overlying residual layer using towers and aircraft platforms (Stutz et al, 2004; Brown et al., 2007a; Brown 2007b) and at mountain sites where the meteorological situation results in the measurement location being above the nocturnal surface layer (Carslaw et al., 1997; Brown et al., 2016; Sobanski et al., 2016).

The lifetime of NO_3 has often been derived using a stationary-state approximation, which relies on direct measurements of NO_3, NO_2 and O_3 (Heintz et al., 1996; Allan et al., 1999; Geyer et al., 2001; Brown et al., 2004; Brown et al., 2009; Stutz et al., 2010; Sobanski et al., 2016). This method is limited to periods when NO_3 mixing ratios are above the instrumental detection limit, which (depending on instrument performance) may restrict the method to periods when NO_3 production rates are high and NO_3 reactivities (i.e. the inverse of NO_3 lifetimes) are low. This is usually not the case during the daytime or even during the nighttime in areas with high BVOC emissions (Liebmann et al., 2018a). Direct NO_3 reactivity measurements not only extend the accessibility to daytime reactivities but also, together with measurements of NO, NO_3, photolysis rates (J_{NO_3}) and VOCs, enables the determination of the fate of the NO_3 radical throughout the diel cycle. Recent direct NO_3 reactivity measurements and model calculations (Liebmann et al., 2019; Foulds et al., 2021) suggest that NO_3 also contributes to daytime alkyl nitrate formation, which typically occurs through the OH-initiated oxidation of BVOC in the presence of NO (Wennberg et al., 2018). Quantifying the contribution of NO_3 + VOC reactions to the NO_3 reactivity is thus central in understanding the role of NO_3, in e.g. SOA formation and NO_X lifetimes.

In this study, the fate of the NO_3 radical on the semi-rural Kleiner Feldberg mountain (in the south-west of Germany) in July and August 2021 (TO2021 campaign) during both day- and nighttime is analysed by direct measurements of NO, photolysis rates (J_{NO_3}) and the first-order NO_3 loss-constant resulting from reaction with VOCs (k^{NO_3}). Measurements of VOCs that are reactive towards NO_3 enable us to calculate their fractional contribution to k^{NO_3}. With the help of NO_3, NO_2, NO and O_3 measurements we derive NO_3 loss-terms via the steady-state assumption (L_{NO_3}) for previous campaigns at this site to assess the impact of differing meteorological and chemical conditions.

2 The TO2021 campaign

The TO2021 campaign took place in July and August 2021 at the Taunus Observatory (TO) at the summit of the Kleiner Feldberg mountain (825 m above sea level). A detailed description of the location has been given elsewhere (Crowley et al., 2010) and only a brief summary is given here. The Kleiner Feldberg is mostly surrounded by coniferous forest, but an area at the summit (~ 100 m^2) is cleared of trees and hosts the meteorological measurements of the German Meteorological Service (Deutscher Wetterdienst, DWD) and permanent measurement containers of the University of Frankfurt and the Hessian Agency for Nature Conservation, Environment and Geology (Hessisches Landesamt für Naturschutz, Umwelt und Geologie,

https://doi.org/10.5194/acp-2022-163
Preprint. Discussion started: 7 March 2022


Atmospheric Chemistry and Physics Discussions

HLNUG). The summit itself is covered with bushes and, especially to the north, with blueberry shrubs. The mountain tops of Altkönig (798 m a.s.l.) and Großer Feldberg (878 m a.s.l.) are in the direct vicinity (< 3 km). Air arriving from the south-west and south-east is impacted by anthropogenic emissions from the densely populated cities of Frankfurt, Wiesbaden and Mainz (20-30 km), whereas air from the north-west, north and north-east is cleaner, with no major cities for 50-70 km.

2.1 Instrumentation

For the duration of the TO2021 campaign, two (stacked) containers including the instruments operated by the Max-Planck-Institute for Chemistry (MPIC) were set up on the site. If not stated otherwise, the instruments sampled from a high-volume-flow stainless-steel tube (10 $m^3 min^{-1}$, 0.2 s residence time) sucking air from ca. 10 m above the ground. Each instrument with measurements used in the analysis is described below.

2.1.1 NO_3 reactivity

The Flow-Tube Cavity Ring Down Spectrometer (FT-CRDS) setup used to quantify VOC-induced NO_3 reactivity (Liebmann et al., 2017) consists of a Teflon coated (FEPD 121, Chemours) glass flow-tube reactor, in which a flow of ambient air is mixed with 30-60 parts per trillion per volume (pptv) of synthetically generated NO_3.

NO_3 is generated by the sequential oxidation of NO and NO_2 (3.5 sccm of 1 parts per million per volume (ppmv) in N_2, Air Liquide) by O_3 (generated by passing synthetic air over a Hg lamp) in an upstream Teflon-coated glass reactor (thermostated to 30°C at a pressure of 1.3 bar) in 400 standard (STP) cubic centimetre per minute (sccm) synthetic air. The flow exiting the NO_3 source is passed through ca. 15 cm ¼ inch (in.) outer diameter (OD) PFA tubing that is heated to 140°C so that N_2O_5 is quantitatively decomposed to NO_3 and NO_2 (R4). The flow from the NO_3 source is then mixed with either 2800 sccm synthetic or ambient air and passed through the flow-tube reactor where it resides for time *t*. The synthetic air used to measure zero reactivities was provided by a commercial zero-air generator (CAP 120, Fuhr GmbH) and humidified to ambient level with a permeation tube (PermaPure, MH-070-24F-4) immersed in deionized water. The ambient air was sampled from the high-flow inlet through ¼ in. (OD) PFA tubing equipped with a Teflon membrane filter (2 µm pore, 47 mm diameter, Pall Corp.).

NO_3 surviving the flow-tube was detected by CRDS at 662 nm. The ring-down time in the absence of NO_3 was determined every ca. 5 min by adding an excess of NO (3 sccm of 100 ppmv in N_2). NO_3 reactivities are deduced from the relative change in NO_3 mixing ratio in ambient air compared to synthetic air. Dynamic dilution of the ambient air with synthetic air was used to keep the NO_3 reactivity in a measureable range when sampling highly reactive air masses.

Since the NO_3 mixing ratio is affected by reactions R1-R4, R7 and R9 in addition to the reaction of interest (R10), a numerical simulation procedure that corrects for the impact of NO and NO_2 is necessary to extract the NO_3 reactivity towards VOCs (k^{NO_3}). The validity of this correction procedure was checked by adding a known amount of NO (1-6 sccm of 245 parts per billion per volume (ppbv) NO in N_2, Air Liquide) every two hours during the zeroing periods throughout the campaign. As shown in Fig. S1a of the Supplement, the model was able to reproduce the observed NO_3 mixing ratios reliably. A further calibration sequence during the campaign, in which five different amounts of NO were added, is displayed in Fig. S1b. The

https://doi.org/10.5194/acp-2022-163
Preprint. Discussion started: 7 March 2022


Atmospheric Chemistry and Physics Discussions

flow-tube predominantly used during TO2021 features a residence time of t = 9.5 s and an NO_3 wall loss rate of 0.001 s^{-1}. The limit of detection (LOD) is mainly defined by the stability of the NO_3 source and baseline, which were improved by thermostating both the NO_3 source and the flowtube and insulating the cavity from thermal gradients in the container so that a signal-stabilty related uncertainty of 16% was achieved. For the numerical simulation procedure, ambient O_3, NO and NO_2 mixing ratios and rate coefficients for (R1-R4, R7) were deployed. Liebmann et al. (2017) showed with the help of Monte Carlo simulations that the uncertainty associated with this simulation is dependent on the ratio between ambient NO_2 and k^{NO_3}. Assuming a typical daytime situation for TO2021 (k^{NO_3} ~ 0.04 s^{-1}, [NO_2] = 2 ppbv NO_2) the numerical simulation introduces an uncertainty of 15 %, resulting in an overall uncertainty of 22 %. However, if for example k^{NO_3} is 0.006 s^{-1} in the presence of 1 ppbv NO_2 (as occasionally detected during the nighttime), the uncertainty caused by the simulation increases to ca. 50 %. During TO2021, the instrument's LOD was 0.006 s^{-1} for this flowtube.

Between the 23rd and 25th July, a larger flow-tube was tested with the intention of extending the LOD to lower reactivities. The residence time (20 s during the day or 32 s during the night according to position of a moveable injector) and wall loss rates were characterised during the campaign as detailed by Liebmann et al. (2017). The factor ~3 longer residence time at night compared to the smaller flow-tube should have extended the LOD to 0.003 s^{-1}. However, the larger flow-tube suffered from a larger NO_3 wall loss rate (> 0.04 s^{-1}), which effectively worsened the LOD. For this reason, the deployment of this flowtube was stopped after two days.

During the nighttime, before being mixed with synthetic NO_3, the air was sampled through a 2 L uncoated glass flask (40 s residence time) that was heated to 35°C. This ensures that ambient NO_3 and N_2O_5 does not reach the flow tube to bias the measurement. The NO mixing ratios that were used in the numerical simulations were corrected (typically by a factor of 0.6) for the reaction with ambient O_3 during residence in the flask.

2.1.2 NO_2 , NO, O_3 and actinic flux

Owing to the importance of co-located NO_2 measurements for interpretation of the k^{NO_3} data, the FT-CRDS set up has a second inlet and cavity to measure NO_2 (Liebmann et al., 2018b) with a total measurement uncertainty (defined by noise and baseline stability) of 8 % and a LOD of 168 pptv (4 s). A further CRDS-based measurement of NO_2 was made using a thermal-dissociation cavity ring-down spectrometer (TD-CRDS) (Friedrich et al., 2020) for measurement of NO_X and NO_Y. At nighttime, when NO was generally < 80 pptv, the NO_X channel of this instrument essentially measures NO_2. The inlet of the NO_X / NO_Y instrument was located on the container roof, ~ 2 m to the north and 2 m lower than the top of the high-flow inlet. In addition, NO_2 was measured with a chemiluminescence (CLD) setup (ECO Physics, CLD 790 SR) equipped with a photolytic converter to convert NO_2 to NO (Tadic et al., 2020; Nussbaumer et al., 2021). This instrument also provided the campaign NO data-set. Calibration (using a dynamically diluted, secondary 5 ppm NO standard) was carried out every 2 hours. The LODs for NO and NO_2 were 7 and 10 pptv, respectively, the total measurement uncertainties were 9 and 19 % for NO and NO_2.

https://doi.org/10.5194/acp-2022-163
Preprint. Discussion started: 7 March 2022

The three sets of NO_2 measurements are compared in the Supplement (Fig. S2). A bivariate linear regression (York, 1966) of the data sets yields offsets below the LOD of the FT-CRDS NO_2 cavity in both cases. An excellent agreement with the TD-CRDS measurement is observed (slope of 0.99), while a fair agreement (slope of 1.09) within associated uncertainties is achieved for the intercomparison with the CLD measurement. O_3 was measured via UV absorption with two identical, commercial ozone monitors (2B technologies, model 205) that were cross-calibrated after the campaign. The instrument background was estimated ca. every two days with synthetic air from the zero-air generator. The uncertainty associated with this measurement is 5 % and the LOD is 2 ppbv.

Actinic flux measurements were made by a spectral radiometer (Metcon GmbH) installed on top of the upper container and converted to photolysis frequencies for NO_3 (J^{NO_3}) using evaluated absorption cross sections and quantum yields (Burkholder et al., 2016) with an overall uncertainty of ca. 15 % (Friedrich et al., 2021).

2.1.3 VOC measurements

VOCs were measured from the 15th to 31st July with a proton-transfer-reaction time-of-flight mass-spectrometer (PTR8000, IONICON Analytik GmbH) (Jordan et al., 2009; Bekö et al., 2020) with a time resolution of 20 s, operated with hydronium ions (H_3O^+) at a pressure of 2.2 mbar and an E/N of 137 Td. Mixing ratios of isoprene, monoterpenes and sesquiterpenes are derived from calibrating to a gas standard containing isoprene, α-pinene and β-caryophyllene (Apel-Riemer Environmental Inc., Colorado, USA). The limit of detection lies in the range of tens of ppt and the uncertainty is defined to be below 20 %.

A second PTR-ToF-MS (VOCUS, Tofwerk AG) provided uncalibrated VOC data for the period between 20th July and 6th August (Krechmer et al., 2018). In order to extend data availability, the VOCUS data for isoprene, monoterpenes and sesquiterpenes were scaled to that of the PTR8000 data set during the common time period.

Both PTR-ToF-MS were located in a permanent container of the TO, ca. 8 m distant from the MPIC container. Air was sampled from the roof of the container (ca. 8 m) through a heated inlet line equipped with a polytetrafluoroethylene (PTFE) filter.

2.1.4 Temperature and relative humidity profiles

Deployment of a drone (EVO-X12, multikopter.de) equipped with a commercial gas sensor (BME680, Bosch Sensortech GmbH) enabled the measurement of vertical profiles of pressure, temperature and relative humidity (time resolution of 1 s) to a height of 100 m AGL.

3 Results and Discussion

An overview of the key meteorological and trace-gas measurements used in the analysis for the TO2021 campaign period from July to August 2021 is given in Fig. 1. Grey shaded areas mark the nighttime periods; sunrise during the measurement period was at ~ 03:30 and sunset at ~ 19:30 UTC. k^{NO_3} shows a distinct daytime to nighttime variability and generally follows the

https://doi.org/10.5194/acp-2022-163
Preprint. Discussion started: 7 March 2022


Atmospheric Chemistry and Physics Discussions

summed mixing ratio of monoterpenes (ΣMTs) which were present at maximum mixing ratios (during the day) of typically between 150 and 400 pptv.

Wind speeds were predominantly between 2 and 4 m s^{-1} with most wind-sectors represented, although wind from the east and south-east originating from the Frankfurt area (SE) were rarely encountered. The local wind-directions and speeds during TO2021 are displayed as a wind rose in Fig. S3a in the Supplement.

There were several periods of rain and fog during TO2021, which is reflected by high relative humidities (RH) mostly between 75 and 100 % at moderate temperatures between 12 and 20°C. Ozone mixing ratios varied between 20 and 60 ppbv. The CLD setup observed NO mixing ratios close to (10 to 20 pptv) or below the LOD of 7 pptv on ca. half of the nights, but also returned values of between 20 to 80 pptv for prolonged periods on some nights. Daytime NO mixing ratios were between 0.5 ppbv and 2 ppbv, with maximum values around midday. Spikes in NO mixing ratios caused by vehicles at the site were removed from the dataset. NO_2 mixing ratios (as measured with the FT-CRDS setup) were generally between 1 and 2 ppbv, with occasional values of up to 6 ppbv. Photolysis rates of NO_3 (J_{NO_3}) of ca. 0.15 s^{-1} were detected at noon. The data-gap between the 3rd and 5th July was caused by a power-failure.

3.1 NO_3 reactivity

As is evident from Fig. 1, k^{NO_3} followed the trend in monoterpene mixing ratios and was generally higher during the daytime compared to the night. As illustrated in a wind rose in the Supplement (Fig. S3b), k^{NO_3} displayed no clear dependence on wind directions. A closer examination of the data reveals that the nights can be roughly divided into two types: On 15 of the 34 nights, NO_3 reactivities remained well above the instrument's LOD of 0.006 s^{-1} (from now on defined as "Type-1" nights), whereas during 14 nights k^{NO_3} was predominantly lower than 0.006 s^{-1} ("Type-2"). The other 5 nights showed a transitional behaviour between those two types.

An example of a Type-1 night is shown in Fig. 2a. Following a late evening value of k^{NO_3} ~ 0.1 s^{-1} the NO_3 reactivity decreased during darkness from 0.08 s^{-1} at 20:00 UTC to 0.02 s^{-1} at 03:00 UTC. During this period, northerly winds with speeds around 4 m s^{-1} prevailed and the decrease in reactivity cannot be related to a change in air-mass origin. At the same time, we observed a decrease in temperature (~17 to ~13 °C) that was accompanied by an increase in the relative humidity (78 to 98%) and a quasi-continuous reduction in O_3 mixing ratios from ~35 to ~25 ppbv. Note that ca. 20-30 pptv of NO were detected during this night, implying that reaction R7 would represent a significant loss process for NO_3. A detailed discussion of this aspect follows in section 3.4.

Figure 2b shows an example of a Type-2 night with a sharp decrease of k^{NO_3} from ~ 0.02 s^{-1} just before sunset to below the LOD (0.006 s^{-1}) within the first hour after sunset. As for Type-1, there is no significant change in the wind direction. However, in contrast to the Type-1 example, after a slight increase just after sunset, O_3 was roughly constant and significantly higher throughout the night with NO below the detection limit during the entire night. In addition the temperature (14 ± 1 °C) and relative humidity (70 ± 5 %) were roughly constant, the latter significantly lower than for the Type-1 example.

https://doi.org/10.5194/acp-2022-163
Preprint. Discussion started: 7 March 2022


Atmospheric Chemistry and Physics Discussions

Low NO_3 reactivities at nighttime (i.e. Type-2 nights) can result from low rate of emission of biogenic VOCs (e.g. owing to low temperatures) but can also be associated with strong vertical gradients, which effectively decouple ground level emissions from the air above. For the latter case, we are dealing with a shallow surface layer with its top below the inlet, so that air is sampled from the nocturnal boundary or residual layer (Brown and Stutz, 2012) in which the NO_3 lifetimes can be very long. This phenomenon has been reported for this and other mountain sites (Carslaw et al., 1997; Brown et al., 2016; Sobanski et al., 2016; Liebmann et al., 2017; Liebmann et al., 2018b). Slow exchange between the surface layer and the residual layer can result in strong gradients in trace gases such as O_3, which undergoes dry-deposition in the surface layer but is long-lived in e.g. the residual layer. The situation for NO_2 is more complex as it may be formed from the O_3-induced oxidation of near-surface emissions of NO and also lost via (slow) reaction with O_3 and dry-deposition (Brown et al., 2003b; Stutz et al., 2004; Brown et al., 2007a).

Figure 3 displays the campaign-averaged diel cycles of k^{NO_3} (along with O_3, RH, T, NO and MTs) classified according to Type-1 or Type-2 nights. k^{NO_3} was on average around 0.015 s^{-1}, during Type-1 nights, with a daytime reactivity of 0.04 s^{-1} (Fig. 3a). The observed orders of magnitude for k^{NO_3} are consistent with the directly measured nighttime NO_3 reactivities ranging between < 0.005 and up to 0.06 s^{-1} during three nights in July 2015 (NOTOMO campaign) with the same instrument (Liebmann et al., 2017).

By definition, the median nighttime reactivity for Type-2 nights is at the instrument's LOD, while the median daytime reactivities prior to Type-2 nights are very similar to those observed prior to Type-1 nights. The median diel cycles for O_3 (Fig. 3b) differ significantly for the two types: during Type-1 nights O_3 decreases continuously (consistent with previous observations on this site (Handisides, 2001)), while during Type-2 nights, O_3 mixing ratios remain fairly constant and higher. There are also significant differences in the median NO mixing ratio, with nighttime values (Fig. 3f) mostly below or close (10-12 pptv) to the LOD during Type-2 nights and values of 30-40 pptv during Type-1 nights.

The lower nighttime k^{NO_3} values observed during Type-2 nights compared Type-1 nights is accompanied by lower (factor ~2.5) monoterpene mixing ratios (Fig. 3c). The median temperature during Type-2 nights are only up to 1 K colder than compared to Type-1 nights (Fig. 3d), which, based on the expression ($E_{MT} \propto \exp(\beta(T - 297K))$ with β = 0.1 K^{-1}, (Guenther et al., 1993)) results in a change of only 10% and is thus insufficient to explain the differences observed in ΣMT on these nights.

With values of 85-95 %, the median relative humidity (Fig. 3e) was higher by around 5 % (and increased continuously) during Type-1 nights, than for Type 2, for which a much smaller increase from 82 to 87 % was observed.

In summary, in addition to very low NO_3 reactivity, Type-2 nights are characterized by (1) larger and constant O_3 mixing ratios, (2) lower but constant RH, and (3) low concentrations of reactive trace gases like NO and monoterpenes. These observations support the presence of a very shallow surface layer with its top located below the tip of the inlet and decoupling of the sampled air from ground-level emissions (i.e. of NO and VOCs). Previous observations of strong gradients in NO_3 mixing ratios and low reactivities have showed that decoupling of the air-mass from ground-level emissions can lead to NO_3 lifetimes of up to hours (Allan et al., 2002; Brown et al., 2016; Sobanski et al., 2016). In order to test the hypothesis that low

https://doi.org/10.5194/acp-2022-163
Preprint. Discussion started: 7 March 2022


Atmospheric Chemistry and Physics Discussions

NO_3 reactivities observed during Type-2 nights are the result of sampling from the nocturnal boundary layer (NBL), we mounted temperature and relative humidity sensors on a multi-copter drone to measure gradients in these parameters on the night of 22-23rd July, which is the same night as depicted in Fig. 2b.

The drone was located ~ 20 m to the NE of the inlet, the starting height (ground level) was about 12 m lower than the top of the inlet. The drone flew a vertical profile with the first ascent/descent started before sunset at 18:30 UTC (blue dotted line, F1 in Fig. 2b) and a second after sunset at 20:20 UTC (red dotted line, F2 in Fig 2b). The flights were restricted to heights of ~ 100 m above ground level owing to operational restrictions in the vicinity of Frankfurt airport.

The gradients in potential temperature θ, for the two flights are shown in Fig. 4a. At 18:30 UTC (blue curve), the potential temperature increases gradually with altitude (positive stratification) as expected for a well-mixed boundary layer (Stull, 1988; Brown et al., 2007b). In contrast, the potential temperature gradient measured at 20:20 UTC reveals a strong increase in the first 3 m, which represents the nocturnal surface layer. Above this, the potential temperature increases more slowly until ca. 20 m above the ground. This zone (shaded in red) represents the stable NBL above which the potential temperature is almost independent of height (neutral stratification), which is the typical behaviour of the residual layer (Stull, 1988; Brown et al., 2007b). The gradient in relative humidity (Fig. 4b) after sunset indicates a similar vertical structure with the top of the NBL characterized by a minimum in the relative humidity (Brown 2007b), also explaining why RH was, on average, lower during Type-2 compared to Type-1 nights (Fig. 3e). The approximate height of our inlet was situated ca. 10 m above the ground and the profile of θ implies that the air we sampled was from a NBL decoupled from ground-level emissions and in which vertical mixing is weak (Brown and Stutz, 2012). Under this scenario, NO originating from soil emissions and VOCs from plant emissions are trapped in the surface layer and only inefficiently entrained into the NBL. Unfortunately, owing to delays in obtaining permission to fly the drone, unfavourable weather conditions and other logistical considerations, these two flights on this one night are the only ones in which vertical profiles of temperature and RH were obtained. None-the-less, these observations provide important clues to how the meteorological situation can influence NO_3 reactivity and NO levels at inlet height.

3.3 Contribution of VOCs to k^{NO_3}

As described above, k^{NO_3} includes the contribution of VOCs only and it is thus expected to correlate with the summed first-order loss rates, $\Sigma k_i[VOC]_i$ derived from the concentration $[VOC]_i$ of each VOC and the corresponding rate constant (k_i) for its reaction with NO_3, provided that all VOCs with a significant contribution were measured.

Unsaturated organic compounds (often of biogenic origin such as isoprene or terpenes) are generally the dominant reaction partners for NO_3 in forested environments (Ng et al., 2017). During TO2021, several hundreds of pptv of isoprene, monoterpenes and sesquiterpenes were detected during the second half of the campaign when VOC measurements became available (see Fig.1 and Fig.S4). Owing to their low rate coefficients (IUPAC, 2022), alkanes, aromatics and saturated, oxygenated species such as acetaldehyde, acetone and methanol were found to contribute negligibly to k^{NO_3}. Consequently,

https://doi.org/10.5194/acp-2022-163
Preprint. Discussion started: 7 March 2022

Atmospheric Chemistry and Physics Discussions

only isoprene and the sum of mono- and sesquiterpenes are relevant for analysis. GC-MS measurements from a previous summer campaign at this site (Sobanski et al., 2017) derived fractional contributions to ΣMT of 50.5%, 28.9% and 20.6% for α-pinene, limonene and myrcene, respectively. Using an accordingly weighted average of evaluated kinetic data (IUPAC, 2022), we derived an effective rate constant of k = 8.9 x 10^{-12} cm^3 $molecule^{-1}$ s^{-1} for NO_3 + monoterpenes reactions at this site. To calculate NO_3 loss rates resulting from its reaction with sesquiterpenes, we used the IUPAC-recommended rate coefficient for NO_3 + β-caryophyllene. Neglecting the uncertainty associated with the assumption that the MT mixture was the same in both campaigns and combining the uncertainty in the measured VOC mixing ratios (20 %) and in the effective rate coefficient (25 %) leads to an overall fractional uncertainty of 33 % in each term of $\Sigma k_i[VOC]_i$.

In Fig. 5a we present a time-series of k^{NO_3} and $k_i[VOC]_i$. Clearly, k^{NO_3} and $\Sigma k_i[VOC]_i$ agree within associated uncertainties most of the time. The poorer agreement observed around the 16th July may have been related to the presence of fog and droplets in the sampling line and that around the 24th July was most probably caused by conditioning effects when switching between flow-tubes. As indicated by the area in purple, the NO_3 reactivity was almost entirely determined by the reaction with monoterpenes. Figure 5b focusses on the Type-2 night previously shown in Fig. 2b (but all k^{NO_3} < LOD set to 0.006 s^{-1}) suspected to be impacted by a boundary layer effect. Within associated uncertainties, the VOC measurements confirm that VOC-induced NO_3 reactivities are close to or below 0.006 s^{-1} for this period. The average contribution of the VOCs to $\Sigma k_i[VOC]_i$ is depicted in Fig. 5c and shows that 84% of the overall reactivity is caused by monoterpenes, while isoprene and sesquiterpenes contribute 7% and 9% respectively.

Figure 6 plots $\Sigma k_i[VOC]_i$ versus k^{NO_3} for which a bivariate regression yields a slope of 1.04 ± 0.03 (2σ) and an intercept of (6.6 ± 0.4) × 10^{-3} s^{-1}. A slope close to unity suggests near closure for the NO_3 reactivity budget while the intercept is the equivalent to the reactivity caused for example by 27 pptv of β-caryophyllene or an overestimation of NO by just 18 pptv. We recall however, that speciated monoterpenes were not measured in TO2021 and the effective rate constant was based on the (non-testable) assumption that the summertime monoterpene composition at this site has remained unchanged over the last 10 years. The true uncertainty associated with the slope is expected to be close to 30%, suggesting that the very good agreement may be partially fortuitous. None-the-less, we can conclude that the vast majority of the reactivity measured directly results from NO_3 + monoterpene interactions.

3.4 Fractional contribution of VOCs to NO_3 losses throughout the diel cycle

The dominant, direct gas-phase loss of NO_3 occurs via photolysis (J_{NO_3}) reaction with NO (k_7[NO]) and reaction with VOCs (k^{NO_3}). Neglecting depositional losses of NO_3, the fractional contribution F of k^{NO_3} to the overall NO_3 loss rate constant, L_{NO_3}, is thus given by:

$$F = \frac{k^{NO_3}}{L_{NO_3}} = \frac{k^{NO_3}}{k^{NO_3} + J_{NO_3} + k_7[NO]} \quad \text{(Eq.2)}$$

https://doi.org/10.5194/acp-2022-163
Preprint. Discussion started: 7 March 2022

Atmospheric Chemistry and Physics Discussions

Based on measured k^{NO_3}, [NO] and J_{NO_3} (calculated from actinic flux measurements), we calculated time dependent values of each loss process throughout the campaign. The resulting mean diel cycle of *F* is depicted in Fig. 7.

During the daytime, photolysis and reaction with NO were the dominant loss processes for NO_3, as expected. The fractional contribution of VOC-induced losses is low at noon (~ 9 %) but increases to up to 30% in the afternoon. The NO_X levels at this site are such that, between sunrise and sunset, reaction with NO is on average (± 1σ) the dominant loss process for NO_3 (53 ± 20 %), followed by photolysis (31 ± 19 %) and reaction with VOCs (16 ± 15 %). This non-negligible contribution of VOCs to the daytime losses of NO_3 is in broad agreement with field measurements in a boreal forest in Finland and on top of the Hohenpeissenberg mountain, where values of ~20 % were reported (Liebmann et al., 2018a; Liebmann et al., 2018b). This underlines that NO_3, often considered to be important only at night, also contributes to the oxidation of BVOC during the day and thus potentially to the formation of organic nitrates (in competition to OH- and O_3-initiated oxidation) throughout the diel cycle for example (Liebmann et al., 2019; Foulds et al., 2021).

At nighttime, in the absence of actinic radiation (to convert NO_2 to NO) and local anthropogenic emissions, NO levels are generally suppressed by reaction with O_3. Fig. 7 reveals that 50-60 % of NO_3 was lost via reaction with VOCs at nighttime during TO2021, the remaining fraction reacting with NO (R7). The contribution of NO to the nighttime NO_3 reactivity is larger than previously observed with the k^{NO_3}-FT-CRDS instrument where reaction with VOCs was identified as the only significant loss process (Liebmann et al., 2018a; Liebmann et al., 2018b). A significant average contribution from NO is readily understood when one considers the large rate coefficient for reaction with NO_3 (k_7 = 1.8 x 10^{-11} cm^3 $molecule^{-1}$ s^{-1} at 298 K (IUPAC, 2022)) and NO mixing ratios well above the detection limit on many nights. Fig. 8 reveals a large night-to-night variability in the NO mixing ratio with minimum values close to the detection limit and maxima > 80 pptv. In the absence of local anthropogenic sources, soil emissions constitute the most likely source of NO at this site. Assuming that reaction with O_3 represents the only NO loss process, and that stationary state as in Eq. 3 is achieved (a valid assumption as the lifetime of NO is only a few minutes in the presence of 20-40 ppbv of O_3) NO emission rates (E_{NO}) of 0.18 to 0.47 pptv s^{-1} are necessary to reproduce the observed nighttime NO mixing ratio within a surface layer of 10 m height.

$$E_{NO} = [NO] \cdot k_1[O_3] \quad \text{(Eq. 3)}$$

In the absence of measurements of NO soil emission fluxes at the site and recognising that that these are highly dependent on temperature, season, soil humidity and degree of fertilization (Pilegaard, 2013), we take an annual mean NO emission flux of 1 kg ha^{-1} yr^{-1} for temperate, uncultivated grassland (Ludwig et al., 2001) to derive (assuming the same layer height of 10 m) an NO emission rate of 0.27 pptv s^{-1}, which lies within the range quoted above. As the summit of the Kleiner Feldberg is covered with blueberry bushes and surrounded by coniferous forest and that soils impacted from blueberry plants or spruce can support higher NO net fluxes than grass-covered soils (Bargsten et al., 2010), significant NO soil emissions at the summit of the Kleiner Feldberg appear to be plausible. Figure 8 also reveals that the highest levels of NO observed at 10 m height occur when O_3 values are lowest. Anti-correlated NO and O_3 mixing ratios are often observed when plumes of freshly emitted NO is mixed into aged air masses containing O_3 and is a result of reaction R1 which converts NO to NO_2. For our observations at 10 m height, chemistry (temperature dependent kinetics), boundary layer dynamics (extent of mixing/decoupling of surface

https://doi.org/10.5194/acp-2022-163
Preprint. Discussion started: 7 March 2022


Atmospheric Chemistry and Physics Discussions

layer and NBL) and plant physiology (emission rates of NO) may all contribute to the extent to which NO and O_3 react. As the large night-to-night variability in the NO mixing ratios cannot be explained by temperature-dependent changes in the rate coefficient k_1 or in the emission rate of NO, we conclude that boundary layer effects dominate and that the height of the surface layer and the degree to which NO is entrained from the surface layer into the NBL are the main controlling factors. We consider two limiting cases: 1) When the top of the nocturnal surface layer is above the inlet, and mixing is sufficient to homogenize the air within the first 10 m above the ground, NO originating from the soil can react with O_3 via R1 (Aneja et al., 2000). This would correspond to observations during Type-1 nights. 2) When the surface-layer is less than 10 m deep and is decoupled from the NBL, soil emitted NO is not sampled by the inlet (ca. 10 m above the ground) and the measured NO mixing ratios are at the instrument's LOD. In this case, levels of O_3 in the NBL remain high, as e.g. observed around 21 July. In reality, trace-gas gradients within the lowest layers will control the extent of mixing and case 1) will only operate when high wind speeds induce turbulent mixing close to the surface. We conclude that the variability in nighttime NO and the anti-correlation with O_3 (see Fig. S5a) reflect rapid changes in boundary layer dynamics and vertical mixing within the lowest layers. Similarly high variability in NO_3 mixing ratios has been attributed to a related phenomenon (Crowley et al., 2011). We note that if the time-scales over which boundary-layer dynamic change is less than the lifetime of NO, our steady-state assumption breaks down. None-the-less, the presence of up to 90 pptv of NO at nighttime in the presence of 20-40 ppbv of O_3 implies significant production of NO_2.

We examined the nighttime generation of NO_2 using box model calculations (FACSIMILE/CHEMCAT (Curtis and Sweetenham, 1987)) employing Reactions R1 to R4 and R7 with IUPAC-recommended, temperature-dependent rate coefficients (S5 of the Supplement) and constrained by measurements of NO, O_3, ambient temperature and pressure. Known loss processes for NO_2 at night are the slow reaction with O_3 (to form NO_3) and with NO_3 to form N_2O_5 (R2–R4) and deposition to surfaces (e.g. foils, soil). Note that this simulation considers R1 as the only NO_2 source and that it is only valid if chemistry and transport happen on a similar time scale.

Figure 9 plots the measured nighttime NO_2 mixing ratios (black symbols) together with the model output using vd_{NO2} = 0.015 cm s^{-1} (which is based on a mean nighttime NO_2 deposition for foliar surfaces (Delaria et al., 2018) and a value that is a factor 10 larger (vd_{NO2} = 0.15 cm s^{-1}) in both cases assuming a surface layer height of 10 m to derive loss rate constants of 1.5×10^{-5} and 1.5×10^{-4} s^{-1} respectively. Clearly, the larger deposition velocity is necessary to roughly align measured and simulated NO_2 mixing ratios. Such large NO_2 deposition velocities have previously been evoked in order to bring observed NO_2 levels and NO emission rates into agreement (Jacob and Wofsy, 1990) and our average, nighttime deposition velocity of 0.15 cm s^{-1} is comparable to values of 0.1-0.57 cm s^{-1} determined in boreal coniferous forests (Rondon et al., 1993) at night and 0.096 cm s^{-1} obtained in a temperate coniferous forest (Breuninger et al., 2013).

The interaction of NO_2 with foliar surfaces, which can serve as both source and sink of NO_2 is complex (Breuninger et al., 2013; Delaria et al., 2018) and a scenario in which the high (but variable) nighttime NO mixing ratios result from soil emissions while NO_2 is simultaneously deposited on foliar surfaces is conceivable. Given that the stratification of the lowermost atmosphere at TO2021 was only examined on one night, and considering the likely variability in NO emission rates and NO_2

https://doi.org/10.5194/acp-2022-163
Preprint. Discussion started: 7 March 2022


Atmospheric Chemistry and Physics Discussions

deposition velocities (Ludwig et al., 2001; Ganzeveld et al., 2002), our interpretation of the nighttime NO and NO_2 data remains speculative. Considering the lack of correlation between wind direction and abundance of nighttime NO (Fig. S5b), an alternative, point NO emission source (e.g. an NO bottle, or exhaust line) seems unlikely. Interferences by other trace-gases or reasons for bias of the CLD instrument could not be identified as causes for the high nocturnal levels of NO.

3.5 NO_3 mixing ratios

During the TO2021 intensive, ambient NO_3 mixing ratios were not monitored. However, as both the total loss term L_{NO_3} and the production term ($P_{NO_3} = (k_2[NO_2][O_3])$) are known, we can derive NO_3 mixing ratios by assuming that NO_3 is in steady-state, i.e. that loss and production are balanced and the derivative of the NO_3 mixing ratios is independent of time. Steady-state calculations of NO_3 lifetimes or NO_3 mixing ratios have been carried out in numerous studies (Platt et al., 1984; Geyer and Platt, 2002; Brown et al., 2011; Crowley et al., 2011; Liebmann et al., 2018a; Liebmann et al., 2018b) and have shown to be valid, when NO_3 reactivities are high enough and the chemical equilibrium to N_2O_5 (R3 and R4) is not perturbed by sudden changes in NO_2 mixing ratios (Brown et al., 2003a; Dewald et al., 2020). Steady-state NO_3 mixing ratios can be calculated with Eq. 4,

$$[NO_3]_{ss} = \frac{P_{NO_3}}{L_{NO_3}} = \frac{k_2[NO_2][O_3]}{k^{NO_3} + J_{NO_3} + k_7[NO]} \quad \text{(Eq. 4)}$$

which neglects both direct and indirect, heterogeneous loss of NO_3 (R8 and R9). Previous estimates of the NO_3 loss by aerosol uptake on the Kleiner Feldberg returned values of ≈ 0.001 s^{-1} or lower (Crowley et al., 2010; Phillips et al., 2016; Sobanski et al., 2016) and are consequently insignificant compared to the average nighttime overall NO_3 loss rate of ≈ 0.03 s^{-1}.

Figure 10 displays a time-series of the calculated overal NO_3 loss-constant, production rate and steady-state mixing ratios for TO2021. Nighttime NO_3 losses vary typically between < 0.006 s^{-1} and 0.03 s^{-1}, while the daytime losses were as large as 0.3 s^{-1}. The NO_3 production rate was, on average, close to ~ 0.02 s^{-1} at nighttime, increasing to 0.1 s^{-1} during the day when NO_2 and/or O_3 mixing ratios were large. NO_3 mixing ratios thus calculated are lower than about 6 pptv for all nights (one exception of 12 pptv on the 10th July) and well below 2 pptv for most of the nights.

3.5.1 Comparison with previous NO_3 measurements at the Kleiner Feldberg

NO_3 measurements with which to compare the present data-set have been recorded at the Kleiner Feldberg during campaigns in 2008, 2011, 2012 and 2015 for which key details (including names and acronyms) are summarized in Tab.1:

https://doi.org/10.5194/acp-2022-163
Preprint. Discussion started: 7 March 2022

Atmospheric Chemistry and Physics Discussions

Table 1: Nighttime NO_3 mixing ratios, median production rates and median nighttime loss rates at the top of the Kleiner Feldberg.

Campaign	Reference	Period	# Nights (< LOD)	P_{NO_3} pptv s^{-1}	L_{NO_3} 10^{-3} s^{-1}	NO_3 pptv	k_8 10^{-3} s^{-1}	k_9 10^{-3} s^{-1}
TO2008	Crowley et al, 2010	May 2008	6 (0)	0.033	2.2[b]	< LOD – 65[a]	1.6	< 0.2
PARADE	Sobanski et al., 2016	Aug-Sep 2011	21 (4)	0.044	4.5[b]	< LOD – 250[a]		2
INUIT	This work	Aug 2012	16 (4)	0.049	3.7[b]	< LOD – 190[a]		
NOTOMO	Sobanski et al., 2017	Jul 2015	24 (10)	0.049	7.5[b]	< LOD – 50[a]		
					< 5 – 40[d]			
TO2021	This work	Jul 2021	34 (14)	0.025	27[a]	0-12[b]		
					< 6 – 40[c]			

Notes: # Nights = Number of nights with measurements, the number in brackets represents the number of nights where either the NO_3 mixing ratio or the directly measured value of k^{NO_3} was below the LOD. Direct (k_8) and indirect (k_9) loss rates of NO_3 by heterogeneous uptake of NO_3 and N_2O_5 were calculated only for TO2008 and PARADE. [a]directly measured. [b]steady-state calculation. [c]directly measured; VOC contribution only. [d]directly measured for 3 nights, no NO measurements available (Liebmann et al., 2017). TO2008 = Mini (un-named) campaign with only NO_3, NO, O_3 and NO_2 measurements. PARADE = PArticles and RAdicals: Diel observations of the impact of urban and biogenic Emissions, INUIT = Ice NUclei research UnIT, NOTOMO = NOcturnal chemistry at the Taunus Observatory: insights into Mechanisms and Oxidation.

The first measurements of NO_3 (and N_2O_5) at the Kleiner Feldberg were performed on 6 nights in May 2008 (Crowley et al., 2010) (this data set is referred as TO2008), on 21 nights in July 2011 (PARADE campaign (Sobanski et al., 2016)), on 16 nights in August 2012 (INUIT campaign) and in September 2015 during the NOTOMO campaign (Liebmann et al., 2017; Sobanski et al., 2017). All previous NO_3 data sets except for INUIT have been published. The time-series of the NO_3, NO_2, O_3 mixing ratios (and resulting P_{NO_3} and L_{NO_3} according to Eq. 4) from each of the campaigns used for this analysis are reproduced in the Supplement (S6, Fig. S6-S9) together with key features of the instruments used (Tab. S1).

The presence of nearby industrial centres imparts a strong wind-direction dependence on the composition of the air (and especially NO_X) at the Kleiner Feldberg with densely populated cities (and thus anthropogenic sources of NO_x) located in the SE and SW sectors. An overview of the prevailing wind directions and NO_2 mixing ratios during each campaign are summarized in Fig. 11. The lowest, average NO_2 mixing ratios were encountered during TO2008 (air arriving mainly from the East) and TO2021 which had a large contribution of air mases arriving from the North and West but almost none from the Frankfurt area (SE-SSE). TO2021 is the only campaign with a significant contribution of air masses arriving from the "clean" Northern sector and the generally lower NO_X levels during TO2021 may also have been a result of changes in vehicle usage in the region as a higher fraction of locally employed people worked from home as a result of the COVID-19 pandemic (Reifenberg et al., 2021).

https://doi.org/10.5194/acp-2022-163
Preprint. Discussion started: 7 March 2022


Atmospheric Chemistry and Physics Discussions

Figure 12 indicates that, in comparison to the previous summer campaigns (PARADE, INUIT and NOTOMO) the temperatures were lower during TO2021 with the maximum value of 22 °C being ~10 °C lower than the maximum value during NOTOMO. TO2021 and PARADE had the highest incidence of very humid days, with a median RH of > 80 % for TO2021 and > 75% for PARADE while for TO2008 the median relative humidity (~51 %) was the lowest.

For comparison of the nighttime NO_3 mixing ratios, periods of daytime-nighttime transitions (when NO_3 mixing ratios strongly change at sunrise or sunset) were excluded. The NO_3 mixing ratios (lower panel), loss rates (middle panel) and production rates (upper panel) for each campaign are depicted in Fig.13 as a box-and-whisker plot. Note that nights on which the NO_3 mixing ratios were > 0 but below the instrument's LOD, were taken into account, whereas for the calculation of L_{NO_3} in the campaigns prior to TO2021, reactivities derived from NO_3 mixing ratios below the LOD (i.e. < 1.5 pptv) were excluded from the analysis so that L_{NO_3} is not biased by values associated with high uncertainties.

Figure 13a shows that, during PARADE, INUIT and NOTOMO, the nighttime NO_3 production rates were similar in terms of both median values (~ 0.05 pptv s^{-1}) and range. Throughout these three campaigns, high production rates (above 0.3 pptv s^{-1}) were occasionally observed, which for PARADE (Sobanski et al., 2016) were linked to winds originating from urban regions. Figure 13a also reveals that the median, nighttime NO_3 production rates during PARADE, INUIT and NOTOMO were higher than during TO2008 and TO2021 (0.033 and 0.025 pptv s^{-1}) which was driven by the lower NO_2 mixing ratios in TO2008 and TO2021 for which air from the cleaner easterly and northerly sectors was encountered more frequently. Campaign-averaged diel cycles of O_3 in the Supplement (Fig. S10) indicate that O_3 during TO2008 and TO2021 were not substantially lower (even higher in the case of TO2008) than during PARADE, INUIT and NOTOMO.

Figure 13b shows clearly that, with a median value of 0.028 s^{-1}, the nighttime NO_3 loss rates (L_{NO_3}) during TO2021 were significantly higher than for all other campaigns, which were 0.0075 s^{-1} for NOTOMO, 0.0045 s^{-1} for PARADE, 0.0037 s^{-1} for INUIT and 0.0022 s^{-1} for TO2008. A partial explanation for the greater NO_3 loss term during TO2021 is found in the nighttime NO mixing ratios, which were significantly larger than those measured in e.g. TO2008 or PARADE. The effect of removing the contribution of NO reaction to L_{NO_3} during PARADE (and TO2008) is minimal, as NO was close or below the LOD (4-10 pptv) on most nights (Crowley et al., 2010; Sobanski et al., 2016), which is confirmed by the corresponding campaign-averaged diel cycles of NO mixing ratios (Fig. S11). In contrast, subtraction of the contribution to NO_3 reactivity of the high nighttime levels of NO observed during TO2021, would reduce L_{NO_3} to ~0.011 s^{-1} (red, horizontal line in Fig. 13b) which is more comparable to that observed during e.g. NOTOMO and PARADE.

We note that, in general, the comparison of NO_3 loss rates derived via the steady-state method and direct reactivity may be complicated by the fact that the steady-state method only works when NO_3 is above the detection limit (often a result of low reactivity) whereas the direct measurement of NO_3 losses performs best when reactivities are high. However, $\Sigma k_i[VOC]_i$ suggests that L_{NO_3} was never below 0.002 s^{-1} on Type-2 nights. As shown in the Supplement, setting values of k^{NO_3} < 0.006 s^{-1} to 0.002 s^{-1} would only occasionally lead to $[NO_3]_{ss}$ > 10 pptv (Fig. S12a) and thus only have a small impact on the distribution of NO_3 mixing ratios (Fig. S12b), so that this bias cannot be fully responsible for the observed difference.

https://doi.org/10.5194/acp-2022-163
Preprint. Discussion started: 7 March 2022


Atmospheric Chemistry and Physics Discussions

None-the-less, Fig. 13a and 13b indicate that TO2021 was exceptional in that P_{NO_3} was the lowest of all campaigns at the Kleiner Feldberg while L_{NO_3} was the highest, which result in a calculated median NO_3 mixing ratio of just 0.7 pptv. This contrasts greatly with median NO_3 mixing ratios of 15, 10, 11 and 4 pptv observed during TO2008, PARADE, INUIT and NOTOMO (Fig. 13c) on the Kleiner Feldberg.

As alluded to above, this difference is partially caused by unusually high nighttime NO levels, but also results from the low NO_3 production rate during TO2021. During PARADE, INUIT and NOTOMO, NO_3 mixing ratios above 100 pptv were measured and linked to nights with exceptionally long NO_3 lifetimes. For PARADE, this was suggested to be a result of sampling from above the surface layer, where NO_3 lifetimes can be large owing to the decoupling from ground-level emissions (Brown et al., 2003b; Sobanski et al., 2016). While there is evidence for a similar situation for TO2021 on 21 Jul (Fig. 4), in the absence of vertically resolved meteorological data on the other nights, it is not clear whether purely meteorological effects are responsible for the observed low reactivities on 14 nights or whether reduced emission rates of reactive trace-gases additionally play a role. We are presently developing a drone-borne NO_3 instrument to provide vertical gradients in NO_3 (as well as T and RH) in order to help resolve this issue.

4 Summary and conclusions

The fate of the NO_3 radical at the summit of the Kleiner Feldberg during the TO2021 intensive in July 2021 was assessed with the help of direct NO_3 reactivity and VOC measurements. Directly measured NO_3 reactivities towards VOCs (k^{NO_3}) were on average ~ 0.011 s^{-1} at night and as large as ~ 0.04 s^{-1} during the day. NO_3 reactivities derived from VOC measurements showed an excellent agreement with k^{NO_3} throughout the diel cycle with VOC-induced NO_3 losses by monoterpenes dominating with a contribution of > 80 %. Sesquiterpenes and isoprene contributed with 9 ± 5 % and 7 ± 4 %, respectively.

During the daytime, NO removed on average 53 ± 20 % of the NO_3, photolysis and reaction with VOCs contributed ~31 ± 19 and ~ 16 ± 15 % respectively. The daytime contribution of VOC-induced reactivity was highly variable and ranged from ca. 10 % at noon to 30 % in the afternoon implying that NO_3 can contribute significantly e.g. to alkyl nitrate formation during daytime.

k^{NO_3} was predominantly below the LOD of 0.006 s^{-1} on 14 of the 34 nights. On one night, for which a vertical temperature and RH gradient were measured, the low NO_3 reactivity was associated with reduced vertical mixing and the decoupling of a shallow surface layer from the layer above in which the trace-gas inlet was situated.

In the absence of direct measurements, NO_3 mixing ratios during TO2021 were calculated from the total loss rate constant (VOCs, photolysis, NO) and the NO_3 production rate to enable comparison with directly measured NO_3 mixing ratios during four previous campaigns between 2008 and 2015 at the Kleiner Feldberg. For TO2021, NO_3 loss rates were ca. a factor 3-5 higher than during previous campaigns while NO_3 production rates were the lowest. Consequently, the calculated steady-state mixing ratios of NO_3 are much lower than those directly measured during TO2008, PARADE and INUIT and NOTOMO. The exceptionally high nighttime NO_3 loss rates during TO2021 are partially related to the presence of several tens of pptvs of NO,

https://doi.org/10.5194/acp-2022-163
Preprint. Discussion started: 7 March 2022


Atmospheric Chemistry and Physics Discussions

so that VOC-induced losses were 50-60 % of the overall loss term. This is in stark contrast to previous observations in forested environments where reactions with VOCs were the only relevant nighttime loss path of NO_3. The observation of NO at levels of 20-80 pptv at nighttime in the presence of 30-40 ppbv of O_3 imply large rates of NO_2 formation. Constrained box-model calculations suggest that rapid losses of NO_2 via e.g deposition would necessary in order to reproduce the observed nighttime NO_2 mixing ratios. In order to confirm this hypothesis, measurements of NO emission and NO_2 deposition rates on the Kleiner Feldberg under similar meteorological conditions are necessary.

Overall, the intercomparison of the NO_3 mixing ratios and NO_3 reactivity revealed high variability in data obtained over a long period on the same site and emphasizes that not only chemical effects but also boundary-layer dynamics and plant-physiological processes may have a great impact on observations.

Coda and Data Availability. Data of the TO2021 campaign is available upon request at https://keeper.mpdl.mpg.de/ to all scientists agreeing to the data protocol. The data of all other campaigns is available upon request from the corresponding author. The FACSIMILE code used for the box model can be found in the Supplement (S5).

Author contributions. PD measured NO_3 reactivity and NO_2 mixing ratios during TO2021, analysed the data and wrote the manuscript. JNC organized the TO2021 campaign, measured NO_x and helped to revise the manuscript. CMN and HF provided NO and NO_2 data. AR, AE and JW provided VOC data. JNC and CMN provided O_3 data. JS measured actinic fluxes and performed vertical profile measurements of temperature, relative humidity and pressure with the drone. All authors commented on the manuscript.

Competing interests. The authors declare that they have no conflict of interest.

Acknowledgements.
We thank Andreas Kürten and Joachim Curtius (Institute for Atmospheric and Environmental Sciences, Goethe University Frankfurt am Main) for logistical support and access to the facilities at the Taunus Observatory. We thank the DWD for the provision of meteorological data and Chemours for the FEP sample used to coat the flowtube reactors.

References

Allan, B. J., Carslaw, N., Coe, H., Burgess, R. A., and Plane, J. M. C.: Observations of the nitrate radical in the marine boundary layer, J. Atmos. Chem., 33, 129-154, doi:10.1023/A:1005917203307, 1999.

Allan, B. J., McFiggans, G., Plane, J. M. C., Coe, H., and McFadyen, G. G.: The nitrate radical in the remote marine boundary layer, J. Geophys. Res.-Atmos., 105, 24191-24204, doi:10.1029/2000JD900314, 2000.

Allan, B. J., Plane, J. M. C., Coe, H., and Shillito, J.: Observations of NO_3 concentration profiles in the troposphere, J. Geophys. Res.-Atmos., 107, 4588, ACH11-1-ACH11-14, doi:10.1029/2002jd002112, 2002.

https://doi.org/10.5194/acp-2022-163
Preprint. Discussion started: 7 March 2022

Aneja, V. P., Mathur, R., Arya, S. P., Li, Y., Murray, G. C., and Manuszak, T. L.: Coupling the Vertical Distribution of Ozone in the Atmospheric Boundary Layer, Environ. Sci. Technol., 34, 2324-2329, doi:10.1021/es990997+, 2000.

Bargsten, A., Falge, E., Pritsch, K., Huwe, B., and Meixner, F. X.: Laboratory measurements of nitric oxide release from forest soil with a thick organic layer under different understory types, Biogeosciences, 7, 1425-1441, doi:10.5194/bg-7-1425-2010, 2010.

Bekö, G., Wargocki, P., Wang, N. J., Li, M. Z., Weschler, C. J., Morrison, G., Langer, S., Ernle, L., Licina, D., Yang, S., Zannoni, N., and Williams, J.: The Indoor Chemical Human Emissions and Reactivity (ICHEAR) project: Overview of experimental methodology and preliminary results, Indoor Air, 30, 1213-1228, doi:10.1111/ina.12687, 2020.

Boggs, P. T., Donaldson, J. R., Byrd, R. H., and Schnabel, R. B.: ODRPACK - Software for Weighted Orthogonal Distance Regression, ACM Trans. Math. Softw., 15, 348-364, doi:10.1145/76909.76913, 1989.

Breuninger, C., Meixner, F. X., and Kesselmeier, J.: Field investigations of nitrogen dioxide (NO_2) exchange between plants and the atmosphere, Atmos. Chem. Phys., 13, 773-790, doi:10.5194/acp-13-773-2013, 2013.

Brown, S. S., Stark, H., and Ravishankara, A. R.: Applicability of the steady state approximation to the interpretation of atmospheric observations of NO_3 and N_2O_5, J. Geophys. Res.-Atmos., 108, 4539, ACH6-1-ACH6-10, doi:10.1029/2003JD003407, 2003a.

Brown, S. S., Stark, H., Ryerson, T. B., Williams, E. J., Nicks, D. K., Trainer, M., Fehsenfeld, F. C., and Ravishankara, A. R.: Nitrogen oxides in the nocturnal boundary layer: Simultaneous in situ measurements of NO_3, N_2O_5, NO_2, NO, and O_3, J. Geophys. Res.-Atmos., 108, 4299, ACH18-1-ACH18-11, doi:10.1029/2002JD002917, 2003b.

Brown, S. S., Dibb, J. E., Stark, H., Aldener, M., Vozella, M., Whitlow, S., Williams, E. J., Lerner, B. M., Jakoubek, R., Middlebrook, A. M., DeGouw, J. A., Warneke, C., Goldan, P. D., Kuster, W. C., Angevine, W. M., Sueper, D. T., Quinn, P. K., Bates, T. S., Meagher, J. F., Fehsenfeld, F. C., and Ravishankara, A. R.: Nighttime removal of NO_x in the summer marine boundary layer, Geophys. Res. Lett., 31, L07108, 1-5, doi:10.1029/2004GL019412, 2004.

Brown, S. S., Dube, W. P., Osthoff, H. D., Stutz, J., Ryerson, T. B., Wollny, A. G., Brock, C. A., Warneke, C., De Gouw, J. A., Atlas, E., Neuman, J. A., Holloway, J. S., Lerner, B. M., Williams, E. J., Kuster, W. C., Goldan, P. D., Angevine, W. M., Trainer, M., Fehsenfeld, F. C., and Ravishankara, A. R.: Vertical profiles in NO_3 and N_2O_5 measured from an aircraft: Results from the NOAA P-3 and surface platforms during the New England Air Quality Study 2004, J. Geophys. Res.-Atmos., 112, D22304, 1-17, doi:10.1029/2007JD008883, 2007a.

Brown, S. S., Dube, W. P., Osthoff, H. D., Wolfe, D. E., Angevine, W. M., and Ravishankara, A. R.: High resolution vertical distributions of NO_3 and N_2O_5 through the nocturnal boundary layer, Atmos. Chem. Phys., 7, 139-149, doi:10.5194/acp-7-139-2007, 2007b.

Brown, S. S., Degouw, J. A., Warneke, C., Ryerson, T. B., Dube, W. P., Atlas, E., Weber, R. J., Peltier, R. E., Neuman, J. A., Roberts, J. M., Swanson, A., Flocke, F., McKeen, S. A., Brioude, J., Sommariva, R., Trainer, M., Fehsenfeld, F. C., and Ravishankara, A. R.: Nocturnal isoprene oxidation over the Northeast United States in summer and its impact on reactive nitrogen partitioning and secondary organic aerosol, Atmos. Chem. Phys., 9, 3027-3042, doi:10.5194/acp-9-3027-2009, 2009.

Brown, S. S., Dube, W. P., Peischl, J., Ryerson, T. B., Atlas, E., Warneke, C., de Gouw, J. A., Hekkert, S. t. L., Brock, C. A., Flocke, F., Trainer, M., Parrish, D. D., Feshenfeld, F. C., and Ravishankara, A. R.: Budgets for nocturnal VOC oxidation by nitrate radicals aloft during the 2006 Texas Air Quality Study, J. Geophys. Res.-Atmos., 116, D24305, 1-15, doi:10.1029/2011jd016544, 2011.

Brown, S. S., and Stutz, J.: Nighttime radical observations and chemistry, Chem. Soc. Rev., 41, 6405–6447, doi:10.1039/C2CS35181A, 2012.

Brown, S. S., Dube, W. P., Tham, Y. J., Zha, Q. Z., Xue, L. K., Poon, S., Wang, Z., Blake, D. R., Tsui, W., Parrish, D. D., and Wang, T.: Nighttime chemistry at a high altitude site above Hong Kong, J. Geophys. Res.-Atmos., 121, 2457-2475, doi:10.1002/2015jd024566, 2016.

https://doi.org/10.5194/acp-2022-163
Preprint. Discussion started: 7 March 2022


Atmospheric Chemistry and Physics Discussions

Burkholder, J. B., Sander, S. P., Abbatt, J., Barker, J. R., Huie, R. E., Kolb, C. E., Kurylo, M. J., Orkin, V. L., Wilmouth, D. M., and Wine, P. H.: Chemical Kinetics and Photochemical Data for Use in Atmospheric Studies, Evaluation No. 18, JPL Publication 15-10, Jet Propulsion Laboratory, Pasadena, available at: http://jpldataeval.jpl.nasa.gov (last access: 4 January 2022), 2016.

Carslaw, N., Plane, J. M. C., Coe, H., and Cuevas, E.: Observations of the nitrate radical in the free troposphere at Izana de Tenerife, J. Geophys. Res.-Atmos., 102, 10613-10622, doi:10.1029/96JD03512, 1997.

Crowley, J. N., Schuster, G., Pouvesle, N., Parchatka, U., Fischer, H., Bonn, B., Bingemer, H., and Lelieveld, J.: Nocturnal nitrogen oxides at a rural mountain site in south-western Germany, Atmos. Chem. Phys., 10, 2795-2812, doi:10.5194/acp-10-2795-2010, 2010.

Crowley, J. N., Thieser, J., Tang, M. J., Schuster, G., Bozem, H., Hasaynali Beygi, Z., Fischer, H., Diesch, J.-M., Drewnick, F., Borrmann, S., Song, W., Yassaa, N., Williams, J., Pöhler, D., Platt, U., and Lelieveld, J.: Variable lifetimes and loss mechanisms for NO_3 and N_2O_5 during the DOMINO campaign: Contrast between marine, urban and continental air, Atmos. Chem. Phys., 11, 10863-10870, doi:10.5194/acp-11-10853-2011, 2011.

Crutzen, P. J., and Lelieveld, J.: Human impacts on atmospheric chemisty, Annu. Rev. Earth Planet. Sci., 29, 17-45, doi:10.1146/annurev.earth.29.1.17, 2001.

Curtis, A. R., and Sweetenham, W. P.: Facsimile, Atomic Energy Research Establishment, Report R-12805, Harwell Laboratory, Oxfordshire, UK, 1987.

Delaria, E. R., Vieira, M., Cremieux, J., and Cohen, R. C.: Measurements of NO and NO_2 exchange between the atmosphere and Quercus agrifolia, Atmos. Chem. Phys., 18, 14161-14173, doi:10.5194/acp-18-14161-2018, 2018.

Dewald, P., Liebmann, J. M., Friedrich, N., Shenolikar, J., Schuladen, J., Rohrer, F., Reimer, D., Tillmann, R., Novelli, A., Cho, C. M., Xu, K. M., Holzinger, R., Bernard, F., Zhou, L., Mellouki, W., Brown, S. S., Fuchs, H., Lelieveld, J., and Crowley, J. N.: Evolution of NO_3 reactivity during the oxidation of isoprene, Atmos. Chem. Phys., 20, 10459-10475, doi:10.5194/acp-20-10459-2020, 2020.

Drewnick, F., Boettger, T., von der Weiden-Reinmueller, S. L., Zorn, S. R., Klimach, T., Schneider, J., and Borrmann, S.: Design of a mobile aerosol research laboratory and data processing tools for effective stationary and mobile field measurements, Atmos. Meas. Tech., 5, 1443-1457, doi:10.5194/amt-5-1443-2012, 2012.

Edwards, P. M., Aikin, K. C., Dube, W. P., Fry, J. L., Gilman, J. B., de Gouw, J. A., Graus, M. G., Hanisco, T. F., Holloway, J., Huber, G., Kaiser, J., Keutsch, F. N., Lerner, B. M., Neuman, J. A., Parrish, D. D., Peischl, J., Pollack, I. B., Ravishankara, A. R., Roberts, J. M., Ryerson, T. B., Trainer, M., Veres, P. R., Wolfe, G. M., Warneke, C., and Brown, S. S.: Transition from high- to low-NO_x control of night-time oxidation in the southeastern US, Nat. Geosci., 10, 490-495, doi:10.1038/Ngeo2976, 2017.

Foulds, A., Khan, M. A. H., Bannan, T. J., Percival, C. J., Lowenberg, M. H., and Shallcross, D. E.: Abundance of NO_3 Derived Organo-Nitrates and Their Importance in the Atmosphere, Atmosphere, 12, doi:10.3390/atmos12111381, 2021.

Friedrich, N., Tadic, I., Schuladen, J., Brooks, J., Darbyshire, E., Drewnick, F., Fischer, H., Lelieveld, J., and Crowley, J. N.: Measurement of NO_x and NO_y with a thermal dissociation cavity ring-down spectrometer (TD-CRDS): instrument characterisation and first deployment, Atmos. Meas. Tech., 13, 5739-5761, doi:10.5194/amt-13-5739-2020, 2020.

Friedrich, N., Eger, P., Shenolikar, J., Sobanski, N., Schuladen, J., Dienhart, D., Hottmann, B., Tadic, I., Fischer, H., Martinez, M., Rohloff, R., Tauer, S., Harder, H., Pfannerstill, E. Y., Wang, N. J., Williams, J., Brooks, J., Drewnick, F., Su, H., Li, G., Cheng, Y. F., Lelieveld, J., and Crowley, J. N.: Reactive nitrogen around the Arabian Peninsula and in the Mediterranean Sea during the 2017 AQABA ship campaign, Atmos. Chem. Phys., 21, 7473-7498, doi:10.5194/acp-21-7473-2021, 2021.

Fry, J. L., Kiendler-Scharr, A., Rollins, A. W., Brauers, T., Brown, S. S., Dorn, H. P., Dube, W. P., Fuchs, H., Mensah, A., Rohrer, F., Tillmann, R., Wahner, A., Wooldridge, P. J., and Cohen, R. C.: SOA from limonene: role of NO_3 in its generation and degradation, Atmos. Chem. Phys., 11, 3879-3894, doi:10.5194/acp-11-3879-2011, 2011.

Fry, J. L., Draper, D. C., Barsanti, K. C., Smith, J. N., Ortega, J., Winkle, P. M., Lawler, M. J., Brown, S. S., Edwards, P. M., Cohen, R. C., and Lee, L.: Secondary Organic Aerosol Formation and Organic Nitrate Yield from NO_3 Oxidation of Biogenic Hydrocarbons, Environ. Sci. Technol., 48, 11944-11953, doi:10.1021/es502204x, 2014.

Ganzeveld, L. N., Lelieveld, J., Dentener, F. J., Krol, M. C., Bouwman, A. J., and Roelofs, G. J.: Global soil-biogenic NO_x emissions and the role of canopy processes, J. Geophys. Res.-Atmos., 107, ACH8-1-CH8-21, doi:10.1029/2001jd001289, 2002.

Geyer, A., Alicke, B., Konrad, S., Schmitz, T., Stutz, J., and Platt, U.: Chemistry and oxidation capacity of the nitrate radical in the continental boundary layer near Berlin, J. Geophys. Res.-Atmos., 106, 8013-8025, doi:10.1029/2000JD900681, 2001.

Geyer, A., and Platt, U.: Temperature dependence of the NO_3 loss frequency: A new indicator for the contribution of NO_3 to the oxidation of monoterpenes and NO_x removal in the atmosphere, J. Geophys. Res.-Atmos., 107, 4431, ACL8-1-ACL-8-12, doi:10.1029/2001JD001215, 2002.

Guenther, A. B., Zimmerman, P. R., Harley, P. C., Monson, R. K., and Fall, R.: Isoprene and Monoterpene Emission Rate Variability - Model Evaluations and Sensitivity Analyses, J. Geophys. Res.-Atmos., 98, 12609-12617, doi:10.1029/93jd00527, 1993.

Hallquist, M., Wangberg, I., Ljungstrom, E., Barnes, I., and Becker, K. H.: Aerosol and product yields from NO_3 radical-initiated oxidation of selected monoterpenes, Environ. Sci. Technol., 33, 553-559, doi:10.1021/es980292s, 1999.

Handisides, G. M.: The influence of peroxy radicals on ozone production, PhD thesis, Fachbereich Geowissenschaften, Johann Wolfgang Goethe Universität, Frankfurt am Main, 2001.

Heintz, F., Platt, U., Flentje, H., and Dubois, R.: Long-term observation of nitrate radicals at the tor station, Kap Arkona (Rugen), J. Geophys. Res.-Atmos., 101, 22891-22910, doi:10.1029/96JD01549, 1996.

IUPAC: Task Group on Atmospheric Chemical Kinetic Data Evaluation, edited by: Ammann, M., Cox, R.A., Crowley, J.N., Herrmann, H., Jenkin, M.E., McNeill, V.F., Mellouki, A., Rossi, M. J., Troe, J. and Wallington, T. J., available at: http://iupac.pole-ether.fr/index.html, last access: 4 January 2022.

Jacob, D. J., and Wofsy, S. C.: Budgets of Reactive Nitrogen, Hydrocarbons, and Ozone over the Amazon-Forest during the Wet Season, J. Geophys. Res.-Atmos., 95, 16737-16754, doi:10.1029/JD095iD10p16737, 1990.

Jordan, A., Haidacher, S., Hanel, G., Hartungen, E., Mark, L., Seehauser, H., Schottkowsky, R., Sulzer, P., and Mark, T. D.: A high resolution and high sensitivity proton-transfer-reaction time-of-flight mass spectrometer (PTR-TOF-MS), Int. J. Mass spectrom., 286, 122-128, doi: 10.1016/j.ijms.2009.07.005, 2009.

Krechmer, J., Lopez-Hilfiker, F., Koss, A., Hutterli, M., Stoermer, C., Deming, B., Kimmel, J., Warneke, C., Holzinger, R., Jayne, J., Worsnop, D., Fuhrer, K., Gonin, M., and de Gouw, J.: Evaluation of a New Reagent-Ion Source and Focusing Ion-Molecule Reactor for Use in Proton-Transfer-Reaction Mass Spectrometry, Anal. Chem., 90, 12011-12018, doi:10.1021/acs.analchem.8b02641, 2018.

Lelieveld, J., Butler, T. M., Crowley, J. N., Dillon, T. J., Fischer, H., Ganzeveld, L., Harder, H., Lawrence, M. G., Martinez, M., Taraborrelli, D., and Williams, J.: Atmospheric oxidation capacity sustained by a tropical forest, Nature, 452, 737-740, doi:10.1038/nature06870, 2008.

Lelieveld, J., Gromov, S., Pozzer, A., and Taraborrelli, D.: Global tropospheric hydroxyl distribution, budget and reactivity, Atmos. Chem. Phys., 16, 12477-12493, doi:10.5194/acp-16-12477-2016, 2016.

Lelieveld, J., Pozzer, A., Poschl, U., Fnais, M., Haines, A., and Munzel, T.: Loss of life expectancy from air pollution compared to other risk factors: a worldwide perspective, Cardiovasc. Res., 116, 1334-1334, doi:10.1093/cvr/cvaa073, 2020.

https://doi.org/10.5194/acp-2022-163
Preprint. Discussion started: 7 March 2022

Liebmann, J. M., Schuster, G., Schuladen, J. B., Sobanski, N., Lelieveld, J., and Crowley, J. N.: Measurement of ambient NO_3 reactivity: Design, characterization and first deployment of a new instrument, Atmos. Meas. Tech., 2017, 1241-1258, doi:10.5194/amt-2016-381, 2017.

Liebmann, J., Karu, E., Sobanski, N., Schuladen, J., Ehn, M., Schallhart, S., Quéléver, L., Hellen, H., Hakola, H., Hoffmann, T., Williams, J., Fischer, H., Lelieveld, J., and Crowley, J. N.: Direct measurement of NO_3 radical reactivity in a boreal forest, Atmos. Chem. Phys., 2018, 3799-3815, doi:10.5194/acp-18-3799-2018, 2018a.

Liebmann, J. M., Muller, J. B. A., Kubistin, D., Claude, A., Holla, R., Plaß-Dülmer, C., Lelieveld, J., and Crowley, J. N.: Direct measurements of NO_3-reactivity in and above the boundary layer of a mountain-top site: Identification of reactive trace gases and comparison with OH-reactivity, Atmos. Chem. Phys., 18, 12045-12059, doi:10.5194/acp-18-12045-2018, 2018b.

Liebmann, J., Sobanski, N., Schuladen, J., Karu, E., Hellen, H., Hakola, H., Zha, Q., Ehn, M., Riva, M., Heikkinen, L., Williams, J., Fischer, H., Lelieyeld, J., and Crowley, J. N.: Alkyl nitrates in the boreal forest: formation via the NO_3-, OH- and O_3-induced oxidation of biogenic volatile organic compounds and ambient lifetimes, Atmos. Chem. Phys., 19, 10391-10403, doi:10.5194/acp-19-10391-2019, 2019.

Ludwig, J., Meixner, F. X., Vogel, B., and Förstner, J.: Soil-air exchange of nitric oxide: An overview of processes, environmental factors and modeling studies, Biogeochemistry, 52, 225-257, doi:10.1023/A:1006424330555, 2001.

Martinez, M., Perner, D., Hackenthal, E. M., Kulzer, S., and Schutz, L.: NO_3 at Helgoland during the NORDEX campaign in October 1996, J. Geophys. Res.-Atmos., 105, 22685-22695, doi:10.1029/2000JD900255, 2000.

Ng, N. L., Brown, S. S., Archibald, A. T., Atlas, E., Cohen, R. C., Crowley, J. N., Day, D. A., Donahue, N. M., Fry, J. L., Fuchs, H., Griffin, R. J., Guzman, M. I., Herrmann, H., Hodzic, A., Iinuma, Y., Jimenez, J. L., Kiendler-Scharr, A., Lee, B. H., Luecken, D. J., Mao, J., McLaren, R., Mutzel, A., Osthoff, H. D., Ouyang, B., Picquet-Varrault, B., Platt, U., Pye, H. O. T., Rudich, Y., Schwantes, R. H., Shiraiwa, M., Stutz, J., Thornton, J. A., Tilgner, A., Williams, B. J., and Zaveri, R. A.: Nitrate radicals and biogenic volatile organic compounds: oxidation, mechanisms, and organic aerosol, Atmos. Chem. Phys., 17, 2103-2162, doi:10.5194/acp-17-2103-2017, 2017.

Nussbaumer, C. M., Parchatka, U., Tadic, I., Bohn, B., Marno, D., Martinez, M., Rohloff, R., Harder, H., Kluge, F., Pfeilsticker, K., Obersteiner, F., Zoger, M., Doerich, R., Crowley, J. N., Lelieveld, J., and Fischer, H.: Modification of a conventional photolytic converter for improving aircraft measurements of NO_2 via chemiluminescence, Atmos. Meas. Tech., 14, 6759-6776, doi:10.5194/amt-14-6759-2021, 2021.

Phillips, G. J., Thieser, J., Tang, M. J., Sobanski, N., Schuster, G., Fachinger, J., Drewnick, F., Borrmann, S., Bingemer, H., Lelieveld, J., and Crowley, J. N.: Estimating N_2O_5 uptake coefficients using ambient measurements of NO_3, N_2O_5, $ClNO_2$ and particle-phase nitrate, Atmos. Chem. Phys., 16, 13231-13249, doi:10.5194/acp-16-13231-2016, 2016.

Pilegaard, K.: Processes regulating nitric oxide emissions from soils, Philos. Trans. R. Soc., B, 368, 1-8, doi:10.1098/rstb.2013.0126, 2013.

Place, B. K., Delaria, E. R., and Cohen, R. C.: Leaf Stomatal Uptake of Alkyl Nitrates, Environ. Sci. Technol. Lett., 9, 186-190, doi:10.1021/acs.estlett.1c00793, 2022.

Platt, U. F., Winer, A. M., Biermann, H. W., Atkinson, R., and Pitts, J. N.: Measurement of Nitrate Radical Concentrations in Continental Air, Environ. Sci. Technol., 18, 365-369, doi:10.1021/es00123a015, 1984.

Pozzer, A., Zimmermann, P., Doering, U. M., van Aardenne, J., Tost, H., Dentener, F., Janssens-Maenhout, G., and Lelieveld, J.: Effects of business-as-usual anthropogenic emissions on air quality, Atmos. Chem. Phys., 12, 6915-6937, doi:10.5194/acp-12-6915-2012, 2012.

Present, P. S. R., Zare, A., and Cohen, R. C.: The changing role of organic nitrates in the removal and transport of NO_x, Atmos. Chem. Phys., 20, 267-279, doi:10.5194/acp-20-267-2020, 2020.

Reifenberg, S. F., Martin, A., Kohl, M., Hamryszczak, Z., Tadic, I., Röder, L., Crowley, D. J., Fischer, H., Kaiser, K., Schneider, J., Dörich, R., Crowley, J. N., Tomsche, L., Marsing, A., Voigt, C., Zahn, A., Pöhlker, C., Holanda, B., Krüger, O. O., Pöschl, U., Pöhlker, M., Jöckel, P., Dorf, M., Schumann, U., Williams, J., Curtius, J., Harder, H., Schlager, H., Lelieveld, J., and Pozzer, A.: Impact of reduced emissions on direct and indirect aerosol radiative forcing during COVID–19 lockdown in Europe, Atmos. Chem. Phys. Discuss., 2021, 1-23, doi:10.5194/acp-2021-1005, 2021.

https://doi.org/10.5194/acp-2022-163
Preprint. Discussion started: 7 March 2022

Atmospheric Chemistry and Physics Discussions

Rollins, A. W., Browne, E. C., Min, K.-E., Pusede, S. E., Wooldridge, P. J., Gentner, D. R., Goldstein, A. H., Liu, S., Day, D. A., Russell, L. M., and Cohen, R. C.: Evidence for NO_x Control over Nighttime SOA Formation, Science, 337, 1210-1212, doi:10.1126/science.1221520, 2012.

Rondon, A., Johansson, C., and Granat, L.: Dry Deposition of Nitrogen-Dioxide and Ozone to Coniferous Forests, J. Geophys. Res.-Atmos., 98, 5159-5172, doi:10.1029/92jd02335, 1993.

Sobanski, N., Tang, M. J., Thieser, J., Schuster, G., Pöhler, D., Fischer, H., Song, W., Sauvage, C., Williams, J., Fachinger, J., Berkes, F., Hoor, P., Platt, U., Lelieveld, J., and Crowley, J. N.: Chemical and meteorological influences on the lifetime of NO_3 at a semi-rural mountain site during PARADE, Atmos. Chem. Phys., 16, 4867-4883, doi:10.5194/acp-16-4867-2016, 2016.

Sobanski, N., Thieser, J., Schuladen, J., Sauvage, C., Song, W., Williams, J., lelieveld, J., and Crowley, J. N.: Day- and Night-time Formation of Organic Nitrates at a Forested Mountain-site in South West Germany, Atmos. Chem. Phys., 17, 4115-4130, doi:10.5194/acp-17-4115-2017, 2017.

Stull, R. B.: Stable Boundary Layer: An Introduction to Boundary Layer Meteorology, edited by: Stull, R. B., Springer Netherlands, Dordrecht, 499-543, 1988.

Stutz, J., Alicke, B., Ackermann, R., Geyer, A., White, A., and Williams, E.: Vertical profiles of NO_3, N_2O_5, O_3, and NO_X in the nocturnal boundary layer: 1. Observations during the Texas Air Quality Study 2000, J. Geophys. Res.-Atmos., 109, D12306, 1-14, doi:10.1029/2003JD004209, 2004.

Stutz, J., Wong, K. W., Lawrence, L., Ziemba, L., Flynn, J. H., Rappenglueck, B., and Lefer, B.: Nocturnal NO_3 radical chemistry in Houston, TX, Atmos. Environ., 44, 4099-4106, doi:10.1016/j.atmosenv.2009.03.004, 2010.

Tadic, I., Crowley, J. N., Dienhart, D., Eger, P., Harder, H., Hottmann, B., Martinez, M., Parchatka, U., Paris, J. D., Pozzer, A., Rohloff, R., Schuladen, J., Shenolikar, J., Tauer, S., Lelieveld, J., and Fischer, H.: Net ozone production and its relationship to nitrogen oxides and volatile organic compounds in the marine boundary layer around the Arabian Peninsula, Atmos. Chem. Phys., 20, 6769-6787, doi:10.5194/acp-20-6769-2020, 2020.

Wayne, R. P., Barnes, I., Biggs, P., Burrows, J. P., Canosa-Mas, C. E., Hjorth, J., Le Bras, G., Moortgat, G. K., Perner, D., Poulet, G., Restelli, G., and Sidebottom, H.: The nitrate radical: Physics, chemistry, and the atmosphere, Atmos. Environ., 25, 1, 1-206, doi:10.1016/0960-1686(91)90192-A, 1991.

Wennberg, P. O., Bates, K. H., Crounse, J. D., Dodson, L. G., McVay, R. C., Mertens, L. A., Nguyen, T. B., Praske, E., Schwantes, R. H., Smarte, M. D., St Clair, J. M., Teng, A. P., Zhang, X., and Seinfeld, J. H.: Gas-Phase Reactions of Isoprene and Its Major Oxidation Products, Chem. Rev., 118, 3337-3390, doi:10.1021/acs.chemrev.7b00439, 2018.

Wu, R., Vereecken, L., Tsiligiannis, E., Kang, S., Albrecht, S. R., Hantschke, L., Zhao, D., Novelli, A., Fuchs, H., Tillmann, R., Hohaus, T., Carlsson, P. T. M., Shenolikar, J., Bernard, F., Crowley, J. N., Fry, J. L., Brownwood, B., Thornton, J. A., Brown, S. S., Kiendler-Scharr, A., Wahner, A., Hallquist, M., and Mentel, T. F.: Molecular composition and volatility of multi-generation products formed from isoprene oxidation by nitrate radical, Atmos. Chem. Phys., 21, 10799-10824, doi:10.5194/acp-21-10799-2021, 2021.

York, D.: Least-Squares Fitting of a Straight Line, Can. J. Phys., 44, 1079-1086, doi:10.1139/p66-090, 1966.

https://doi.org/10.5194/acp-2022-163
Preprint. Discussion started: 7 March 2022

Atmospheric Chemistry and Physics Discussions

Figures

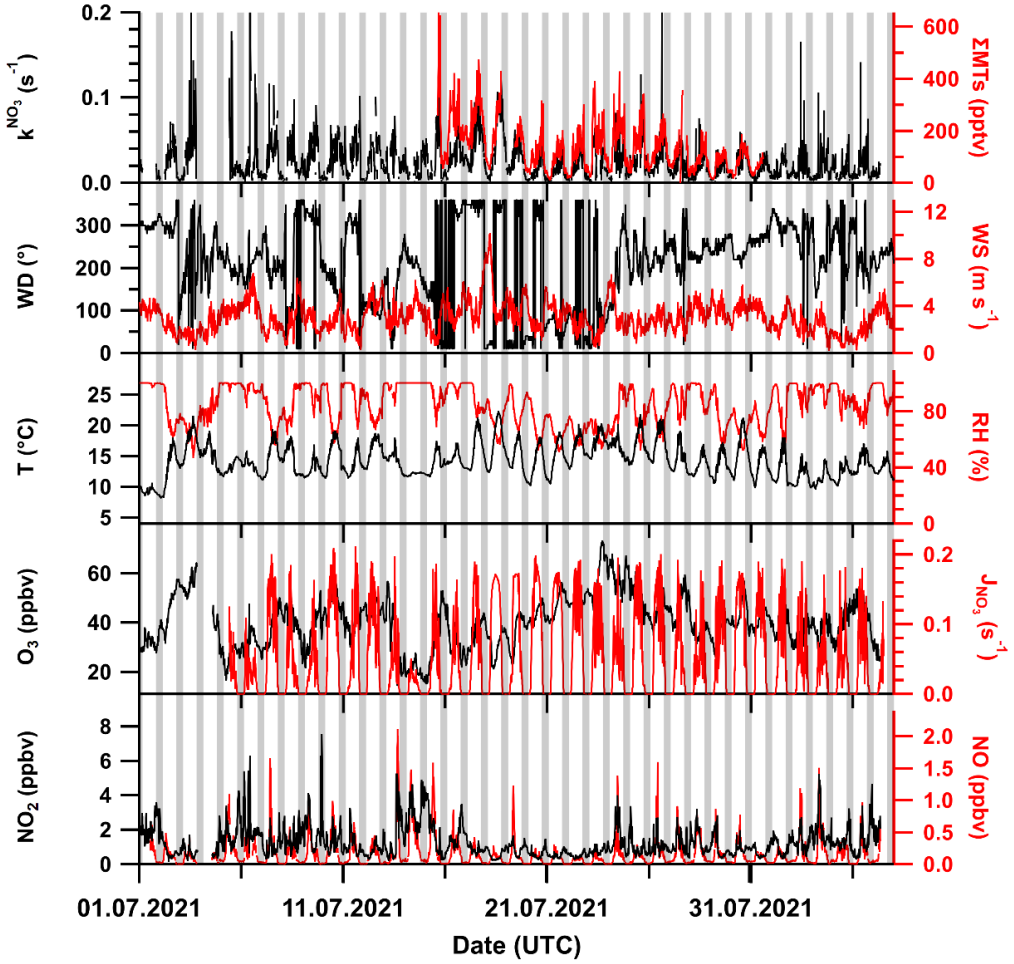

Figure 1: Overview of key measurements during the TO2021 campaign with wind direction (WD), temperature (T), sum of monoterpenes (ΣMT), wind speed (WS), relative humidity (RH), NO_3 photolysis rate coefficient (J_{NO_3}). Meteorological data was provided by the German Meteorological Service (DWD). Nighttime periods are shaded grey. The x-axis ticks are at 00:00 UTC.

https://doi.org/10.5194/acp-2022-163
Preprint. Discussion started: 7 March 2022

Atmospheric Chemistry and Physics Discussions

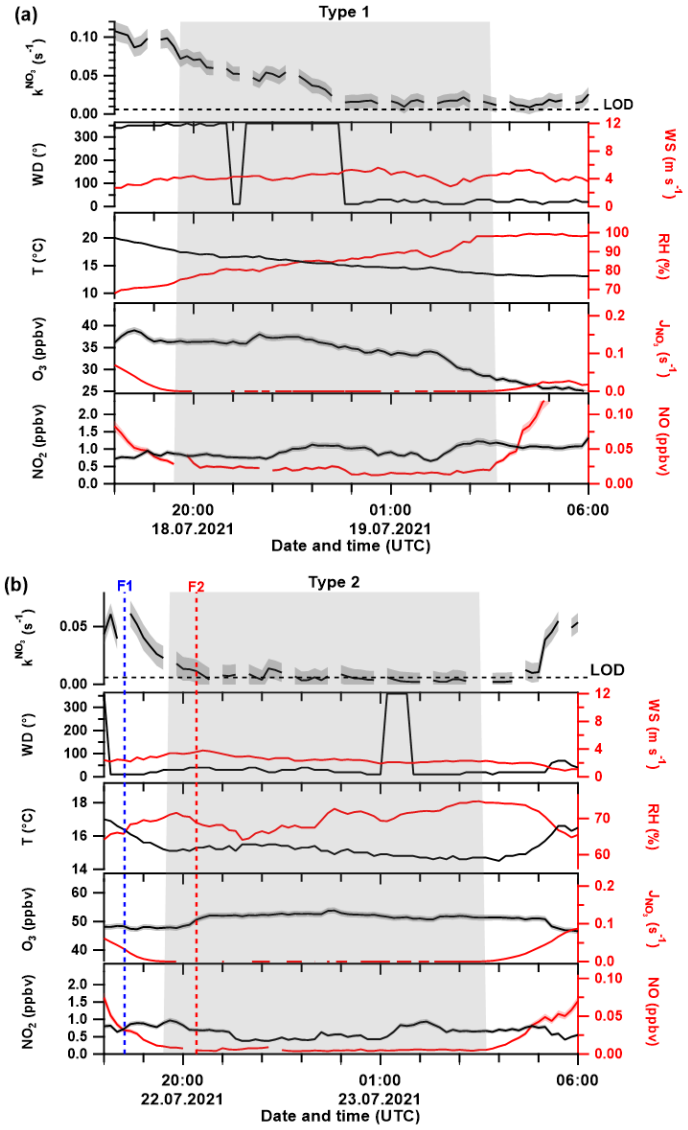

Figure 2: Time-series of directly measured NO_3 reactivity (k^{NO_3}) together with auxiliary measurements during Type-1 (a) and Type-2 nights night (b). F1 and F2 mark times at which drone-assisted temperature and relative humidity profiles wer measured. The grey-shaded area represents nighttime. Abbreviations are defined in caption of Fig.1. The shaded areas in the colour of the lines denotes the corresponding uncertainty of the measured parameter.

https://doi.org/10.5194/acp-2022-163
Preprint. Discussion started: 7 March 2022

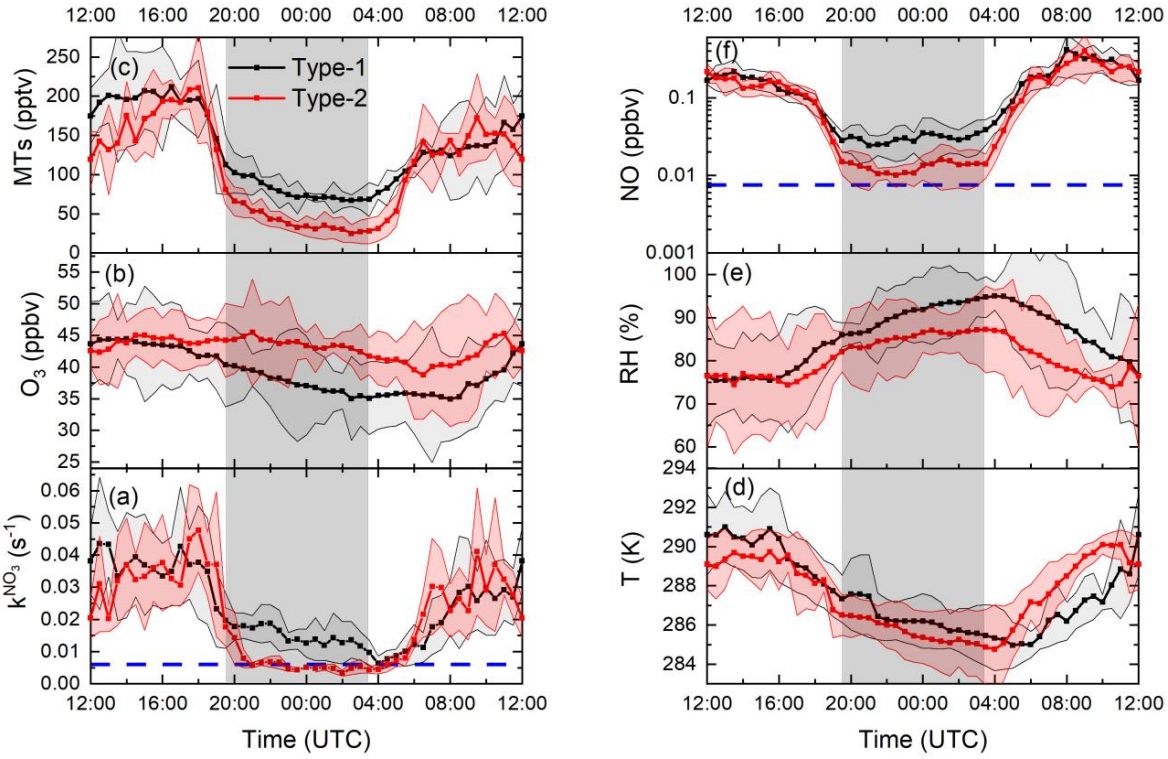

Figure 3: Median diel profiles of (a) directly measured NO_3 reactivities, (b) O_3 mixing ratios, (c) monoterpenes, (d) temperature, (e) relative humidity, and (f) NO mixing ratios classified by night types (Type-1 in black, Type-2 in red). The grey shaded area represents the nighttime period. The shaded areas in line colour represent the 25th and 75th percentiles. The blue lines denote the LODs of the instruments used to measure NO_3 reactivity and NO.

https://doi.org/10.5194/acp-2022-163
Preprint. Discussion started: 7 March 2022

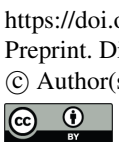

Atmospheric Chemistry and Physics Discussions

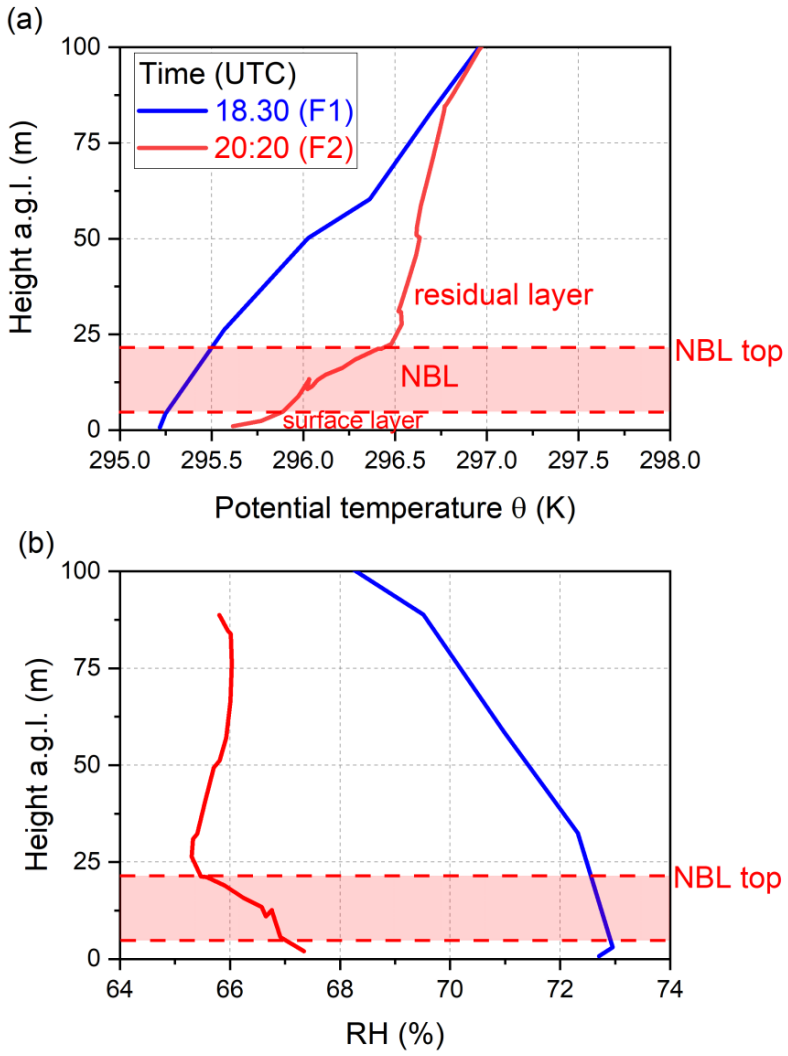

Figure 4: Vertical profiles of potential temperature (a) and relative humidity (b) at the summit of the Kleiner Feldberg at 18:30 UTC (blue) and 20:20 UTC (red). The nocturnal boundary layer (NBL) at 20:20 UTC is shaded red.

https://doi.org/10.5194/acp-2022-163
Preprint. Discussion started: 7 March 2022

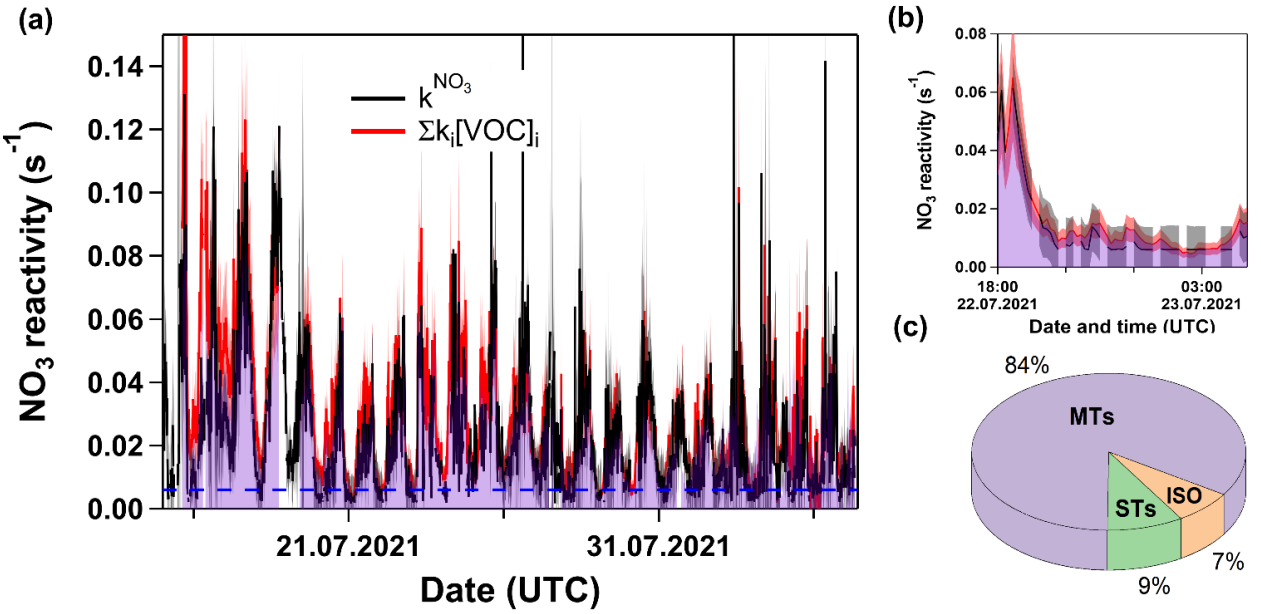

Figure 5: (a) Time-series of k^{NO_3} and $\Sigma k_i[VOC]_i$. Dashed blue line marks the LOD of the k^{NO_3} measurement. The purple shade represents the contribution of monoterpenes. (b) Same as (a) but with a detailed view of the night between the 22nd and 23rd July presented in Fig.2b (c) Pie-chart of fractional contributions of isoprene, monoterpenes and sesquiterpenes to $\Sigma k_i[VOC]_i$ over this time period.

https://doi.org/10.5194/acp-2022-163
Preprint. Discussion started: 7 March 2022

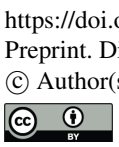

Atmospheric Chemistry and Physics Discussions

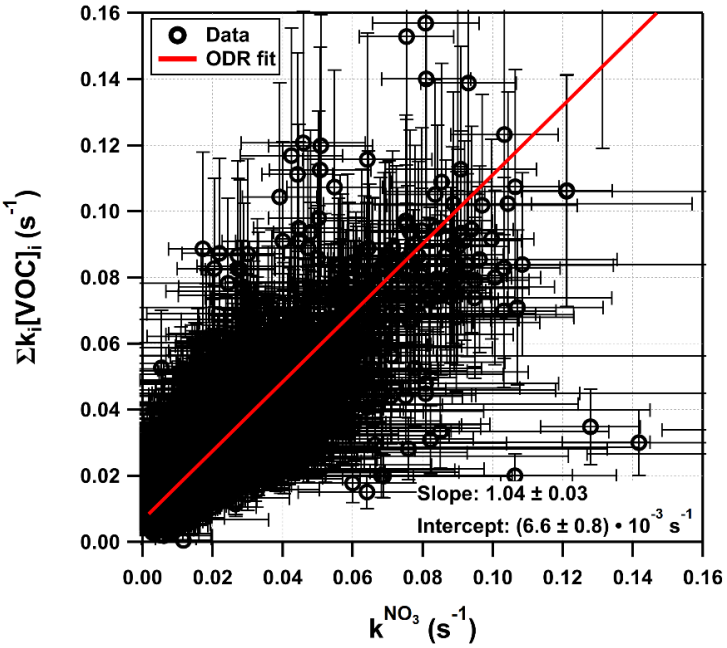

Figure 6: Plot of k^{NO_3} versus $\Sigma k_i[VOC]_i$. The red solid line represents an orthogonal distance regression (ODR) with a slope of 1.04 and an intercept of 6.6 x 10^{-3} s^{-1}.

795

https://doi.org/10.5194/acp-2022-163
Preprint. Discussion started: 7 March 2022

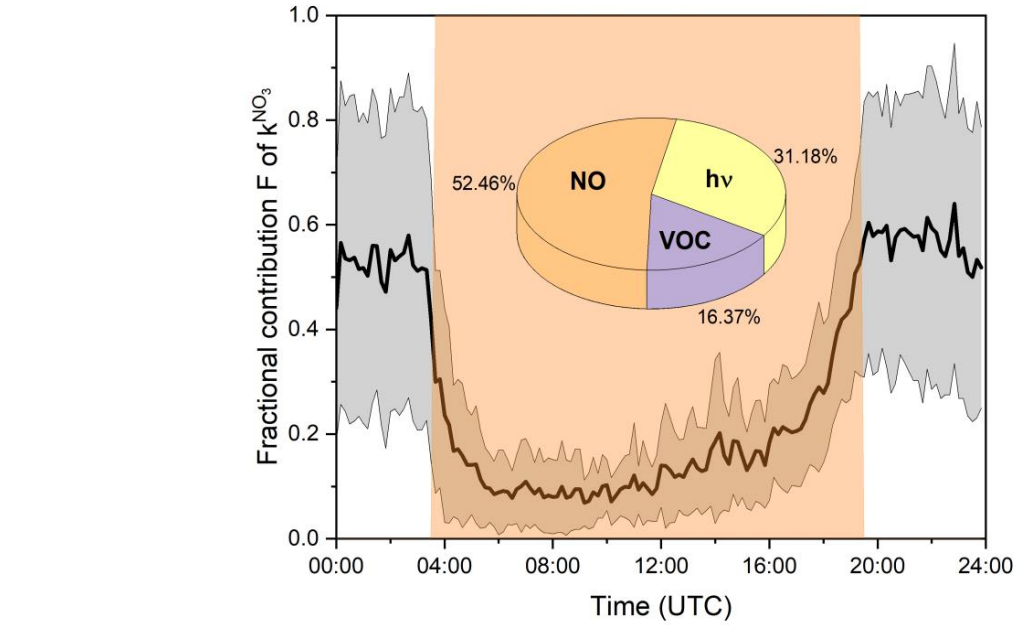

Figure 7: Mean, fractional contribution (F) of $\boldsymbol{k^{NO_3}}$ to the overall NO_3 loss rate over the diel-cycle. The grey shaded area represents the standard deviation (1σ) of the mean values. Orange shaded area indicates daytime. The pie-chart shows the mean fractional contribution to NO_3 loss of reaction with NO, photolysis and reaction with VOCs during the daytime.

https://doi.org/10.5194/acp-2022-163
Preprint. Discussion started: 7 March 2022

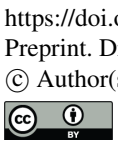

Atmospheric Chemistry and Physics Discussions

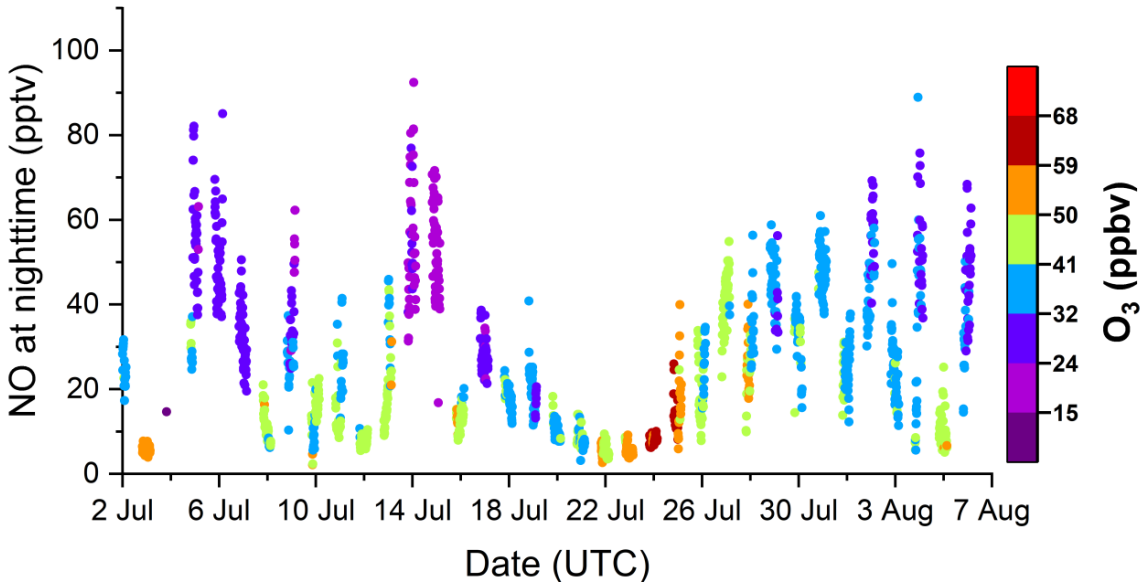

Figure 8: Nighttime NO mixing ratios (colour-coded by O_3 mixing ratios) during TO2021. The x-axis Ticks represent 00:00 UTC.

https://doi.org/10.5194/acp-2022-163
Preprint. Discussion started: 7 March 2022

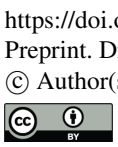

Atmospheric Chemistry and Physics Discussions

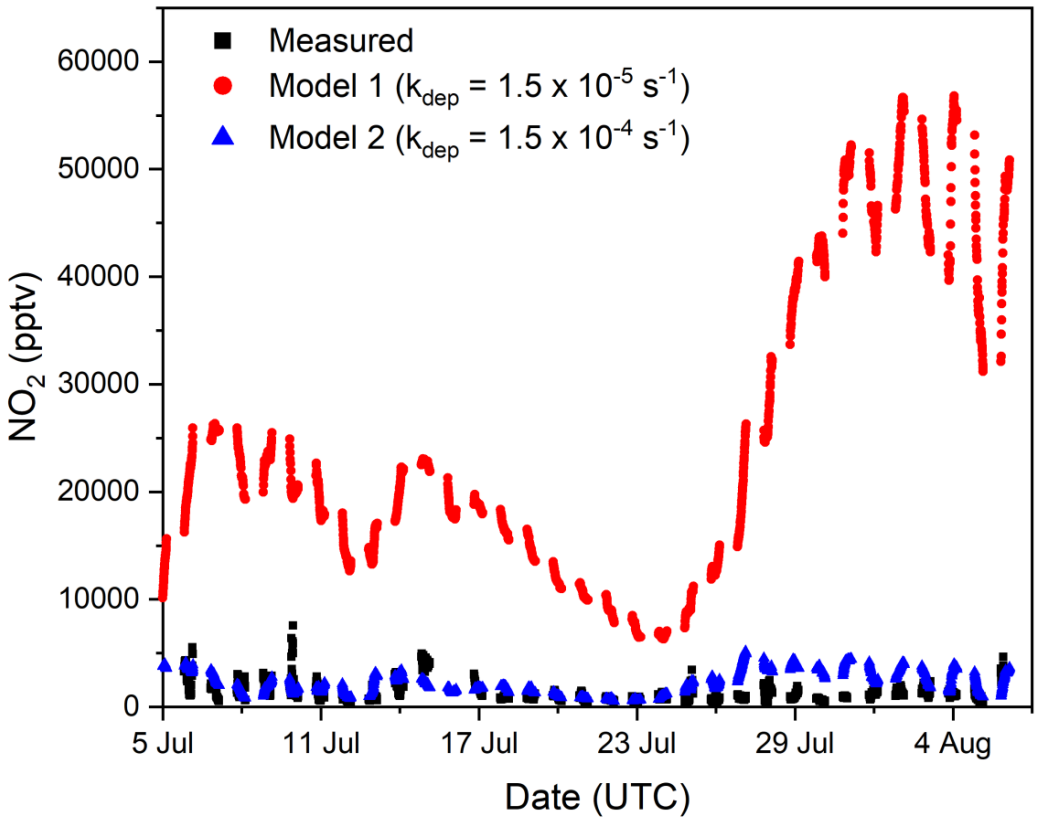

Figure 9: Time-series of measured nighttime NO_2 mixing ratios during TO2021 (black squares) and modelled NO_2 mixing ratios using deposition loss constants of 1.5 x 10^{-5} s^{-1} (Model 1, red circles) and 1.5 x 10^{-4} s^{-1} (Model 2, blue triangles).

https://doi.org/10.5194/acp-2022-163
Preprint. Discussion started: 7 March 2022

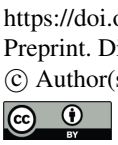

Atmospheric Chemistry and Physics Discussions

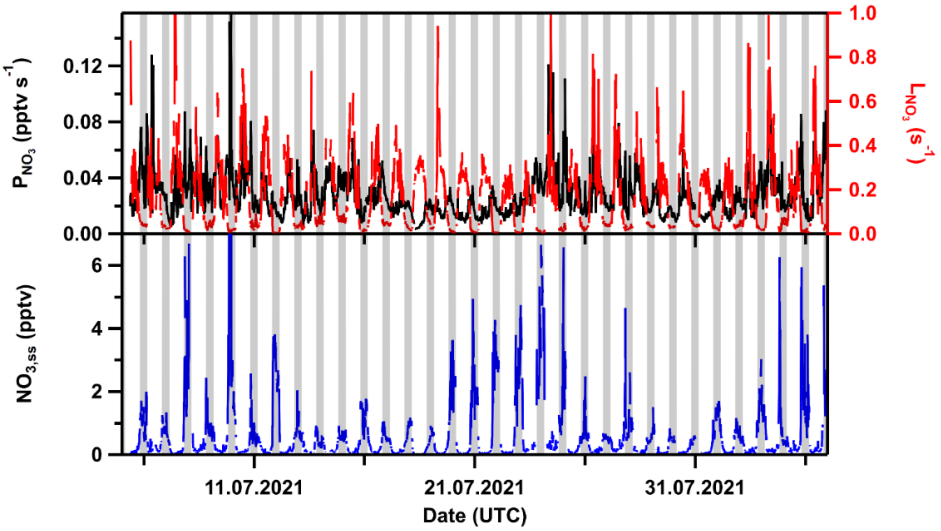

Figure 10: Upper panel: NO_3 production (left) and loss rates (right) during TO2021. Lower panel: steady-state NO_3 mixing ratios. Ticks represent 00:00 UTC. Grey shaded areas denote nighttime.

https://doi.org/10.5194/acp-2022-163
Preprint. Discussion started: 7 March 2022

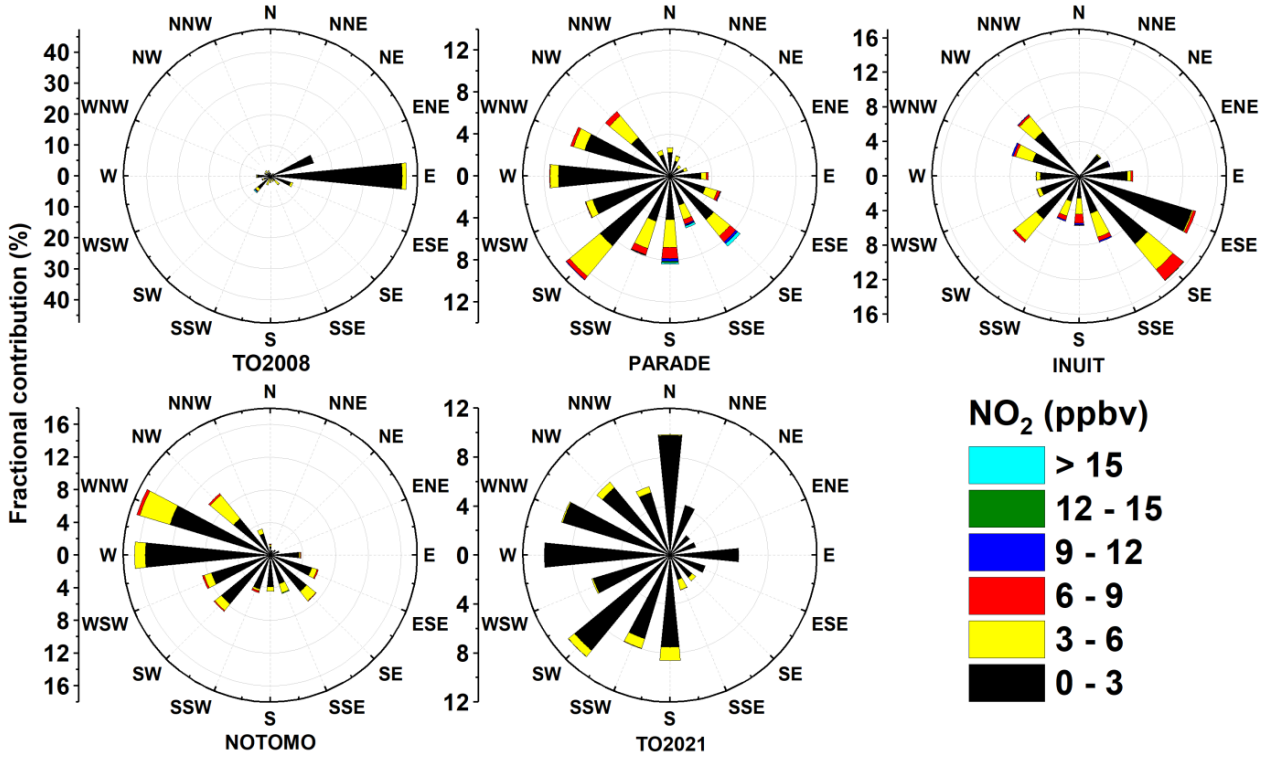

835 **Figure 11:** Wind roses indicating the dependence of NO_2 mixing ratio on the wind direction during TO2008, PARADE, INUIT, NOTOMO and TO2021. Wind directions were provided by HLNUG for TO2008 and NOTOMO, by a weather station in PARADE and INUIT (Drewnick et al., 2012) and by the German meteorological service DWD in TO2021.

https://doi.org/10.5194/acp-2022-163
Preprint. Discussion started: 7 March 2022

Atmospheric Chemistry and Physics Discussions

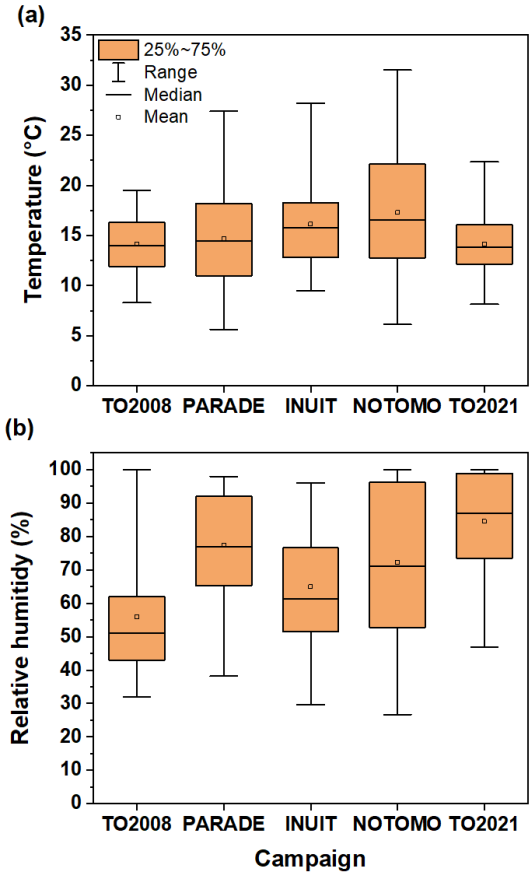

840 **Figure 12:** Distributions of (a) temperature and (b) relative humidity during five campaigns at the Kleiner Feldberg between 2008 and 2021. Boxes represent the range between the first and third quartiles, whiskers denote the full range of values.

https://doi.org/10.5194/acp-2022-163
Preprint. Discussion started: 7 March 2022

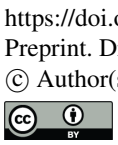

Atmospheric Chemistry and Physics Discussions

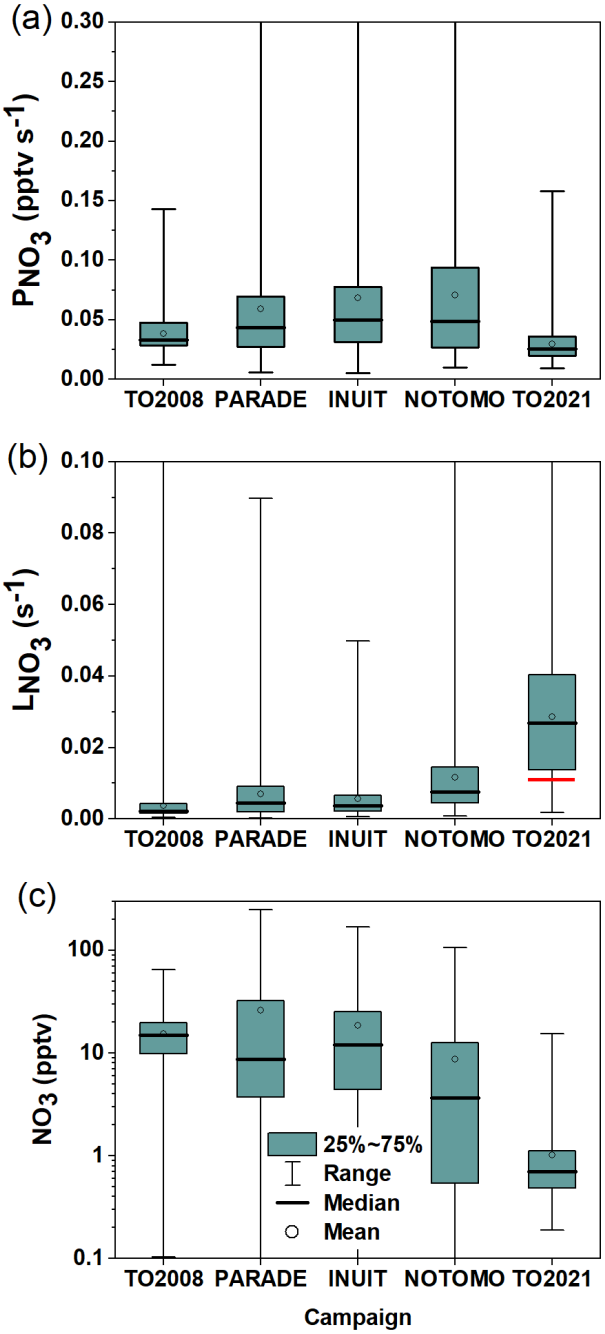

845 **Figure 13:** NO_3 production rates (a), loss rates (b) and mixing ratios (c) measured during 5 campaigns on the summit of Kleiner Feldberg between 2008 and 2021. Boxes represent the range between the first and third quartiles, whiskers denote the full range of values. The red line represents the median of directly measured k^{NO_3} during TO2021 at nighttime.

CHAPTER 7

NO_3 reactivity inside a laboratory

The results of the following chapter have not yet been published and deal with a pilot study on indoor measurements of NO_3 mixing ratios and NO_3 reactivity. Together with measurements of NO_2, O_3 and NO_x, not only the NO_3 production rate via R20 (see Eq.2.2) but also the important NO_3 loss rates through R22 and R25 become accessible. This test measurement serves to estimate, whether there are conditions during which NO_3 may become a significant indoor oxidant.

Author contribution
I did all measurements except for NO_x and NO_2, performed the presented analysis and wrote the chapter.

7.1 Introduction

The majority of human lifetime is spent inside, which is why indoor air quality is in the focus of current research (Klepeis et al., 2001). Similarly to tropospheric chemistry outdoors, the major oxidants are O_3, OH and NO_3 (Weschler et al., 1992; Weschler and Shields, 1997). Whereas the role of O_3 and OH are thoroughly investigated (Weschler and Shields, 1996; Weschler, 2000; Carslaw et al., 2017), studies about the role of the nitrate radical during indoor oxidation are very limited (Nøjgaard, 2010; Arata et al., 2018). Especially considering the diminished NO_3 photolysis rates that are expected to occur indoors, the nitrate radical may become a more potent oxidizing agent (Weschler et al., 1992). Given the fact that terpenes, which are highly reactive towards NO_3, often become abundant in indoor environments due to their occurrence in cleaning products, the NO_3 radical may be a dominant oxidizing agent considering typical indoor concentrations of OH, O_3 and NO_3 (Nazaroff and Weschler, 2004). As depicted

in Fig. 2.1, the NO_3 production (and its whole subsequent chemistry) relies on the abundance of ozone and NO_2. However, predominantly in residential, unventilated environments with high anthropogenic impact, indoor ozone is rapidly depleted (Zhang and Lioy, 1994). However, indoor ozone (and NO_x) concentrations are often elevated in buildings equipped with ventilation systems (Weschler, 2000) so that indoor NO_3 production rates potentially increase, and measurable steady-state concentrations of NO_3 may occur in indoor environments. Arata et al. (2018) detected several pptv of NO_3 in a residential kitchen, as long as the NO_3 production rate was artificially forced high enough by continuous addition of 40 ppbv O_3 with an ozone generator. This observation underlines that in (un)ventilated rooms, high NO_3 loss rates make it difficult to assess the impact of the nitrate radical. Up to now, no direct indoor NO_3 reactivity measurements have ever been reported. In addition, with outbreak of the COVID-19 pandemic, the thorough ventilation of indoor environments is favoured (Bhagat et al., 2020; Shah et al., 2021), which should also support the transport of O_3 and NO_x into the rooms. A simultaneous indoor measurement of NO_3 mixing ratios, NO_3 production rate and NO_3 reactivity would thus help to gain a deeper insight into the fate of NO_3 radicals in this closed environment. For that reason, the nitrogen oxides NO, NO_2, NO_3 and N_2O_5 were measured together with O_3 and NO_3 reactivity inside a laboratory serving as a ventilated test-indoor-environment over a weekend period in October 2021.

7.2 Experimental

The three CRDS instruments deployed to quantify NO, NO_2, NO_3, N_2O_5 mixing ratios and NO_3 reactivity were already described in Chapter 4, which is why descriptions of these below mostly focus on modifications. The indoor environment, a ventilated laboratory of the MPIC, is described and characterized subsequently.

7.2.1 Instrumentation

NO_3 reactivity

Briefly, the underlying measurement principle of this set-up is based on comparing the NO_3 mixing ratios observed in synthetic air (which forms the reference point of no NO_3 reactivity, i.e. $k^{NO_3} = 0$) with that in ambient air. To achieve this, synthetic or ambient air is mixed with $\sim$ 30-50 pptv of NO_3 provided by an in-situ source based on the subsequent oxidation of NO by O_3 (R4 and R20). In a fluoroethylenepropylene-coated (FEPD-121, Chemours) reactor, this mixture is allowed to react within the residence time of 10.5 s. The residual NO_3 is sampled through an injector inside the flow-tube to the cavity, where it is quantified with means of CRDS at a wavelength of 662 nm. During the residence in the flow-tube, the resulting NO_3 concentration is not only determined by the loss process of interest, i.e. NO_3 + VOCs (R25), but also by reaction with NO (R22), the thermal equilibrium to N_2O_5 and NO_2 (R23) and loss

on the reactor walls (with loss rate k_{wall} = 0.001 s^{-1}). As presented in Liebmann et al. (2017), a numerical simulation procedure taking measured NO and NO_2 mixing ratios into account is carried out in order to correct for the impact of these processes so that the NO_3 reactivity exclusively towards VOC, named k^{NO_3}, is deduced. The instrument's lower LOD is typically 0.005 s^{-1}. Diluting highly reactive ambient air with synthetic air extends the upper LOD to 1.7 s^{-1}. The total uncertainties are mostly determined by the numerical simulation procedure in polluted environments like the laboratory and highly dependent on the ratio between NO_2 and k^{NO_3} (Liebmann et al., 2017).
Air was sampled with 3 standard (STP) litres per minute (SLPM) through a ca. 1.5 m 1/4 inch (in.) outer diameter (OD) PFA tube equipped with a polytetrafluoroethylene (PTFE) membrane filter (2 µm pore, 47 mm diameter, Pall Corp.).

NO_3 and N_2O_5

NO_3 and N_2O_5 mixing ratios were monitored with two cavities of the 5-channel CRDS setup that was used for the study in Chapter 5 and is thoroughly described in Sobanski et al. (2016a). Both cavities are also based on the detection of NO_3 at a wavelength of 662 nm using a laser diode modulated at 625 Hz. One cavity is thermostated to 303 K and only detects ambient NO_3, while the second one is equipped with a Teflon-coated quartz glass tube connected upstream, both thermostated to 373 K. All ambient N_2O_5 is dissociated to NO_3 (R26) prior to entering the second cavity, thus measuring NO_3 + N_2O_5. The NO_3 transmission through both cavities was found to be 89 %, so N_2O_5 is deduced by simple subtraction of NO_3 mixing ratios from the channel with unheated inlet. The NO_3 and N_2O_5 measurements are associated with ca. 25 % uncertainty. The LODs for NO_3 and N_2O_5 were 1.5 and 3.5 pptv respectively. Air was sampled with a total flow of 15 SLPM through 1 m 1/4 in. PFA tubing and a PTFE membrane filter (2 µm pore, 47 mm diameter, Pall Corp.).

NO_x and NO_2

NO_x and NO_2 mixing ratios were monitored with the TD-CDRS instrument as characterized in Friedrich et al. (2020). The setup features two cavities both operated with a square-wave modulated laser diode at a wavelength of 405 nm and is generally able to detect NO_2 at ambient temperature. Prior to the first cavity, an excess amount of O_3 is added to the sampled ambient air and passed through ca. 1 m 1/2 in. PFA tubing in order to convert all NO to NO_2 (R4). This way, the sum of NO and NO_2 (NO_x) is detected. The second cavity, usually used to detect NO_y, was modified for this experiment and directly samples 3 SLPM ambient air (without O_3 addition) through a Teflon membrane filter (see above), so that only NO_2 is detected. NO mixing ratios were then derived by subtracting NO_2 from NO_x. For the NO_2 measurement, the LOD is 41 pptv and the total uncertainty is 8 %. In case of the NO mixing ratios, the LOD is 98 pptv and the total measurement uncertainty is 11 %.

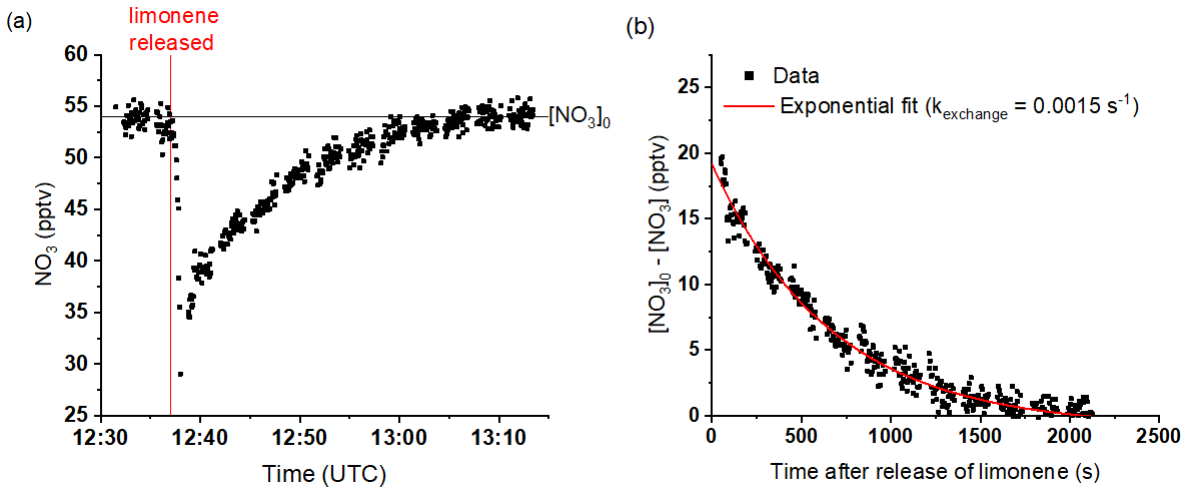

Figure 7.1: *Sampling diluted ambient air with the NO_3 reactivity setup before and after opening a limonene bottle inside the laboratory at 12:37 UTC. (a) Time series of NO_3 mixing ratio in the flowtube. (b) Difference between NO_3 mixing ratios before and after the release of limonene. The red line represents an exponential decay fit.*

Other measurements

O_3 mixing ratios were recorded with a commercial ozone monitor (2B Technologies, model 205) that has a detection limit of 2 ppbv and and delivers values associated with an uncertainty of 5 %. Actinic fluxes were measured with a spectral radiometer (Metcon GmbH) and, with the help of evaluated quantum yields and absorption cross-sections, converted to photolysis frequencies ($\jmath$) of NO_3. Relative humidity and temperature were measured with a commercial sensor (1st Innovative Sensor Technology, HYT939) at the NO_3 reactivity setup by sampling separately 0.5 SLPM ambient air through ca. 1 m 1/4 in. PFA tubing.

7.2.2 Laboratory and characterization

The laboratory used to carry out is darkened and has a size of $\sim$ 90 m^3. During the whole measurement period the instruments quantifying the above-mentioned trace gases were the only experiments operated. In addition to these three CRDS setups, the SCHARK is placed inside the laboratory. The chamber was flushed with 5 SLPM synthetic air throughout the whole measurement period. To avoid contamination of the sampled air by the experiments itself, any air exiting the CRDS setups and the chamber was lead to an exhaust. The NO bottles used to run the CRDS setups were stored in a separate ventilated safety cabinet and each line thoroughly checked for leakages in order to ensure that the indoor chemistry is only impacted by the exchange with outdoor air from the ventilation system which was operated in *night-mode* (i.e. reduced exchange rate) throughout the whole period. Room light was switched off during the whole weekend and at night during work days.

Important parameters to characterise are the mixing time and air exchange rate within the laboratory. For this reason, indoor air (diluted in humidity-matched synthetic air) was sampled

with the NO_3 reactivity setup and mixed with $\sim$ 50 pptv NO_3 originating from the source. During a period with fairly constant ambient NO_3 reactivity, a limonene bottle ((*S*)-(−)-limonene, 96 %, 100 *mL*, Sigma-Aldrich) was opened in the middle of the laboratory room for 15 s at 12:37 UTC. The time series of remaining measured NO_3 with the FT-CRDS setup is shown in Fig.7.1a: At 12:38 UTC, limonene already reaches the FT-CRDS setup in one of the corners of the room and the NO_3 sharply decreases. This observation thus suggests that homogenisation of the air is achieved within 1 minute. Furthermore, it takes $\sim$ 20 minutes to re-establish the initial NO_3 mixing ratio ($[NO_3]_0$) prior to limonene exposure.

The lifetime of limonene serves as measure for the air exchange rate inside the laboratory. To deduce the exchange rate from the NO_3 signal, the difference between $[NO_3]_0$ and measured NO_3 was plotted against the time t with the time-point of limonene emission defined as $t = 0s$. Figure 7.1b shows the resulting plot and an exponential fit of the data implying an air exchange rate $k_{exchange}$ of 0.0015 s^{-1} during reduced fan operation mode. This corresponds to an air exchange rate of 5.4 h^{-1}, a value that is comparable to those found in buildings equipped with ventilation systems and in other indoor air studies (Bekö et al., 2020). On the other hand, this room is not representative for residential indoor environments, where air exchange rates are with typically $\sim$ 0.5 h^{-1} significantly lower (Arata et al., 2021). These considerations are only valid under the condition that during the measurement, air exchange was the only loss process for limonene inside the laboratory. Assuming potential steady-state indoor concentrations of 1 pptv NO_3 (only expected for periods when NO is completely depleted), 18 ppbv O_3 (as observed in this room, see below) and 10^5 molecules cm^{-3} OH as most potential oxidizing agents and using the corresponding IUPAC-recommended rate coefficients would lead to a summed loss rate of $\sim$ 4 x 10^{-4} s^{-1}. Gas-phase reactions could consequently contribute to 27% to the observed overall loss rate in Fig. 7.1b, which would reduce $k_{exchange}$ to 4 h^{-1}. The role of deposition processes of limonene on surfaces or particles available in the laboratory are difficult to constrain, which is why this experiment was repeated with 2,3-dimethyl-2-butene (DMB). DMB has a similar reactivity towards NO_3 and OH and a rate coefficient only one order of magnitude higher for the reaction with O_3 (IUPAC, 2022). Loss due to gas-phase oxidation should thus be comparable to that of limonene. On the other hand, DMB is with a vapour pressure of 133 hPa at 293 K much more volatile than limonene (2.04 hPa at 293 K) (GESTIS, 2022) and, as a consequence, deposits less efficiently on surfaces. Exponential regression of the data yields an exchange rate of 4.32 h^{-1} (see Fig. D.1). The initially derived value of 5.4 h^{-1} hence serves as an upper limit.

Impact of outside air

The laboratory is located inside the Max Planck Institute for Chemistry building which is in direct vicinity to commercial, residential as well as university buildings, in the suburb of Mainz ($\sim$ 5 km to the city center) and surrounded by busy two- and four-lane roads (Friedrich et al., 2020). Mainz itself (217 000 inhabitants) is situated in the highly populated Rhine-Main area

close to Frankfurt and Wiesbaden. Air sampled from outside (and inside) is thus expected to be polluted with mostly anthropogenic emissions. Due to usage of the ventilation system, the air composition inside the laboratory should be highly impacted by the air composition outside. The chemistry considered in these experiments is mainly determined by the abundance of O_3 and NO_2. To get an idea how much the inside air differs from the outside air, NO_2 and O_3 mixing ratios were subsequently measured inside and outside (same inlet line passed through a port, 12 m above ground level).

Figure 7.2 shows the resulting time-series and reveals that the inside to outside ratio (I/O ra-

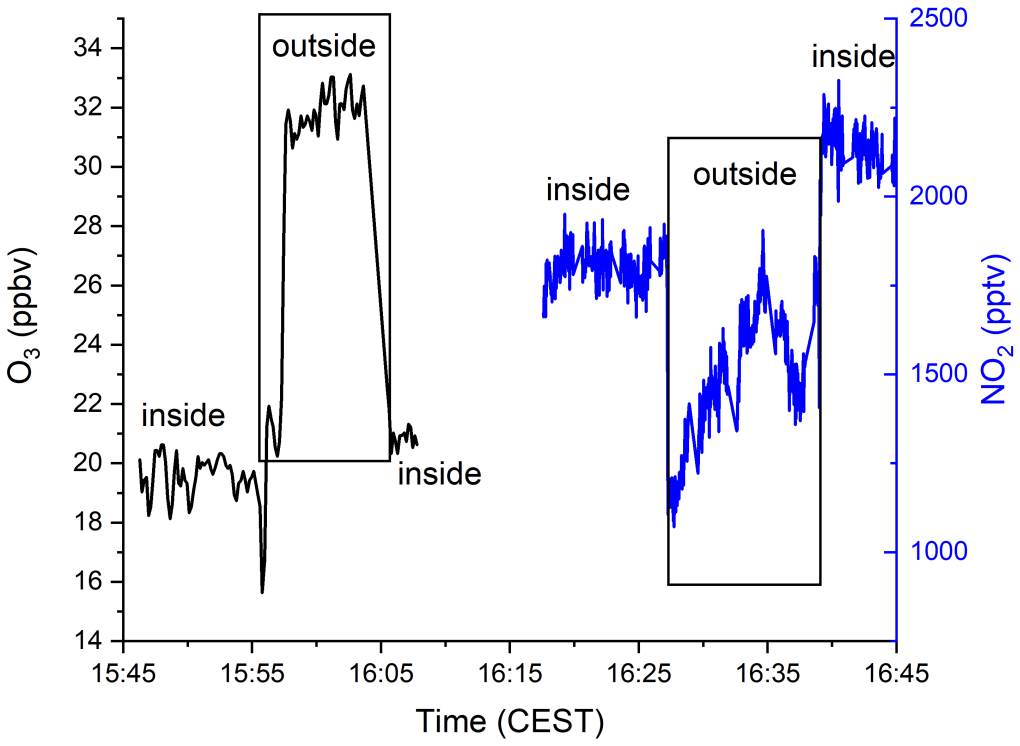

Figure 7.2: *Comparison between mixing ratios of O_3 (black) and NO_2 (blue) inside the laboratory and outside the building.*

tio) of O_3 is <1, whereas in case of NO_2 a value > 1 is obtained. This observation implies that indoors, O_3 is effectively titrated by NO which produces further NO_2. As shown below, this explanation is consolidated by simultaneous measurements of NO, NO_2 and O_3 (see below). One aspect to take into account is the potential loss of O_3 and NO_x during their transport through the ventilation system. The effect of heterogeneous losses of organic compounds of lower volatility within the ventilation system may be of even higher significance.

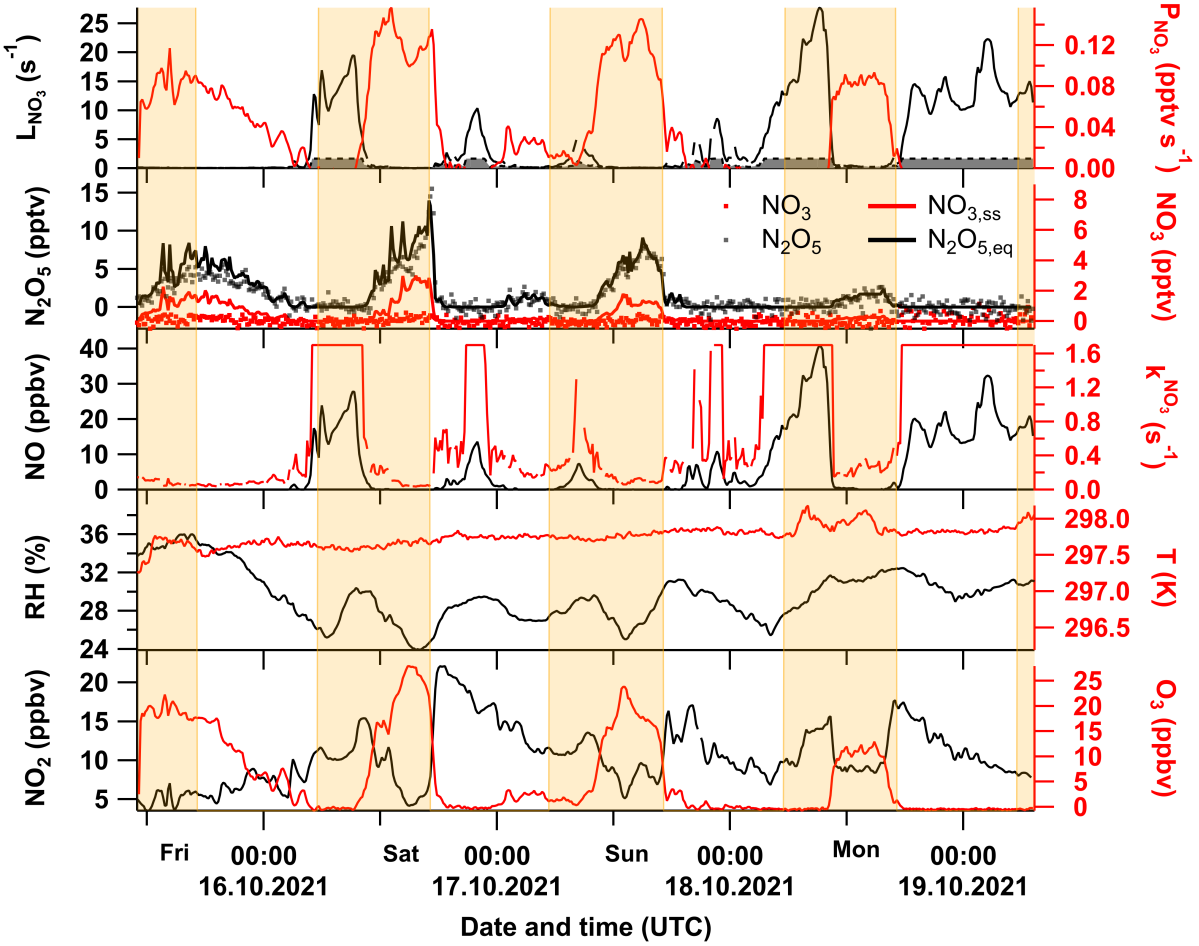

Figure 7.3: *4-day period of NO_3, NO_2, NO, N_2O_5, NO_3 reactivity, relative humidity (RH) and temperature (T) measurements inside a laboratory. The grey area in the upper panel shows the contribution of k^{NO_3} to L_{NO_3}. In the second panel, calculated NO_3 (red) and N_2O_5 (black) mixing ratios using Eq. 7.2 and Eq. 7.3 are shown with solid lines, while measured values are represented by squares in the same color. Yellow shaded areas mark daytime.*

7.3 Results and Discussion

An overview of the data set is depicted in Fig 7.3. The corresponding approximate sunrise and sunset times are marked in orange and the plot reveals that most of the N_2O_5 was measured during the day. The temperature inside the laboratory was 297-298 K with relative humidities between 30-37 %. The O_3 and NO_2 mixing ratios are strongly anti-correlated during the day and vary between 0-25 ppbv and 4-20 ppbv respectively. NO was also highly variable ranging from values below the LOD of 98 pptv and 40 ppbv. As soon as several ppbv of NO were present in the room, the NO_3 reactivity setup reached its upper detection limit (1.7 s^{-1} in this configuration) since all NO_3 from the source was titrated thus impeding the quantification of k^{NO_3}. During NO-depleted periods, the VOC-induced NO_3 reactivity was typically around 0.1 - 0.4 s^{-1}. Several pptv of N_2O_5 were detected under these conditions, whereas the NO_3 signal remained below the instrument's LOD of 1.5 pptv at all time.

7.3.1 Comparison to steady-state calculations

In order to evaluate the reliability of the NO_3 and N_2O_5 measurements, steady-state calculations of NO_3 as described in Chapter 2 were performed. In this case, the NO_3 loss rate is the sum of the directly measured (VOC-induced) NO_3 reactivity (k^{NO_3}, R25) and the NO-induced loss (R22):

$$L_{NO_3} = k^{NO_3} + k_{22} \cdot [NO] \tag{7.1}$$

Rearranging Eq. 2.3 in Chapter 2 leads to steady-state NO_3 concentrations $[NO_3]_{ss}$:

$$[NO_3]_{ss} = \frac{k_{20}[O_3][NO_2]}{L_{NO_3}} \tag{7.2}$$

N_2O_5 mixing ratios $[N_2O_5]_{eq}$ can be derived according to R23 using the IUPAC-recommended, temperature-dependent equilibrium constants K_{eq} (Wayne et al., 1991; Brown, 2003; Crowley et al., 2010):

$$[N_2O_5]_{eq} = K_{eq}[NO_2][NO_3]_{ss} \tag{7.3}$$

Overall uncertainties in $[NO_3]_{ss}$ and $[N_2O_5]_{eq}$ take uncertainties in measured mixing ratios (NO_2, O_3), NO_3 reactivity (variable) and rate coefficients (k_{20}, k_{23}, k_{-23}) into account. During NO-rich periods, neither NO_3 nor N_2O_5 was detected because overall NO_3 loss rates clearly exceed NO_3 production rates. During these periods, the O_3 concentrations drop below the monitor's LOD of 2 ppbv, whereas NO mixing ratios reach the ppbv range because O_3 is consumed in reaction with NO (R4). This is why each sharp drop of O_3 mixing ratios close to the LOD is accompanied by both sharply increasing NO and NO_2 mixing ratios. At the same time, NO_3 production rates are directly correlated with the O_3 concentrations and approach zero ($\ll$ 0.005 pptv/s), while the NO_3 loss rates mostly follow the NO concentrations and surpass the upper LOD of 1.7 s^{-1}. The lack of NO_3 (and N_2O_5) is thus supported by both low NO_3 production rates and titration with NO.

On the other hand, there are periods with N_2O_5 mixing ratios well above the CRDS instrument's LOD. Up to 12 pptv N_2O_5 were detected on a Saturday afternoon inside the laboratory, when (1) the NO_3 production rate increased to approximately 0.15 pptv $\cdot s^{-1}$, (2) no detectable amounts of NO were present and (3) the NO_3 reactivity was low. Note that in the analysis NO_3 loss via photolysis (mostly through the path R21) is not important. To analyse the system as long as significant amounts of N_2O_5 (and NO_3) were abundant in the laboratory, a case study focussing on the daytime period on the 17th October is considered in more detail in Fig.7.4. The temperature was fairly constant at 297.8 K with relative humidities between 25-30 %. NO_2 was always present with mixing ratios varying between 5 and 15 ppbv. At the beginning, between 8 and 10 UTC, neither NO_3 nor N_2O_5 is measured which agrees with steady-state calculations. At that time, the reaction with NO is the dominant loss process of NO_3 with loss rates between 1 and 5 s^{-1}. After 10 UTC, NO concentrations decrease from 2 ppbv to below 98 pptv, which is why O_3 mixing ratios and NO_3 production rates increase to $\sim$ 20 ppbv and 0.12 pptv s^{-1} respectively. During this period, reaction of NO_3 with VOCs becomes the only remaining loss

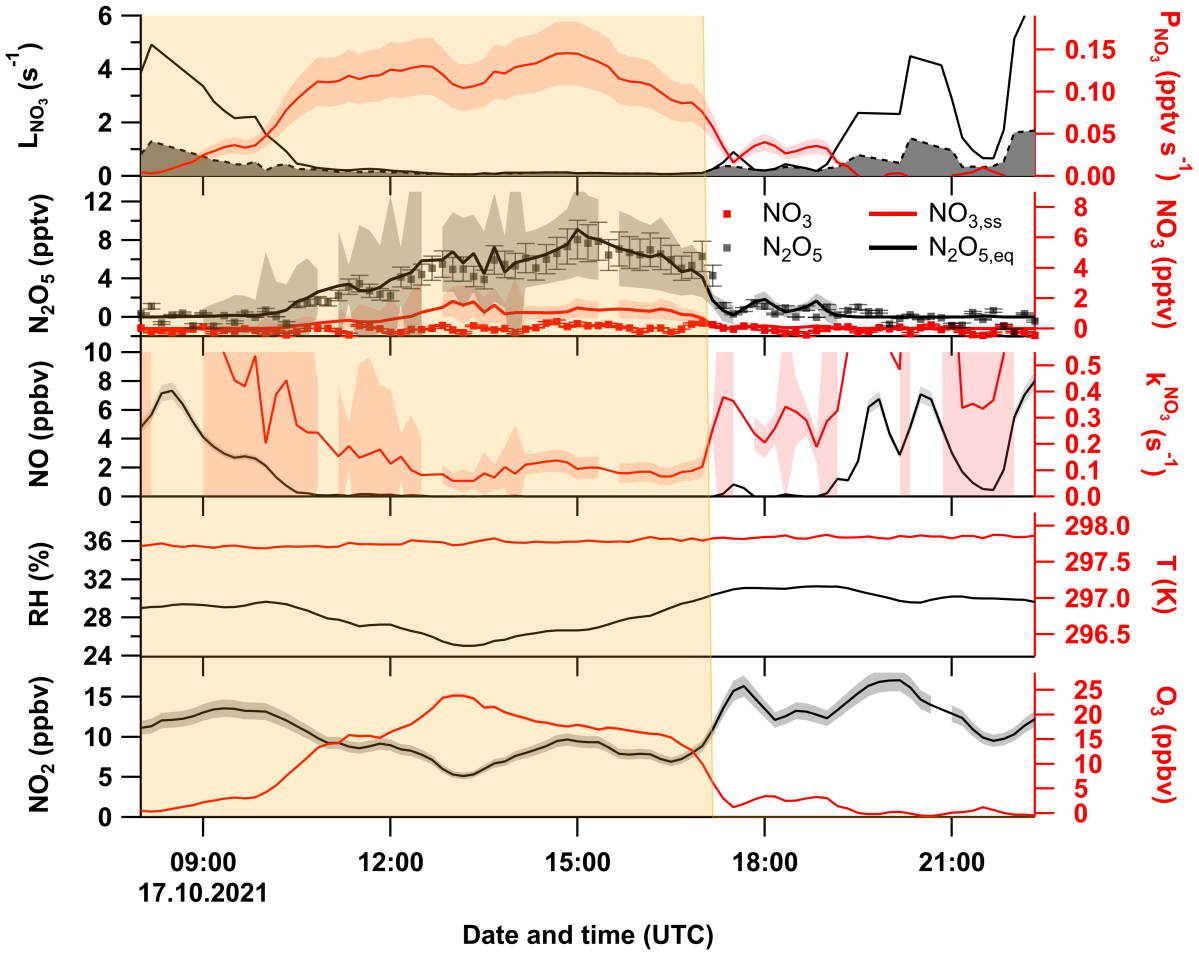

Figure 7.4: *Case study of the 4-day period of NO_3, NO_2, NO, N_2O_5, NO_3 reactivity, relative humidity (RH) and temperature (T) measurements inside a laboratory. Shaded areas represent the total measurement uncertainty of trace gas measurements or calculated steady-state NO_3/N_2O_5 mixing ratios. Error bars denote associated uncertainties in NO_3 and N_2O_5 measurements. See caption of Fig. 7.3 for further details.*

process with a rate of $\sim 0.1\ s^{-1}$. According to Eq. 7.2, this would lead to a steady-state NO_3 mixing ratio of $\sim$ 1.2 pptv and N_2O_5 mixing ratios ranging between 4 and 8 pptv. While the measured N_2O_5 concentrations are well reproduced by Eq. 7.3, no NO_3 was detected during the whole measurement period, clearly disagreeing with steady-state mixing ratios obtained with Eq. 7.2. In this calculation neither photolysis of NO_3 nor deposition of NO_3 or N_2O_5 were considered which would increase L_{NO_3} and hence decrease steady-state NO_3 concentrations. However, due to the thermal equilibrium between NO_3 and N_2O_5, any additional loss of NO_3 would lead to a decrease in the observed N_2O_5 mixing ratios and vice versa. Since measured and calculated values of N_2O_5 mixing ratios agree while that of NO_3 do not, selective loss of NO_3 during the sampling process forms a more likely explanation: NO_3 and N_2O_5 were sampled through a short (< 1 m) 1/4 in. OD PFA tubing with 15 SLPM to keep the residence time short enough. However, the air was passed through a Teflon (PTFE) filter that was not changed between Friday and Monday. During field measurements it is common to change the filter on an hourly basis to avoid losses on the filter that become contaminated with particles

over time (Sobanski et al., 2016a). As shown in Fig.D.2 in Appendix D, the inlet filter significantly became contaminated during the weekend and depending on the composition of the particles NO_3 may be lost on the filter, while N_2O_5 is not. A previous study sampling urban aerosols in the same area (ca. 300 m apart from this site) revealed that NO_3 readily deposited on such particles, while N_2O_5 was lost much less efficiently ($\gamma_{NO_3}/\gamma_{N_2O_5} > 15$ with γ being the heterogeneous uptake coefficient) (Tang et al., 2010). This would support the scenario that the heterogeneous uptake of N_2O_5 is insignificant compared to the indirect N_2O_5 loss via NO_3 + VOCs, while all ambient NO_3 is removed by the contaminated filter surface.

7.3.2 Fate of the NO_3 radical in the laboratory

The comparison between the direct measurements and steady-state calculations of NO_3 and N_2O_5 implies that the reactions with NO and VOCs are the only important NO_3 loss processes in the laboratory, the contribution of heterogeneous reactions and photolysis are negligible. The abundance of airborne particles is (as verified by measurements in the laboratory conducted by using a scanning mobility particle sizer) lower than outside, which appears plausible considering that the air is passed through the ventilation system prior to entering the room. Negligible NO_3 photolysis in indoor environments in the absence of natural sunlight is known (Weschler et al., 1992; Carslaw, 2007; Arata et al., 2018). This was verified with measurements of actinic fluxes within the laboratory. As depicted in Fig. D.3 in the Supplement, photolysis rates of NO_3 were well below 5 x 10^{-4} s^{-1}. In the direct vicinity to the room lights, J_{NO_3} increases to up to 0.004 s^{-1}, which is still of minor importance compared to the observed measured NO_3 reactivities mostly between 0.1 and 0.4 s^{-1} during VOC-dominated periods. In order to quantify the fraction F of NO_3 that is lost to VOCs, the ratio between the directly measured NO_3 reactivity k^{NO_3} and the overall NO_3 loss rate L_{NO_3} was calculated:

$$F = \frac{k^{NO_3}}{L_{NO_3}} = \frac{k^{NO_3}}{k^{NO_3} + k_{20}[NO]} \tag{7.4}$$

A time-series of the resulting F compared with k^{NO_3} from this 4-day period is depicted in Fig. 7.5. It is evident that NO_3 + VOC is a significant contributor to NO_3 at all times (mostly 20-40%) and > 90 % during some periods, when N_2O_5 (and thus calculated NO_3) was > LOD. At the same time, NO_3 reactivities (0.05-0.2 s^{-1}) are lowest during this time period. VOC measurements are not available making an assignment of the observed reactivities to individual trace gases impossible. Given the urban location of the institute, isoprene or monoterpenes are not expected to be present at high mixing ratios. Moreover, the laboratory was not cleaned during the measurements, so that monoterpenes originating from cleaning products (Arata et al., 2021) should not contribute. Kurtenbach et al. (2002) identified that cresols are emitted from traffic and can become a significant sink for NO_3 in urban environments. On the other

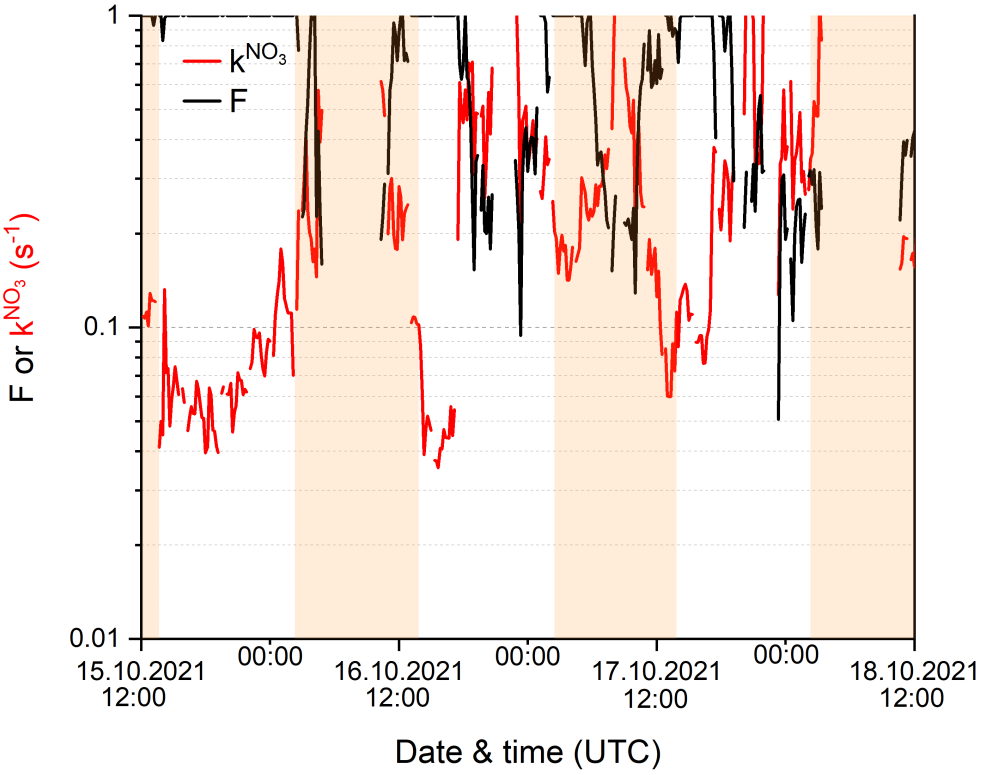

Figure 7.5: *Time series of the directly measured NO_3 reactivities (red) and its fractional contribution F to the overall NO_3 loss rate (black). Yellow shaded area represents daytime period outside.*

hand, given their low vapour pressure of 0.15 hPa at 298 K (*p*-cresol, GESTIS (2022)) and high reactivity to OH radicals (IUPAC, 2022) it is very unlikely, that cresols are transported to the laboratory. Moreover, compounds related to traffic emissions are expected to coincide with periods when NO_x concentrations are high. Turning the focus to anthropogenic emissions, short-chained alkenes such as propene, pentene or substituted butenes (Warneke et al., 2007) are much more likely to contribute to the observed NO_3 reactivities.

7.4 Summary and conclusions

NO_3 reactivity was measured together with NO, NO_2, O_3, N_2O_5 and NO_3 mixing ratios over a 4-day-period inside a ventilated, dimmed laboratory. Detectable amounts of N_2O_5 (up to 12 pptv) only arose when NO was quantitatively converted to NO_2 but O_3 was left to produce NO_3. No NO_3 was detected at any time which is most probably owed to inlet filter losses. Intercomparison between measured N_2O_5 mixing ratios with those derived from a steady-state approximation using measured k^{NO_3}, NO, NO_2, O_3, the corresponding rate coefficients and the equilibrium constant were in agreement within uncertainties, confirming that neither heterogeneous reactions nor photolysis are relevant NO_3 loss paths in this study. Furthermore,

the calculations revealed that steady-state concentrations of up to 2 pptv of NO_3 were expected inside the laboratory. Reactions with VOCs and NO form the only relevant loss paths with VOC-induced losses contributing mostly with between 20-100% rendering NO_3 + VOCs a competitive loss path during most of the time inside the laboratory. This consolidates the hypothesis that NO_3 may become a significant indoor oxidant for VOCs, as longs as the NO_3 production rate is high enough and at the same time NO_3 (and O_3) not entirely consumed by NO. Finally, this pilot study suggests that further measurements of NO_3 mixing ratios and NO_3 reactivity especially together with VOC measurements in other (ventilated) indoor environments are required.

CHAPTER 8

Conclusions and outlook

In the scope of this work, the NO_3 + isoprene system was investigated in two chamber studies, namely (1) during the NO3ISOP campaign with the SAPHIR chamber in Jülich and (2) in laboratory experiments with our own Teflon chamber SCHARK.
The analysis obtained during NO3ISOP focused on NO_3 reactivity and direct NO_3 measurements in order to investigate the role of the NO_3 radical during the isoprene oxidation process. Direct NO_3 reactivity measurements revealed that NO_3 reactivity was entirely determined by isoprene suggesting that secondary oxidation of closed-shell products forms an insignificant loss path. Nonstationary-state calculations using NO_3 production rates and measured NO_3 mixing ratios according to McLaren et al. (2010) expands the view to overall NO_3 loss rates, i.e. every NO_3 loss path including losses on chamber walls and reactions with radicals is taken into account. Intercomparison between measured, calculated and modelled NO_3 reactivities implies that the rate coefficient for the reaction between NO_3 and isoprene-derived RO_2 is twice the value expected from reference alkyl peroxy compounds such as the ethyl peroxy radical (Jenkin et al., 2015; IUPAC, 2022). For isoprene-derived RO_2, this rate coefficient has never been directly measured so that kinetic measurements of the latter are required to test previous results based on model calculations (Hjorth et al., 1990; Dewald et al., 2020). The fate of the initially formed RO_2 radicals determines which kind of products are actually formed in this system and consequently also the yield of alkyl nitrates (Schwantes et al., 2015; Wennberg et al., 2018) that might contribute to the sequestering of NO_x.
The second chamber study carried out with the SCHARK dealt with the detection (based on TD-CRDS) of the main product species formed by the NO_3 + isoprene system, namely alkyl nitrates. In contrast to commonly used reference compounds for ANs such as isopropyl nitrate, isoprene-derived organic nitrates show broad dissociation profiles interfering with the detection of PNs. Laboratory investigations imply that this phenomenon is linked to ozone-

assisted heterogeneous reactions on the quartz glass walls of the thermal-dissociation inlets. This underlines the importance of characterizing instruments with compounds actually abundant in the atmosphere and, in addition, as close as possible to ambient conditions, i.e. humidity and complex mixtures, that can be found in the troposphere. Note that alkyl nitrates in field measurements may also originate from other VOCs than isoprene (Ng et al., 2017) so that future work should include chamber studies with e.g. NO_3 + monoterpenes. Such experiments should become routine for proper characterization of instruments based on TD so that it can be checked if the newly designed thermal dissociation inlets are also suitable for ANs derived from monoterpenes and verify the reliability of the measurements under real ambient conditions.

NO_3 reactivity was measured during a field campaign (TO2021) on the Kleiner Feldberg. Comparison with VOC measurements showed, that monoterpenes contributed 84% to the measured NO_3 reactivity, while isoprene and sesquiterpenes contributed only 7% and 9% respectively. This emphasizes again the necessity of more chamber studies investigating the reaction between NO_3 and mixtures of monoterpenes in order to assess the role of the nitrate radical in the evolution of the oxidation process. During TO2021, the fractional contribution of k^{NO_3} was on average ca. 16% during the daytime. This is in broad agreement with findings of previous studies (Liebmann et al., 2018, 2019; Foulds et al., 2021) and indicates that even during daytime NO_3 can significantly contribute to alkyl nitrate formation. Because of the abundance of NO even at nighttime on this site, k^{NO_3} contributed 50-60 % at night, which is low compared to previous field measurements (Liebmann et al., 2018, 2019). Measurements of NO_x fluxes near the soil at this site would help to constrain the origin of nighttime NO in particular. Steady-state calculations enabled deduction of NO_3 mixing ratios and allowed comparison to previous NO_3 measurements performed during four other campaigns between 2008 and 2015. The intercomparison underlined the high variability of the results, most likely induced by boundary layer dynamics and lock-down regulations due to the COVID-19 pandemic. Moreover, the intercomparison emphasizes that simultaneous measurements of NO_3 mixing ratios and NO_3 reactivity are desirable, as both measurements complement mutually and potentially allow closure of the nitrogen budget. Finally, further drone-assisted measurements of temperature profiles (or of other parameters) are necessary to investigate the effect of boundary layer dynamics.

Given the sparse availability of indoor NO_3 and NO_3 reactivity measurements, both were measured together with NO, NO_2, O_3 and N_2O_5 inside a laboratory over a four day period. This pilot study showed that N_2O_5 as well as NO_3 are abundant indoors both day and night. Steady-state calculations of N_2O_5 showed good agreement with measured N_2O_5 within uncertainties and demonstrate the power of simultaneous measurements of k^{NO_3} and NO_3. Moreover, given the high variability of the fractional contributions of k^{NO_3} to the overall NO_3 loss rate, it is worth studying the importance of the NO_3 radical in ventilated indoor areas in more detail together with measurements of VOCs.

References

Arata, C., Zarzana, K. J., Misztal, P. K., Liu, Y., Brown, S. S., Nazaroff, W. W., and Goldstein, A. H.: Measurement of NO_3 and N_2O_5 in a Residential Kitchen, Environ. Sci. Technol. Lett., 5, 595–599, doi:10.1021/acs.estlett.8b00415, URL https://doi.org/10.1021/acs.estlett.8b00415, 2018.

Arata, C., Misztal, P. K., Tian, Y., Lunderberg, D. M., Kristensen, K., Novoselac, A., Vance, M. E., Farmer, D. K., Nazaroff, W. W., and Goldstein, A. H.: Volatile organic compound emissions during HOMEChem, Indoor Air, 31, 2099–2117, doi:10.1111/ina.12906, URL https://onlinelibrary.wiley.com/doi/abs/10.1111/ina.12906, 2021.

Atkinson, R. and Arey, J.: Atmospheric Degradation of Volatile Organic Compounds, Chem. Rev., 103, 4605–4638, doi:10.1021/cr0206420, URL https://pubs.acs.org/doi/10.1021/cr0206420, 2003.

Bekö, G., Wargocki, P., Wang, N., Li, M., Weschler, C. J., Morrison, G., Langer, S., Ernle, L., Licina, D., Yang, S., Zannoni, N., and Williams, J.: The Indoor Chemical Human Emissions and Reactivity (ICHEAR) project: Overview of experimental methodology and preliminary results, Indoor Air, 30, 1213–1228, doi:10.1111/ina.12687, URL https://onlinelibrary.wiley.com/doi/abs/10.1111/ina.12687, 2020.

Berden, G., Peeters, R., and Meijer, G.: Cavity ring-down spectroscopy: Experimental schemes and applications, Int. Rev. Phys. Chem., 19, 565–607, doi:10.1080/014423500750040627, URL https://doi.org/10.1080/014423500750040627, 2000.

Bhagat, R. K., Davies Wykes, M. S., Dalziel, S. B., and Linden, P. F.: Effects of ventilation on the indoor spread of COVID-19, J. Fluid Mech., 903, F1–1–F1–18, doi:10.1017/jfm.2020.720, URL https://doi.org/10.1017/jfm.2020.720, 2020.

Biswas, M. S., Pandithurai, G., Aslam, M., Patil, R. D., Anilkumar, V., Dudhambe, S. D., Lerot, C., Smedt, I. D., Roozendael, M. V., and Mahajan, A. S.: Effect of Boundary Layer Evolution on Nitrogen Dioxide (NO_2) and Formaldehyde (HCHO) Concentrations at a High-altitude Observatory in Western India, Aerosol Air Qual. Res., 21, 200 193, doi:10.4209/aaqr.2020.05.0193, URL https://doi.org/10.4209%2Faaqr.2020.05.0193, 2021.

BMU: Climate Action Plan 2050 - Principles and goals of the German government's climate policy, Bundesministerum für Umwelt, Naturschutz und nukleare Sicherheit, URL https://www.bmu.de/fileadmin/Daten_BMU/Pools/Broschueren/klimaschutzplan_2050_en_bf.pdf, last access: 03.02.2022, 2016.

Brown, S. S.: Absorption Spectroscopy in High-Finesse Cavities for Atmospheric Studies, Chem. Rev., 103, 5219–5238, doi:10.1021/cr020645c, URL https://doi.org/10.1021/cr020645c, 2003.

Brown, S. S. and Stutz, J.: Nighttime radical observations and chemistry, Chem. Soc. Rev., 41, 6405–6447, doi:10.1039/C2CS35181A, URL http://dx.doi.org/10.1039/C2CS35181A, 2012.

Brown, S. S., Stark, H., and Ravishankara, A. R.: Applicability of the steady state approximation to the interpretation of atmospheric observations of NO_3 and N_2O_5, J. Geophys. Res.: Atmos., 108, ACH6–1–ACH6–10, doi:https://doi.org/10.1029/2003JD003407, URL https://agupubs.onlinelibrary.wiley.com/doi/abs/10.1029/2003JD003407, 2003.

Brown, S. S., Dubé, W. P., Osthoff, H. D., Stutz, J., Ryerson, T. B., Wollny, A. G., Brock, C. A., Warneke, C., de Gouw, J. A., Atlas, E., Neuman, J. A., Holloway, J. S., Lerner, B. M., Williams, E. J., Kuster, W. C., Goldan, P. D., Angevine, W. M., Trainer, M., Fehsenfeld, F. C., and Ravishankara, A. R.: Vertical profiles in NO_3 and N_2O_5 measured from an aircraft: Results from the NOAA P-3 and surface platforms during the New England Air Quality Study 2004, J. Geophys. Res.: Atmos., 112, 1–17, doi:https://doi.org/10.1029/2007JD008883, URL https://agupubs.onlinelibrary.wiley.com/doi/abs/10.1029/2007JD008883, 2007a.

Brown, S. S., Dubé, W. P., Osthoff, H. D., Wolfe, D. E., Angevine, W. M., and Ravishankara, A. R.: High resolution vertical distributions of NO_3 and N_2O_5 through the nocturnal boundary layer, Atmos. Chem. .Phys., 7, 139–149, doi:10.5194/acp-7-139-2007, URL https://acp.copernicus.org/articles/7/139/2007/, 2007b.

Brown, S. S., deGouw, J. A., Warneke, C., Ryerson, T. B., Dubé, W. P., Atlas, E., Weber, R. J., Peltier, R. E., Neuman, J. A., Roberts, J. M., Swanson, A., Flocke, F., McKeen, S. A., Brioude, J., Sommariva, R., Trainer, M., Fehsenfeld, F. C., and Ravishankara, A. R.: Nocturnal isoprene oxidation over the Northeast United States in summer and its impact on reactive nitrogen partitioning and secondary organic aerosol, Atmos. Chem. Phys., 9, 3027–3042, doi:10.5194/acp-9-3027-2009, URL https://acp.copernicus.org/articles/9/3027/2009/, 2009.

Carslaw, N.: A new detailed chemical model for indoor air pollution, Atmos. Environ., 41, 1164–1179, doi:10.1016/j.atmosenv.2006.09.038, URL https://www.sciencedirect.com/science/article/pii/S1352231006009940, 2007.

Carslaw, N., Fletcher, L., Heard, D., Ingham, T., and Walker, H.: Significant OH production under surface cleaning and air cleaning conditions: Impact on indoor air quality, Indoor Air, 27, 1091–1100, doi:10.1111/ina.12394, URL https://onlinelibrary.wiley.com/doi/abs/10.1111/ina.12394, 2017.

Chameides, W., Lindsay, R., Richardson, J., and Kiang, C.: The role of biogenic hydrocarbons in urban photochemical smog: Atlanta as a case study, Science, 241, 1473–1475, doi:10.1126/science.3420404, URL https://science.sciencemag.org/content/241/4872/1473, 1988.

Crowley, J. N., Schuster, G., Pouvesle, N., Parchatka, U., Fischer, H., Bonn, B., Bingemer, H., and Lelieveld, J.: Nocturnal nitrogen oxides at a rural mountain-site in south-western Germany, Atmos. Chem. Phys., 10, 2795–2812, doi:10.5194/acp-10-2795-2010, URL https://acp.copernicus.org/articles/10/2795/2010/, 2010.

Crowley, J. N., Thieser, J., Tang, M. J., Schuster, G., Bozem, H., Beygi, Z. H., Fischer, H., Diesch, J.-M., Drewnick, F., Borrmann, S., Song, W., Yassaa, N., Williams, J., Pöhler, D., Platt, U., and Lelieveld, J.: Variable lifetimes and loss mechanisms for NO_3 and N_2O_5 during the DOMINO campaign: contrasts between marine, urban and continental air, Atmos. Chem. Phys., 11, 10 853–10 870, doi:10.5194/acp-11-10853-2011, URL https://acp.copernicus.org/articles/11/10853/2011/, 2011.

Crutzen, P. and Lelieveld, J.: Human Impacts on Atmospheric Chemistry, Annu. Rev. Earth Planet. Sci., 29, 17–45, doi:10.1146/annurev.earth.29.1.17, URL https://doi.org/10.1146/annurev.earth.29.1.17, 2001.

Crutzen, P. and Stoermer, E.: The "Anthropocene", IGBP Global Change Newsletter, 41, 17–18, 2000.

Crutzen, P. J.: Estimates of possible future ozone reductions from continued use of fluoro-chloro-methanes (CF_2Cl_2, $CFCl_3$), Geophys. Res. Lett., 1, 205–208, doi:10.1029/GL001i005p00205, URL https://agupubs.onlinelibrary.wiley.com/doi/abs/10.1029/GL001i005p00205, 1974.

Crutzen, P. J.: The Role of NO and NO_2 in the Chemistry of the Troposphere and Stratosphere, Annu. Rev. Earth Planet. Sci., 7, 443–472, doi:10.1146/annurev.ea.07.050179.002303, URL https://doi.org/10.1146/annurev.ea.07.050179.002303, 1979.

Day, D. A., Wooldridge, P. J., Dillon, M. B., Thornton, J. A., and Cohen, R. C.: A thermal dissociation laser-induced fluorescence instrument for in situ detection of NO_2, peroxy nitrates, alkyl nitrates, and HNO_3, J. Geophys. Res.: Atmos., 107, ACH 4–1–ACH 4–14, doi:10.1029/2001JD000779, URL https://agupubs.onlinelibrary.wiley.com/doi/abs/10.1029/2001JD000779, 2002.

Dewald, P., Liebmann, J. M., Friedrich, N., Shenolikar, J., Schuladen, J., Rohrer, F., Reimer, D., Tillmann, R., Novelli, A., Cho, C., Xu, K., Holzinger, R., Bernard, F., Zhou, L., Mellouki, W., Brown, S. S., Fuchs, H., Lelieveld, J., and Crowley, J. N.: Evolution of NO_3 reactivity during the oxidation of isoprene, Atmos. Chem. Phys., 20, 10 459–10 475, doi:10.5194/acp-20-10459-2020, URL https://acp.copernicus.org/articles/20/10459/2020/, 2020.

Di Carlo, P., Aruffo, E., Busilacchio, M., Giammaria, F., Dari-Salisburgo, C., Biancofiore, F., Visconti, G., Lee, J., Moller, S., Reeves, C. E., Bauguitte, S., Forster, G., Jones, R. L., and Ouyang, B.: Aircraft based four-channel thermal dissociation laser induced fluorescence instrument for simultaneous measurements of NO_2, total peroxy nitrate, total alkyl nitrate, and HNO_3, Atmos. Meas. Tech., 6, 971–980, doi:10.5194/amt-6-971-2013, URL https://amt.copernicus.org/articles/6/971/2013/, 2013.

Duncan, B. N., Yoshida, Y., Olson, J. R., Sillman, S., Martin, R. V., Lamsal, L., Hu, Y., Pickering, K. E., Retscher, C., Allen, D. J., and Crawford, J. H.: Application of OMI observations to a space-based indicator of NO_x and VOC controls on surface ozone formation, Atmos. Environ., 44, 2213–2223, doi:10.1016/j.atmosenv.2010.03.010, URL https://www.sciencedirect.com/science/article/pii/S1352231010002050, 2010.

Finlayson-Pitts, B. and Pitts, J.: Chemistry of the Upper and Lower Atmosphere, pp. 179–293, Academic Press, San Diego, doi:10.1016/B978-012257060-5/50009-5, URL http://www.sciencedirect.com/science/article/pii/B9780122570605500095, 2000.

Fischer, E. V., Jacob, D. J., Yantosca, R. M., Sulprizio, M. P., Millet, D. B., Mao, J., Paulot, F., Singh, H. B., Roiger, A., Ries, L., Talbot, R. W., Dzepina, K., and Pandey Deolal, S.: Atmospheric peroxyacetyl nitrate (PAN): a global budget and source attribution, Atmos. Chem. Phys., 14, 2679–2698, doi:10.5194/acp-14-2679-2014, URL https://acp.copernicus.org/articles/14/2679/2014/, 2014.

Fisher, J. A., Jacob, D. J., Travis, K. R., Kim, P. S., Marais, E. A., Chan Miller, C., Yu, K., Zhu, L., Yantosca, R. M., Sulprizio, M. P., Mao, J., Wennberg, P. O., Crounse, J. D., Teng, A. P., Nguyen, T. B., St. Clair, J. M., Cohen, R. C., Romer, P., Nault, B. A., Wooldridge, P. J., Jimenez, J. L., Campuzano-Jost, P., Day, D. A., Hu, W., Shepson, P. B., Xiong, F., Blake, D. R., Goldstein, A. H., Misztal, P. K., Hanisco, T. F., Wolfe, G. M., Ryerson, T. B., Wisthaler, A., and Mikoviny, T.: Organic nitrate chemistry and its implications for nitrogen budgets in

an isoprene- and monoterpene-rich atmosphere: constraints from aircraft (SEAC^{4}RS) and ground-based (SOAS) observations in the Southeast US, Atmos. Chem. Phys., 16, 5969–5991, doi:10.5194/acp-16-5969-2016, URL https://acp.copernicus.org/articles/16/5969/2016/, 2016.

Foulds, A., Khan, M. A. H., Bannan, T. J., Percival, C. J., Lowenberg, M. H., and Shallcross, D. E.: Abundance of NO_3 Derived Organo-Nitrates and Their Importance in the Atmosphere, Atmosphere, 12, doi:10.3390/atmos12111381, URL https://www.mdpi.com/2073-4433/12/11/1381, 2021.

Friedrich, N., Tadic, I., Schuladen, J., Brooks, J., Darbyshire, E., Drewnick, F., Fischer, H., Lelieveld, J., and Crowley, J. N.: Measurement of NO_x and NO_y with a thermal dissociation cavity ring-down spectrometer (TD-CRDS): instrument characterisation and first deployment, Atmos. Meas. Tech., 13, 5739–5761, doi:10.5194/amt-13-5739-2020, URL https://amt.copernicus.org/articles/13/5739/2020/, 2020.

Fry, J. L., Kiendler-Scharr, A., Rollins, A. W., Brauers, T., Brown, S. S., Dorn, H.-P., Dubé, W. P., Fuchs, H., Mensah, A., Rohrer, F., Tillmann, R., Wahner, A., Wooldridge, P. J., and Cohen, R. C.: SOA from limonene: role of NO_3 in its generation and degradation, Atmos. Chem. Phys., 11, 3879–3894, doi:10.5194/acp-11-3879-2011, URL https://acp.copernicus.org/articles/11/3879/2011/, 2011.

Fry, J. L., Brown, S. S., Middlebrook, A. M., Edwards, P. M., Campuzano-Jost, P., Day, D. A., Jimenez, J. L., Allen, H. M., Ryerson, T. B., Pollack, I., Graus, M., Warneke, C., de Gouw, J. A., Brock, C. A., Gilman, J., Lerner, B. M., Dubé, W. P., Liao, J., and Welti, A.: Secondary organic aerosol (SOA) yields from NO_3 radical + isoprene based on nighttime aircraft power plant plume transects, Atmos. Chem. Phys., 18, 11 663–11 682, doi:10.5194/acp-18-11663-2018, URL https://acp.copernicus.org/articles/18/11663/2018/, 2018.

GESTIS: Substance database. Information system on hazardous substances of the German Social Accident Insurance, URL https://gestis-database.dguv.de, last access: 03.02.2022, 2022.

Geyer, A. and Platt, U.: Temperature dependence of the NO_3 loss frequency: A new indicator for the contribution of NO_3 to the oxidation of monoterpenes and NO_x removal in the atmosphere, J. Geophys. Res.: Atmos., 107, ACL 8–1–12, doi:10.1029/2001JD001215, URL https://agupubs.onlinelibrary.wiley.com/doi/abs/10.1029/2001JD001215, 2002.

Geyer, A. and Stutz, J.: Vertical profiles of NO_3, N_2O_5, O_3, and NO_x in the nocturnal boundary layer: 2. Model studies on the altitude dependence of composition and chemistry, J. Geophys. Res.: Atmos., 109, D12 307, doi:10.1029/2003JD004211, URL https://agupubs.onlinelibrary.wiley.com/doi/abs/10.1029/2003JD004211, 2004.

Geyer, A., Alicke, B., Ackermann, R., Martinez, M., Harder, H., Brune, W., di Carlo, P., Williams, E., Jobson, T., Hall, S., Shetter, R., and Stutz, J.: Direct observations of daytime NO_3: Implications for urban boundary layer chemistry, J. Geophys. Res.-Atmos., 108, ACH7–1–ACH7–11, doi:https://doi.org/10.1029/2002JD002967, URL https://agupubs.onlinelibrary.wiley.com/doi/abs/10.1029/2002JD002967, 2003.

Gligorovski, S., Strekowski, R., Barbati, S., and Vione, D.: Environmental Implications of Hydroxyl Radicals (OH), Chem. Rev., 115, 13 051–13 092, doi:10.1021/cr500310b, URL https://pubs.acs.org/doi/10.1021/cr500310b, 2015.

Guenther, A. B., Jiang, X., Heald, C. L., Sakulyanontvittaya, T., Duhl, T., Emmons, L. K., and Wang, X.: The Model of Emissions of Gases and Aerosols from Nature version 2.1 (MEGAN2.1): an extended and updated framework for modeling biogenic emissions, Geosci. Model Dev., 5, 1471–1492, doi:10.5194/gmd-5-1471-2012, URL https://gmd.copernicus.org/articles/5/1471/2012/, 2012.

Haagen-Smit, A. J.: Chemistry and Physiology of Los Angeles Smog, Ind. Eng. Chem., 44, 1342–1346, doi:10.1021/ie50510a045, URL https://doi.org/10.1021/ie50510a045, 1952.

Hakola, H., Tarvainen, V., Laurila, T., Hiltunen, V., Hellén, H., and Keronen, P.: Seasonal variation of VOC concentrations above a boreal coniferous forest, Atmos. Environ., 37, 1623–1634, doi:https://doi.org/10.1016/S1352-2310(03)00014-1, URL https://www.sciencedirect.com/science/article/pii/S1352231003000141, 2003.

Hakola, H., Hellén, H., Hemmilä, M., Rinne, J., and Kulmala, M.: In situ measurements of volatile organic compounds in a boreal forest, Atmos. Chem. Phys., 12, 11 665–11 678, doi:10.5194/acp-12-11665-2012, URL https://acp.copernicus.org/articles/12/11665/2012/, 2012.

Hamilton, J. F., Bryant, D. J., Edwards, P. M., Ouyang, B., Bannan, T. J., Mehra, A., Mayhew, A. W., Hopkins, J. R., Dunmore, R. E., Squires, F. A., Lee, J. D., Newland, M. J., Worrall, S. D., Bacak, A., Coe, H., Percival, C., Whalley, L. K., Heard, D. E., Slater, E. J., Jones, R. L., Cui, T., Surratt, J. D., Reeves, C. E., Mills, G. P., Grimmond, S., Sun, Y., Xu, W., Shi, Z., and Rickard, A. R.: Key Role of NO_3 Radicals in the Production of Isoprene Nitrates and Nitrooxyorganosulfates in Beijing, Environ. Sci. Technol., 55, 842–853, doi:10.1021/acs.est.0c05689, URL https://doi.org/10.1021/acs.est.0c05689, 2021.

Heintz, F., Platt, U., Flentje, H., and Dubois, R.: Long-term observation of nitrate radicals at the Tor Station, Kap Arkona (Rügen), J. Geophys. Res.: Atmos., 101, 22 891–22 910, doi:10.1029/96JD01549, URL https://agupubs.onlinelibrary.wiley.com/doi/abs/10.1029/96JD01549, 1996.

Hjorth, J., Lohse, C., Nielsen, C. J., Skov, H., and Restelli, G.: Products and mechanisms of the gas-phase reactions between nitrate radical and a series of alkenes, J. Phys. Chem., 94, 7494–7500, doi:10.1021/j100382a035, URL https://pubs.acs.org/doi/10.1021/j100382a035, 1990.

Horowitz, L. W., Fiore, A. M., Milly, G. P., Cohen, R. C., Perring, A., Wooldridge, P. J., Hess, P. G., Emmons, L. K., and Lamarque, J.-F.: Observational constraints on the chemistry of isoprene nitrates over the eastern United States, J. Geophys. Res.: Atmos., 112, D12S08, doi:10.1029/2006JD007747, URL https://agupubs.onlinelibrary.wiley.com/doi/abs/10.1029/2006JD007747, 2007.

IPCC: Observations: Atmosphere and Surface, p. 159–254, Cambridge University Press, doi:10.1017/CBO9781107415324.008, 2014.

IPCC: Sixth Assessment Report, Working Group I - The Physical Science Basis, URL https://www.ipcc.ch/report/ar6/wg1/downloads/report/IPCC_AR6_WGI_Headline_Statements.pdf, last access: 02.12.2021, 2021.

IUPAC: Task Group on Atmospheric Chemical Kinetic Data Evaluation, edited by: Ammann, M., Cox, R.A., Crowley, J.N., Herrmann, H., McNeill, V.F., Mellouki, A., Rossi, M.J., Troe, J. and Wallington, T.J., URL http://iupac.pole-ether.fr/index.html, last access: 18.02.2022, 2022.

Jacob, D.: Introduction to Atmospheric Chemistry, pp. 211–215, Princeton University Press, URL http://acmg.seas.harvard.edu/people/faculty/djj/book/, 1999.

Jenkin, M. E., Young, J. C., and Rickard, A. R.: The MCM v3.3.1 degradation scheme for isoprene, Atmos. Chem. Phys., 15, 11 433–11 459, doi:10.5194/acp-15-11433-2015, URL https://acp.copernicus.org/articles/15/11433/2015/, 2015.

Kampa, M. and Castanas, E.: Human health effects of air pollution, Environ. Pollut., 151, 362–367, doi:10.1016/j.envpol.2007.06.012, URL http://www.sciencedirect.com/science/article/pii/S0269749107002849, 2008.

Keehan, N. I., Brownwood, B., Marsavin, A., Day, D. A., and Fry, J. L.: A thermal-dissociation–cavity ring-down spectrometer (TD-CRDS) for the detection of organic nitrates in gas and particle phases, Atmos. Meas. Tech., 13, 6255–6269, doi:10.5194/amt-13-6255-2020, URL https://amt.copernicus.org/articles/13/6255/2020/, 2020.

Kirchner, F., Mayer–Figge, A., Zabel, F., and Becker, K. H.: Thermal stability of Peroxynitrates, Int. J. Chem. Kinet., 31, 127–144, doi:10.1002/(SICI)1097-4601(1999)31:2<127::AID-KIN6>3.0.CO;2-L, URL https://onlinelibrary.wiley.com/doi/abs/10.1002/%28SICI%291097-4601%281999%2931%3A2%3C127%3A%3AAID-KIN6%3E3.0.CO%3B2-L, 1999.

Klepeis, N., Nelson, W., Ott, W., Robinson, J., Tsang, A., Switzer, P., Behar, J., Hern, S., and Engelmann, W.: The National Human Activity Pattern Survey (NHAPS): a resource for assessing exposure to environmental pollutanats, J. Exposure Sci. Environ. Epidemiol., 11, 231–252, doi:10.1038/sj.jea.7500165, URL https://www.nature.com/articles/7500165, 2001.

Kurtenbach, R., Ackermann, R., Becker, K., Geyer, A., Gomes, J., Lörzer, J., Platt, U., and Wiesen, P.: Verification of the Contribution of Vehicular Traffic to the Total NMVOC Emissions in Germany and the Importance of the NO_3 Chemistry in the City Air, J. Atmos. Chem., 42, 395–411, doi:10.1023/A:1015778616796, URL https://link.springer.com/article/10.1023/A:1015778616796, 2002.

Kwan, A. J., Chan, A. W. H., Ng, N. L., Kjaergaard, H. G., Seinfeld, J. H., and Wennberg, P. O.: Peroxy radical chemistry and OH radical production during the NO_3-initiated oxidation of isoprene, Atmos. Chem. Phys., 12, 7499–7515, doi:10.5194/acp-12-7499-2012, URL https://acp.copernicus.org/articles/12/7499/2012/, 2012.

LaFranchi, B. W., Wolfe, G. M., Thornton, J. A., Harrold, S. A., Browne, E. C., Min, K. E., Wooldridge, P. J., Gilman, J. B., Kuster, W. C., Goldan, P. D., de Gouw, J. A., McKay, M., Goldstein, A. H., Ren, X., Mao, J., and Cohen, R. C.: Closing the peroxy acetyl nitrate budget: observations of acyl peroxy nitrates (PAN, PPN, and MPAN) during BEARPEX 2007, Atmos. Chem. Phys., 9, 7623–7641, doi:10.5194/acp-9-7623-2009, URL https://acp.copernicus.org/articles/9/7623/2009/, 2009.

Larsen, B., Di Bella, D., Glasius, M., Winterhalter, R., Jensen, N., and Hjorth, J.: Gas-Phase OH Oxidation of Monoterpenes: Gaseous and Particulate Products., J. Atmos. Chem., 38, 231–276, doi:10.1023/A:1006487530903, URL https://link.springer.com/article/10.1023/A:1006487530903, 2001.

Leighton, P.: Photochemistry of air pollution, Academic Press, New York, 1961.

Lelieveld, J., Butler, T. M., Crowley, J. N., Dillon, T. J., Fischer, H., Ganzeveld, L., Harder, H., Lawrence, M. G., Martinez, M., Taraborrelli, D., and Williams, J.: Atmospheric oxidation capacity sustained by a tropical forest, Nature, 452, 737–740, doi:10.1038/nature06870, URL https://doi.org/10.1038/nature06870, 2008.

Lelieveld, J., Evans, J. S., Fnais, M., Giannadaki, D., and Pozzer, A.: The contribution of outdoor air pollution sources to premature mortality on a global scale, Nature, 525, 367–371, doi:10.1038/nature15371, URL https://doi.org/10.1038/nature15371, 2015.

Lelieveld, J., Gromov, S., Pozzer, A., and Taraborrelli, D.: Global tropospheric hydroxyl distribution, budget and reactivity, Atmos. Chem. Phys., 16, 12 477–12 493, doi:

10.5194/acp-16-12477-2016, URL https://acp.copernicus.org/articles/16/12477/2016/, 2016.

Lelieveld, J., Pozzer, A., Pöschl, U., Fnais, M., Haines, A., and Münzel, T.: Loss of life expectancy from air pollution compared to other risk factors: a worldwide perspective, Cardiovasc. Res., doi:10.1093/cvr/cvaa025, URL https://doi.org/10.1093/cvr/cvaa025, 2020.

Liebmann, J., Sobanski, N., Schuladen, J., Karu, E., Hellén, H., Hakola, H., Zha, Q., Ehn, M., Riva, M., Heikkinen, L., Williams, J., Fischer, H., Lelieveld, J., and Crowley, J. N.: Alkyl nitrates in the boreal forest: formation via the NO_3-, OH- and O_3-induced oxidation of biogenic volatile organic compounds and ambient lifetimes, Atmos. Chem. Phys., 19, 10 391–10 403, doi:10.5194/acp-19-10391-2019, URL https://acp.copernicus.org/articles/19/10391/2019/, 2019.

Liebmann, J. M., Schuster, G., Schuladen, J. B., Sobanski, N., Lelieveld, J., and Crowley, J. N.: Measurement of ambient NO_3 reactivity: design, characterization and first deployment of a new instrument, Atmos. Meas. Tech., 10, 1241–1258, doi:10.5194/amt-10-1241-2017, URL https://amt.copernicus.org/articles/10/1241/2017/, 2017.

Liebmann, J. M., Muller, J. B. A., Kubistin, D., Claude, A., Holla, R., Plass-Dülmer, C., Lelieveld, J., and Crowley, J. N.: Direct measurements of NO_3 reactivity in and above the boundary layer of a mountaintop site: identification of reactive trace gases and comparison with OH reactivity, Atmos. Chem. Phys,, 18, 12 045–12 059, doi:10.5194/acp-18-12045-2018, URL https://acp.copernicus.org/articles/18/12045/2018/, 2018.

Liu, T., Hong, Y., Li, M., Xu, L., Chen, J., Bian, Y., Yang, C., Dan, Y., Zhang, Y., Xue, L., Zhao, M., Huang, Z., and Wang, H.: Atmospheric oxidation capacity and ozone pollution mechanism in a coastal city of southeastern China: analysis of a typical photochemical episode by an observation-based model, Atmos. Chem. Phys., 22, 2173–2190, doi:10.5194/acp-22-2173-2022, URL https://acp.copernicus.org/articles/22/2173/2022/, 2022.

McLaren, R., Wojtal, P., Majonis, D., McCourt, J., Halla, J. D., and Brook, J.: NO_3 radical measurements in a polluted marine environment: links to ozone formation, Atmos. Chem. Phys., 10, 4187–4206, doi:10.5194/acp-10-4187-2010, URL https://acp.copernicus.org/articles/10/4187/2010/, 2010.

Molina, M. J. and Rowland, F. S.: Stratospheric sink for chlorofluoromethanes: chlorine atom-catalysed destruction of ozone, Nature, 249, 810–812, doi:10.1038/249810a0, URL https://doi.org/10.1038/249810a0, 1974.

Monks, P. S.: Gas-phase radical chemistry in the troposphere, Chem. Soc. Rev., 34, 376–395, doi:10.1039/B307982C, URL http://dx.doi.org/10.1039/B307982C, 2005.

Morin, J. and Bedjanian, Y.: Thermal decomposition of n-propyl and n-butyl nitrates: Kinetics and products, J. Anal. Appl. Pyrolysis, 124, 576–583, doi:10.1016/j.jaap.2017.01.014, URL https://www.sciencedirect.com/science/article/pii/S0165237016308609, 2017.

MTES: French Stratergy for Energy and Climate, Ministère de la Transition Écologique et Solidaire, URL https://www.gouvernement.fr/sites/default/files/locale/piece-jointe/2020/08/2020-french_strategy_for_energy_and_climate.pdf, last access: 18.02.2022, 2019.

Mutzel, A., Zhang, Y., Böge, O., Rodigast, M., Kolodziejczyk, A., Wang, X., and Herrmann, H.: Importance of secondary organic aerosol formation of α-pinene, limonene, and m-cresol comparing day- and nighttime radical chemistry, Atmos. Chem. Phys., 21, 8479–8498, doi:10.5194/acp-21-8479-2021, URL https://acp.copernicus.org/articles/21/8479/2021/, 2021.

Nazaroff, W. W. and Weschler, C. J.: Cleaning products and air fresheners: exposure to primary and secondary air pollutants, Atmos. Environ., 38, 2841–2865, doi:10.1016/j.atmosenv.2004.02.040, URL https://www.sciencedirect.com/science/article/pii/S1352231004002171, 2004.

Ng, N. L., Brown, S. S., Archibald, A. T., Atlas, E., Cohen, R. C., Crowley, J. N., Day, D. A., Donahue, N. M., Fry, J. L., Fuchs, H., Griffin, R. J., Guzman, M. I., Herrmann, H., Hodzic, A., Iinuma, Y., Jimenez, J. L., Kiendler-Scharr, A., Lee, B. H., Luecken, D. J., Mao, J., McLaren, R., Mutzel, A., Osthoff, H. D., Ouyang, B., Picquet-Varrault, B., Platt, U., Pye, H. O. T., Rudich, Y., Schwantes, R. H., Shiraiwa, M., Stutz, J., Thornton, J. A., Tilgner, A., Williams, B. J., and Zaveri, R. A.: Nitrate radicals and biogenic volatile organic compounds: oxidation, mechanisms, and organic aerosol, Atmos. Chem. Phys., 17, 2103–2162, doi:10.5194/acp-17-2103-2017, URL https://acp.copernicus.org/articles/17/2103/2017/, 2017.

Nguyen, T. B., Tyndall, G. S., Crounse, J. D., Teng, A. P., Bates, K. H., Schwantes, R. H., Coggon, M. M., Zhang, L., Feiner, P., Milller, D. O., Skog, K. M., Rivera-Rios, J. C., Dorris, M., Olson, K. F., Koss, A., Wild, R. J., Brown, S. S., Goldstein, A. H., de Gouw, J. A., Brune, W. H., Keutsch, F. N., Seinfeld, J. H., and Wennberg, P. O.: Atmospheric fates of Criegee intermediates in the ozonolysis of isoprene, Phys. Chem. Chem. Phys., 18, 10 241–10 254, doi:10.1039/C6CP00053C, URL https://pubs.rsc.org/en/content/articlelanding/2016/cp/c6cp00053c, 2016.

Nøjgaard, J. K.: Indoor measurements of the sum of the nitrate radical, NO_3, and nitrogen pentoxide, N_2O_5 in Denmark, Chemosphere, 79, 898–904, doi:10.1016/j.chemosphere.2010.02.025, URL https://www.sciencedirect.com/science/article/pii/S0045653510001712, 2010.

Orlando, J. J., Tyndall, G. S., and Wallington, T. J.: The Atmospheric Chemistry of Alkoxy Radicals, Chem. Rev., 103, 4657–4690, doi:10.1021/cr020527p, URL https://doi.org/10.1021/cr020527p, 2003.

Orphal, J., Fellows, C. E., and Flaud, P.-M.: The visible absorption spectrum of NO_3 measured by high-resolution Fourier transform spectroscopy, J. Geophys. Res.: Atmos., 108, ACH1–1–ACH1–11, doi:10.1029/2002JD002489, URL https://agupubs.onlinelibrary.wiley.com/doi/abs/10.1029/2002JD002489, 2003.

Phillips, G. J., Thieser, J., Tang, M., Sobanski, N., Schuster, G., Fachinger, J., Drewnick, F., Borrmann, S., Bingemer, H., Lelieveld, J., and Crowley, J. N.: Estimating N_2O_5 uptake coefficients using ambient measurements of NO_3, N_2O_5, $ClNO_2$ and particle-phase nitrate, Atmos. Chem. Phys., 16, 13 231–13 249, doi:10.5194/acp-16-13231-2016, URL https://acp.copernicus.org/articles/16/13231/2016/, 2016.

Pilegaard, K.: Processes regulating nitric oxide emissions from soils, Philos. Trans. R. Soc., B, 368, 20130 126, doi:10.1098/rstb.2013.0126, URL https://royalsocietypublishing.org/doi/abs/10.1098/rstb.2013.0126, 2013.

Pozzer, A., Zimmermann, P., Doering, U. M., van Aardenne, J., Tost, H., Dentener, F., Janssens-Maenhout, G., and Lelieveld, J.: Effects of business-as-usual anthropogenic emissions on air quality, Atmos. Chem. Phys., 12, 6915–6937, doi:10.5194/acp-12-6915-2012, URL https://www.atmos-chem-phys.net/12/6915/2012/, 2012.

Pusede, S. E., Steiner, A. L., and Cohen, R. C.: Temperature and Recent Trends in the Chemistry of Continental Surface Ozone, Chem. Rev., 115, 3898–3918, doi:10.1021/cr5006815, URL https://doi.org/10.1021/cr5006815, 2015.

Romer Present, P. S., Zare, A., and Cohen, R. C.: The changing role of organic nitrates in the removal and transport of NO_x, Atmos. Chem. Phys., 20, 267–279, doi:10.5194/acp-20-267-2020, URL https://acp.copernicus.org/articles/20/267/2020/, 2020.

Schwantes, R. H., Teng, A. P., Nguyen, T. B., Coggon, M. M., Crounse, J. D., St. Clair, J. M., Zhang, X., Schilling, K. A., Seinfeld, J. H., and Wennberg, P. O.: Isoprene NO_3 Oxidation Products from the RO_2 + HO_2 Pathway, J. Phys. Chem. A, 119, 10 158–10 171, doi:10.1021/acs.jpca.5b06355, URL https://pubs.acs.org/doi/10.1021/acs.jpca.5b06355, 2015.

Shah, Y., Kurelek, J., Peterson, S. D., and Yarusevych, S.: Experimental investigation of indoor aerosol dispersion and accumulation in the context of COVID-19: Effects of masks and ventilation, Phys. Fluids, 33, 0733 151–1–0733 151–14, doi:10.1063/5.0057100, URL https://aip.scitation.org/doi/full/10.1063/5.0057100, 2021.

Shepson, P., Hastie, D., So, K., Schiff, H., and Wong, P.: Relationships between PAN, PPN and O_3 at urban and rural sites in Ontario, Atmos. Environ. A, 26, 1259–1270, doi: https://doi.org/10.1016/0960-1686(92)90387-Z, URL https://www.sciencedirect.com/science/article/pii/096016869290387Z, 1992.

Skov, H., Hjorth, J., Lohse, C., Jensen, N., and Restelli, G.: Products and mechanisms of the reactions of the nitrate radical (NO_3) with isoprene, 1,3-butadiene and 2,3-dimethyl-1,3-butadiene in air, Atmos. Environ. A, 26, 2771–2783, doi:10.1016/0960-1686(92)90015-D, URL https://www.sciencedirect.com/science/article/pii/096016869290015D, 1992.

Sobanski, N., Schuladen, J., Schuster, G., Lelieveld, J., and Crowley, J. N.: A five-channel cavity ring-down spectrometer for the detection of NO_2, NO_3, N_2O_5, total peroxy nitrates and total alkyl nitrates, Atmos. Meas. Tech., 9, 5103–5118, doi:10.5194/amt-9-5103-2016, URL https://amt.copernicus.org/articles/9/5103/2016/, 2016a.

Sobanski, N., Tang, M. J., Thieser, J., Schuster, G., Pöhler, D., Fischer, H., Song, W., Sauvage, C., Williams, J., Fachinger, J., Berkes, F., Hoor, P., Platt, U., Lelieveld, J., and Crowley, J. N.: Chemical and meteorological influences on the lifetime of NO_3 at a semi-rural mountain site during PARADE, Atmos. Chem. Phys., 16, 4867–4883, doi:10.5194/acp-16-4867-2016, URL https://acp.copernicus.org/articles/16/4867/2016/, 2016b.

Solomon, S., Garcia, R. R., Rowland, F. S., and Wuebbles, D. J.: On the depletion of Antarctic ozone, Nature, 321, 755–758, doi:10.1038/321755a0, URL https://doi.org/10.1038/321755a0, 1986.

Stroud, C. A., Roberts, J. M., Williams, E. J., Hereid, D., Angevine, W. M., Fehsenfeld, F. C., Wisthaler, A., Hansel, A., Martinez-Harder, M., Harder, H., Brune, W. H., Hoenninger, G., Stutz, J., and White, A. B.: Nighttime isoprene trends at an urban forested site during the 1999 Southern Oxidant Study, J. Geophys. Res.: Atmos., 107, ACH 7–1–ACH 7–14, doi:10.1029/2001JD000959, URL https://agupubs.onlinelibrary.wiley.com/doi/abs/10.1029/2001JD000959, 2002.

Stull, R. B.: Stable Boundary Layer, pp. 499–543, Springer Netherlands, Dordrecht, doi: 10.1007/978-94-009-3027-8_12, URL https://link.springer.com/chapter/10.1007/978-94-009-3027-8_12, 1988.

Stull, R. B.: Atmospheric Boundary Layer, pp. 687–722, University of British Columbia, Vancouver, URL https://www.eoas.ubc.ca/books/Practical_Meteorology/, 2017.

Stutz, J., Alicke, B., Ackermann, R., Geyer, A., White, A., and Williams, E.: Vertical profiles of NO_3, N_2O_5, O_3, and NO_x in the nocturnal boundary layer: 1. Observations during the Texas Air Quality Study 2000, J. Geophys. Res.: Atmos., 109, D12 306, doi:10.1029/

2003JD004209, URL https://agupubs.onlinelibrary.wiley.com/doi/abs/10.1029/2003JD004209, 2004.

Tang, M. J., Thieser, J., Schuster, G., and Crowley, J. N.: Uptake of NO_3 and N_2O_5 to Saharan dust, ambient urban aerosol and soot: a relative rate study, Atmos. Chem. Phys., 10, 2965–2974, doi:10.5194/acp-10-2965-2010, URL https://acp.copernicus.org/articles/10/2965/2010/, 2010.

Thieser, J., Schuster, G., Schuladen, J., Phillips, G. J., Reiffs, A., Parchatka, U., Pöhler, D., Lelieveld, J., and Crowley, J. N.: A two-channel thermal dissociation cavity ring-down spectrometer for the detection of ambient NO_2, RO_2NO_2 and $RONO_2$, Atmos. Meas. Tech., 9, 553–576, doi:10.5194/amt-9-553-2016, URL https://amt.copernicus.org/articles/9/553/2016/, 2016.

van Meeningen, Y., Schurgers, G., Rinnan, R., and Holst, T.: BVOC emissions from English oak (*Quercus robur*) and European beech (*Fagus sylvatica*) along a latitudinal gradient, Biogeosciences, 13, 6067–6080, doi:10.5194/bg-13-6067-2016, URL https://bg.copernicus.org/articles/13/6067/2016/, 2016.

Vereecken, L., Carlsson, P. T. M., Novelli, A., Bernard, F., Brown, S. S., Cho, C., Crowley, J. N., Fuchs, H., Mellouki, W., Reimer, D., Shenolikar, J., Tillmann, R., Zhou, L., Kiendler-Scharr, A., and Wahner, A.: Theoretical and experimental study of peroxy and alkoxy radicals in the NO3-initiated oxidation of isoprene, Phys. Chem. Chem. Phys., 23, 5496–5515, doi:10.1039/D0CP06267G, URL http://dx.doi.org/10.1039/D0CP06267G, 2021.

Wagner, N. L., Riedel, T. P., Roberts, J. M., Thornton, J. A., Angevine, W. M., Williams, E. J., Lerner, B. M., Vlasenko, A., Li, S. M., Dubé, W. P., Coffman, D. J., Bon, D. M., de Gouw, J. A., Kuster, W. C., Gilman, J. B., and Brown, S. S.: The sea breeze/land breeze circulation in Los Angeles and its influence on nitryl chloride production in this region, J. Geophys. Res.: Atmos., 117, 1–15, doi:10.1029/2012JD017810, URL https://agupubs.onlinelibrary.wiley.com/doi/abs/10.1029/2012JD017810, 2012.

Warneke, C., McKeen, S. A., de Gouw, J. A., Goldan, P. D., Kuster, W. C., Holloway, J. S., Williams, E. J., Lerner, B. M., Parrish, D. D., Trainer, M., Fehsenfeld, F. C., Kato, S., Atlas, E. L., Baker, A., and Blake, D. R.: Determination of urban volatile organic compound emission ratios and comparison with an emissions database, J. Geophys. Res.: Atmos., 112, 1–13, doi:https://doi.org/10.1029/2006JD007930, URL https://agupubs.onlinelibrary.wiley.com/doi/abs/10.1029/2006JD007930, 2007.

Wayne, R., Barnes, I., Biggs, P., Burrows, J., Canosa-Mas, C., Hjorth, J., Le Bras, G., Moortgat, G., Perner, D., Poulet, G., Restelli, G., and Sidebottom, H.: The nitrate radical: Physics,

chemistry, and the atmosphere, Atmos. Environ. Part A. General Topics, 25, 1–203, doi: https://doi.org/10.1016/0960-1686(91)90192-A, URL https://www.sciencedirect.com/science/article/pii/096016869190192A, 1991.

Wennberg, P. O., Bates, K. H., Crounse, J. D., Dodson, L. G., McVay, R. C., Mertens, L. A., Nguyen, T. B., Praske, E., Schwantes, R. H., Smarte, M. D., St Clair, J. M., Teng, A. P., Zhang, X., and Seinfeld, J. H.: Gas-Phase Reactions of Isoprene and Its Major Oxidation Products, Chem. Rev., 118, 3337–3390, doi:10.1021/acs.chemrev.7b00439, URL https://doi.org/10.1021/acs.chemrev.7b00439, 2018.

Weschler, C.: Ozone in Indoor Envrionments: Concentration and chemistry, Indoor Air, 10, 269–288, doi:10.1034/j.1600-0668.2000.010004269.x, URL https://onlinelibrary.wiley.com/doi/abs/10.1034/j.1600-0668.2000.010004269.x, 2000.

Weschler, C. J. and Shields, H. C.: Production of the Hydroxyl Radical in Indoor Air, Environ. Sci. Technol., 30, 3250–3258, doi:10.1021/es960032f, URL https://pubs.acs.org/doi/10.1021/es960032f, 1996.

Weschler, C. J. and Shields, H. C.: Potential reactions among indoor pollutants, Atmos. Environ., 31, 3487–3495, doi:10.1016/S1352-2310(97)00219-7, URL https://www.sciencedirect.com/science/article/pii/S1352231097002197, 1997.

Weschler, C. J., Brauer, M., and Koutrakis, P.: Indoor ozone and nitrogen dioxide: a potential pathway to the generation of nitrate radicals, dinitrogen pentoxide, and nitric acid indoors, Environ. Sci. Tech., 26, 179–184, doi:10.1021/es00025a022, URL https://pubs.acs.org/doi/abs/10.1021/es00025a022, 1992.

Wild, R. J., Edwards, P. M., Dubé, W. P., Baumann, K., Edgerton, E. S., Quinn, P. K., Roberts, J. M., Rollins, A. W., Veres, P. R., Warneke, C., Williams, E. J., Yuan, B., and Brown, S. S.: A Measurement of Total Reactive Nitrogen, NO_y, together with NO2, NO, and O_3 via Cavity Ring-down Spectroscopy, Environ. Sci. Technol., 48, 9609–9615, doi:10.1021/es501896w, URL https://pubs.acs.org/doi/10.1021/es501896w, 2014.

Wu, R., Vereecken, L., Tsiligiannis, E., Kang, S., Albrecht, S. R., Hantschke, L., Zhao, D., Novelli, A., Fuchs, H., Tillmann, R., Hohaus, T., Carlsson, P. T. M., Shenolikar, J., Bernard, F., Crowley, J. N., Fry, J. L., Brownwood, B., Thornton, J. A., Brown, S. S., Kiendler-Scharr, A., Wahner, A., Hallquist, M., and Mentel, T. F.: Molecular composition and volatility of multi-generation products formed from isoprene oxidation by nitrate radical, Atmos. Chem. Phys. Discuss., 2020, 1–37, doi:10.5194/acp-2020-1180, URL https://acp.copernicus.org/preprints/acp-2020-1180/, 2020.

Zare, A., Romer, P. S., Nguyen, T., Keutsch, F. N., Skog, K., and Cohen, R. C.: A comprehensive organic nitrate chemistry: insights into the lifetime of atmospheric organic ni-

trates, Atmos. Chem. Phys., 18, 15 419–15 436, doi:10.5194/acp-18-15419-2018, URL https://acp.copernicus.org/articles/18/15419/2018/, 2018.

Zel'dovich, Y.: The Oxidation of Nitrogen in Combustion Explosions, Acta Physicochim. URSS, 21, 577–628, 1946.

Zhang, J. and Lioy, P. J.: Ozone in Residential Air: Concentrations, I/O Ratios, Indoor Chemistry, and Exposures, Indoor Air, 4, 95–105, doi:10.1111/j.1600-0668.1994.t01-2-00004.x, URL https://onlinelibrary.wiley.com/doi/abs/10.1111/j.1600-0668.1994.t01-2-00004.x, 1994.

Appendices

APPENDIX A

Supplement of Chapter 4

Supplement of Atmos. Chem. Phys., 20, 10459–10475, 2020
https://doi.org/10.5194/acp-20-10459-2020-supplement

Atmospheric Chemistry and Physics
Open Access
EGU

Supplement of

Evolution of NO_3 reactivity during the oxidation of isoprene

Patrick Dewald et al.

Correspondence to: John N. Crowley (john.crowley@mpic.de)

Box-Model

Table S1: Reactions, rate coefficients and definitions in the model used for analysis. The isoprene oxidation scheme until the 3rd / 4th generation from the Master Chemical Mechanism (MCM) version 3.3.1 is used (Jenkin et al., 2015). Any change from MCMv3.3.1 is annotated.

Reaction	Reaction constant	Annotations
NOx chemistry		
N2O5 → NO3 + NO2	((1.3e-3*(T/300)@-3.5*exp(-11000/T))*M* (9.7e14*(T/300)@0.1*exp(-11080/T)))/((1.3e-3* (T/300)@-3.5*exp(-11000/T))*M+(9.7e14*(T/300)@0.1* exp(-11080/T)))*10@(log10(0.35)/(1+(log10((1.3e-3*(T/300)@-3.5 *exp(-11000/T))*M/(9.7e14*(T/300)@0.1*exp(-11080/T))) /(0.75-1.27*log10(0.35)))@2))	
NO2 + NO3 → N2O5	((3.6e-30*(T/300)@-4.1)*M*(1.9e-12*(T/300)@0.2)) /((3.6e-30*(T/300)@-4.1)*M+(1.9e-12*(T/300)@0.2))* 10@(log10(0.35)/(1+(log10((3.6e-30*(T/300)@-4.1)* M/(1.9e-12*(T/300)@0.2))/(0.75-1.27*log10(0.35)))@2))	
NO + O3 → NO2 + O2	1.8E-11*exp(110/T)	
NO2 + O3 → NO3 + O2	1.4E-13 * exp (-2470/T)	
NO + O3 → NO2 + O2	2.07E-12 * exp (-1400/T)	
NO3 + CO →	4E-19	Hjorth et al., 1986
OH + NO2 →HNO3	((3.2e-30*(T/300)@-4.5)*M*(3.0e-11))/ ((3.2e-30*(T/300)@-4.5)*M+(3.0e-11))*10@(log10(0.41)/ (1+(log10((3.2e-30*(T/300)@-4.5)*M/(3.0e-11))/ (0.75-1.27*log10(0.41)))@2))	
OH + NO3 →HO2 + NO2	2E-11	
HO2 + NO3 → OH + NO2	4E-12	
OH + NO → HONO	((7.4e-31*(T/300)@-2.4)*M*(3.3e-11*(T/300)@-0.3))/ ((7.4e-31*(T/300)@-2.4)*M+(3.3e-11*(T/300)@-0.3))* 10@(log10(0.81)/(1+(log10((7.4e-31*(T/300)@-2.4)*M/ (3.3e-11*(T/300)@-0.3))/(0.75-1.27*log10(0.81)))@2))	
HO2 + NO → OH + NO2	3.45E-12*exp(270/T)	
HO2 + NO2 → HO2NO2	((1.4e-31*(T/300)@-3.1)*M*(4.0e-12))/ ((1.4e-31*(T/300)@-3.1)*M+(4.0e-12))*10@(log10(0.4)/ (1+(log10((1.4e-31*(T/300)@-3.1)*M/(4.0e-12))/ (0.75-1.27*log10(0.4)))@2))	
HO2NO2 + OH → NO2	3.2e-13*EXP(690/T)	
HO2NO2 → HO2 + NO2	((4.1e-5*exp(-10650/T))*M*(6.0e15*exp(-11170/T)))/ ((4.1e-5*exp(-10650/T))*M+(6.0e15*exp(-11170/T)))* 10@(log10(0.4)/(1+(log10((4.1e-5*exp(-10650/T))*M/ (6.0e15*exp(-11170/T)))/(0.75-1.27*log10(0.4)))@2))	

OH + HONO → NO2	2.5e-12*EXP(260/T)	
OH + HNO3 → NO3	2.40E-14*EXP(460/T) + ((6.50E-34*EXP(1335/T)*M)/ (1+(6.50E-34*EXP(1335/T)*M/2.70E-17*EXP(2199/T))))	
HOx chemistry		
OH + O3 → HO2	1.70E-12*EXP(-940/T)	
HO2 + O3 → OH	2.03E-16*(T/300)@4.57*EXP(693/T)	
OH + HO2 →	4.8E-11*EXP(250/T)	
HO2 + HO2 → H2O2	2.20E-13*(1+(1.40E-21*EXP(2200/T)*H2O))*EXP(600/T)	
OH + H2O2 → HO2	2.9E-12*exp(-160/T)	
OH + CO → HO2	1.44E-13*(1+(M/4.2E19))	
Primary oxidation of isoprene		
NO3 + C5H8 → NISOPO2	2.95E-12 * exp (-450/T)	IUPAC, 2019
O3 + C5H8 → CH2OOE + MACR	0.3 * 1.03E-14 * exp (-1995/T)	
O3 + C5H8 → CH2OOE + MVK	0.2 * 1.03E-14 * exp (-1995/T)	
O3 + C5H8 → HCHO + MACROOA	0.3 * 1.03E-14 * exp (-1995/T)	
O3 + C5H8 → HCHO + MVKOOA	0.2 * 1.03E-14 * exp (-1995/T)	
OH + C5H8 → CISOPA	0.288*2.7E-11 * exp (390/T)	
OH + C5H8 → CISOPC	0.238*2.7E-11 * exp (390/T)	
OH + C5H8 → ISOP34O2	0.022*2.7E-11 * exp (390/T)	
OH + C5H8 → ME3BU3ECHO + HO2	0.02*2.7E-11 * exp (390/T)	
OH + C5H8 → PE4E2CO + HO2	0.042*2.7E-11 * exp (390/T)	
OH + C5H8 → TISOPA	0.288*2.7E-11 * exp (390/T)	
OH + C5H8 → TISOPC	0.102*2.7E-11 * exp (390/T)	
Secondary oxidation (1st generation)		
NISOPO2 + HO2 → NISOPOOH	0.706*2.91E-13 * EXP(1300/T)	
NISOPO2 + NO3 → NISOPO + NO2	2.3E-12	
NISOPO2 + RO2 → ISOPCNO3	0.2*1.3E-12	
NISOPO2 + RO2 → NC4CHO	0.2*1.3E-12	
NISOPO2 + RO2 → NISOPO	0.6*1.3E-12	
CH2OOE → CH2OO	0.22*1E6	
CH2OOE → CO	0.51*1E6	
CH2OOE → HO2 + CO + OH	0.27*1E6	
MACR + NO3 → MACO3 + HNO3	3.4E-15	

MACR + O3 → HCHO + MGLYOOB	0.12*1.4E-15*EXP(-2100/T)	
MACR + O3 → MGLYOX + CH2OOG	0.88*1.4E-15*EXP(-2100/T)	
MACR + OH → MACO3	0.45*8.0E-12*EXP(380/T)	
MACR + OH → MACRO2	0.47*8.0E-12*EXP(380/T)	
MACR + OH → MACROHO2	0.08*8.0E-12*EXP(380/T)	
MVK + O3 → MGLOOA + HCHO	0.5*8.5E-16*EXP(-1520/T)	
MVK + O3 → MGLYOX + CH2OOB	0.5*8.5E-16*EXP(-1520/T)	
MVK + OH → HVMKAO2	0.3*2.6E-12*EXP(610/T)	
MVK + OH → HMVKBO2	0.7*2.6E-12*EXP(610/T)	
HCHO + NO3 → HNO3 + CO + HO2	5.5E-16	
HCHO + OH → HO2 + CO	5.4E-12 * exp (135/T)	
MACROOA → C3H6	0.255*1E6	
MACROOA → CH3CO3 + HCHO + HO2	0.255*1E6	
MACROOA → MACROO	0.22*1E6	
MACROOA → OH + CO +CH3CO3 + HCHO	0.27*1E6	
MVKOOA → C3H6	0.255*1E6	
MVKOOA → CH3O2 + HCHO + CO + HO2	0.255*1E6	
MVKOOA → MVKOO	0.22*1E6	
MVKOOA → OH + MVKO2	0.27*1E6	
CISOPA + O2 → CISOPAO2	3.5E-12	
CISOPA + O2 → ISOPBO2	3E-12	
CISOPC + O2 → CISOPCO2	2E-12	
CISOPC + O2 → ISOPDO2	3.5E-12	
ISOP34O2 + HO2 → ISOP34OOH	2.91E-13 * EXP(1300/T)	
ISOP34O2 + NO3 → ISOP34O + NO2	2.3E-12	
ISOP34O2 + RO2 → HC4CHO	0.1*2.65E-12	
ISOP34O2 + RO2 → ISOP34O	0.8*2.65E-12	
ISOP34O2 + RO2 → ISOPDOH	0.1*2.65E-12	
ME3BU3ECHO + NO3 → NC526O2	3.3E-13	

ME3BU3ECHO + O3 → CH2OOC + CO2C3CHO	0.33*1.6E-17	
ME3BU3ECHO + O3 → HCHO + CO2C3OOB	0.67*1.6E-17	
ME3BU3ECHO + OH → C530O2	0.712*7.3E-11	
ME3BU3ECHO + OH → ME3BU3ECO3	0.288*7.3E-11	
PE4E2CO + NO3 → NC51O2	1.2E-14	
PE4E2CO + O3 → CH2OOB + CO2C3CHO	0.43*1E-17	
PE4E2CO + O3 → HCHO + CO2C3OOA	0.57*1E-17	
PE4E2CO + OH → C51O2	2.71E-11	
TISOPA + O2 → ISOPAO2	2.5E-12*exp(-480/T)	
TISOPA + O2 → ISOPBO2	3E-12	
TISOPC + O2 → ISOPCO2	2.5E-12*exp(-480/T)	
TISOPC + O2 → ISOPDO2	3.5E-12	
Secondary oxidation (2nd generation)		
NISOPOOH + OH → NC4CHO + OH	1.03E-10	
NISOPO + O2 → NC4CHO + HO2	2.50E-14*EXP(-300/T)	
ISOPCNO3 + OH → INCO2	1.12E-10	
NC4CHO + NO3 → NC4CO3 + HNO3	4.25*1.4E-12*EXP(-1860/T)	
NC4CHO + OH → C510O2	0.52*4.16E-11	
NC4CHO + OH → NC4CO3	0.48*4.16E-11	
NC4CHO + O3 → NOA + GLYOOC	0.5*2.4E-17	
NC4CHO + O3 → GLYOX + NOAOOA	0.5*2.4E-17	
CH2OO + CO → HCHO	1.2E-15	
CH2OO + NO2 → HCHO + NO3	1E-15	
MACO3 + NO3 → CH3C2H2O2 + NO2	1.74 * 2.3E-12	
MACO3 + HO2 → CH3C2H2O2	0.44 * 5.2E-13*EXP(980/T)	
MACO3 + HO2 →	0.66 5.2E-13*EXP(980/T)	
MACO3 + RO2 → CH3C2H2O2	0.7*1E-11	
MACO3 + RO2 →	0.3*1E-11	

MGLYOOB → MGLYOO	0.18*1E6	
MGLYOOB → OH + CO + CH3CO3	0.82*1E6	
MGLYOX + NO3 → CH3CO3 + CO + HNO3	2.4*1.4E-12*EXP(-1860/T)	
MGLYOX + OH → CH3CO3 + CO	1.9E-12*exp(575/T)	
CH2OOG → CH2OO	0.37*1E6	
CH2OOG → CO	0.47*1E6	
CH2OOG → HO2 + CO + OH	0.16*1E6	
MACRO2 + HO2 → MACROOH	0.625*2.91E-13 * EXP(1300/T)	
MACRO2 + NO3 → MACRO + NO2	2.3E-12	
MACRO2 + RO2 → ACETOL	9.2E-14	
MACROHO2 + HO2 → (MACROHOOH)	0.625*2.91E-13 * EXP(1300/T)	
MACROHO2 + NO3 → MACROHO + NO2	2.3E-12	
MACROHO2 + RO2 → (div)	1.4E-12	
MGLOOA → CH3CHO	0.2*1E6	
MGLOOA → OH + CO + CH3CO3	0.36*1E6	
MGLOOA → CH3CO3 + HCHO + HO2	0.2*1E6	
MGLOOA → MGLOO	0.24*1E6	
CH2OOB → CH2OO	0.24*1E6	
CH2OOB → CO	0.4*1E6	
CH2OOB → HO2 + CO + OH	0.36*1E6	
HMVKAO2 + HO2 → (HMVKAOOH)	0.625*2.91E-13 * EXP(1300/T)	
HMVKAO2 + NO3 → NO2 + HMVKAO	2.3E-12	
HMVKAO2 + RO2 → (div)	2E-12	
HMVKBO2 + HO2 → (HMVKBOOH)	0.625*2.91E-13 * EXP(1300/T)	
HMVKBO2 + NO3 → NO2 + HMVKBO	2.3E-12	
HMVKBO2 + RO2 → (div)	8.8E-13	
C3H6 + O3 → CH2OOB + CH3CHO	0.5*5.5E-15*EXP(-1880/T)	

C3H6 + O3 → CH3CHOOA + HCHO	0.5*5.5E-15*EXP(-1880/T)	
C3H6 + NO3 → PRONO3AO2	0.35*4.6E-13*EXP(-1155/T)	
C3H6 + NO3 → PRONO3BO2	0.65*4.6E-13*EXP(-1155/T)	
C3H6 + OH → HYPROPO2	0.87* ((8e-27*(T/300)@-3.5)*M*(3.0e-11*(T/300)@-1))/ ((8e-27*(T/300)@-3.5)*M+(3.0e-11*(T/300)@-1))* 10@(log10(0.5)/(1+(log10((8e-27*(T/300)@-3.5)*M/ (3.0e-11*(T/300)@-1))/(0.75-1.27*log10(0.5)))@2))	
C3H6 + OH → IPROPOLO2	0.13* ((8e-27*(T/300)@-3.5)*M*(3.0e-11*(T/300)@-1))/ ((8e-27*(T/300)@-3.5)*M+(3.0e-11*(T/300)@-1))* 10@(log10(0.5)/(1+(log10((8e-27*(T/300)@-3.5)*M/ (3.0e-11*(T/300)@-1))/(0.75-1.27*log10(0.5)))@2))	
CH3CO3 + HO2 → CH3CO2H + O3	5.2E-13*EXP(980/T)	
CH3CO3 + NO3 → NO2 + CH3O2	4E-12	
CH3CO3 + RO2 → CH3CO2H	0.3*1E-11	
CH3CO3 + RO2 → CH3O2	0.7*1E-11	
MACROO + CO → MACR	1.2e-15	
MACROO + NO2 → MACR + NO3	1E-15	
CH3O2 + HO2 →	3.8E-13*EXP(780/T)*(1-1/(1+498*EXP(-1160/T)))	
CH3O2 + HO2 → HCHO	3.8E-13*EXP(780/T)*(1/(1+498*EXP(-1160/T)))	
CH3O2 + NO3 → CH3O + NO2	1.2E-12	
CH3O2 + RO2 → CH3OH	0.5* 2*1.03E-13*EXP(365/T)*0.5*(1-7.18*EXP(-885/T))	
CH3O2 + RO2 → HCHO	0.5* 2*1.03E-13*EXP(365/T)*0.5*(1-7.18*EXP(-885/T))	
MVKOO + CO → MVK	1.2E-15	
MVKOO + NO2 → MVK + NO3	1E-15	
MVKO2 + HO2 → (MVKOOH)	0.625*2.91E-13 * EXP(1300/T)	
MVKO2 + NO3 → NO2	2.3E-12	
MVKO2 + RO2 → (div)	2E-12	
CISOPAO2 + HO2 → ISOPAOOH	0.706*2.91E-13 * EXP(1300/T)	
CISOPAO2 + NO3 → CISOPAO + NO2	2.3E-12	
CISOPAO2 → C536O2	0.5*2.20E10*EXP(-8174/T)*EXP(1.00E8/T@3)	
CISOPAO2 → C5HPALD1 + HO2	0.5*2.20E10*EXP(-8174/T)*EXP(1.00E8/T@3)	
CISOPAO2 → CISOPA	5.22E15*EXP(-9838/T)	
CISOPAO2 + RO2→ CISOPAO	0.8*2.4E-12	

CISOPAO2 + RO2 → HC4ACHO	0.1*2.4E-12	
CISOPAO2 + RO2 → ISOPAOH	0.1*2.4E-12	
ISOPBO2 + HO2 → ISOPBOOH	0.706*2.91E-13 * EXP(1300/T)	
ISOPBO2 + NO3 → ISOPBO + NO2	2.3E-12	
ISOPBO2 + RO2 → ISOPBO	0.8*8E-13	
ISOPBO2 + RO2 → ISOPBOH	0.2*8E-13	
CISOPCO2 + HO2 → ISOPCOOH	0.706*2.91E-13 * EXP(1300/T)	
CISOPCO2 + NO3 → CISOPCO + NO2	2.3E-12	
CISOPCO2 → C537O2	0.5*2.20E10*EXP(-8174/T)*EXP(1.00E8/T@3)	
CISOPCO2 → C5HPALD2 + HO2	0.5*2.20E10*EXP(-8174/T)*EXP(1.00E8/T@3)	
CISOPCO2 → CISOPC	3.06E15*EXP(-10254/T)	
CISOPCO2 + RO2 → CISOPCO	0.8*2E-12	
CISOPCO2 + RO2 → HC4CCHO	0.2*2E-12	
CISOPCO2 + RO2 → ISOPAOH	0.2*2E-12	
ISOPDO2 + HO2 → ISOPDOOH	0.706*2.91E-13 * EXP(1300/T)	
ISOPDO2 + NO3 → ISOPDO + NO2	2.3E-12	
ISOPDO2 + RO2 → ISOPDO	0.8*2.9E-12	
ISOPDO2 + RO2 → HCOC5	0.1*2.9E-12	
ISOPDO2 + RO2 → ISOPDOH	0.1*2.9E-12	
ISOP34OOH + OH → HC4CHO + OH	9.73E-11	
ISOP34O → MACR + HCHO + HO2	1E6	
HC4CHO + OH → C58O2	0.829*1.04E-10	
HC4CHO + OH → HC4CO3	0.171*1.04E-10	
ISOPDOH + OH → HCOC5 + HO2	7.38E-11	
NC526O2 + NO3 → NO2 +	2.3E-12	
NC526O2 + RO2 →	9.20E-14	
CH2OOC → CH2OO	0.18*1E6	
CH2OOC → HO2 + CO+ OH	0.82*1E6	
CO2C3CHO + NO3 → HNO3 + CO2C3CO3	4* 1.4E-12*EXP(-1860/T)	

CO2C3CHO + OH → CO2C3CO3	7.15E-11	
CO2C3OOB → C4CO2O2 + OH	0.82*1E6	
CO2C3OOB → CO2C3OO	0.18*1E6	
C530O2 + HO2 →	0.706*2.91E-13 * EXP(1300/T)	
C530O2 + NO3 → NO2 +	2.3E-12	
C530O2 + RO2 →	9.2E-14	
ME3BU3ECO3 + HO2 → C45O2 + OH + NO2	0.44*1.4E-12*EXP(-1860/T)	
ME3BU3ECO3 + HO2 →	0.56*2.91E-13 * EXP(1300/T)	
ME3BU3ECO + NO3 → C45O2 + NO2	1.6*2.3E-12	
ME3BU3ECO3 + RO2 → C45O2	1E-11	
NC510O2 + HO2 →	0.625*2.91E-13 * EXP(1300/T)	
NC510O2 + NO3 → NO2 +	2.3E-12	
NC510O2 + RO2 →	8.8E-12	
CO2C3OOA → C4CO2O2 + OH	0.36*1E6	
CO2C3OOA → CH2COCH2O2 + HO2	0.2*1E6	
CO2C3OOA → CH2COCH3	0.2*1E6	
CO2C3OOA → CO2C3OO	0.24*1E6	
C51O2 + HO2 →	0.706*2.91E-13 * EXP(1300/T)	
C51O2 + NO3 → NO2 +	2.3E-12	
ISOPAO2 + HO2 → ISOPAOOH	0.706*2.91E-13 * EXP(1300/T)	
ISOPAO2 + NO3 → NO2 + ISOPAO	2.3E-12	
ISOPAO2 + RO2 → HC4ACHO	0.1*2.4E-12	
ISOPAO2 + RO2 → ISOPAO	0.8*2.4E-12	
ISOPAO2 + RO2 → ISOPAOH	0.1*2.4E-12	
ISOPCO2 + HO2 → ISOPCOOH	0.706*2.91E-13 * EXP(1300/T)	
ISOPCO2 + NO3 → NO2 + ISOPCO	2.3E-12	
ISOPCO2 + RO2 → HC4CCHO	0.1*2E-12	
ISOPCO2 + RO2 → ISOPAOH	0.1*2E-12	
ISOPCO2 + RO2 → ISOPCO	0.8*2E12	
Secondary oxidation (3rd + generation)		
INCO2 + HO2 →	0.706*2.91E-13 * EXP(1300/T)	
INCO2 + NO3 → NO2 +	2.3E-12	
INCO2 + RO2 →	2.9E-12	

NC4CO3 + HO2 → NOA + CO+ HO2 + OH	0.44*5.2E-13*EXP(980/T)	
NC4CO3 + HO2 →	0.66*5.2E-13*EXP(980/T)	
NC4CO3 + NO3 → NOA + CO + HO2 + NO2	1.74*2.3E-12	
NC4CO3 + RO2 →	0.3*1E-11	
NC4CO3 + RO2 → NOA + HO2 + CO	0.7*1E-11	
NOA + OH → MGLYOX + NO2	1.3E-13	
C510O2 + HO2 →	0.706*2.91E-13 * EXP(1300/T)	
C510O2 + NO3 → NO2	2.3E-12	
C510O2 + RO2 →	9.2E-14	
GLYOOC → GLYOO	0.11*1E6	
GLYOOC → OH + HO2 + CO + CO	0.89*1E6	
GLYOO + NO2 → GLYOX + NO3	1E-15	
NOAOOA → NOAOO	0.11*1E6	
NOAOOA → OH + NO2 + MGLYOX	0.89*1E6	
NOAOO + NO2 → NOA + NO3	1E-15	
CH3C2H2O2 → CH3CO3 + HCHO	0.35*1E6	
CH3C2H2O2 → HCHO + CH3O2 + CO	0.65*1E6	
MGLYOO + NO2 → MGLYOX + NO3	1E-15	
MACROOH + OH → ACETOL + CO + OH	3.77E-11	
MACRO → ACETOL + CO+ HO2	1E6	
MACROHO → MGLYOX + HCHO + HO2	1E6	
MGLOO + NO2 → MGLYOX + NO3	1E-15	
HMVKAO → MGLYOX + HCHO + HO2	1E6	
HMVKBO → CH3CO3 + HOCH2CHO	1E6	
CH3CHOOA → CH3CHOO	0.24*1E6	

CH3CHOOA → CH3O2 + CO + OH	0.36*1E6	
CH3CHOOA → CH3O2 + HO2	0.2*1E6	
CH3CHOOA →	0.2*1E6	
CH3CHOO+ CO → CH3CHO	1.2E-15	
CH3CHOO + NO2 → CH3CHO + NO3	1E-15	
PRONO3AO2 + HO2 →	0.520*2.91E-13 * EXP(1300/T)	
PRONO3AO2 + NO3 → NO2 +	2.3E-12	
PRONO3AO2 + RO2 →	0.2*6E-13	
PRONO3BO2 + HO2 →	0.520*2.91E-13 * EXP(1300/T)	
PRONO3BO2 + NO3 → NO2 +	2.3E-12	
PRONO3BO2 + RO2 →	0.2*4E-14	
HYPROPO2 + HO2 →	0.520*2.91E-13 * EXP(1300/T)	
HYPROPO2 + NO3 → NO2 +	2.3E-12	
HYPROPO2 + RO2 →	8.8E-13	
IPROPOLO2 + HO2 →	0.520*2.91E-13 * EXP(1300/T)	
IPROPOLO2 + NO3 → NO2 +	2.3E-12	
IPROPOLO2 + RO2 →	2E-12	
MVKOOH + OH → VGLYOX	2.55E-11	
MVKOOH + OH → MVKO2	1.90E-12*EXP(190/T)	
VGLYOX + NO3 →	2.0*1.4E-12*EXP(-1860/T)	
CH3CO2H + OH → CH3O2	8E-13	
ISOPAOOH + OH → HC4ACHO	0.05*1.54E-10	
ISOPAOOH + OH → IEPOXA + OH	0.93*1.54E-10	
ISOPAOOH + OH → ISOPAO2	0.02*1.54E-10	
HC4ACHO + NO3 → HC4ACO3 + HNO3	4.25*1.4E-12*EXP(-1860/T)	
HC4ACHO + O3 → ACETOL + GLYOX	0.5*2.4E-17	
HC4ACHO + O3 → CO +	0.5*2.4E-17	
HC4ACHO + OH → C58O2	0.52*4.52E-11	
HC4ACHO + OH → HC4ACO3	0.49*4.52E-11	
C58O2 + HO2 →	0.706*2.91E-13 * EXP(1300/T)	
C58O2 + NO3 → NO2 +	2.3E-12	
C58O2 + RO2 →	9.2E-14	
HC4ACO3 + HO2 →	5.2E-13*EXP(980/T)	
HC4ACO3 + NO3 → NO2 +	1.74*2.3E-12	
HC4ACO3 + RO2 →	1E-11	

HC4ACO3 → HO2 +	2.20E10*EXP(-8174/T)*EXP(1.00E8/T@3)	
CISOPAO → C526O2	0.19*1E6	
CISOPAO → HC4CCHO + HO2	0.63*1E6	
CISOPAO → HO2 + M3F	0.18*1E6	
C526O2 + HO2 →	0.706*2.91E-13 * EXP(1300/T)	
C526O2 + NO3 → NO2 +	2.3E-12	
C526O2 + RO2 →	9.20E-14	
C526O2 → CO + OH	3.00E7*EXP(-5300/T)	
M3F + NO3 → NO2 +	1.9E-11	
M3F + O3 →	2E-17	
M3F + OH → HO2 +	9E-11	
C536O2 + HO2 →	0.706*2.91E-13 * EXP(1300/T)	
C536O2 + NO3 → NO2 +	2.3E-12	
C536O2 + RO2 →	9.20E-14	
C536O2 → CO + OH	3.00E7*EXP(-5300/T)	
C5HPALD1 + NO3 → OH + HNO3 +	4.25*1.4E-12*EXP(-1860/T)	
C5HPALD1 + O3 → MGLYOOA	0.73*2.4E-17	
C5HPALD1 + O3 → MGLYOX	0.27*2.4E-17	
MGLYOOA → MGLYOO	0.11*1E6	
MGLYOOA → CH3CO3 + OH +CO	0.89*1E6	
C5HPALD1 + OH → OH +	5.2E-11	
ISOPAOH + OH → HC4ACHO+ HO2	0.5*9.3E-11	
ISOPAOH + OH → HC4CCHO + HO2	0.5*9.3E-11	
HC4CCHO + NO3 → HC4CCO3 + HNO3	4.25*1.4E-12*EXP(-1860/T)	
HC4CCHO + O3 →	2.4E-17	
HC4CCHO + OH → C57O2	0.52*4.52E-11	
HC4CCHO + OH → HC4CCO3	0.48*4.52E-11	
HC4CCO3 + HO2 →	5.2E-13*EXP(980/T)	
HC4CCO3 + NO3 → NO2 +	1.74*2.3E-12	
HC4CCO3 + RO2 →	1E-11	
C57O2 + HO2 →	0.706*2.91E-13 * EXP(1300/T)	
C57O2 + NO3 → NO2 +	2.3E-12	
C57O2 + RO2 →	9.20E-14	
ISOPBOOH + OH → IEPOXB + OH	0.92*5E-11	

ISOPBOOH + OH → ISOPBO2	0.08*5E-11	
IEPOXB + OH → IEB1O2	0.5*9.05E-12	
IEPOXB + OH → IEB2O2	0.5*9.05E-12	
IEB1O2 + HO2 →	0.706*2.91E-13 * EXP(1300/T)	
IEB1O2 + NO3 → NO2 +	2.3E-12	
IEB1O2 + RO2 →	9.20E-14	
IEB1O2 + HO2 →	0.706*2.91E-13 * EXP(1300/T)	
IEB1O2 + NO3 → NO2 +	2.3E-12	
IEB1O2 + RO2 →	8.8E-13	
ISOPBO → MVK + HCHO + HO2	1E6	
ISOPBOH + OH → ISOPBO	3.85E-11	
ISOPCOOH + OH → HC4CCHO + OH	0.05*1.54E-10	
ISOPCOOH + OH → IEPOXC + OH	0.93*1.54E-10	
ISOPCOOH + OH → ISOPCO2	0.02*1.54E-10	
IEPOXC + OH → IEC1O2	0.719*1.5E-11	
IEPOXC + OH →	0.281*1.5E-11	
IEC1O2 + HO2 →	0.706*2.91E-13 * EXP(1300/T)	
IEC1O2 + NO3 → NO2 +	2.3E-12	
IEC1O2 + RO2 →	9.2E-14	
CISOPCO → C527O2	0.3*1E6	
CISOPCO → HC4ACHO	0.52*1E6	
CISOPCO → HO2 + M3F	0.18*1E6	
C527O2 + HO2 →	0.706*2.91E-13 * EXP(1300/T)	
C527O2 + NO3 → NO2 +	2.3E-12	
C527O2 + RO2 →	8.8E-13	
C527O2 → CO + OH	3.00E7*EXP(-5300/T)	
C537O2 + HO2 →	0.706*2.91E-13 * EXP(1300/T)	
C537O2 + NO3 → NO2 +	2.3E-12	
C537O2 + RO2 →	9.2E-14	
C537O2 → CO + OH	3.00E7*EXP(-5300/T)	
C5HPALD2 + NO3 → OH + HNO3 +	4.25*1.4E-12*EXP(-1860/T)	
C5HPALD2 + O3 → MGLYOOC	0.73*2.4E-17	
C5HPALD2 + O3 → MGLYOX	0.27*2.4E-17	
C5HPALD2 + OH → OH	5.2E-11	
ISOPAOH + OH → HC4ACHO + HO2	0.5*9.3E-11	

ISOPAOH + OH → HC4CCHO + HO2	0.5*9.3E-11	
ISOPDOOH + OH → HCOC5 + OH	0.22*1.15E-10	
ISOPDOOH + OH → IEPOXB + OH	0.75*1.15E-10	
ISOPDOOH + ISOPDO2	0.03*1.15E-10	
OH + HCOC5 → C59O2	3.81E-11	
C59O2 + HO2 →	0.706*2.91E-13 * EXP(1300/T)	
C59O2 + NO3 → NO2 +	2.3E-12	
C59O2 + RO2 →	9.2E-14	
ISOPDO → MACR + HCHO + HO2	1E6	
ISOPDOH + OH → HCOC5	7.38E-11	
HC4CO3 + HO2 →	0.56*2.91E-13 * EXP(1300/T)	
HC4CO3 + HO2 → MACR + HO2 + OH	0.44*2.91E-13 * EXP(1300/T)	
HC4CO3 + NO3 → MACR + HO2 + NO2	1.5*2.3E-12	
HC4CO3 → MACR + HO2	1E-11	
CO2C3CO3 + HO2 → CH3COCH2O2	0.44*2.91E-13 * EXP(1300/T)	
CO2C3CO3 + HO2 →	0.56*2.91E-13 * EXP(1300/T)	
CO2C3CO3 + NO3 → CH3COCH2O2 + NO2	1.74*2.3E-12	
CO2C3CO3 → CH3COCH2O2	1E-11	
CH3COCH2O2 + HO2 → OH +	0.15*1.36E-13*EXP(1250/T)	
CH3COCH2O2 + HO2 →	0.85*1.36E-13*EXP(1250/T)	
CH3COCH2O2 + NO3 → NO2 +	2.3E-12	
CH3COCH2O2 + RO2 → ACETOL	0.2* 2*(3.5E-13*8E-12)@0.5	
CH3COCH2O2 + RO2 →	0.6* 2*(3.5E-13*8E-12)@0.5	
CH3COCH2O2 + RO2 → MGLYOX	0.2* 2*(3.5E-13*8E-12)@0.5	
CO2C3OO + CO →	1.2E-15	
CO2C3OO + NO2 → NO3 +	1E-15	
C4CO2O2 + HO2 →	0.625*2.91E-13 * EXP(1300/T)	
C4CO2O2 + NO3 → NO2 +	2.3E-12	
C4CO2O2 + RO2 →	8.8E-12	
C45O2 + HO2 →	0.625*2.91E-13 * EXP(1300/T)	
C45O2 + NO3 → NO2 +	2.3E-12	

C45O2 + RO2 →	1.3E-12	
ISOPAO → C524O2	0.25*1E6	
ISOPAO → HC4CHO + HO2	0.75*1E6	
C524O2 + HO2 →	0.706*2.91E-13 * EXP(1300/T)	
C5242 + NO3 → NO2 +	2.3E-12	
C5242 + RO2 →	2.9E-12	
ISOPCOOH + OH → HC4CCHO + OH	0.05*1.54E-10	
ISOPCOOH + OH → IEPOXC + OH	0.93*1.54E-10	
ISOPCOOH + ISOPCO2	0.02*1.54E-10	
ISOPCO → HC4ACHO + HO2	0.75*1E6	
ISOPCO → HC4CCHO + HO2	0.25*1E6	
β-caryophyllene		Jenkin et al., 2012
BCARY + NO3 → NBCO2	1.9E-11	
NBCO2 + NO3 →	2.3E-12	
BCARY + O3 → BCAOO	0.435*1.2E-14	
BCARY + O3 → BCBOO	0.435*1.2E-14	
BCARY + O3 →	0.13*1.2E-14	
BCAOO → BCSOZ	8E1	
BCBOO → BCSOZ	1.2E2	
SAPHIR chamber		
Y + OH → HO2	1.44E-13*(1+(M/4.2E19))	OH background reactivity; behaving like CO (Fuchs et al., 2013)
Z + wall →	3.86E-6	Wall loss for O_3, H_2O_2, HO_2, HONO and HNO_3 (Richter, 2007)
NO3 + wall →	1.6E-3	Wall loss NO_3
N2O5 + wall →	3.3E-4	Wall loss N_2O_5
Definitions		
RO2	NISOPO2 + ISOP34O2 + CH3C2H2O2 + MACO3 + MACRO2 + MACROHO2 + CH3CO3 + HMVKAO2 + HMVKBO2 + CH3O2 + MVKO2 + CISOPAO2 + ISOPBO2 + CISOPCO2 + ISOPDO2 + NC526O2 + C530O2 + M3BU3ECO3 + C45O2 + NC51O2 + C51O2 + ISOPAO2 + ISOPCO2 + INCO2 + NC4CO3 + C510O2 + PRONO3AO2 + PRONO3BO2 + HYPROPO2 + IPROPOLO2 + C536O2 + C537O2 + INAO2 + C58O2 + HC4CO3 + CO2C3CO3 + CH3COCH2O2 + C4CO2O2 + C527O2 + C526O2 + HC4ACO3 HC4CCO3 + C57O2 + C59O2 + C524O2	organic peroxides
kNO3_all	C5H8*2.95E-12*exp(450/T) + BCARY*1.9E-11 + C3H6*4.6E-13*exp(-1155/T) + (2.3E-12*(NISOPO2 + ISOPAO2 +	overall NO_3 reactivity

	ISOPBO2 + ISOPCO2 + ISOPDO2 + CH3C2H2O2 + MACO3 + MACRO2 + MACROHO2 + HMVKAO2 + HMVKBO2 + MVKO2 + INCO2 + CISOPAO + CISOPAO2 + (NC4CO3*1.74) + C510O2 + NBCO2 + PRONO3AO2 + PRONO3BO2 + HYPROPO2 + IPROPOLO2 + INAO2 + C524O2 + (HC4ACO3*1.74) + (1.6*HC4CO3) + C58O2 + INB1O2 + (HC4CCO3*2.74) + INDO2 + C57O2 + C59O2 + C51O2 + IEB1O2 + IEB2O2 + IEC1O2 + ISOP34O2 + CISOPCO2 + NC526O2 + C527O2 + C526O2 + C536O2 + C537O2 + C530O2 + C45O2 + 1.6*M3BU3ECO3 + INB2O2 + NC51O2 + 1.74*CO2C3CO3 + CH3COCH2O2 + C4CO2O2)) + (4E-12*CH3CO3) + (1.2E-12*CH3O2) + (HO2*4E-12) + (5.5E-16*HCHO) + (4E-19*CO) + 1.4E-12*EXP(-1860/T)*(NC4CHO*4.25 + HC4ACHO*4.25 + HC4CCHO*4.25 + 2.4*MGLYOX + 4*CO2C3CHO + 4.25*C5HPALD1 + 4.25*C5HPALD2 +2*VGLYOX) + 3.3E-13*ME3BU3ECHO + (M3F*1.9E-11) + (1.2E-14*PE4E2CO)	
kNO3_stable	C5H8*2.95E-12*exp(450/T) + BCARY*1.9E-11 + C3H6*4.6E-13*exp(-1155/T) + (5.5E-16*HCHO) + (4E-19*CO) + 1.4E-12*EXP(-1860/T)*(NC4CHO*4.25 + HC4ACHO*4.25 + HC4CCHO*4.25 + 2.4*MGLYOX + 4*CO2C3CHO + 4.25*C5HPALD1 + 4.25*C5HPALD2 +2*VGLYOX) + 3.3E-13*ME3BU3ECHO + (M3F*1.9E-11) + (1.2E-14*PE4E2CO)	NO_3 reactivity measurable by FT-CRDS
M	P*(3.24E16)*(298/T)	Total molecular concentration using measured pressure P in Torr and temperature T in K

Exemplary comparison of isoprene measurements

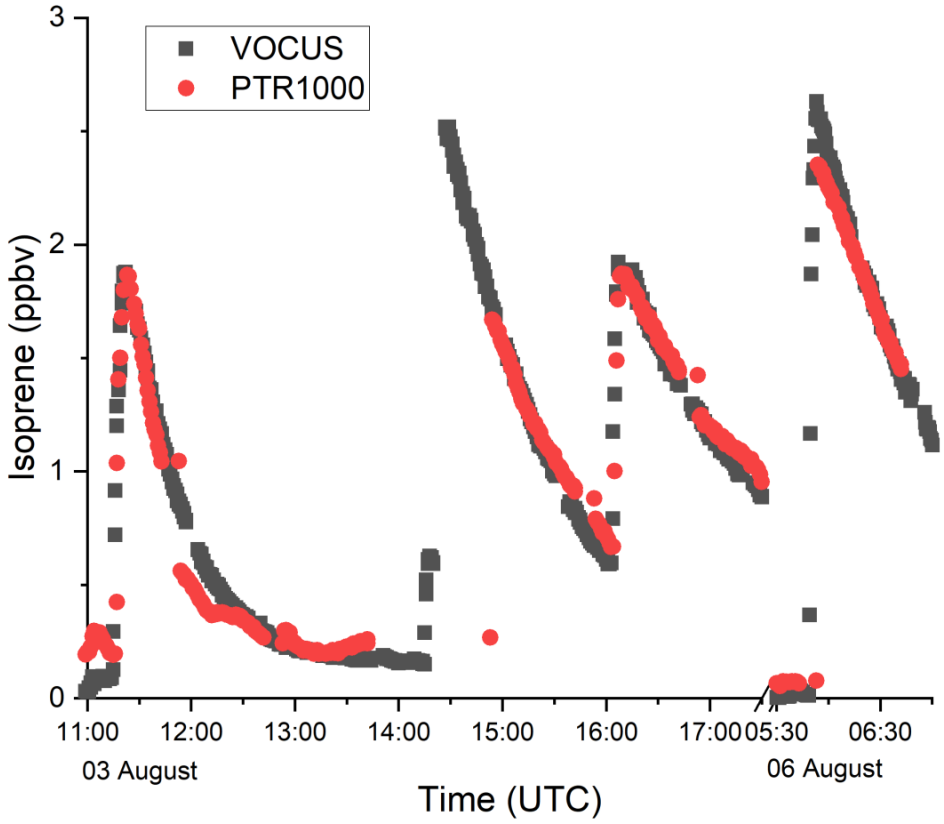

Figure S1: Amounts of isoprene during parts of the experiments on the 3rd and 6th August as measured by the two available PTR-ToF-MS instruments Vocus (black) and PTR1000 (red).

50

Comparison of k^{OH} and k^{NO_3}

During NO3ISOP, k^{OH} was measured with an instrument based on laser photolysis – laser induced fluorescence (LP-LIF) (Hofzumahaus et al., 2009; Lou et al., 2010; Fuchs et al., 2017a; Fuchs et al., 2017b). Ambient air was passed at a flow rate of 19 L min^{-1} through a flow tube and part of the air was drawn into an OH fluorescence detection cell. OH radicals were produced within a few nanoseconds in the flow tube by pulsed laser-photolysis of O_3 (at 266 nm) with subsequent reaction of $O(^1D)$ atoms with water vapour. OH concentration profiles were recorded by LIF, with k^{OH} determined from the exponential decay constant after correction for diffusion / wall loss (1.8 ± 0.15 s^{-1}). The time resolution of the k^{OH} measurements was 90 s with a limit of detection of 0.5 s^{-1}. The resulting accuracy of k^{OH} is (5-10) % ± 0.2 s^{-1} at NO mixing ratios below 20 ppbv.

Each isoprene injection results in an increase in reactivity of both OH and NO_3. Within the first few minutes after an isoprene injection, the contribution of secondary oxidation products to both k^{NO_3} and k^{OH} is negligible. Hence, the increase in the OH- and NO_3 reactivity (Δk^{OH} and Δk^{NO_3}) directly after an isoprene injection scales with the amount of isoprene injected and the corresponding rate coefficient ($k_{NO_3+C_5H_8}$ = 6.5 × 10^{-13} cm^3 molecule^{-1} s^{-1}, $k_{OH+C_5H_8}$ = 1 × 10^{-10} cm^3 molecule^{-1} s^{-1} at 298 K (IUPAC, 2019)). For any particular injection, both approaches should lead to similar isoprene concentrations as shown in Eq. S1.

$$[\text{Isoprene}] = \frac{\Delta k^{OH}}{k_{OH+C_5H_8}} = \frac{\Delta k^{NO_3}}{k_{NO_3+C_5H_8}} \quad \text{(S1)}$$

Figure S2 plots the isoprene mixing ratios derived from measurements of Δk^{OH} versus those derived from Δk^{NO_3}. For experiments with isoprene mixing ratios below ~5 ppbv a slope of 0.88 ± 0.11 was obtained. During two injections, when high concentrations of isoprene (~11 and ~22 ppbv) were injected in the chamber, the Δk^{OH} measurement returns isoprene mixing ratios that are significantly lower than those derived from Δk^{NO_3} and the mixing ratio expected from the amount of isoprene injected. On these days, a combination of the low laser power and a small number of points to fit the (rapid) exponential decay mean that the OH reactivity must be considered a lower-limit.

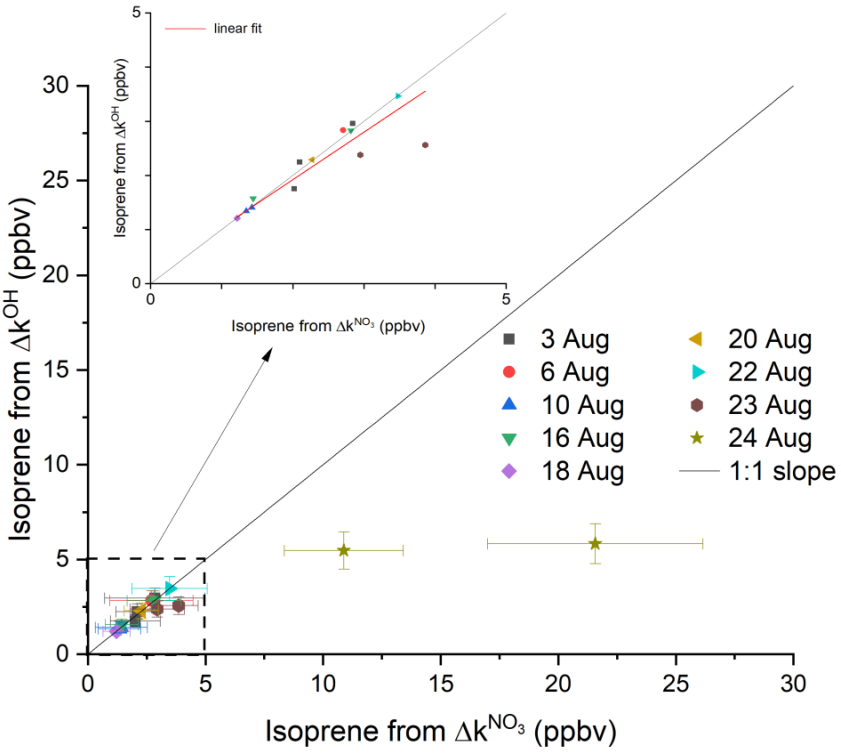

Figure S2: Isoprene mixing ratios deduced from Δk^{OH} against those from Δk^{NO_3} under the usage of Eq. (S1) for isoprene injections of different experiments (days). The error bars denote the associated uncertainties in Δk^{NO_3} (4-70%, Liebmann et al., 2017) and $k_{NO_3+C_5H_8}$ (41% (IUPAC, 2019)) and Δk^{OH} (10%, for [isoprene] < 5 ppbv) and $k_{OH+C_5H_8}$(15% (IUPAC, 2019)). The black line indicates the case of ideal 1:1 correlation, the red line shows an orthogonal linear regression (slope: 0.88 ± 0.11, intercept: 0.17 ± 0.23) for data points < 5 ppbv.

Validity of the steady-state assumption

The validity of the steady-state assumption was checked with the help of a correlation plot between the steady-state ($k_{SS}^{NO_3}$) and non-steady-state ($k_{nss}^{NO_3}$) reactivity as depicted in Fig. S3a. A slope close to 1 is found for most of the experiments. At injection points of NO_2 or at low reactivities larger differences are observed which are related to short-term perturbation of the equilibrium between NO_3 and N_2O_5 and deviation from steady-state.

Figure S3b compares $k_{\mathrm{ss}}^{\mathrm{NO3}}$ with $k_{\mathrm{nss}}^{\mathrm{NO3}}$ on the 2nd August. Between 9:00 and 11:00 UTC only NO_2 and O_3 were injected into chamber so that the influence of the chamber alone (reaction with the walls and the dilution flow) determines the NO_3 losses. As the NO_3 loss rate is low under these circumstances, nearly half an hour is necessary to achieve steady-state. This is confirmed by the difference between $k_{\mathrm{nss}}^{\mathrm{NO3}}$ and $k_{\mathrm{ss}}^{\mathrm{NO3}}$. Under the experimental conditions, the equilibrium between NO_3 and N_2O_5 is reached more rapidly than the steady state (Brown et al., 2003). Consequently, $k_{\mathrm{nss}}^{\mathrm{NO3}}$ acquires a constant value earlier than $k_{\mathrm{ss}}^{\mathrm{NO3}}$. A reinjection of NO_2 at ~10:50 perturbs the stationary-state and therefore strongly affects $k_{\mathrm{ss}}^{\mathrm{NO3}}$ whereas $k_{\mathrm{nss}}^{\mathrm{NO3}}$ remains mostly unchanged. After the injection of isoprene the high NO_3-reactivity means that the steady-state assumption becomes valid, which leads to an agreement between the two methods.

(a)

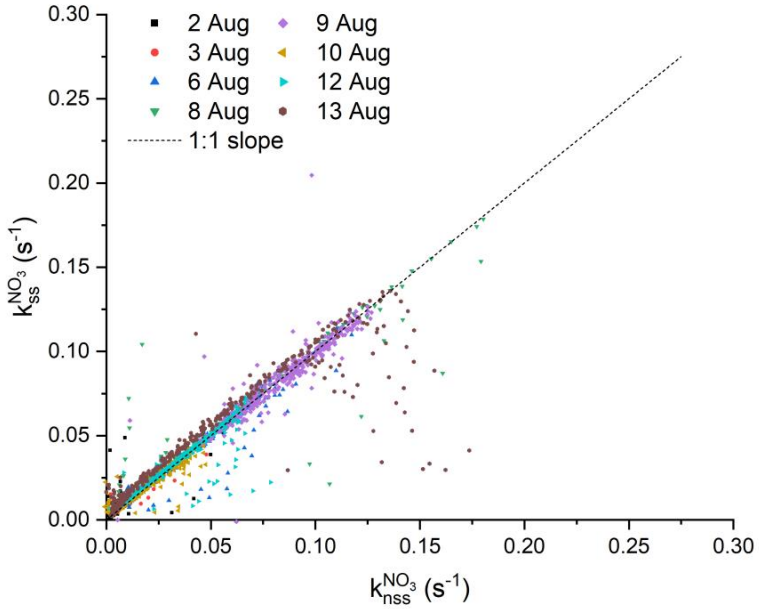

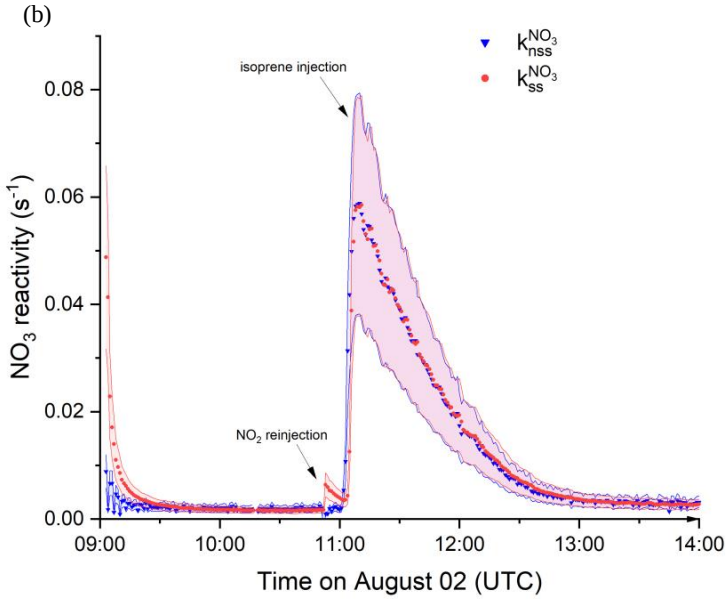

Figure S3: (a) Steady-state $k_{SS}^{NO_3}$ and non-steady-state $k_{nss}^{NO_3}$ reactivities sorted by experiment. The dotted line through the origin with a slope of 1 represents perfect agreement. (b) Comparison between steady- (red) and non-steady-state (blue) reactivities on the experiment of the 2nd August. The respective uncertainties obtained from error propagation of the uncertainties in k_2 (15%; IUPAC, 2019) and the NO_3, NO_2 and O_3 mixing ratios (25%, 9% and 5%, respectively) are indicated by areas in the same colour of the data points.

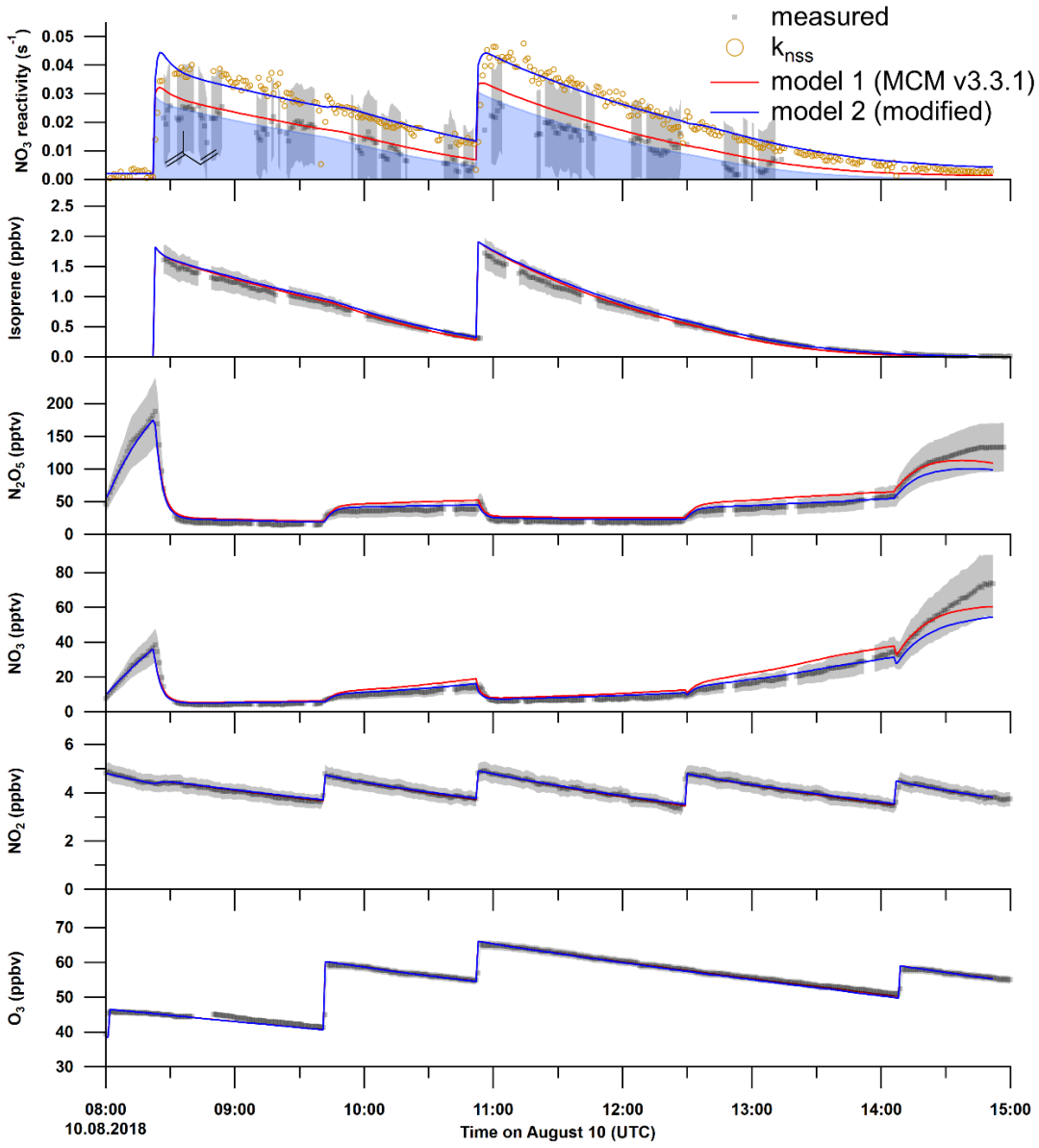

Figure S4: O_3, NO_2, NO_3, N_2O_5 and isoprene mixing ratios as well as the NO_3 reactivity on the experiment of the 10th August (black). The grey shaded area symbolizes the overall uncertainty associated with each measurement. Orange circles denote the non-steady-state reactivity obtained from Eq.(3). The results of the numerical simulation using MCM v.3.3.1 (with NO_3 and N_2O_5 wall loss rate of 0.016 s^{-1} and 3.3 x 10^{-4} s^{-1} respectively) for each of the reactants is shown by a red line, whereas the blue line shows the result of the same model with ~~a doubled reaction constant for NO_3 + RO_2 reactions~~ ($k_{NO_3+RO_2}$ = 9.2 x 10^{-12} $cm^3 molecule^{-1} s^{-1}$~~).~~

References

Brown, S. S., Stark, H., and Ravishankara, A. R.: Applicability of the steady state approximation to the interpretation of atmospheric observations of NO_3 and N_2O_5, J. Geophys. Res. -Atmos., 108, Art. 4539, doi:10.1029/2003JD003407, 2003.

Fuchs, H., Hofzumahaus, A., Rohrer, F., Bohn, B., Brauers, T., Dorn, H. P., Haseler, R., Holland, F., Kaminski, M., Li, X., Lu, K., Nehr, S., Tillmann, R., Wegener, R., and Wahner, A.: Experimental evidence for efficient hydroxyl radical regeneration in isoprene oxidation, Nat. Geosci., 6, 1023-1026, doi:10.1038/Ngeo1964, 2013.

Fuchs, H., Novelli, A., Rolletter, M., Hofzumahaus, A., Pfannerstill, E. Y., Kessel, S., Edtbauer, A., Williams, J., Michoud, V., Dusanter, S., Locoge, N., Zannoni, N., Gros, V., Truong, F., Sarda-Esteve, R., Cryer, D. R., Brumby, C. A., Whalley, L. K., Stone, D., Seakins, P. W., Heard, D. E., Schoemaecker, C., Blocquet, M., Coudert, S., Batut, S., Fittschen, C., Thames, A. B., Brune, W. H., Ernest, C., Harder, H., Muller, J. B. A., Elste, T., Kubistin, D., Andres, S., Bohn, B., Hohaus, T., Holland, F., Li, X., Rohrer, F., Kiendler-Scharr, A., Tillmann, R., Wegener, R., Yu, Z. J., Zou, Q., and Wahner, A.: Comparison of OH reactivity measurements in the atmospheric simulation chamber SAPHIR, Atmos. Meas. Tech., 10, 4023-4053, doi:10.5194/amt-10-4023-2017, 2017a.

Fuchs, H., Tan, Z. F., Lu, K. D., Bohn, B., Broch, S., Brown, S. S., Dong, H. B., Gomm, S., Haseler, R., He, L. Y., Hofzumahaus, A., Holland, F., Li, X., Liu, Y., Lu, S. H., Min, K. E., Rohrer, F., Shao, M., Wang, B. L., Wang, M., Wu, Y. S., Zeng, L. M., Zhang, Y. S., Wahner, A., and Zhang, Y. H.: OH reactivity at a rural site (Wangdu) in the North China Plain: contributions from OH reactants and experimental OH budget, Atmos. Chem. Phys., 17, 645-661, doi:10.5194/acp-17-645-2017, 2017b.

Hjorth, J., Ottobrini, G., and Restelli, G.: Reaction of the NO3 radical with CO: Determination of an upper limit for the rate constant using FTIR spectroscopy, Int. J. Chem. Kinet., 18, 819-827, doi:10.1002/kin.550180802, 1986.

Hofzumahaus, A., Rohrer, F., Lu, K. D., Bohn, B., Brauers, T., Chang, C. C., Fuchs, H., Holland, F., Kita, K., Kondo, Y., Li, X., Lou, S. R., Shao, M., Zeng, L. M., Wahner, A., and Zhang, Y. H.: Amplified Trace Gas Removal in the Troposphere, Science, 324, 1702-1704, 2009.

IUPAC: Task Group on Atmospheric Chemical Kinetic Data Evaluation, (Ammann, M., Cox, R.A., Crowley, J.N., Herrmann, H., Jenkin, M.E., McNeill, V.F., Mellouki, A., Rossi, M. J., Troe, J. and Wallington, T. J.) http://iupac.pole-ether.fr/index.html., 2019.

Jenkin, M. E., Wyche, K. P., Evans, C. J., Carr, T., Monks, P. S., Alfarra, M. R., Barley, M. H., McFiggans, G. B., Young, J. C., and Rickard, A. R.: Development and chamber evaluation of the MCM v3.2 degradation scheme for beta-caryophyllene, Atmos. Chem. Phys., 12, 5275-5308, doi:10.5194/acp-12-5275-2012, 2012.

Jenkin, M. E., Young, J. C., and Rickard, A. R.: The MCM v3.3.1 degradation scheme for isoprene, Atmos. Chem. Phys., 15, 11433-11459, doi:10.5194/acp-15-11433-2015, 2015.

Lou, S., Holland, F., Rohrer, F., Lu, K., Bohn, B., Brauers, T., Chang, C. C., Fuchs, H., Haseler, R., Kita, K., Kondo, Y., Li, X., Shao, M., Zeng, L., Wahner, A., Zhang, Y., Wang, W., and Hofzumahaus, A.: Atmospheric OH reactivities in the Pearl River Delta - China in summer 2006: measurement and model results, Atmos. Chem. Phys., 10, 11243-11260, doi:10.5194/acp-10-11243-2010, 2010.

Richter, C.A.: Ozone Production in the Atmosphere Simulation Chamber SAPHIR, Ph.D. thesis, Forschungszentrum Jülich GmbH, University of Köln, http://juser.fz-juelich.de/record/62596/files/Energie&Umwelt_02.pdf, 2007.

APPENDIX B

Supplement of Chapter 5

Supplement of Atmos. Meas. Tech., 14, 5501–5519, 2021
https://doi.org/10.5194/amt-14-5501-2021-supplement

Atmospheric Measurement Techniques
Open Access
EGU

Supplement of

Impact of ozone and inlet design on the quantification of isoprene-derived organic nitrates by thermal dissociation cavity ring-down spectroscopy (TD-CRDS)

Patrick Dewald et al.

Correspondence to: John N. Crowley (john.crowley@mpic.de)

Supplement

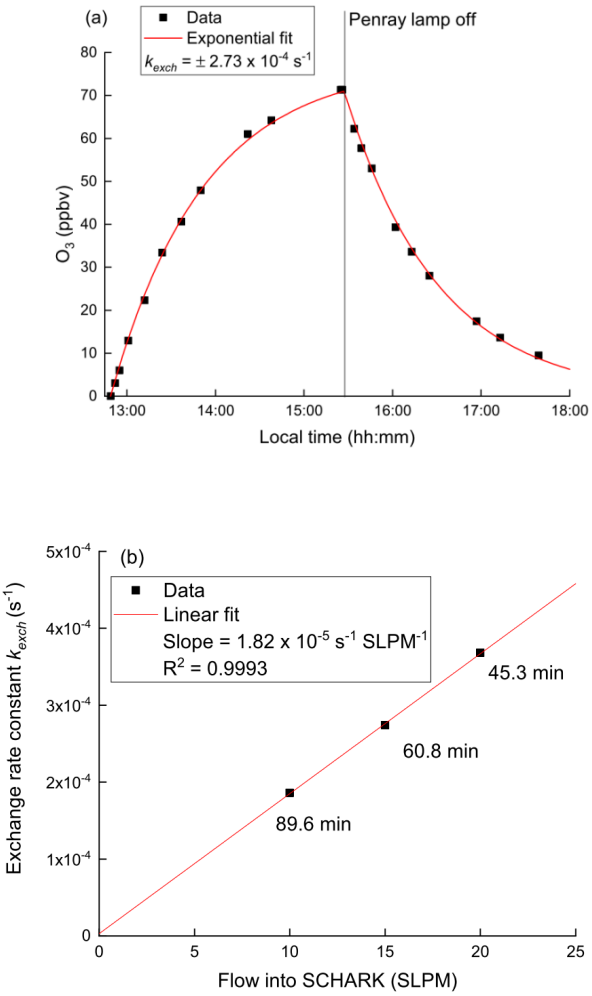

Figure S1: (a) Time-series of O_3 in the SCHARK at a flow rate of 15 SLPM dry zero-air. The Penray lamp used to generate O_3 was switched on at ~12:50 LT and switched off at 13:28 LT. The growth and depletion of the O_3 signal are reproduced by exponential expressions to derive the exchange constant (k_{exch}) **(b)** Dependence of k_{exch} on the total flow rate into the SCHARK. The linear regression indicates k_{exch} = 1.82 x 10^{-5} s^{-1} SLPM^{-1}.

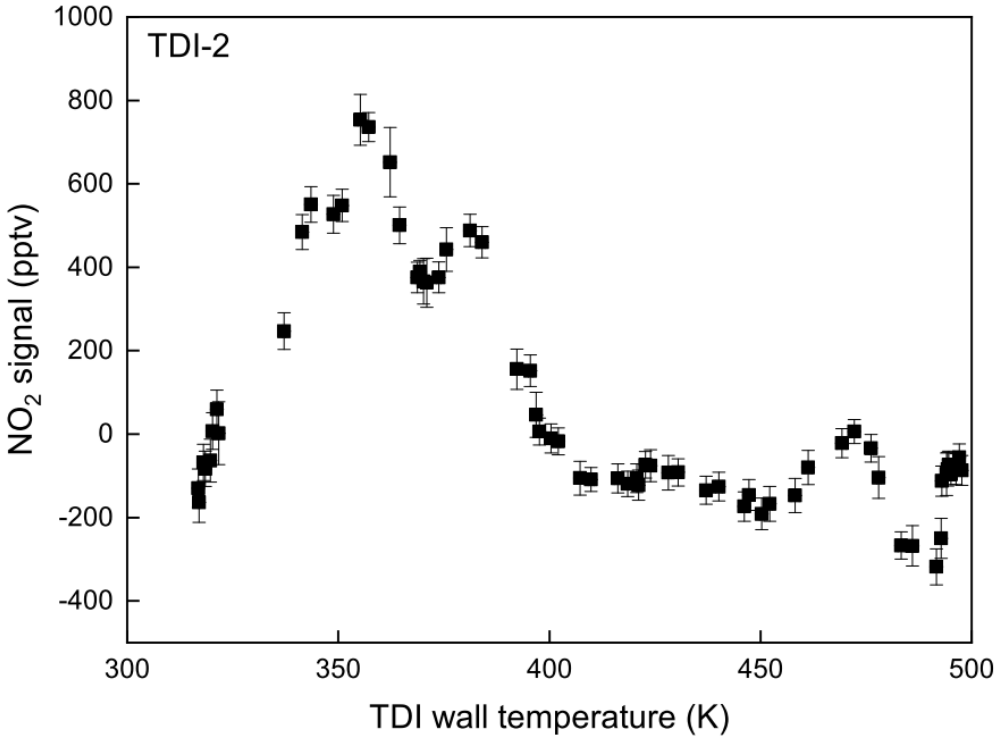

Figure S2: Dependence of NO_2 detection on TD temperature when sampling a mixture of 10.8 ppbv NO_2 in 15 SLPM humidified synthetic air (RH = 40%, 23°C) through TDI- 2. The NO_2 signal measured in the NO_2 cavity (unheated inlet) has been subtracted. The error bars represent standard deviation (1σ, 1 min) of the signal.

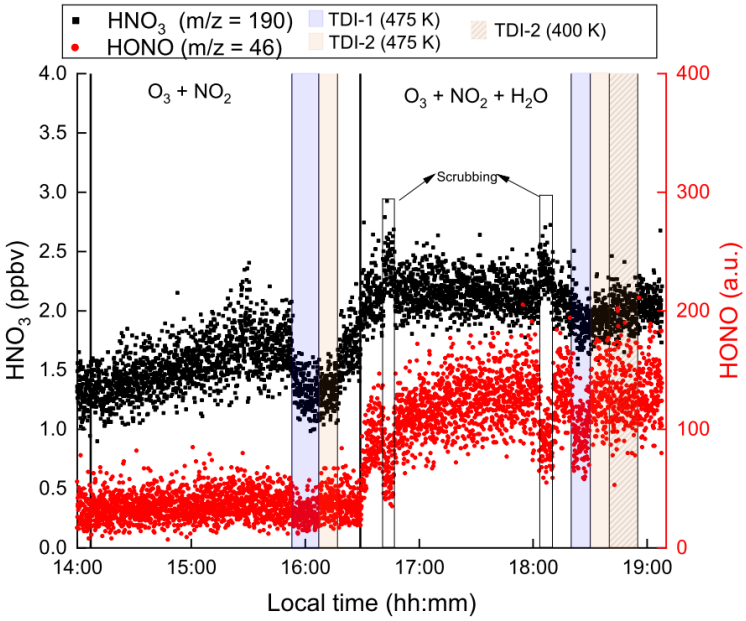

Figure S3: CIMS measurement of HNO_3 and HONO during an experiment in which NO_2 (10.8 ppbv) and O_3 (150 ppbv) were mixed in the SCHARK. At 16:30 LT the zero-air was humidified (RH = 23%, 23°C). Periods during which air from the SCHARK was first passed through TDI-1 or -2 prior to entering the CIMS are marked in blue and orange respectively. When the air was heated to 400 K while flowing through TDI-2 (yellow hatched) no effect was observed in the signal.

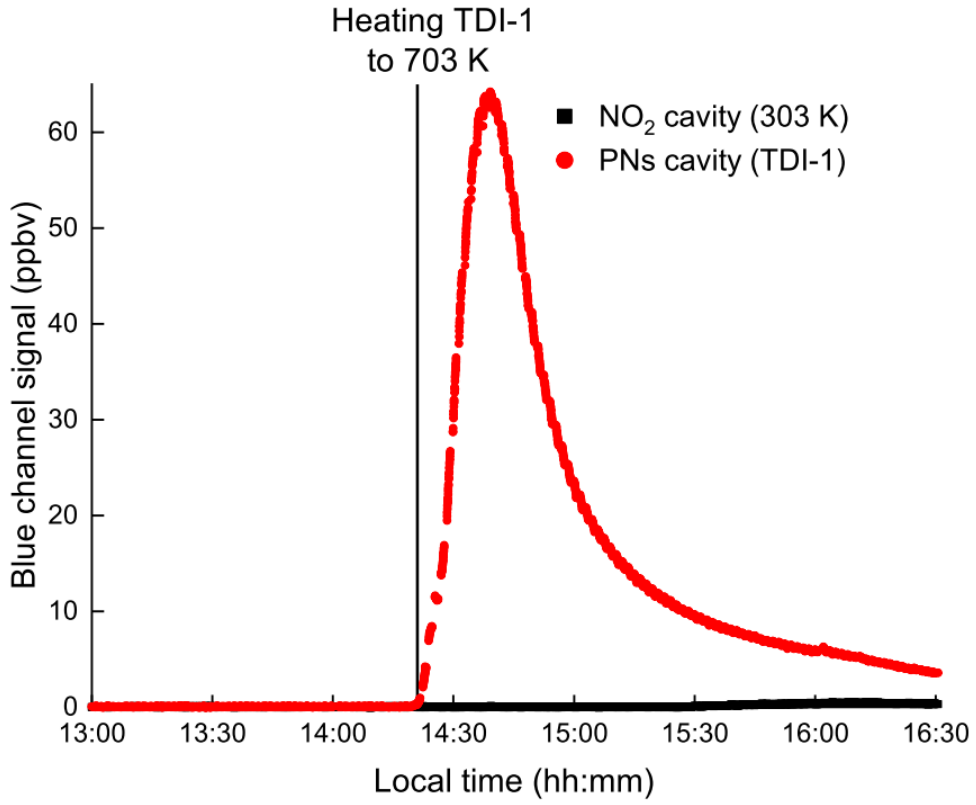

Figure S4: Unexpected detection of NO_2 in dry synthetic air when adding 120 ppbv O_3 to TDI-1. Initially, TDI-1 was at room temperature, with heating (to 703 K) of the TDI starting at ~14:20. When sampling via TDI-1 ~ 60 ppbv of NO_2 were observed, while no signal was registered when sampling into the NO_2 cavity through a cold inlet.

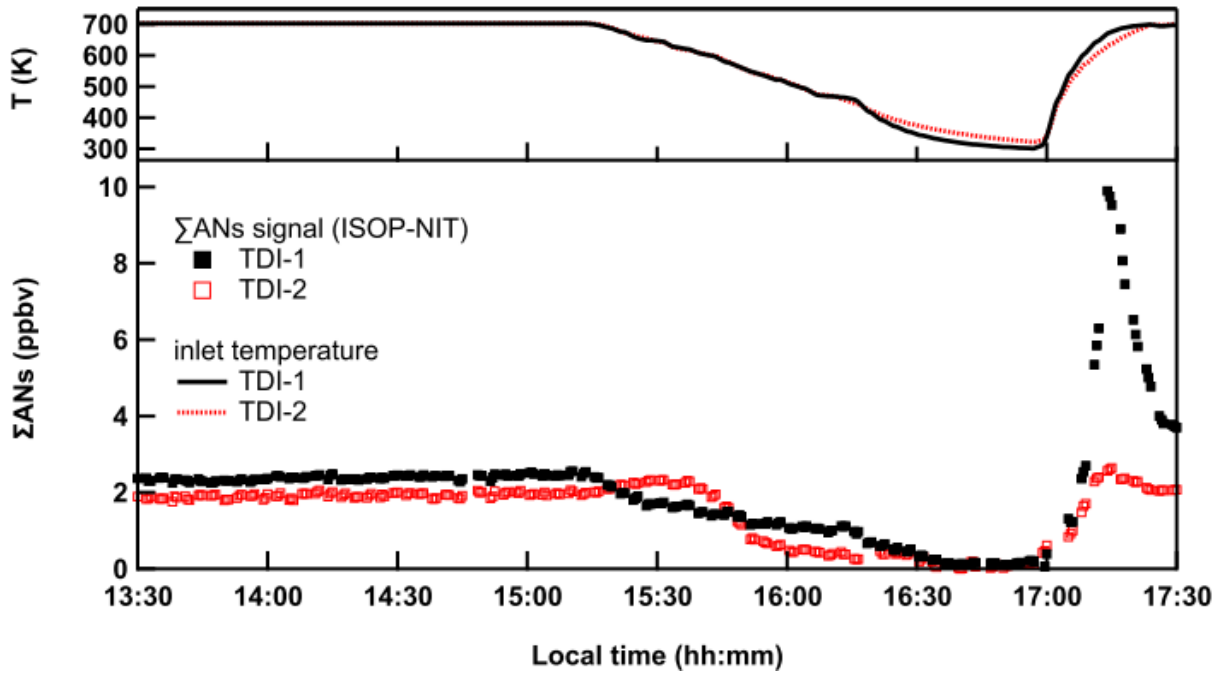

Figure S5: Mixing ratios of ISOP-NIT when sampling via TD-1 and TD-2 and different temperatures. ISOP-NIT was formed by flowing NO_2 (150 sccm of 1 ppmv) isoprene (9.8 sccm of 46.5 ppmv) and O_3 in 15 SLPM synthetic air into the SCHARK. The solid and dotted lines in the upper panel indicate the temperature of each TDI. At ~15:15 LT (when the signals were stable and the system in steady-state) the TDI temperatures were decreased to obtain a thermogram. For 30 min, starting at 16:30 LT both TDIs were kept close to room temperature before being re-heated to ~700 K at 17:00 LT. The strong increase in signal (above that observed at e.g. 15:00) observed when sampling via TD-1 indicates that ISOP-NIT can deposit on the glass beads and frit at lower temperatures. This effect is not observed for TDI-2 and is clearly related to the use of the glass-beads.

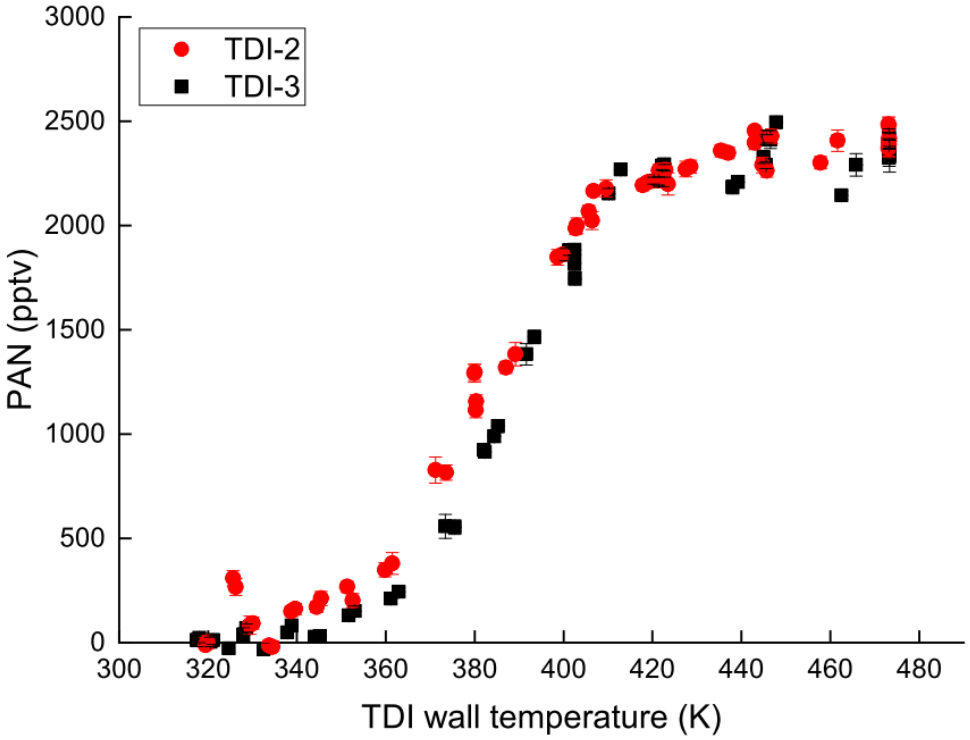

Figure S6: Thermograms of peroxy acetyl nitrate (PAN) obtained when sampling via TDI-2 and TDI-3. PAN (together with ~ 1.2 ppbv NO_2) was produced from a photochemical source as described recently (Eger et al., 2019) using the 285 nm photolysis of acetone in the presence of NO (Warneck and Zerbach, 1992; Flocke et al., 2005). The error bars represent standard deviation (1σ, 1 min) of the signal.

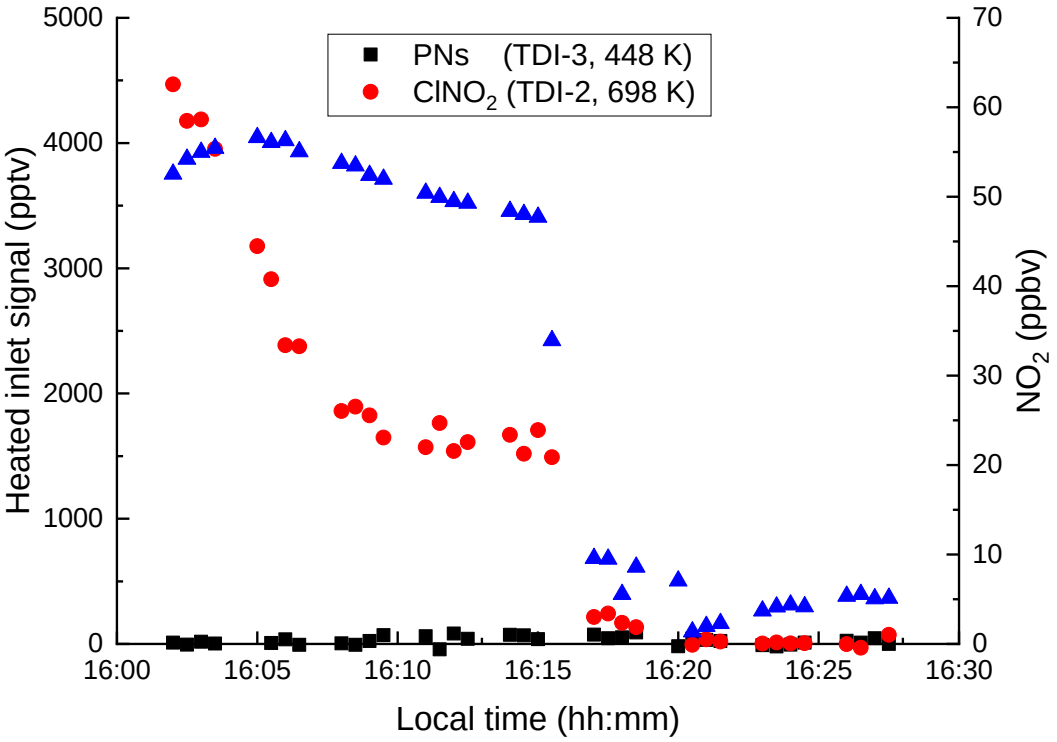

Figure S7: Mixing ratios of NO_2, PNs (measured with TDI-3 at 448 K) and $ClNO_2$ (measured with TDI-2 at 698 K) recorded with the TD-CRDS setup during an experiment in which Cl_2 (1-10 sccm of 50 ppmv in N_2) was passed through a glass bulb with sodium nitrate and diluted in 10 SLPM dry synthetic air. Variation of the amounts of $ClNO_2$ and NO_2 was achieved by changing the flow of Cl_2. The NO_2 signal measured with an unheated inlet was subtracted from the channels with TDIs. Note that, as expected, no signal additional to NO_2 was observed with TDI-3 at 448 K. Using TDI-2 at 698 K, $ClNO_2$ was detectable implying that it interferes detection of ANs.

S8 Detection of PAN, HONO and HNO_3 with I-CIMS

A chemical ionization mass spectrometer using iodide primary ions (I-CIMS) described recently (Dörich et al., 2021) was deployed to detect PAN, HONO and HNO_3. The I-CIMS was coupled to the SCHARK via ≈ 2m of ¼ inch PFA tubing heated to 40 °C. The flow rate through the PFA-tubing was ~2.1 SLM. Iodide anions were generated by passing 4 sccm of 400 ppmv methyl iodide (CH_3I in N_2) diluted in 750 sccm N_2 (Westfalen, 5.0) through a 370 MBq polonium (^{210}Po) source. PAN was thermally dissociated in an heated inlet (PFA tube at 170°C, residence time of 40 ms) to peroxy acetyl radicals which are detected as acetate ions $CH_3CO_2^-$ (*m/z* 59) after reaction with I^- (Phillips et al., 2013). Calibration was performed using a photochemical PAN source (Warneck and Zerbach, 1992). HNO_3 was detected as the $I^-(HNO_3)$ cluster ion at *m/z* 190 and calibrated using an HNO_3 permeation source characterised by optical absorption. HONO was detected as NO_2^- (*m/z* 46) using acetate anions (Veres et al., 2008) generated by adding a high concentration of PAN to the TD-inlet.

S9 Reaction scheme used for numerical simulations in inlets

```
*  Thermolysis of ozone and alkyl nitrates               ;

* ======================================================= ;
variable N2O5 NO3 NO OH HO2 HNO3 H2O2 HONO
HO2NO2 H2O ISOP O PROD PROD1 PROD2 ISOPNIT O3 NO2         ;
* ------------------------------------------------------- ;
* INITIAL CONCENTRATIONS                                  ;
* ------------------------------------------------------- ;
parameter O3i    3.53e12                                  ;
parameter NO2i   8.83e10                                 ;
parameter ISOPi  1.8e11                                  ;
parameter NO3i   8.82e7                                  ;
parameter N2O5i  8.82e8                                  ;
parameter NOi    0.0e10                                  ;
parameter O2                                             ;
parameter k1 k2 k2 k3 k4 k5 k6 k7 k8 k9 k10 k11 k12 k13 k14;
parameter k15 k16 k17 k18 k19 k20 k21 k22 k23 k24 k25 k26  ;
parameter k27 k28 k29 k30 k31 k32 k33 k34 k35              ;
parameter M                                              ;
parameter ISOPNITi 1.8E10                                ;
parameter kWall 90                                       ;
* ------------------------------------------------------- ;
parameter P 543.478                                      ;
parameter T 298                                          ;
* -------------------------------------------------------;
*                                                        ;
COMPILE GENERAL                                          ;
M = P * 3.24E16 * 298/T                                  ;
O2 = 0.2*M                                               ;
**                                                       ;
COMPILE INITIAL                                          ;
N2O5  = N2O5i                                            ;
NO2 = NO2i                                               ;
O3 = O3i                                                 ;
O2 = O2i                                                 ;
NO = NOi                                                 ;
NO3 = NO3i                                               ;
ISOP = ISOPi                                             ;
ISOPNIT = ISOPNITi                                       ;
**                                                       ;
COMPILE EQUATIONS                                        ;
* -------------------------------------------------------;
* HOx and NOx chemistry                                  ;
*-------------------------------------------------------;
% k1               : N2O5 = NO3 + NO2                   ;
% k2               : NO2 + NO3 = N2O5                   ;
% k3               : NO + NO3 = NO2 + NO2               ;
% k4               : NO2 + O3 = NO3 + O2                ;
% k5               : NO + O3 = NO2 + O2                 ;
% k6               : OH + O3 = HO2 + O2                 ;
% k7               : HO2 + O3 = OH + O2 + O2            ;
% k8               : OH + HO2 = H2O + O2                ;
% k9               : OH + NO2 = HNO3                    ;
% k10              : OH + NO3 = HO2 + NO2               ;
% k11              : HO2 + NO3 = OH + NO2 + O2          ;
% k12              : OH + H2O2 = HO2 + H2O              ;
% k13              : HO2 + HO2 = H2O2 + O2              ;
% k14              : OH + NO = HONO                     ;
% k15              : HO2 + NO = OH + NO2                ;
% k16              : HO2 + NO2 = HO2NO2                 ;
% k17              : HO2NO2 + OH = NO2 + H2O + O2       ;
% k18              : OH + HONO = NO2 + H2O              ;
% k19              : OH + HNO3 = NO3 + H2O              ;
% k20              : HO2NO2 = HO2 + NO2                 ;
*-------------------------------------------------------;
* ISOPRENE oxidation                                     ;
*-------------------------------------------------------;
% k21*0.74         : ISOP + O3 = PROD                   ;
% k21*0.26         : ISOP + O3 = OH                     ; IUPAC recommended yield
% k22              : ISOP + NO3 = PROD                  ;
```

```
% k23               : ISOP + OH = PROD                 ;
*-----------------------------------------------------;
* Ox chemistry                                        ;
*-----------------------------------------------------;
% k24               : O3 = O + O2                      ; Peukert et al.
% k25               : O + O3 = O2 + O2                 ; IUPAC
% k26               : O + O2 = O3                      ; IUPAC
% k27               : O + H2O = OH + OH                ;
% kWall             : O =                              ;
% k28               : NO2 + O = O2 + NO                ; bimolecular
% k29               : NO2 + O = NO3                    ; termolecular
% k30               : NO3 + O = O2 + NO2               ;
% k31               : O + NO = NO2                     ;
*-----------------------------------------------------;
* Thermolysis of alkyl nitrates                       ;
*-----------------------------------------------------;
% k32             : ISOPNIT = NO2 + PROD1              ;
% k33             : ISOPNIT + O = NO2 + PROD2 + O2     ;
% k34             : ISOP + O = PROD                    ;
% k21             : ISOPNIT + O3 = NO2 + PROD2 + OH    ;
*-----------------------------------------------------;
*Rate equations                                       ;
k1 = ((1.3e-3*(T/300)@-3.5*exp(-11000/T))*M*
(9.7e14*(T/300)@0.1*exp(-11080/T)))/((1.3e-3*
(T/300)@-3.5*exp(-11000/T))*M+(9.7e14*(T/300)@0.1*
exp(-11080/T)))*10@(log10(0.35)/(1+(log10((1.3e-3*(T/300)@-3.5
*exp(-11000/T))*M/(9.7e14*(T/300)@0.1*exp(-11080/T)))
/(0.75-1.27*log10(0.35)))@2))                        ; N2O5 decomp IUPAC
k2 = ((3.6e-30*(T/300)@-4.1)*M*(1.9e-12*(T/300)@0.2))
/((3.6e-30*(T/300)@-4.1)*M+(1.9e-12*(T/300)@0.2))*
10@(log10(0.35)/(1+(log10((3.6e-30*(T/300)@-4.1)*
M/(1.9e-12*(T/300)@0.2))/(0.75-1.27*log10(0.35)))@2))  ; NO2 + NO3 IUPAC
k3 = 1.8E-11*exp(110/T)                              ;IUPAC NO + NO3 (220-420)K
k4 = 1.4E-13 * exp (-2470/T)                         ;IUPAC NO2 + O3 (230-360)K
k5 = 2.07E-12 * exp (-1400/T)                        ;IUPAC NO + O3 (195-310)K
k6 = 1.70E-12*EXP(-940/T)                            ;IUPAC OH + O3 (220-450)K
k7 = 2.03E-16*(T/300)@4.57*EXP(693/T)                ;IUPAC HO2 + O3 (250-340)K
k8 = 4.8E-11*EXP(250/T)                              ;IUPAC HO2 + OH (250-400)K
k9 = ((3.2e-30*(T/300)@-4.5)*M*(3.0e-11))/
((3.2e-30*(T/300)@-4.5)*M+(3.0e-11))*10@(log10(0.41)/
(1+(log10((3.2e-30*(T/300)@-4.5)*M/(3.0e-11))/
(0.75-1.27*log10(0.41)))@2))                         ; IUPAC HNO3 formation
k10 = 2E-11                                          ; IUPAC OH + NO3 (298K)
k11 = 4E-12                                          ; IUPAC HO2 + NO3 (298K)
k12 = 2.9E-12*exp(-160/T)                            ; IUPAC OH + H2O2 (240-460)K
k13 = 2.20E-13*(1+(1.40E-21*EXP(2200/T)*H2O))*EXP(600/T)   ; IUPAC H2O2 formation (230-420)K
k14 = ((7.4e-31*(T/300)@-2.4)*M*(3.3e-11*(T/300)@-0.3))/
((7.4e-31*(T/300)@-2.4)*M+(3.3e-11*(T/300)@-0.3))*
10@(log10(0.81)/(1+(log10((7.4e-31*(T/300)@-2.4)*M/
(3.3e-11*(T/300)@-0.3))/(0.75-1.27*log10(0.81)))@2))  ; IUPAC HONO formation
k15 = 3.45E-12*exp(270/T)                            ; IUPAC HO2 + NO (200-400)K
k16 = ((1.4e-31*(T/300)@-3.1)*M*(4.0e-12))/
((1.4e-31*(T/300)@-3.1)*M+(4.0e-12))*10@(log10(0.4)/
(1+(log10((1.4e-31*(T/300)@-3.1)*M/(4.0e-12))/
(0.75-1.27*log10(0.4)))@2))                          ; IUPAC HO2 + NO2
k17 = 3.2e-13*EXP(690/T)                             ; IUPAC HO2NO2 + OH (210-300)K
k18 = 2.5e-12*EXP(260/T)                             ; IUPAC HONO + OH (290-380)K
k19 = 2.40E-14*EXP(460/T) + ((6.50E-34*EXP(1335/T)*M)/
(1+(6.50E-34*EXP(1335/T)*M/2.70E-17*EXP(2199/T))))   ; IUPAC OH + HNO3
k20 = ((4.1e-5*exp(-10650/T))*M*(6.0e15*exp(-11170/T)))/
((4.1e-5*exp(-10650/T))*M+(6.0e15*exp(-11170/T)))*
10@(log10(0.4)/(1+(log10((4.1e-5*exp(-10650/T))*M/
(6.0e15*exp(-11170/T)))/(0.75-1.27*log10(0.4)))@2))  ; IUPAC HO2NO2 decomposition
k21 = 1.05E-14*exp(-2000/T)                          ; O3 + ISOP - IUPAC
k22 = 2.95E-12*exp(-450/T)                           ; NO3 + ISOP - IUPAC
k23 = 2.1E-11*exp(465/T)                             ; OH + ISOP - IUPAC
k24 = (37800*(T@-4.37)*EXP(-13738/T))*M*(1370000000000000*
(T@-0.67)*EXP(-13080/T))*10@(LOG10((1-0.647)*
EXP(-T/0.000391)+0.6417*EXP(-T/8680.74)+EXP(-6060.75/T))/
(1+(LOG10((37800*(T@-4.37)*EXP(-13738/T))*M/
(1370000000000000*(T@-0.67)*EXP(-13080/T)))/
(0.75-1.27*LOG10((1-0.647)*EXP(-T/0.000391)+0.6417*
EXP(-T/8680.74)+EXP(-6060.75/T))))@2))/
```

```
((37800*(T@-4.37)*EXP(-13738/T))*M+(1370000000000000*(T@-0.67)*
EXP(-13080/T)))                                          ; O3 thermolysis (T>700K), Peukert et al., 2013
k25 = 8E-12*exp(-2060/T)                                 ; IUPAC O + O3 (200-400)K
k26 = 6.0E-34*((T/300)@-2.6)*M                           ; IUPAC O + O2 (200-300)K
k27 = 8.44E-14*(T@0.946)*exp(-8571/T)                    ; O(3P) + H2O (250-2400)K Lifshitz et al., 1990
k28 = 5.1E-12*exp(198/T)                                 ; IUPAC NO2 + O (220-420)K
k29 = ((1.3e-31*(T/300)@-1.5)*M*(2.3e-11*(T/300)@0.24))/
((1.3e-31*(T/300)@-1.5)*M+(2.3e-11*(T/300)@0.24))*10@(log10(0.6)/
(1+(log10((1.3e-31*(T/300)@-1.5)*M/(2.3E-11*(T/300)@0.24))/
(0.75-1.27*log10(0.6)))@2))                              ; IUPAC termol NO2 + O
k30 = 1.7E-11                                            ; IUPAC NO3 + O (298K)
k31 = ((1.0e-31*(T/300)@-1.6)*M*(5e-11*(T/300)@-0.3))/
((1.0e-31*(T/300)@-1.6)*M+(5e-11*(T/300)@-0.3))*10@(log10(0.85)/
(1+(log10((1.0e-31*(T/300)@-1.6)*M/(5e-11*(T/300)@-0.3))/
(0.75-1.27*log10(0.85)))@2))                             ; IUPAC O + NO

k32 = 7.34E15*exp(-19676/T)                              ; thermolysis n-propylnitrate
k33 = 3.9E-12*exp(680/T)                                 ; 2-methyl-2-butene - Herron & Huie, 1973 (298-400K)
k34 = 3.5E-11                                            ; Paulson et al., 1995 (298K)
**                                                      ;
COMPILE INSTANT                                         ;
open 7   "thermo.sim" new                               ;
**                                                        ;
COMPILE BLOCK 3                                           ;
PSTREAM 3                                                 ;
**                                                        ;
COMPILE BLOCK 4                                           ;
T = 425                                                   ;
**                                                        ;
COMPILE BLOCK 5                                           ;
T = 298                                                   ;
**                                                        ;
COMPILE BLOCK 6                                           ;
T = 303                                                   ;
**                                                        ;
PSTREAM 3 7                                               ;
time O3 O NO2 M T PROD1 PROD2 ISOPNIT                     ;
**                                                        ;
when
1)  time = 0 + 0.01*128 call block 3                      ;
2)  time = 0.007 call block 4 restart                     ;
3)  time = 0.335 call block 5   restart                    ;
4)  time = 1.08 call block 6  restart                     ;
**                                                        ;
*hmax 0.01                                                ;
BEGIN                                                     ;
STOP                                                      ;
```

References

Dörich, R., Eger, P., Lelieveld, J., and Crowley, J. N.: Iodide-CIMS and m/z 62: The detection of HNO_3 as NO_3^- in the presence of PAN, peracetic acid and O3, Atmos. Meas. Tech. Discuss., 2021, 1-26, doi:10.5194/amt-2021-57, 2021.

Eger, P. G., Helleis, F., Schuster, G., Phillips, G. J., Lelieveld, J., and Crowley, J. N.: Chemical ionization quadrupole mass spectrometer with an electrical discharge ion source for atmospheric trace gas measurement, Atmos. Meas. Tech., 12, 1935-1954, doi:10.5194/amt-12-1935-2019, 2019.

Flocke, F. M., Weinheimer, A. J., Swanson, A. L., Roberts, J. M., Schmitt, R., and Shertz, S.: On the measurement of PANs by gas chromatography and electron capture detection, J. Atmos. Chem., 52, 19-43, 2005.

Phillips, G. J., Pouvesle, N., Thieser, J., Schuster, G., Axinte, R., Fischer, H., Williams, J., Lelieveld, J., and Crowley, J. N.: Peroxyacetyl nitrate (PAN) and peroxyacetic acid (PAA) measurements by iodide chemical ionisation mass spectrometry: first analysis of results in the boreal forest and implications for the measurement of PAN fluxes, Atmospheric Chemistry and Physics, 13, 1129-1139, doi:10.5194/acp-13-1129-2013, 2013.

Veres, P., Roberts, J. M., Warneke, C., Welsh-Bon, D., Zahniser, M., Herndon, S., Fall, R., and de Gouw, J.: Development of negative-ion proton-transfer chemical-ionization mass spectrometry (NI-PT-CIMS) for the measurement of gas-phase organic acids in the atmosphere, Int. J. Mass Spectrom., 274, 48-55, doi:10.1016/j.ijms.2008.04.032, 2008.

Warneck, P., and Zerbach, T.: Synthesis of peroxyacetyl nitrate in air by acetone photolysis, Environ. Sci. Technol., 26, 74-79, doi: 10.1021/es00025a005, 1992.

APPENDIX C

Supplement of Chapter 6

Supplement

S1 Calibration of the FT-CRDS with NO

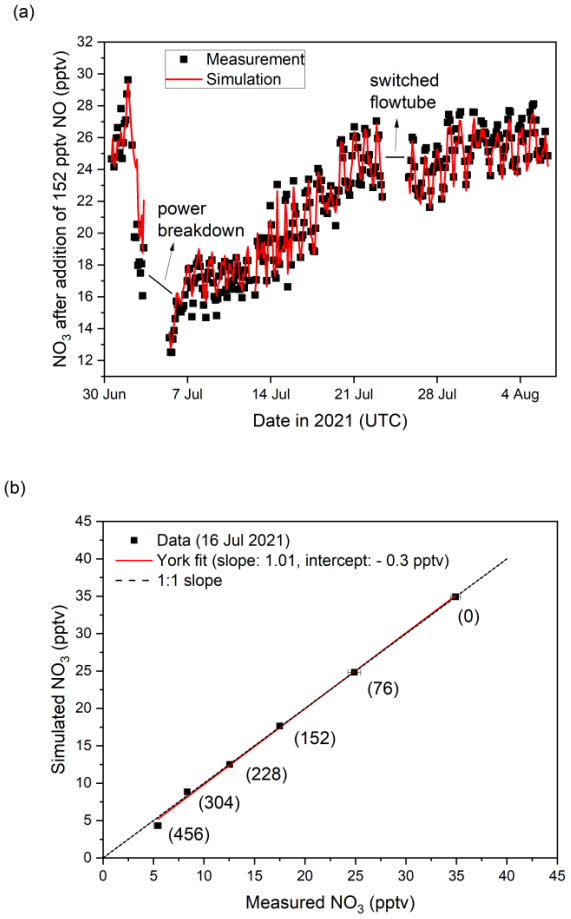

Figure S1: (a) Measured and simulated mixing ratios of (synthetic) NO_3 in the flow-tube obtained after adding 152 pptv of NO ca. every two hours. Ticks represent 00:00 UTC. (b) Comparison between measured and simulated mixing ratios after adding five different, known amounts of NO (values in brackets denote added NO concentrations in pptv). The red line represents a York fit (slope = 1.01 and an intercept of -0.3 pptv). Dashed line indicates 1:1 agreement.

S2 Intercomparison of NO_2 measurements

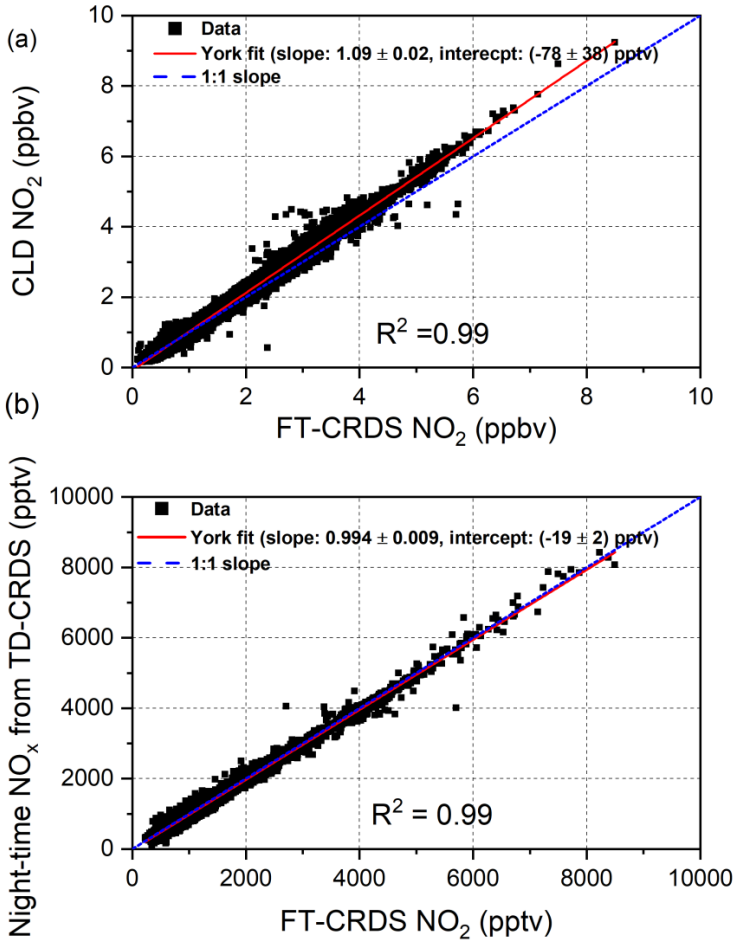

Figure S2: Correlation between NO_2 mixing measured with the FT-CRDS setup and (a) night-time NO_x mixing ratios measured with the TD-CRDS setup (b) NO_2 mixing ratios measured with the CLD instrument. The red solid line indicates a York fit, while the dashed blue line represents an ideal 1:1 agreement.

S3 Wind direction and NO_3 reactivity

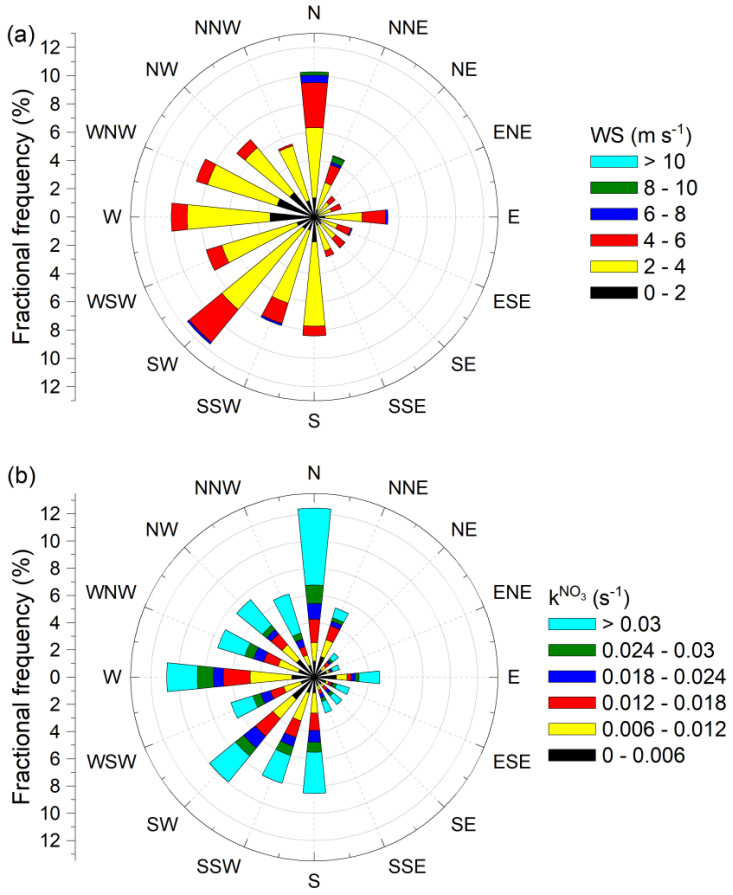

Figure S3: Wind rose of (a) wind speed and (b) NO_3 reactivity measured during the TO2021 campaign.

S4 VOC measurements

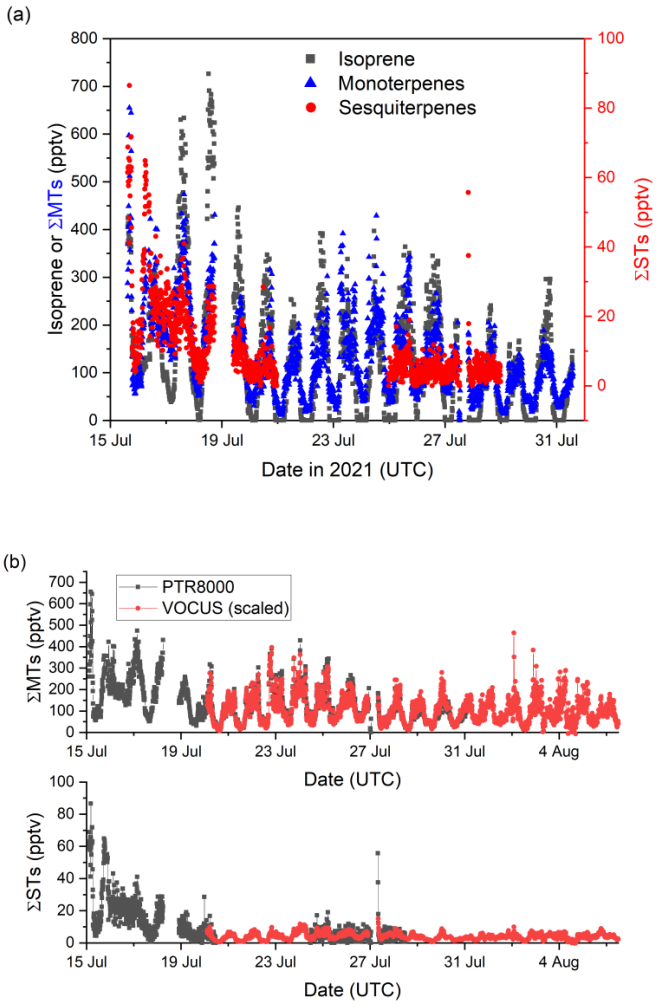

Figure S4: (a) Time-trace of PTR-MS measurements (PTR8000) of isoprene (black squares, left axis), the sum of monoterpenes (ΣMTs, blue triangles, left axis) and the sum of sesquiterpenes (ΣSTs, red circles, right axis) during the second half of the TO2021 campaign. Major ticks mark 00:00 UTC. (b) Time-series of monoterpenes signals (upper panel) and sesquiterpene signals (lower panel) from the VOCUS data (red) scaled to the calibrated data from the PTR8000 setup (black).

S5 Nighttime NO: Model calculation and correlation plots

```
*  NIGHTIME NO EMISSION SIMULATION                          ;
* ================================                          ;
variable N2O5 NO3 NO2 O2                                    ;
* ----------------------------------------                   ;
* INITIAL CONCENTRATIONS                                     ;
* ----------------------------------------                   ;
parameter T 284.6                                           ;
parameter O3i 6137372069288.082                             ;
parameter NOi 1E-99                                         ;
parameter P 688                                             ;
parameter M                                                  ;
parameter k1                                                 ;
parameter k2                                                 ;
parameter k3                                                 ;
parameter k4                                                 ;
parameter k5                                                 ;
parameter kVOC                                               ;
parameter kVOCi 0.03561                                      ;
parameter NO                                                 ;
parameter <5> INPARAM                                        ;
parameter varia press temp ozone EM                          ;
parameter kdep 1.5E-5                                        ;
* ---------------------------------------------------        ;
*                                                            ;
COMPILE GENERAL                                              ;
M = P * 3.24E16 * (298/T)                                    ;
**                                                           ;
COMPILE INITIAL                                              ;
NO  = NOi                                                    ;
O3 = O3i                                                     ;
kVOC = kVOCi                                                 ;
**                                                           ;
COMPILE EQUATIONS                                            ;
* ------------------------------------------------          ;
% k1                : N2O5 = NO3 + NO2                    ;
% k2                : NO2 + NO3 = N2O5                    ;
% k3                : NO + NO3 = NO2 + NO2                ;
% k4                : NO2 + O3 = NO3 + O2                 ;
% k5                : NO + O3 = NO2 + O2                  ;
% kVOC              : NO3 =                               ;
% kdep              : NO2 =                               ;
* ------------------------------------                       ;
*Rate equations                                              ;
k1 = ((1.3e-3*(T/300)@-3.5*exp(-11000/T))*M*
(9.7e14*(T/300)@0.1*exp(-11080/T)))/((1.3e-3*
(T/300)@-3.5*exp(-11000/T))*M+(9.7e14*(T/300)@0.1*
exp(-11080/T)))*10@(log10(0.35)/(1+(log10((1.3e-3*(T/300)@-3.5
*exp(-11000/T))*M/(9.7e14*(T/300)@0.1*exp(-11080/T)))
/(0.75-1.27*log10(0.35)))@2))                               ; N2O5 decomp IUPAC
```

```
k2 = ((3.6e-30*(T/300)@-4.1)*M*(1.9e-12*(T/300)@0.2))
/((3.6e-30*(T/300)@-4.1)*M+(1.9e-12*(T/300)@0.2))*
10@(log10(0.35)/(1+(log10((3.6e-30*(T/300)@-4.1)*
M/(1.9e-12*(T/300)@0.2))/(0.75-1.27*log10(0.35)))@2))      ; NO2 + NO3 IUPAC
k3 = 1.8E-11*exp(110/T)                                    ;IUPAC
k4 = 1.4e-13 * exp (-2470/T)                               ;IUPAC
k5 = 2.07e-12 * exp (-1400/T)                              ;IUPAC
**                                                        ;
COMPILE INSTANT                                           ;
open 7   "no3.sim" new                                    ;
open 20 "forFAC.dat" old                                  ;
**                                                        ;
COMPILE BLOCK 3                                           ;
PSTREAM 3                                                 ;
**                                                        ;
COMPILE BLOCK 4                                           ;
READ 20 INPARAM <5>                                       ;
varia = INPARAM<0>                                        ;
press = INPARAM<1>                                        ;
temp = INPARAM<2>                                         ;
ozone = INPARAM<3>                                        ;
EM = INPARAM<4>                                           ;

P = press                                                 ;
T = temp                                                  ;
NO = EM                                                   ;
O3 = ozone                                                ;
KVOC = varia                                              ;
**                                                        ;
PSTREAM 3 7                                               ;
time NO NO3 NO2 O3 N2O5 M T kVOC                          ;
**                                                        ;
when
1)  time = 0 + 600*1798 call block 3                      ;
2)  time = time + 600 call block 4 restart                ;
**                                                        ;
*hmax 0.1                                                 ;
BEGIN                                                     ;
STOP                                                      ;
```

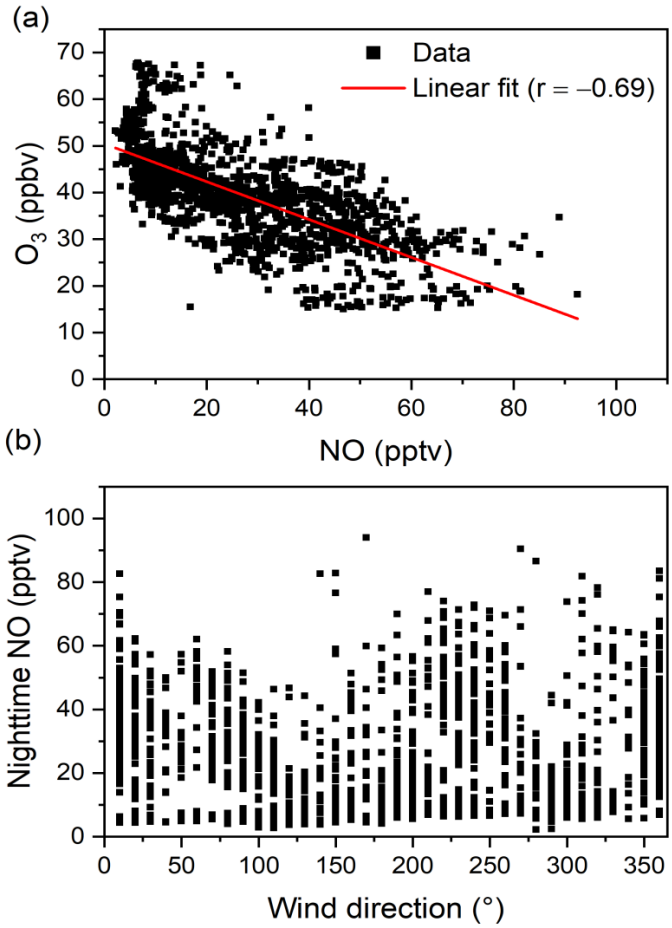

130 **Figure S5**: (a) Nighttime NO mixing ratios plotted against O_3. The red line represents a linear, least-squares fit (correlation coefficient r is −0.69). (b) Dependence of nighttime NO mixing ratios on the wind direction.

S6 Previous measurements on the Kleiner Feldberg

Table S1: Overview of the key parameters of the set-ups deployed to measure NO_2, O_3 and NO_3 mixing ratios during the TO2008, PARADE, INUIT and NOTOMO campaign on the Kleiner Feldberg.

Campaign (Reference)	**NO_2**	**O_3**	**NO_3**
		LOD (Uncertainty) Method; Reference	
TO2008	80 pptv (10%)	2 ppbv (5%)	1-2 pptv (15%)
(Crowley et al., 2010)	CLD; Crowley et al., 2010	UV, Crowley et al., 2010	CRDS; Schuster et al. 2009
PARADE	30 pptv (6%)	1 ppbv (5%)	2 pptv (15%)
(Sobanski et al., 2016b)	CRDS; Thieser et al., 2016	UV; Drewnick et al., 2012	CRDS; Schuster et al., 2009
INUIT	30 pptv (6%)	1 ppbv (5%)	2 pptv (15%)
	CRDS; Thieser at al., 2016	UV; Drewnick et al., 2012	CRDS; Schuster et al., 2009
NOTOMO	60 pptv (6.5%)	2 ppbv (2%)	1.5 pptv (25%)
(Sobanski et al., 2017)	CRDS; Sobanski et al., 2016a	UV; Sobanski et al., 2016b	CRDS; Sobanski et al., 2016a

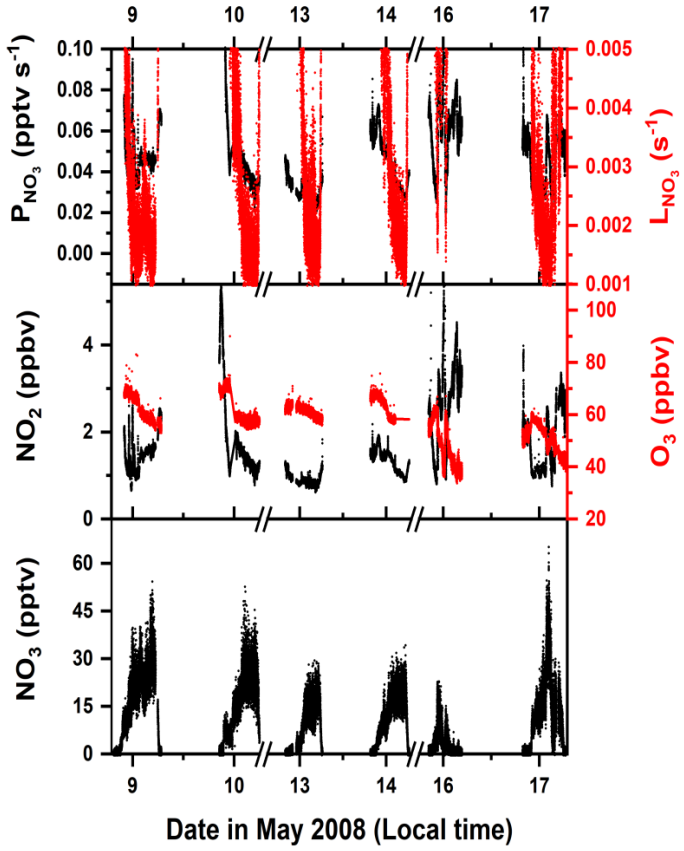

Figure S6: Time-series of NO_3, NO_2 and O_3 mixing ratios as well as NO_3 production and loss rates during the TO2008 campaign. Major ticks represent 00:00 local time. Data was published in Crowley et al. (2010).

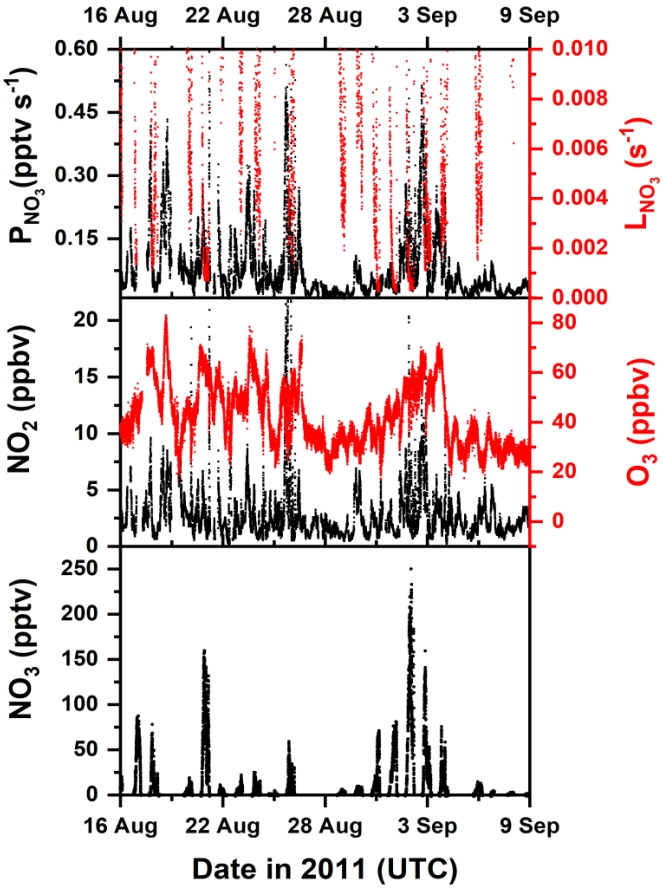

145 **Figure S7:** Time-series of NO_3, NO_2 and O_3 mixing ratios as well as NO_3 production and loss rates during the PARADE campaign. Major ticks represent 00:00 UTC. Data was published in Sobanski et al. (2016b).

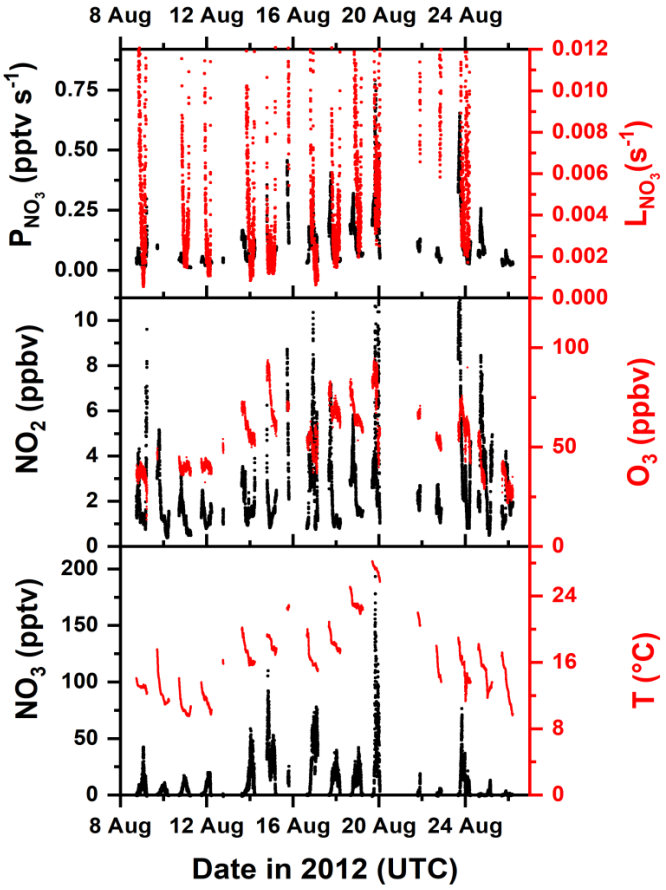

Figure S8: Time-series of temperature, NO_3, NO_2 and O_3 mixing ratios as well as NO_3 production and loss rates during the INUIT campaign. Major ticks represent 00:00 UTC.

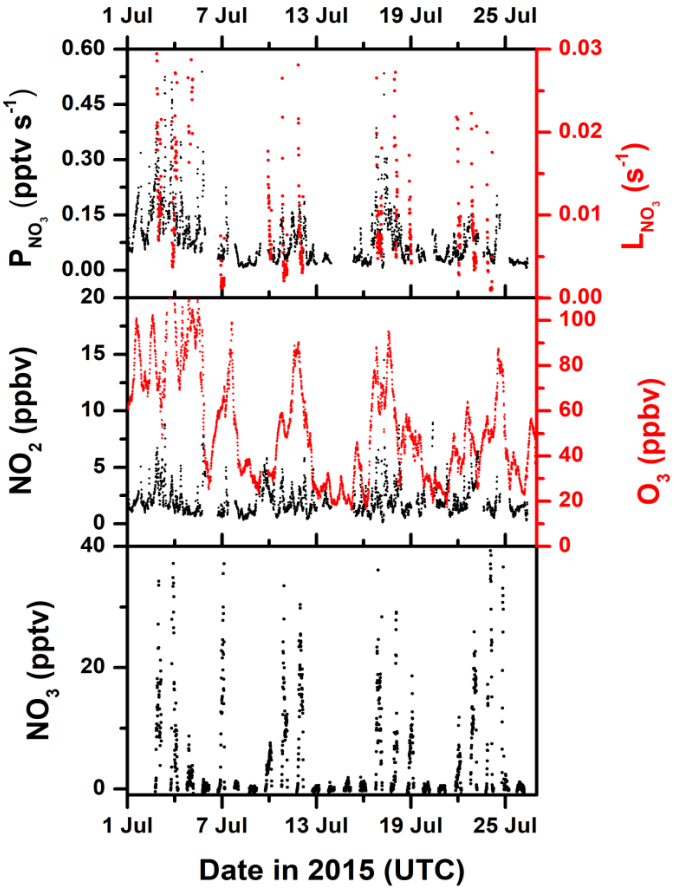

Figure S9: Time-series of NO_3, NO_2 and O_3 mixing ratios as well as NO_3 production and loss rates during the NOTOMO campaign. Major ticks represent 00:00 UTC. Data was published in Sobanski et al. (2017).

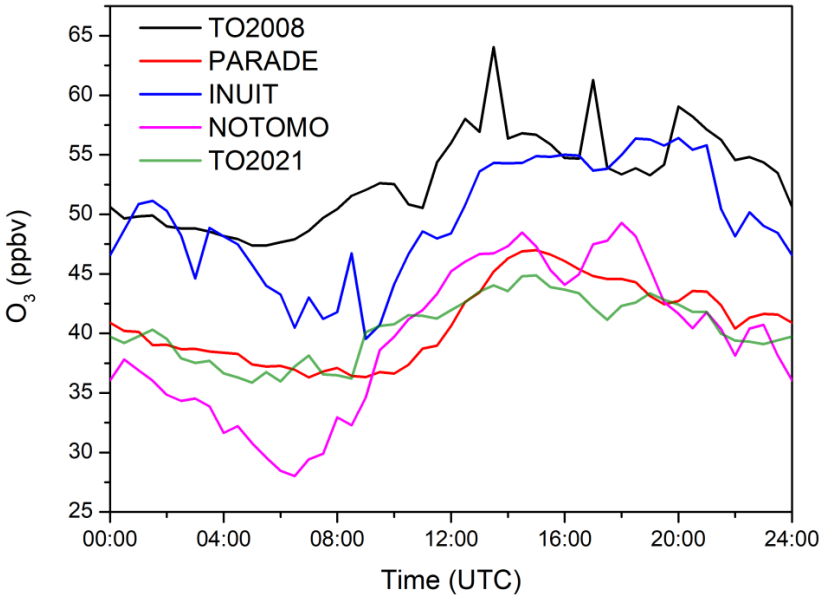

Figure S10: Median diel cycles of O_3 mixing ratios measured during TO2008, PARADE, INUIT, NOTOMO and TO2021.

160

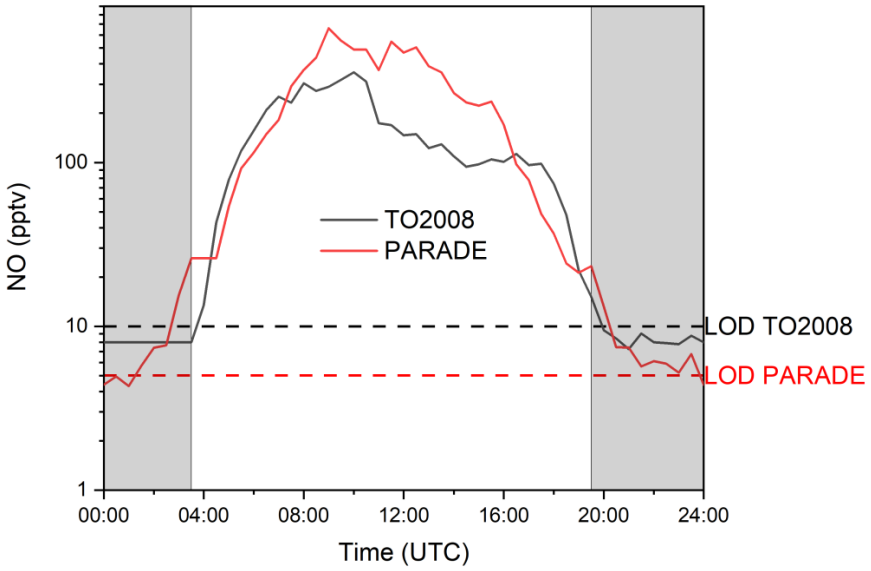

Figure S11: Median diel cycles of NO mixing ratios during TO2008 (black) and PARADE (red). Both measurements were performed with a previous modification of the same CLD setup (Li et al., 2015) described in the main text. Dashed line mark the LODs during the corresponding campaigns. Grey shaded areas denote the nighttime period.

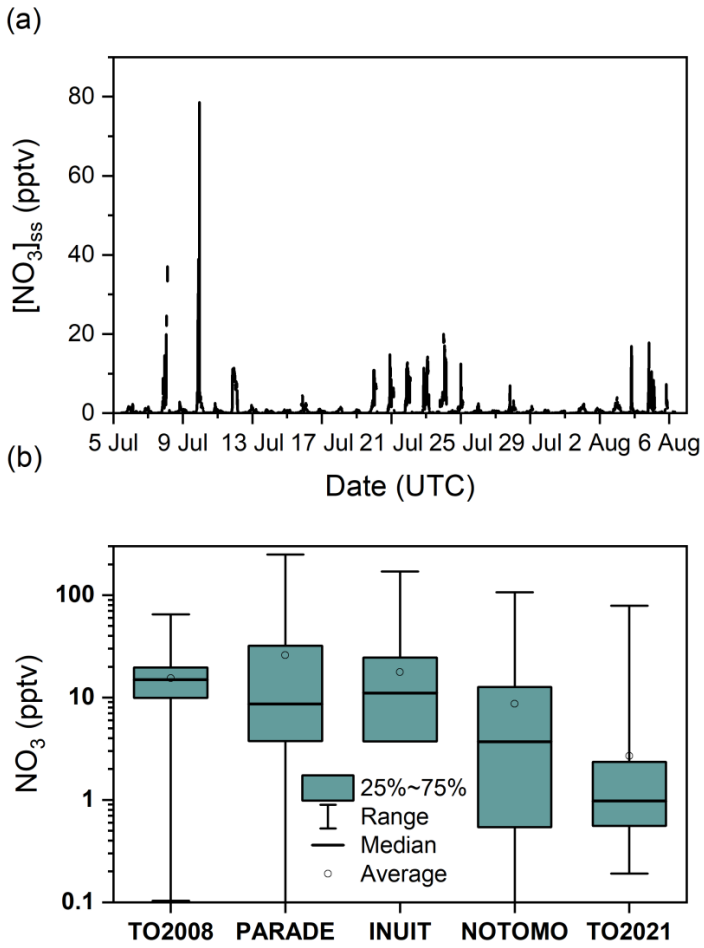

Figure S12: (a) Calculated NO_3 mixing ratios according to Eq. (4) for TO2021 with values for k^{NO_3} < LOD set to 0.002 s^{-1}. (b) Same as Fig. 13c in the main text but using nighttime NO_3 mixing ratios as in Fig. S12a.

References

Crowley, J. N., Schuster, G., Pouvesle, N., Parchatka, U., Fischer, H., Bonn, B., Bingemer, H., and Lelieveld, J.: Nocturnal nitrogen oxides at a rural mountain site in south-western Germany, Atmos. Chem. Phys., 10, 2795-2812, doi:10.5194/acp-10-2795-2010, 2010.

Drewnick, F., Boettger, T., von der Weiden-Reinmueller, S. L., Zorn, S. R., Klimach, T., Schneider, J., and Borrmann, S.: Design of a mobile aerosol research laboratory and data processing tools for effective stationary and mobile field measurements, Atmos. Meas. Tech., 5, 1443-1457, doi:10.5194/amt-5-1443-2012, 2012.

IUPAC: Task Group on Atmospheric Chemical Kinetic Data Evaluation, edited by: Ammann, M., Cox, R.A., Crowley, J.N., Herrmann, H., Jenkin, M.E., McNeill, V.F., Mellouki, A., Rossi, M. J., Troe, J. and Wallington, T. J., available at: http://iupac.pole-ether.fr/index.html, last access: 4 January 2022.

Li, J., Reiffs, A., Parchatka, U., and Fischer, H.: In situ measurements of atmospheric CO and its correlation with NOx and O_3 at a rural mountain site, Metrol. Meas. Sys. , XXII, 25-38, doi:10.1515/mms-2015-0001, 2015.

Schuster, G., Labazan, I., and Crowley, J. N.: A cavity ring down / cavity enhanced absorption device for measurement of ambient NO_3 and N_2O_5, Atmos. Meas. Tech., 2, 1-13, doi:10.5194/amt-2-1-2009, 2009.

Sobanski, N., Schuladen, J., Schuster, G., Lelieveld, J., and Crowley, J. N.: A five-channel cavity ring-down spectrometer for the detection of NO_2, NO_3, N_2O_5, total peroxy nitrates and total alkyl nitrates, Atmos. Meas. Tech., 9, 5103-5118, doi:10.5194/amt-9-5103-2016, 2016a.

Sobanski, N., Tang, M. J., Thieser, J., Schuster, G., Pöhler, D., Fischer, H., Song, W., Sauvage, C., Williams, J., Fachinger, J., Berkes, F., Hoor, P., Platt, U., Lelieveld, J., and Crowley, J. N.: Chemical and meteorological influences on the lifetime of NO_3 at a semi-rural mountain site during PARADE, Atmos. Chem. Phys., 16, 4867-4883, doi:10.5194/acp-16-4867-2016, 2016b.

Sobanski, N., Thieser, J., Schuladen, J., Sauvage, C., Song, W., Williams, J., lelieveld, J., and Crowley, J. N.: Day- and Night-time Formation of Organic Nitrates at a Forested Mountain-site in South West Germany, Atmos. Chem. Phys., 17, 4115-4130, doi:10.5194/acp-17-4115-2017, 2017.

Thieser, J., Schuster, G., Phillips, G. J., Reiffs, A., Parchatka, U., Pöhler, D., Lelieveld, J., and Crowley, J. N.: A two-channel, thermal dissociation cavity-ringdown spectrometer for the detection of ambient NO_2, RO_2NO_2 and $RONO_2$, Atmos. Meas. Tech., 9, 553-576, doi:10.5194/amt-9-553-2016, 2016.

APPENDIX D

Supplement to Chapter 7

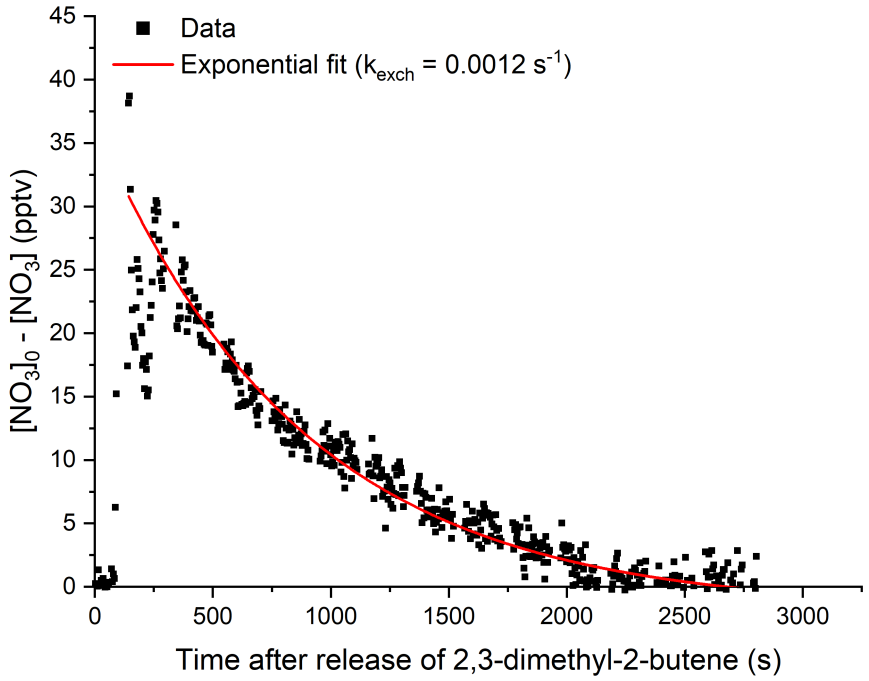

Figure D.1: *Difference between NO_3 mixing ratios before and after the release of 2,3-dimethyl-2-butene (DMB) similar to the experiment described in Fig. 7.1. The red line represents an exponential decay fit.*

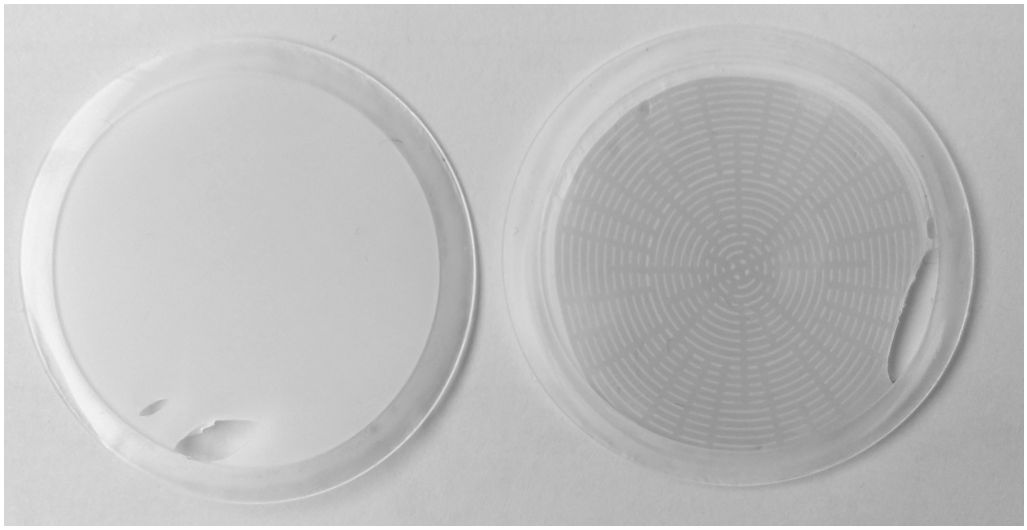

Figure D.2: *left: A new, unused filter for comparison. right: Teflon filter situated in front of the red channel after sampling lab air between friday afternoon and monday morning during the period in Fig.7.3. The filter is clearly darkened due to deposition of particles.*

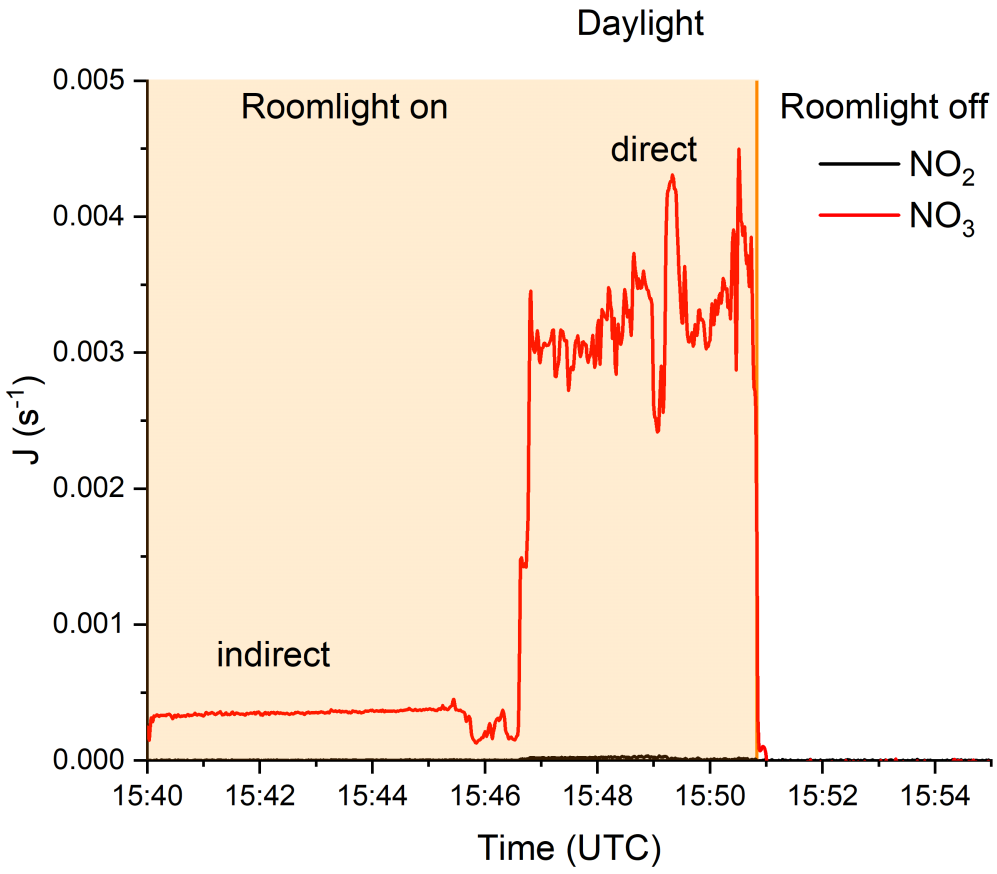

Figure D.3: *Photolysis rates of NO_2 (black line) and NO_3 during the day inside the laboratory. Orange shaded area marks the period when the roomlight was switched on. A small but negligible photoloysis rate < 0.005 s^{-1} was found for NO_3. No significant photolysis rates were observed for neither of the molecules as soon as room light was switched off.*

Acknowledgements - Danksagung

Mein Dank gilt von der für die Betreuung sowie für die Bereitschaft zur Übernahme des Erstgutachtens.
Ausserdem danke ich unter anderem für die Möglichkeit am unter sehr angenehmen Bedingungen zu forschen, für Anmerkungen bei der Durchsicht von Manuskripten und für die Finanzierung der Projekte.
Insbesondere danke ich für diverse (äußerst hilfreiche) Diskussionen und Denkanstöße, für die unendliche Geduld und auch für den ansteckenden Optimismus.
Ferner bedanke ich mich bei , der das PAC zusammen mit , und komplettiert hat. In diesem Zusammenhang auch ein Dankeschön an für den mentalen Support.
Bei bedanke ich für die andauernde Unterstützung bei technischen Fragen und natürlich für sehr viele aufheiternde Gespräche.
Für die sehr spaßige Zeit in der Arbeitsgruppe und am Institut bedanke ich mich ausserdem bei und .
Besonderer Dank gilt ausserdem (für langjährige mentale, aber auch sonstige Unterstützung) meiner und .

CURRICULUM VITAE